8-2014

# Projections of Future US Design Wind Speeds Due to Climate Change for Estimating Hurricane Losses

Fangqian Liu
*Clemson University*, fangqil@g.clemson.edu

# PROJECTIONS OF FUTURE US DESIGN WIND SPEEDS DUE TO CLIMATE CHANGE FOR ESTIMATING HURRICANE LOSSES

---

A Dissertation
Presented to
the Graduate School of
Clemson University

---

In Partial Fulfillment
of the Requirements for the Degree
Doctor of Philosophy
Civil Engineering

---

by
Fangqian Liu
August 2014

---

Accepted by:
Dr. Weichiang Pang, Committee Chair
Dr. Scott D. Schiff
Dr. Sezer Atamturktur
Dr. Nigel B. Kaye

# ABSTRACT

Hurricane is among the most dangerous and costliest natural hazards that affect the coastal environment of the United States (U.S.) every year. Hurricane activities have been observed to change in many aspects since the last century including the changes in both intensity and annual storm frequency. The extent to which aspect of climate change contributes to the variation in hurricane activities from long-term historical statistics is still not clearly understood at this point. This study examines the impacts of two climate change effects (change in annual storm frequency and sea surface temperature) on future U.S. design wind speeds for the coastal regions and projects potential hurricane losses under different speculated future climate scenarios.

To realize the goal of investigating climate change effect on hurricane activities, a baseline hurricane simulation model was first developed and was used to simulate 200,000 years of hurricanes without considering climate change effects. The landfall rates, central pressures at landfall and other relevant parameters of the simulated hurricanes were validated against historical observations. Next, the baseline hurricane simulation program was modified to include the effects of two climate change factors, namely, change in annual storm frequency and change in sea surface temperature (SST).

Three annual frequency models were utilized to simulate the effect of change in annual storm frequency. The first model is a baseline model which assumes the annual storm frequency to remain stationary over time with a constant mean and a constant standard deviation. The second model was a linear moving average (LMA) mean model which assumes the mean annual storm frequency follows a linear trend. The third model

was an oscillating moving average (OMA) model which has similar oscillating periods with the Atlantic multi-decadal oscillation of sea surface temperature. These three annual storms frequency models were used to simulate and project annual number of storms through the end of the century.

SST is one of the key inputs that affect the storm intensity. Its changes over time are projected based on the global climate models (GCMs) under multiple future climate scenarios in the United Nations Intergovernmental Panel on Climate Change (IPCC) fifth assessment report (AR5). Four SST projections were considered in this study. Similar to the annual storm frequency model, a baseline SST model, which assumes the mean SST remains stationary over time, was employed. The other three SST models were based on the IPCC Representative Concentration Pathway (RCP) of different greenhouse gases emission scenarios and projected radiative forcing for the year 2100. The three RCPs utilized in this study are (1) a climate change mitigation scenario leading to a very low forcing level of 2.6 $W/m^2$ (RCP2.6), (2) a medium stabilization scenario (RCP4.5) and (3) a high emission scenario (RCP8.5).

Six hurricane databases considering different climate change scenarios were generated. Each climate scenario considers the effects of changes in annual storm frequency and SST. Four scenarios consider the effects of changes in storm frequency and SST jointly while the other two scenarios consider the effects of changes in SST and annual storm frequency independent of each other.

Using the simulated hurricane databases, future design wind speeds under the speculated climate change scenarios were computed and compared to those in the current

design code (ASCE 7-10). It is found that the design wind speeds for Occupancy Category II (700 years MRI) buildings, which were developed based on the current climate condition, may increase significantly by the end of the century under the most drastic climate change scenario (increase in storm frequency and RCP8.5). While changes in annual storm frequency and SSTs both contribute to increases in design wind speeds, it was found that with the rise in SSTs having the most influence on design wind speeds.

In order to examine the influence of climate change on future hurricane activities and the associated hurricane losses in coastal environment, a hurricane simulation program was developed and the simulated hurricanes were utilized to perform loss assessments.

To evaluate the financial impact of climate change, loss estimations were performed using HAZUS-MH program for four coastal cities (New Orleans, LA, Miami, FL, Charleston, SC and New York, NY). A methodology to select hazard-consistent hurricane events for loss assessment was developed and ensembles of full-track hurricanes were selected for the four case study cities. The hurricane ensemble selection procedure was developed to capture the event-to-event uncertainty. In addition to consider changes in wind hazards, changes in building resistances (with and without wind retrofits) were also considered in loss estimation study. To evaluate the effectiveness of existing wind retrofits for mitigating the effects of climate change, it was assumed either none of the residential buildings were retrofitted or 100% of the residential buildings were retrofitted with all wind retrofits available in the HAZUS-MH program. From the

loss estimation study, it was determined that implementing wind retrofits is a win-win strategy regardless of whether the future hurricane wind hazard is rising or is stationary. Retrofitted buildings not only reduce the losses due to climate change but also the variability in the losses.

# DEDICATION

I dedicate this study to my parents, Mr. Honglin Liu (刘红林) and Mrs. Fang Sun (孙芳)

because of their love that make me go this far.

Also, I dedicate my work to Mr. Bin Pei (裴镔) who makes me stay and think.

.

# ACKNOWLEDGMENTS

I would like to express my gratitude to my advisor Dr. Weichiang Pang for the opportunity and instructions he gave me to complete my doctoral study. His guidance and support made me proceed on my study, especially when I met the “bottle necks”.

Also, I am grateful to my committee members Dr. Scott Schiff, Dr. Sezer Atamturktur and Dr. Nigel Kaye, for being supportive during the entire five years of my study.

I would like to thank my dear friends and colleagues, Michael Grayson and Alexander Kosloski for their helps on my research and courses.

Finally, I would like to present special thanks to Dr. Hui Wu from Beijing University of Civil Engineering and Architecture who encouraged me to study in the U.S, for his trust and devotion to his students.

This study acknowledges the World Climate Research Programme's Working Group on Coupled Modelling, which is responsible for CMIP, and we thank the climate modeling group for producing and making available their model output. For CMIP the U.S. Department of Energy's Program for Climate Model Diagnosis and Intercomparison provides coordinating support and led development of software infrastructure in partnership with the Global Organization for Earth System Science Portals.

TABLE OF CONTENTS

Page

Table of Contents (Continued)

Page

Table of Contents (Continued)

Page

Table of Contents (Continued)

Page

LIST OF TABLES

Table Page

LIST OF FIGURES

Figure Page

Figure Page

Figure Page

Figure Page

Figure Page

Figure Page

# CHAPTER ONE: INTRODUCTION

The design wind maps in ASCE 7-10 "Minimum Design Loads for Buildings and Other Structures" (ASCE 2010) provide the basic design wind speeds to determine the wind loads on structures. There are three sets of wind speed maps in ASCE 7-10. Each of the maps corresponds to a specific hazard level (return period) and a specific design occupancy category. The assignment of occupancy category to a particular structure depends on the function of structure and the potential risk to human life in the event of failure. For the four occupancy categories named in ASCE 7-10, the return period of 300 years is assigned for occupancy category I, 700 years is for occupancy category II, and 1700 years is for occupancy category III and IV (ASCE 2010, Cook et al. 2011).

The ASCE 7-10 wind speed maps are derived from two sets of wind speeds: namely, hurricane and non-hurricane winds. The non-hurricane wind speeds are based on the statistical model fitted to wind speeds measurements obtained from the National Climatic Data Center (NCDC) weather monitoring stations (Peterka and Shahid 1998). The hurricane wind speeds are derived from a stochastic hurricane simulation model described in Vickery et al. (2000) and Vickery et al. (2009a).

Figure 1.1 shows the annual Atlantic tropical storm and hurricane counts from 1851 to 2013. As shown in the Figure, the annual storm frequency demonstrates an upward trend. This upward trend is also correlated to the rise in sea surface temperature (SST) (Vecchi and Knutson 2008). The effects of climate change on design wind speeds are not currently considered in ASCE 7-10. As the ASCE 7-10 design wind speeds of the

coastal regions are dominated by hurricane winds, the observed changes in annual storm frequency and SST may influence the future design wind speeds.

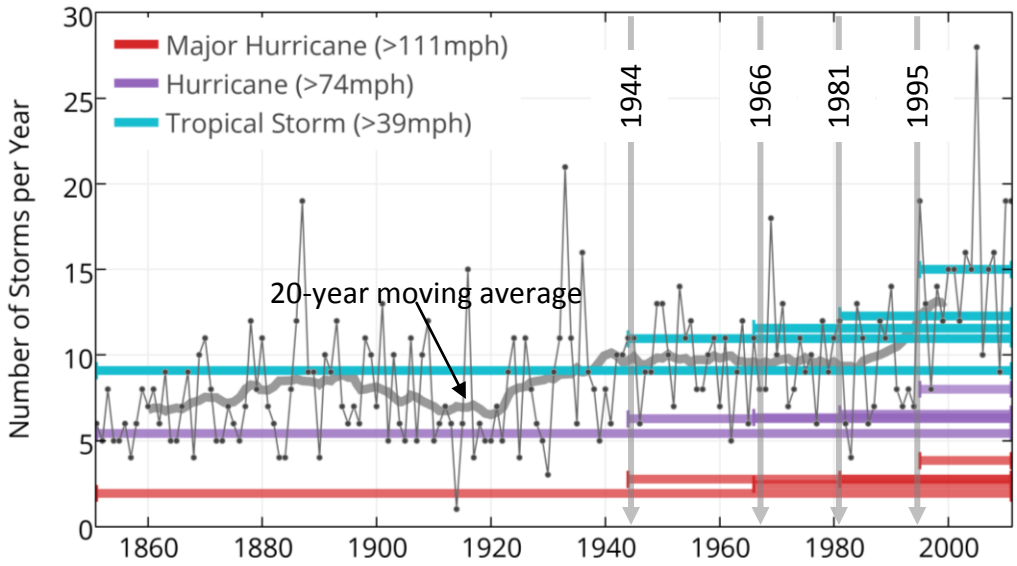


Figure 1.1: Number of storms spawned in the Atlantic basin per year from 1851 to 2013. Twenty-year moving averages of storm numbers vs. time shown as bold grey line. Average numbers of tropical storm, hurricane and major hurricane over time windows since 1861 (begin of data collection), 1944 (start of aircraft reconnaissance), 1966 (start of polar orbiting satellite coverage) and 1995 (start of the most recent warm Atlantic era).

## 1.1 Objectives and Scope of Research

The overall objectives of this study were to examine the influence of climate change on future hurricane activities and to quantify the changes in design wind speeds and losses due to hurricanes. The results of this research provide guidance on whether climate change needs to be considered in the design of new structures or planning of coastal cities. In order to achieve the main objectives, a research framework was established and the major research tasks are listed below:

(1) **Development of a baseline stochastic hurricane simulation model**

The baseline hurricane simulation model was developed based on historical hurricane data without considering the effects of climate change. To gauge the accuracy of the baseline model, simulation results such as the storm landfall frequencies and central pressures at landfall were compared to actual observations.

(2) **Development of a hurricane simulation framework which accounts for climate change**

Based on the baseline model, two effects of climate change: namely, changes in annual storm frequency and sea surface temperature were considered.

*I. Development of annual hurricane frequency projection models*

The upward trend of annual number of storms (both hurricanes and tropical storms) was analyzed and fitted into three different storm frequency projection models, which were implemented into the hurricane simulation model to simulate future hurricane activities.

*II. Implementation of SST projection from climate change scenarios into hurricane simulation model*

Sea surface temperature is an important variable in determination of hurricane intensity. The projected future SST under different climate scenarios developed from global climate models by others was utilized to simulate future hurricane activities.

(3) **Quantification of climate change impact on future hurricane risk**

The influences of climate change on future hurricane risk were evaluated in two aspects of structural reliability:

I. Change in demand or wind hazard: Comparisons between the current design wind speeds in ASCE 7-10 to those simulated in this research considering the effects of climate change were made to quantify the relative change (increase or decrease) in future design wind speeds.

II. Change in consequences or hurricane induced losses: Scenario-based hurricane loss assessments were performed to compare the property losses estimated using hurricane events generated with and without considering climate change.

On the completion of the listed tasks, this research (1) provides an improved understanding of the relative contribution of climate change to the total hurricane risk of the coastal built environment; (2) advances the current state-of-the-art hurricane simulation procedure by developing simulation procedures which account for selected climate change parameters; while preparing concrete validations for the finds above, works were done to (3) generate seven full-track synthetic hurricane databases from seven different climate scenarios; (4) develop hurricane simulation application package in Matlab program. The simulation application allows users to define climate scenario and query simulation database with arbitrary number of years. The synthetic hurricanes are exported with the same information as observation in HURDAT with date and time measured to 6-hour intervals; (5) refine simulation results for risk assessment. For risk

assessment use, hazard level (e.g. surface gust wind) is quantified with annual exceedance probability and is categorized in return period or mean recurrence interval (MRI). A set of program is developed to quantify the high wind risk for locations of point, circular and arbitrary area using the simulation database as input. Applications of high wind risk quantification for different location types include: extreme wind speed quantification for typical MRIs, events selection for specific MRIs and impact quantification of individual events.

## 1.2 Thesis Organization

A literature review is presented in Chapter Two, focusing on the climate change scenarios, changes observed on the hurricane activities and hurricane simulation techniques. In Chapter Three, the development of the hurricane simulation model used in this study is presented with detail descriptions of the key components in the modeling framework. Chapter Four consists of two parts: model validation and sensitivity study. In the first part, the validation results of the baseline model (i.e. without climate change) are presented by comparing the landfall information of simulated hurricanes to that of the historical events. The second part of Chapter Four presents the results of sensitivity and convergence studies of modelling parameters, including tracking and intensity parameters. In Chapter Five, the effects of two climate change variables, annual storm rate and sea surface temperature, were added to the baseline hurricane simulation model to derive six new simulation models that account for different climate change scenarios. In this Chapter, characteristic parameters (e.g. landfall rate and central pressure deficit) of the

simulated hurricane events considering climate change effects and the associated wind speeds were compared with those obtained from the baseline model. Chapter Six presents eight applications of the simulated hurricane events. Among these applications, the determination of wind speed for specific MRI is essential in quantification of hurricane risk. The procedure is extensionally applied to various areal enclosures for quantification of MRIs, including point locations, circular areas and irregular areas on the map. Wind speeds of events affecting the areas above were ranked by exceeding probability in the areal enclosure. The distribution of extreme winds was inversely used to assess the hazard level of any individual event out of the database by matching the extreme wind speeds produced and locating the specific event in the entire range of simulated hazard level. Events representing typical likelihood of occurrence in the areas were selected for further computational use, such as loss estimation and storm surge evaluation. In Chapter Seven, loss assessments were performed using simulated hurricanes (without and without climate change) as input for four coastal regions (Miami, New Orleans, Charleston, and New York City). To explore the effectiveness of conventional wind retrofits to mitigate climate change effects, comparisons between the hurricane losses for the four selected coastal regions, with and without retrofits, were evaluated. Finally, summary of research outcomes and conclusions are provided in Chapter Eight.

# CHAPTER TWO: LITERATURE REVIEW

## 2.1 Background on Climate Change

The term climate change refers to the changes in statistical properties of the climate system over a long period of time (IPCC 2013; IPCC 2007a). The term climate change is often used synonymously and erroneously with the term global warming in public media and news. Within scientific communities, global warming refers to increase in surface temperature on the earth, while climate change includes global warming as well as other changes to the earth climate system (Conway 2008). The drivers of climate change are those environmental factors that alter the energy balance on the surface of the earth, which come from both the earth's natural processes and human activities (IPCC 2013; National Research Council 2010; IPCC 2007a). One of these factors is the level of greenhouse gases (GHGs). The increasing amount of GHGs is closely related with human activities for its current level far exceeds the long-term historical range (IPCC 2013; IPCC 2007a).

In 2013, the United Nations Intergovernmental Panel on Climate Change (IPCC) issued its fifth assessment report (AR5) on climate change (IPCC 2013). The report shows that the average global land and ocean temperature has increased by approximately $0.85^{o}$C from 1880 to 2012. Figure 2.1 shows the sea surface temperature (SST) anomalies of North Hemisphere (NCDC 2014). The difference between the lowest point in 1909 and the highest point in 2006 exceeds $1^{o}$C. Under the worst case greenhouse gas emission scenario, the projected global average sea surface warming will continue to increase by as

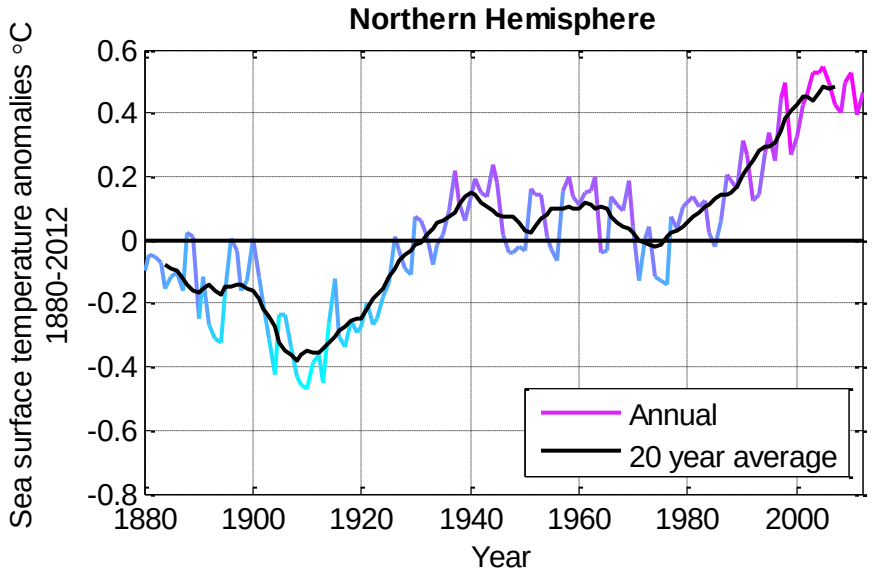


Figure 2.1: The annual Northern Hemisphere temperature anomalies from 1880 to 2013.

much as 2.6 to 4.8 $^{o}$C by the end of the century (IPCC 2013). The changes in climate extremes have profound influence on the occurrences of natural hazards such as hurricanes or tropical cyclones because the formations of natural hazards rely heavily on the climate conditions. For example, the formation of tropical cyclone requires the persistence in atmospheric circulation, relative warm sea surface temperature and other conditions to happen at the same time and location (IPCC 2012).

## 2.2 Increasing Hurricane Risk to the U.S. Coastal Regions

The IPCC has concluded that the intensity of the near future hurricanes is likely to increase, with higher extreme wind speeds and heavier precipitation as a result of the rise in sea surface temperature. According to Emanuel (2000), a 1$^{o}$C increase in sea surface temperature translates to approximately 5% increase in hurricane wind speed. For the projected worst-case scenario (RCP 8.5) in the IPCC AR5, the bound of likely range is

from 2.6 to 4.8 $^{o}$C increase in sea surface temperature (IPCC 2013). It means that the wind speed in hurricane prone regions may increase by more than 24% by the end of the century. It should be noted that the wind pressure exerted on a building envelope is proportional to the square of wind speed (*V*). In ASCE 7-10, the wind pressure on the surface of low-rise buildings (e.g. single family house) is calculated as (Ellingwood and Tekie 1999):

$$W = q_h \left[ GC_p - GC_{pi} \right] \tag{1}$$

where the value of $GC_p$ for low-rise building is determined based on the zone of the building envelope considered; $q_h$ is velocity pressure at mean roof height; G is gust factor, $C_p$ is the exterior pressure coefficient and $C_{pi}$ is the interior pressure coefficient. The equation to calculate the velocity pressure on the building envelope is given as (Ellingwood and Tekie 1999):

$$q_h = 0.00256 K_z K_{zt} K_d V^2 \tag{2}$$

where $K_z$ is the velocity pressure coefficient; $K_{zt}$ is the topography factor; $K_d$ is the wind directionality factor.

For the given range of SST increase by the end of the century in IPCC AR5, a projection in the change of wind speed was done and sketched on the horizontal axis in Figure 2.2. Furthermore, the change range in wind pressure was estimated based on the wind speed. As a result, a 24% increase in wind speed will yield approximately 54% increase in wind pressure or suction (see Figure 2.2). The projected 54% increase in wind pressure will have great impacts on the coastal communities. A separate study by the Climate Change Science Program (CCSP) puts the increase of hurricane surface wind

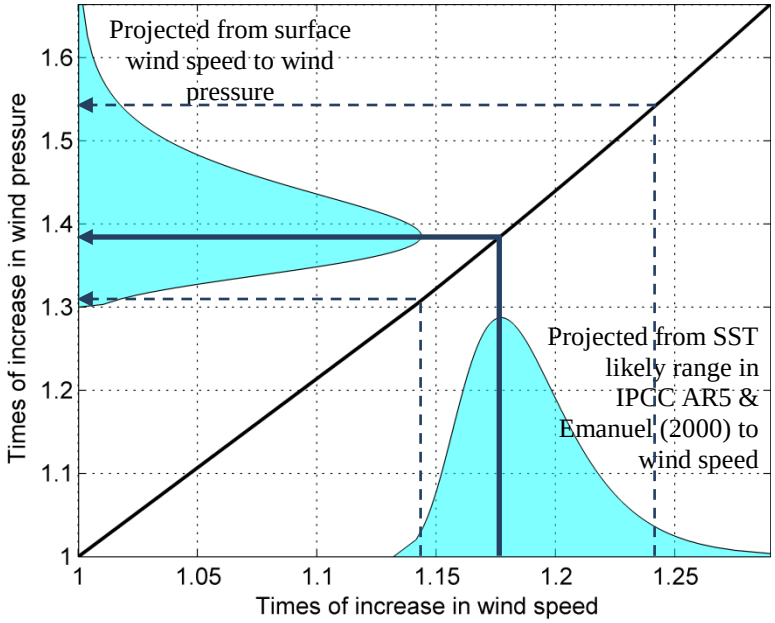


Figure 2.2: Projected percent increase in wind speed and wind pressure by the end of the century.

speed at 1% to 8% for every 1$^{o}$C increase in sea surface temperature (CCSP 2008). This translates into approximately 10% to as much as 90% increases in wind pressure, estimated based on the projected 4.8 $^{o}$C increase in sea surface temperature by the end of the century (see Figure 2.2).

The current wind design provisions in ASCE 7-10 are derived from both hurricane and non-hurricane winds. With the aforementioned potential increase in future wind hazard, the actual return period of the design wind speed event may be considerably shorter than that speculated in the design code (i.e. ASCE 7-10), in particular for the coastal regions. In other words, the reliability of structures designed via ASCE 7-10 wind provisions might be considerably less safe than the safety level speculated in the building code. This hypothesis is also supported by a separate study on hurricane induced storm surge in which the investigators of the study have shown that today's "100-year storm"

may occur once every 3 to 20 years with the change in future hurricane climate (Lin et al. 2010). Hurricane wind is the main driving force for coastal storm surge. In addition to increase in wind loads on structures, change in future hurricane climate combined with sea level rise may result in compounding effects on the severity of coastal hurricane induced losses.

The average normalized annual hurricane loss from 1900 to 2005 was estimated at $10 billion US dollars (Pielke et al. 2008). Continued population growth along the coastal areas and more high value properties being exposed to hurricane threats compounds with climate changes will likely result in future hurricane damage greatly exceeding the current annual loss of $10 billion dollars. In other word, the risk of wind hazard depends on not only the hazard itself but also the exposure and vulnerability in the potential hazardous region. These changes in exposure and vulnerability conditions are under anthropogenic influence and related with people's understanding and knowledge on the hurricane risk. These types of influences are termed as disaster risk management and climate change adaption. They are recommended to be considered in the process of evaluating disaster risk (IPCC 2012).

The extent to which aspect of climate change contributes to the variation in hurricane activities from long-term historical statistics is still not clearly understood at this point. Some researchers or scientists believe that the change in hurricane pattern observed over the years is due mostly to natural phenomena while others believe that anthropogenic forcing (human activities) contribute to the change. Even though not all scientists agree on the main cause of the change in the global weather patterns (sea

surface temperature, hurricane intensity and etc.), but the majority of scientists agrees that changes do occur.

The most recent IPCC AR5 report states that it is *extremely likely* (with 95% confident) that human activity is the dominant cause of the observed warming since the mid-20th century (IPCC 2013). Yet, as previously stated, it is not the intent of this research to prove one way or the other, but rather investigate the influence of different hurricane trends predicted using historical data and/or studies by other scientists on the change in hurricane risk of coastal construction. The main objective of this research is to quantify the impacts of hurricane climate change on future wind speeds and future hurricane losses in the coastal regions of the United States.

## 2.3 Changes in Tropical Cyclone Activity in the North Atlantic Ocean

### 2.3.1 North Atlantic Hurricane Database

A tropical cyclone that forms in the North Atlantic Ocean is commonly referred as *Atlantic hurricane* or *tropical storm*. The Hurricane Research Division (HRD) of the United States National Oceanic and Atmospheric Administration (NOAA) maintains a database of historical hurricane and tropical cyclone records, called HURDAT (Jarvinen et al. 1984). The first hurricane season documented in HURDAT can be traced back to the year of 1851. The HURDAT database contains the following information recorded at a 6-hour interval for each storm: (1) storm track, expressed in terms of latitude and longitude of the storm eye, (2) central pressure, (3) storm forward speed, (4) storm heading angle, (5) maximum sustained wind speed, and (6) radius to maximum wind.

This hurricane database has been used for various purposes, including developing stochastic models for simulating hurricane tracks and intensities (e.g. Vickery et al. 2000, Lee and Rosowsky 2007), and hurricane loss assessments (Legg et al. 2010 and Pei et al. 2014). A new and improved version of the hurricane database, termed HURDAT2, was released in 2013 (Landsea et al. 2013), as shown in Figure 2.3. The major revision from HURDAT to HURDAT2 is that more detailed parameters are provided in HURDAT2 for hurricane wind field. The original database (i.e. HURDAT) only records one radius to maximum wind entry for each 6-hour time step and the direction where the maximum sustained wind speed occurred is not recorded. In HURDAT2, the radii to wind speeds for all four quadrants are provided. The new information in HURDAT2 allows one to reconstruct asymmetrical hurricane wind fields.

People's interest about tropical cyclones is largely attributed to the fatal impact to human life and properties. Tropical cyclones are known to associate with extreme winds which threat the integrality of building envelope. Moreover, storm surge and freshwater flood from extreme rainfall due to tropical cyclones can cause great portion of loss of life and properties in the total of tropical cyclone related losses (Rappaport 2000). The intensity of storms which is quantified by the maximum sustained wind or central pressure is an important influential factor to the damage on building envelope and the formation of storm surge. The frequency of tropical cyclones occurred in each hurricane season will affect the quantification of return interval for wind speeds. The structure and areal extent of the wind field also play an important role in evaluation of impact, especially from storm surge (Irish and Resio 2010). Besides the mentioned aspects about

tropical cyclone, there are still many factors closely related to the tropical cyclone observation. These measures, such as genesis frequency, intensity, duration and track pattern, are all included in the broad definition of *tropical cyclone activity*.

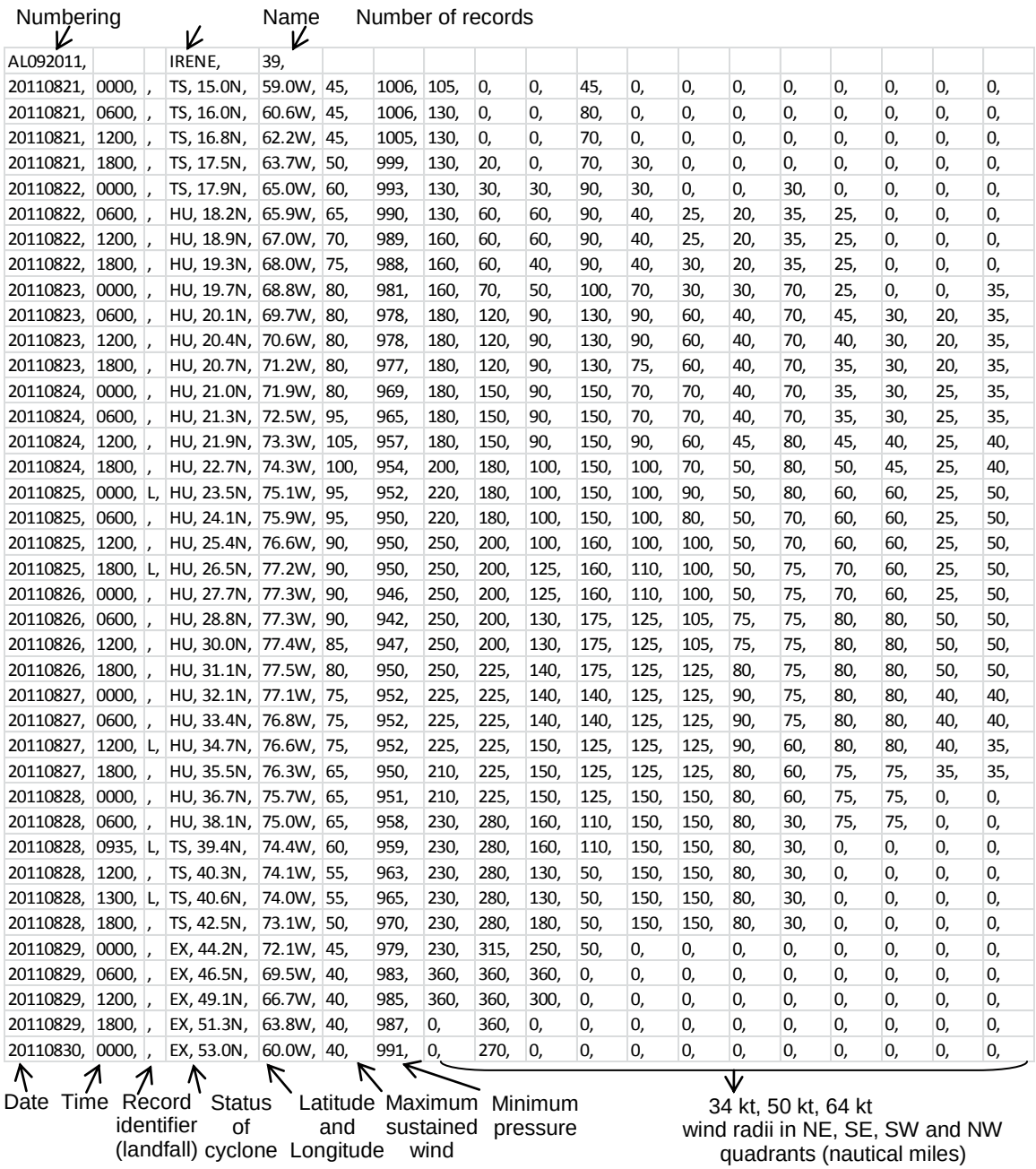


Figure 2.3: A selection of the NHC hurricane database (HURDAT2).

### 2.3.2 Changes in Frequency

According to the records in HURDAT, there has been an increasing trend in the number of storms observed over the past decades in the North Atlantic Ocean. The number of storms recorded in HURDAT since 1851 was plotted in Figure 1.1. The statistics of storm number since 1851 was summarized by Blake et al. (2011) and classified into the categories of tropical storm, hurricane and major hurricane. Table 2.1 shows these statistical data in the same format with those in Blake et al. (2011) but updated to 2012 data. It can be clearly seen in Figure 1.1 that the number of storms spawned in the Atlantic Ocean per year follows an oscillating pattern along the time. The amplitude of the oscillation (i.e. the number of storms) appears to increase following each subsequent oscillation cycle. It also can be observed that the annual storm frequency exhibits an increasing trend over the entire period with records and the most notable upswing in storm frequencies can be observed since 1995. As indicated in Table 2.1, the average numbers of events from all three categories are found increased in more recent time window from the entire record period. Especially the average numbers in the most recent 18 years are found apparently higher than the averages over the periods covering earlier years.

Holland and Webster (2007) analyzed these records in HURDAT and their results indicated that the number of tropical cyclones in the North Atlantic Ocean had been doubled in the past century. This increase occurred in three relative stable regimes divided from the past century with 50% more events found in each regime than the previous one. The increasing numbers of events over the regimes were also found

matching with distinct patterns of sea surface temperature to some degree. Mann and Emanuel (2006) also suggested a positive correlation between SST and storm frequency based on observations from 1871 to 2005. Goldenberg et al. (2001) also pointed out that the hurricane activities was raised to a higher level compared to those earlier years in the last century.

On the other side, as some studies suggested, the increase in storm monitoring capabilities due to the availability of modern technologies such as the satellites (1966) and reconnaissance aircrafts (1944) could affect the recorded storm frequencies over different technology eras. As stated by Landsea et al. (2004) and Landsea (2007), it was not wise to treat the record prior to the 1940s as those more recent ones due to the deficiency of the detection method during that time. The chance of the existing storm to encounter any ships was depend on the density of the ships, which was uneven on different parts on the ocean. And detection of the events can be affected and missed in this way.

Regardless of the monitoring technologies, the increasing trend of the storm number per year is obvious for all three levels of storm categories from Figure 1.1 and Table 2.1. In particular, the annual number of major hurricanes doubled from 1.9 over the period of 1851 to 2011 to 3.8 over the period of 1995 to 2011. Consider only the post-satellite era data (later than 1966), one can see that the annual storm frequencies still exhibit an increasing trend over this period. This suggests that there is an up-swing in recent storm activities.

Table 2.1: Average number of tropical cyclones [(a)] which reached storm, hurricane and major hurricane status. (Updated from Blake et al. 2011)

| Period | Number of years | Average number of Tropical storms | Average number of hurricanes | Average number of major hurricanes |
|---|---|---|---|---|
| 1851-2011 | 161 | 9.08 | 5.42 | 1.91 |
| 1944[(b)]-2011 | 68 | 10.96 | 6.26 | 2.74 |
| 1966[(c)]-2011 | 46 | 11.57 | 6.35 | 2.43 |
| 1981-2011 | 31 | 12.29 | 6.55 | 2.74 |
| 1995[(d)]-2011 | 17 | 15 | 8 | 3.82 |

[(a)] Includes subtropical storms after 1967; [(b)] Start of aircraft reconnaissance;
[(c)] Start of polar orbiting satellite coverage;
[(d)] Start of the most recent warm Atlantic era (Goldenberg et al. 2001);
[(e)] A major hurricane is a category 3, 4, or 5 hurricanes on the Saffir/Simpson hurricane wind scale.

### 2.3.3 Changes in Intensity

The intensity of a storm is commonly measured by the maximum wind speed or the central pressure in the wind field. The monitoring of storm intensity is even more dependent on the changing technology compared to counting the number of the storms. The complete central pressure records were applicable only for the events after 1979 (included) in HURDAT. The records before that are either incomplete or blank due to the lack of monitoring methodology.

The maximum wind speed records are more accessible compared to central pressure. Thus, the storm intensity can be measured using the Saffir-Simpson Hurricane scale, which classifies a hurricane into one of the five categories based on the maximum sustained wind speed (Table 2.2). The Saffir-Simpson scale is intended to describe the potential damage and storm surge a hurricane will cause during its landfall. In the IPCC AR4 report summary, it is concluded that an increase in the intensity of tropical cyclones has occurred since 1970 with certainty of higher than 66% from the observations.

Beside central pressure and maximum wind speed, other intensity measures, such as the minimum surface pressure and potential intensity (Emanuel 1987, Emanuel 2000 and Camargo et al. 2007), have also been proposed. From these measurements, the concept of power dissipation index (PDI) was introduced to integrate storm frequency, wind speed and duration (Emanuel 2005):

$$PDI = \int_0^{\tau} V_{\max}^3 dt \tag{3}$$

where $V_{max}$ is the maximum sustained wind speed at 10 m height; $\tau$ is the radius of outer storm limit. The PDI index is considered as a better indicator of hurricane threat than frequency or intensity alone. By analyzing the PDI values of historical hurricanes, Emanuel (2007) found there was an increasing trend in the North Atlantic Ocean in the past 25 years. It indicates greater energy has been evolved in form of tropical cyclones by observing either more quantity or higher intensity of the events or both. A separate study conducted by the Climate Change Science Program (CCSP 2008) also concluded that the increase in Atlantic power dissipation is substantial since the 1950s. Emanuel (2007) showed that the PDI value is directly correlated to the Atlantic sea surface temperature. This suggests that the recent increase in global average temperature will likely result in more intense storms with increased wind speeds. CCSP also confirmed that there is a strong statistical connection between the rise in sea surface temperature in the hurricane formation regions and the increased hurricane activity observed over the past 50 years (CCSP 2008).

Table 2.2: Saffir-Simpson hurricane scale.

| Category | Wind Speed (mph) | Damage |
|---|---|---|
| 1 | 74 – 95 | Very dangerous winds; Some damage will occur |
| 2 | 96 – 110 | Extremely dangerous winds; Extensive damage will occur |
| 3 | 111 – 130 | Devastating damage will occur |
| 4 | 131 – 155 | Catastrophic damage will occur |
| 5 | > 155 | Catastrophic damage will occur |

### 2.3.4 Causes of the Changes

It has been debated with broad evidence on the direct connection between the changes in hurricane activities and the increased SST in many studies. The relationship revealed is straightforward that the increased SST results in some changes in the thermodynamic state on the ocean and finally manifests on the variability of tropical cyclones. The most supportive argument to prove this relationship was built up on the framework of potential intensity theory (Bister and Emanuel 1998). In the framework, the potential intensity of tropical cyclones generally refers to the upper bound of the storm intensity. The evaluation of this upper bound of intensity relies on the transfer of heat and momentum between the sea and air. And it is the transfer that contributes to the energy generation and dissipation in the atmospheric boundary layer (Emanuel 2000; Bister and Emanuel 1998). So the changes in the ambient potential intensity due to climate change could lead to more intensified events, as the upper bound shifts up. In fact, a positive correlation between SST and the potential intensity has been revealed by analyzing the historical records, which verifies that the increased SST contributes to the changes in hurricane activities, especially in the aspect of intensity (Emanuel 2000; Wing et al. 2007).

The environmental causes to the changes in hurricane activities in the broad sense are not clearly identified at this time (IPCC 2012). The effects from natural variability in short term (i.e. El Nino) and global warming (greenhouse gases and human influence) in the long term are difficult to distinguish. As indicated in Knutson et al (2010), there is only low confidence discovered in current stage for the attribution of changes in hurricane activities from the climate change and anthropogenic influences. Even though, there are studies projecting the warming trend of tropical SSTs with the increasing greenhouse gases in addition to the natural variability with proofs (Knutson et al. 2006; Gillett et al. 2008). The same trend is projected in the future climate scenarios for the next 100 year by IPCC. In these projection scenarios, the warming trend was found across different descriptions of future environment, ecology and society development (IPCC 2000). As mentioned in the previous section, it is the intention of the study to inspect the long term effect of hurricane risk with consideration and emphasis on global warming. It is not the intention of this study to investigate the attributions of the changes in term of physical mechanism, but inspect the potential impact to structural safety due to the possible climate change.

## 2.4 Basis of Climate Change Study

### 2.4.1 Global Climate Model

The general circulation model (GCM), also known as the global climate model, is a complex system of numerical models representing the general circulation of a planetary atmosphere and ocean. The basis of those numerical models involves the laws of physics, chemistry, fluid motion and etc. The two main components in GCM are atmosphere

circulation, which relatively represent the global pattern of air movements (e.g. trade winds and storm cyclones) and ocean circulation (e.g. eddies and equatorial flow) that would exchange heat with the atmosphere. The GCMs nowadays are constructed into a three-dimensional grid system with the measures of latitude and longitude as horizontal grids and height or pressure as the vertical grids. The development and evaluation of GCM has been remarkably depended on the development of computational ability (Lorenz 1967; Weart 2003).

The development of GCM was based on a set of seven "primitive equations" describing the behavior of heat and air motion derived back to the 1920s. These differential equations were solved on a grid of cells for a certain enclosure of terrain. The same solving technique was employed when GCM was constructed in computer codes. Ever since the year of 1956 when the first GCM was established on a primitive computer, the GCM has been gradually growing into a more sophisticated and powerful model with the improvement of computer power and better monitoring measurements (Weart 2003).

Besides the change in the computational complexity, GCM also started to produce results from local to global and from short-term to long-term. In the year of 1967, a set of comparison was made by raising the level of $CO_2$ to doubled benchmark level and find out how much the temperature would alter in order to test the sensitivity of climate model. It is the beginning of the investigation on climatic warming in aspect of greenhouse gas (Weart 2003). From then on, the development of GCM headed into two different directions: one is the numerical weather prediction (NWP) model; the other is what we still call global climate model which simulate the changes in climate (Geerts and Linacre

1998). A NWP predicts the movement of atmosphere in short term (1-10 days). While the GCM runs much longer for years or centuries so it can produce the statistics of variables about the state of the climate (Geerts and Linacre 1998). Both models share the same theory and modeling techniques and yield the same types of output about motion of atmosphere. Weart (2003) pointed out that the weather prediction is an "initial value" problem which is solved based on the current weather condition given. To calculate the climate is a "boundary layer" problem which resolves and reproduces the conditions of the Earth (Weart 2003).

The front of GCM in this century is the development of more comprehensively coupled ocean-atmosphere models and the evaluation of the transient response between two states of climate instead of computing the separated states of "before and after" (Weart 2003). More factors which are tied to atmosphere and ocean have been or will be considered, such as those from biology, ecology, human activity (agriculture) and etc. The GCM is heading into the direction of building up an "Earth System Model" (Weart 2003).

### 2.4.2 United Nations Intergovernmental Panel on Climate Change

The Intergovernmental Panel on Climate Change (IPCC) is the most authoritative and influential organization to assess the science basis and publish reports related to climate change. The members on the panel are the experts from all over the world and their assessments are made in a global perspective. The panel provides assessment on the scientific basis, impacts, future risks, options for adaptation and mitigation of climate change (IPCC 2013). The publications of IPCC include assessment reports, special

reports, methodology reports and other type of supporting materials and they are available online (IPCC 2014). The IPCC assessment reports are a set of comprehensive reports that summarize the scientific information and global issues concerning climate change in the aspects of physical basis, impacts and mitigation. The assessment reports are issued about every 6 years since the year of 1990. The latest official version is the fifth assessment report (AR5). Its first part (i.e. WGI report) has recently been released (IPCC 2013) while the reports for WGII and WGIII are scheduled to be released in 2014.

A complete series of assessment reports (i.e. the AR4 report) contains the works from three research groups and a synthesis of the assessments from all three groups. The first working group (WGI) focuses on the physical science basis behind the climate change, which includes summaries of observed changes in climate and their effects on natural and human systems, and assessment on causes of the observed changes (IPCC 2007a). Working group two (WGII) provides assessment of the impacts of climate change, the vulnerability of natural and built environments, and potential adaptation strategies to mitigate the negative consequences of climate change (IPCC 2007b). Lastly, working group three (WGIII) explores mitigation of climate change via policymaking worldwide (IPCC 2007c). The AR4 report includes the summaries from thousands of scientific studies around the world, making it one of the most detailed reports on the latest information and development on issues related to climate change.

Besides the assessment reports, the topics of two special reports published by IPCC are closely related to this study. The first one is the special report on "Managing the Risks of Extreme Events and Disasters to Advance Climate Change Adaptation

(SREX)" (IPCC 2012). This report provides information particularly about natural hazards risk for their changes and influence. Observations and conclusions were made from both modules in risk assessment: the hazard part which includes the observed changes in extreme climate events; and the resistance part that is the changes in vulnerability of human society and ecosystem. Population as an important factor in determination of vulnerability is also discussed and projected in this report. The idea of adoption of climate change into current policy and criterion is analyzed and discussed in the report for its significance in developing better strategy to manage the current and future risk.

### 2.4.3 Climate Change Scenarios

The other important special report is the "IPCC Special Report on Emissions Scenarios (SERS)", which developed a family of projection scenarios describing the future levels of climate variable and conditions of human society.

Human activities result in emissions of four long-lived greenhouse gases (GHGs): $CO_2$, methane ($CH_4$), nitrousoxide ($N_2O$) and halocarbons. Changes in the atmospheric concentrations of GHGs are among the reasons that alter the energy balance of the climate system and are drivers of climate change. It has been shown that the global atmospheric concentrations of $CO_2$, $CH_4$ and $N_2O$ have increased dramatically as a result of human activities since 1750 (IPCC 2000). The levels of these GHGs are anticipated to continue to grow over the next few decades even with the current climate change mitigation policies and related sustainable development practices (IPCC 2007a).

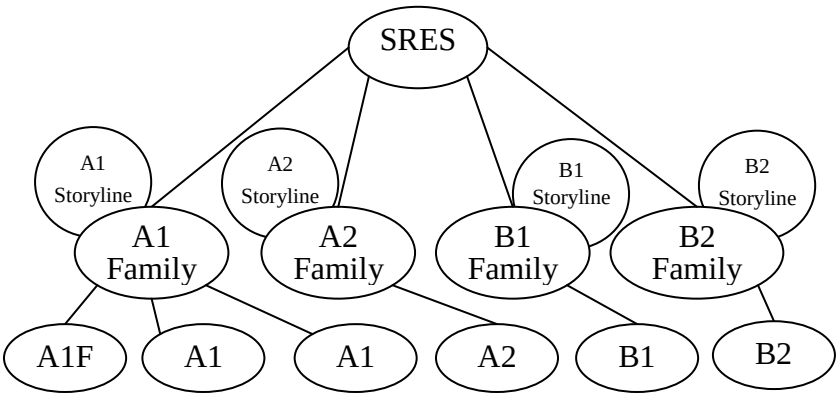


Figure 2.4: Schematic illustration of SRES scenarios

The GHGs emissions projections with respect to causative factors such as socio-economic, demographic and technological change were developed by IPCC. Based on the intensity levels of these causative factors, future climate scenarios were defined and projected in the IPCC Special Report on Emissions Scenarios (IPCC 2000). Those emission scenarios have been widely used in the assessments of future climate change, vulnerability and impact to environment. The schematic structure of emission scenarios are shown in Figure 2.4 and general descriptions for the hypothetical world development scenarios are given in Table 2.3.

The Representative Concentration Pathways (RCPs) is the latest set of GHGs emission scenarios developed to facilitate future assessment of climate change prepared by IPCC since 2007 (van Vuuren et al. 2011). This new set of emission scenarios is intended to replace and extend the scenarios used in earlier IPCC assessments. These new RCPs have been shown to provide a good basis for exploring the range of future climate scenarios (van Vuuren et al. 2011). Different from the SRES scenarios, which is

classified by the degree of global development; the RCPs are directly named according to the projected radiative forcing[1] for the year of 2100.

The radiative forcing of the climate system is dominated by the long-lived greenhouse gases. The level of radiative forcing for a certain climate scenario indicates its potential in altering the balance of incoming and outgoing energy in the earth's atmosphere system. Thus, it is also an index of the potential climate change mechanism. In AR4 Synthesis Report, radiative forcing values are defined by the differences between the forcing values in year 2100 and pre-industrial conditions defined for the year of 1750 and are expressed in watts per square meter ($W/m^2$). So the advantage of using RCPs is the user can be more specific with the levels of radiative forcing which indicate the degree of climate change explicitly. A higher radiative forcing suggests a higher potential impact on the future earth climate and climate extremes (e.g. hurricanes).

There are four RCPs projections which include one climate change mitigation scenario leading to a very low forcing level (RCP2.6), two medium stabilization scenarios (RCP4.5/RCP6) and one high emission scenarios (RCP8.5). The scenarios are sufficiently separated (by about 2 $W/m^2$) in terms of the radiative forcing pathways to provide distinguishable future climate scenarios. Table 2.4 lists the hypothetical considerations for each RCP scenario and the corresponding projected range of temperature change for each scenario. RCP scenarios will be considered in this research to investigate their effects on future hurricane activities.

[1] Radiative forcing is used in climate science to quantify warming of the earth, expressed in terms of the difference between radiant energy received on the surface of the earth and that radiated back to space. The units of radiative forcing are typically expressed in watts per square meter of the earth surface. A positive value means warming of the earth system and vice versa, a negative forcing means cooling of the earth system.

Table 2.3: SRES scenario families (IPCC 2007a).

| Emission scenario | Storyline | Temperature change (°C at 2090-2099 relative to 1980-1999) | |
|---|---|---|---|
| | | Best estimate | Likely range |
| A1 | A future world of very rapid economic growth, global population that peaks in mid-century and declines thereafter, and the rapid introduction of new and more efficient technologies. A1FI-fossil intensive; A1T-nonfossil energy sources; A1B-balance across all sources. | A1F1- 4.0<br>A1T- 2.4<br>A1B-2.8 | 2.4 – 6.4<br>1.4 – 3.8<br>1.7 – 4.4 |
| A2 | A very heterogeneous world with continuously increasing global population. Economic development is primarily regionally oriented and per capita economic growth and technological change are more fragmented and slower than in other storylines | 3.4 | 2.0-5.4 |
| B1 | A convergent world with the same global population that peaks in mid-century and declines thereafter, but with rapid changes in economic structures toward a service and information economy, with reductions in material intensity, and the introduction of clean and resource-efficient technologies. | 1.8 | 1.1-2.9 |
| B2 | A world emphasizes on local solutions to economic, social and environmental sustainability, with continuously increasing global population at a rate lower than A2, intermediate levels of economic development, and less rapid and more diverse technological change than in the B1 and A1 storylines. While the scenario is also oriented toward environmental protection and social equity, it focuses on local and regional levels. | 2.4 | 1.4-3.8 |

Table 2.4: RCP projections (Rogelj et al. 2012; van Vuuren et al. 2011; Moss et al. 2010)

| Scenario Component/Feature | RCP 2.6 | RCP 4.5 | RCP 6.0 | RCP 8.5 |
|---|---|---|---|---|
| Greenhouse gas emissions | Very low | Very low baseline; Medium-low mitigation | Medium baseline; high mitigation | High baseline |
| Agricultural area | Medium for cropland and pasture | Very low for both cropland and pasture | Medium for cropland but very low for pasture | Medium for both cropland and pasture |
| Air pollution | Medium-Low | Medium | Medium | Medium-high |
| Radiative forcing | Peak at ~ 3 $Wm^{-2}$ before 2100 then declines | ~ 4.5 $Wm^{-2}$ at stabilization after 2100 | ~ 6 $Wm^{-2}$ at stabilization after 2100 | > 8.5 $Wm^{-2}$ in 2100 |
| Pathway | Peak and decline | Stabilization without overshoot | Stabilization without overshoot | Rising |
| Median of temperature change (°C at 2090-2099 relative to 1980-1999) | 1.5 | 2.4 | 2.9 | 4.6 |

## 2.5 Hurricane Simulation Models for Long-term Risk Quantification

The severity of damage to the coastal built environment during a hurricane event is directly governed by (1) the storm track which determines the proximity of the storm to the structures on land, and (2) the storm intensity which is commonly defined in terms of either the extreme wind speed or central pressure. Since the late 1960s, significant efforts have been taken to the development of stochastic hurricane simulation models (Vickery et al. 2009b). Several state-of-the-art hurricane models were developed for hurricane

hazard mapping and risk assessment. For instance, the model developed by Vickery et al. (2009a) was used to develop the U.S. design wind speed maps included in the ASCE 7-10, *Minimum Design Loads for Buildings and Other Structures* (ASCE 2010).

To quantify the risk associated with different return periods, also referred as the mean recurrence intervals (MRIs), large numbers of stochastic hurricane events are required. The adequate amount of simulation years is far more than the length of current records especially for long recurrence interval risk. A review on different types of hurricane models has been elaborated by Vickery et al. (2009b). A brief summary of the probabilistic models and methods to obtain extreme wind speed distributions is given below with applications using each of these methods.

### 2.5.1 Site Specific Probabilistic Model

This type of model refers to the approach that employs Monte Carlo simulation to sample hurricane characteristic parameters and apply them into a physical wind field model to generate the radial structure of the storm. The wind speeds at the site of interest can be evaluated from the mathematic expression of the storm radial structure considering the effect of the storm's proximity to the land. This type of model is site specific because all the distributions of the characteristic parameters were prepared with statistics found around that site and they will change for the simulation at a different site.

The framework of this approach was first established by Russell (1971) then adopted by Neumann (1987) and many other studies. Due to the nature of the approach that it is only valid to a single site, Newmann (1987) introduced a method to expend the wind speed distribution from a single site to an area around the site which refers as the

areal wind speed distribution. However, the range of expansion is limited to compensate the involved modeling error.

In Huang et al. (2001), the site specific probabilistic model was used to estimate surface wind speed of 50-year MRI and coupled with loss estimation model to evaluated losses in North Carolina, South Carolina and Florida. The distributions of key parameters used in this application were calibrated in Huang et al. (1999) and Huang (1999). The same set of parameter distributions and the produced wind speed distribution is used again in Jain and Davidson (2007) to investigate hurricane risk on wood-frame houses with considerations of possible changes on structure safety over time.

### 2.5.2 Probabilistic Model with Complete Path

This type of model refers to the state-of-the-art hurricane simulation technique with tracking model as one of the components in the simulation. With the tracking model introduced in the probabilistic framework, the model realized both spatial and temporal evaluation of hurricane events in the simulation domain (i.e. the Atlantic Basin). The first model of this type is developed by Vickery et al. (2000) then updated in Vickery et al. (2009a). Emanual et al. (2006) established a different approach composed of a stochastic tracking model and evaluation of hurricane states from a deterministic intensity model. Both approaches by Vickery and Emanual produced database containing large number of simulated hurricanes from which the events striking/effecting the sites of interest can be found and the return period can be inferred.

One of the most important applications of this approach is the development of design wind map in the U.S. (e.g. ASCE 7-10). Besides that, there are many applications

related to quantification of hurricane risk using this simulation framework. For example, in Lee and Rosowsky (2007) a synthetic hurricane database was developed to provide wind speed distribution in the southeastern U.S.; In Liu and Pang (2013) and Mudd et al. (2014), this approach is coupled with climate change projection to investigate the possible variance in hurricane activities in the future.

### 2.5.3 Modeling Hurricane Extreme Intensity with Extreme Value Distribution

On top of either type of models aforementioned, attempts that used generalized extreme-value (GEV) theory to fit the distribution of hurricane intensity parameter or wind speed were made by several studies, such as Jagger and Elsner (2006). The use of Extreme Value (EV) distributions can improve the accuracy in modeling the tail of extreme events on the distribution and provide extrapolation to extraordinary long-term return periods. An application of EV distribution is given in Yeo et al. (2014). In this study, probabilistic models that describing the distribution of hurricane wind speed were derived using Extreme Value (EV) distributions (i.e. Gumbel and Weibull distribution). The models were derived from hurricane wind speed distributions developed by large number of synthetic hurricane events. With the use of Extreme Value distributions, the models were able to present wind speeds up to MRI of 10,000,000 years at the site of interest. The wind speeds of MRI larger than 1,700 years, as pointed out by Yeo et al., may be significant for the performance-based design.

## 2.6 Long-term Hurricane Simulation Coupled with Climate Change Effect

The impact of climate change on hurricane hazards has received increasing attention in recent years. In order to adapt wind design criterion to account for climate change, a quantitative assessment of climate change on design level wind speeds is needed. Several attempts have been made to evaluate the effects of climate change on tropical cyclone activities and to quantify the potential changes in design wind speeds in coastal regions.

Projections of future hurricane activities were performed by Mudd et al. (2013a), Mudd et al. (2013b), Wang et al. (2012) and Nishijima et al. (2012). In their approaches, climatic inputs (e.g. sea surface temperature) projected from future climate scenarios using GCM were implemented in a hurricane simulation model to generate future hurricane events. In Mudd et al. (2013a, b) and Wang et al. (2012), stochastic hurricane simulation techniques were used to generate 10,000 years of hurricane events under both current and a possible future climate condition (RCP 2.6). The 50-year maximum wind speed distribution at selected coastal locations and the joint distribution of maximum wind speed and storm size for the Northeast U.S. coastline were compared between the current and future climate conditions. Wang et al. (2012) found that the 50-year maximum wind speeds for New York City may increase by 25 m/s to 35 m/s under the low greenhouse gas concentration scenario (i.e. RCP2.6). In a recent study by Emanuel (2013), a large number of simulated hurricane events were compared between those generated using the climate of 1950-2005 and that projected for 2006-2100 under the high greenhouse gas emission scenario (RCP 8.5). It was found that both the frequency

and intensity of tropical cyclones increase during the 21st century. In addition, a 40% increase globally in the number of major events (Saffir-Simpson category 3 and higher events) can be expected.

An impact assessment of climate change on Japan typhoon risk was performed by Nishijima et al. (2012) using two sets of stochastic typhoon events (current climate and future climate). Maximum 10-minute sustained wind speeds were computed from these two sets of events for multiple locations in Japan. They found that the extreme events, with 10-min sustained wind speed exceed 30 m/s, are more likely to occur. The projected wind speeds were then coupled with the wind resistance of residential buildings to quantify the change in hurricane risk. Assuming the profile of the building portfolio in Japan remains unchanged over time, they found that the number of damaged residential buildings is likely to decreases for most of the locations in Japan. According to Nishijima et al. (2012), this is because while the intensity of future typhoons is projected to increase, the frequency of damaging typhoon events is projected to reduce. Emanuel (2011) conducted an impact assessment of climate change on U.S. hurricane risk. Two sets of hurricane events were simulated for two different time scale, one based on the 20th century climate and the other based on the project 21st century under the IPCC A1B scenario (IPCC 2000). Note that the A1B scenario is an earlier scenario used by the IPCC in the AR4 report, which corresponds to a projected greenhouse gas concentration level in year 2100 between the RCP 6 and RCP 8.5 scenarios in AR4 report (Table 2.4). The simulation of each time scale was repeated for 1000 times and the simulation results were utilized to estimate the damage to a portfolio of insured property using wind-damage

functions. Their result indicated a tendency of increased damage with global warming. The combined effects of changes in climate and demographic information, such as changes in average house value and house numbers on hurricane losses in U.S. were investigated by Bjarnadottir et al. (2011). This study shows that climate change may have a substantial impact on future hurricane losses and certain adaptation strategies can be used to mitigate the additional damage induced by climate change.

# CHAPTER THREE: HURRICANE SIMULATION MODEL

In this Chapter, the hurricane simulation model employed in this study is introduced. The simulation framework presented in this Chapter does not consider climate change effects and it is referred to herein as the *baseline model*. The simulation methodology is based on the probabilistic hurricane simulation approach introduced in Vickery et al. (2000). The simulation model consists of several modules, which includes hurricane formation (genesis) model, tracking model, intensity (central pressure) model, central pressure filling rate (decay) model, wind field model and boundary layer model. The statistical model of each module is calibrated using historical hurricane data (HURDAT). The Marko Chain Monte Carlo simulation technique is applied to simulate the spatial and temporal evolutions of the storm states from the initial formation of the storm to final dissipation.

The simulation domain is defined by latitudes from 10N ˚ to 60N ˚ and longitudes from 0˚ to 100W˚ (Figure 3.1). For modeling purpose, the simulation domain is sub-divided into 5˚ by 5˚ grids and the coefficients of the statistical models (e.g. tracking model, intensity model and etc.) for each cell are fitted from historical data. Those cells with sufficient historical record for establishing the cell specific coefficients are marked with bold black fonts. The light grey fonts indicate the cells with insufficient data and their cell coefficients are copied from the neighboring cells. There are 135 and 111 cells over the entire domain of 220 with sufficient tracking data for coefficient fitting of easterly and westerly travelling storms, respectively. There are 114 and 89 cells over the total of 169 cells on the sea or partially on the sea with sufficient intensity data for

easterly and westerly, respectively. There are total of 65 cells with sufficient tracking and intensity data for both directions over the entire domain of 220 cells. In the hurricane simulation model, the state of a storm is described by seven parameters (Figure 2.3) that are updated at a 6-hour interval. These seven parameters are: (1) latitude and (2) longitude of the storm eye, (3) storm forward speed ($V_t$), (4) heading angle ($\theta$), (5) central pressure ($P_c$), (6) storm size expressed as radius to maximum wind ($R_{max}$), and (7) pressure profile parameter (also known as Holland *B* parameter). The outline of the simulation framework is shown in Figure 3.3. The following sections discuss the statistical models used to simulate these parameters.

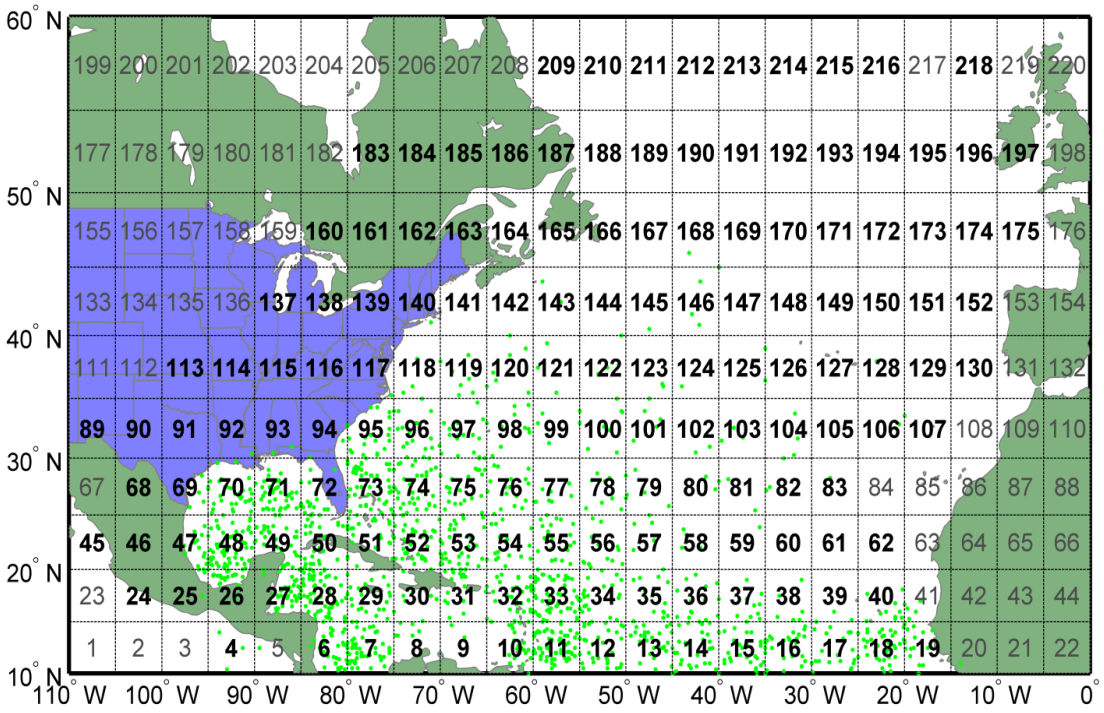


Figure 3.1: 5° by 5° grids in Atlantic Basin and initial locations of historical storms. Bold black fonts indicate cells with six or more 6-hour interval records of either tracking or intensity information for coefficient fitting. Grey fonts indicate cells without sufficient records for coefficient fitting.

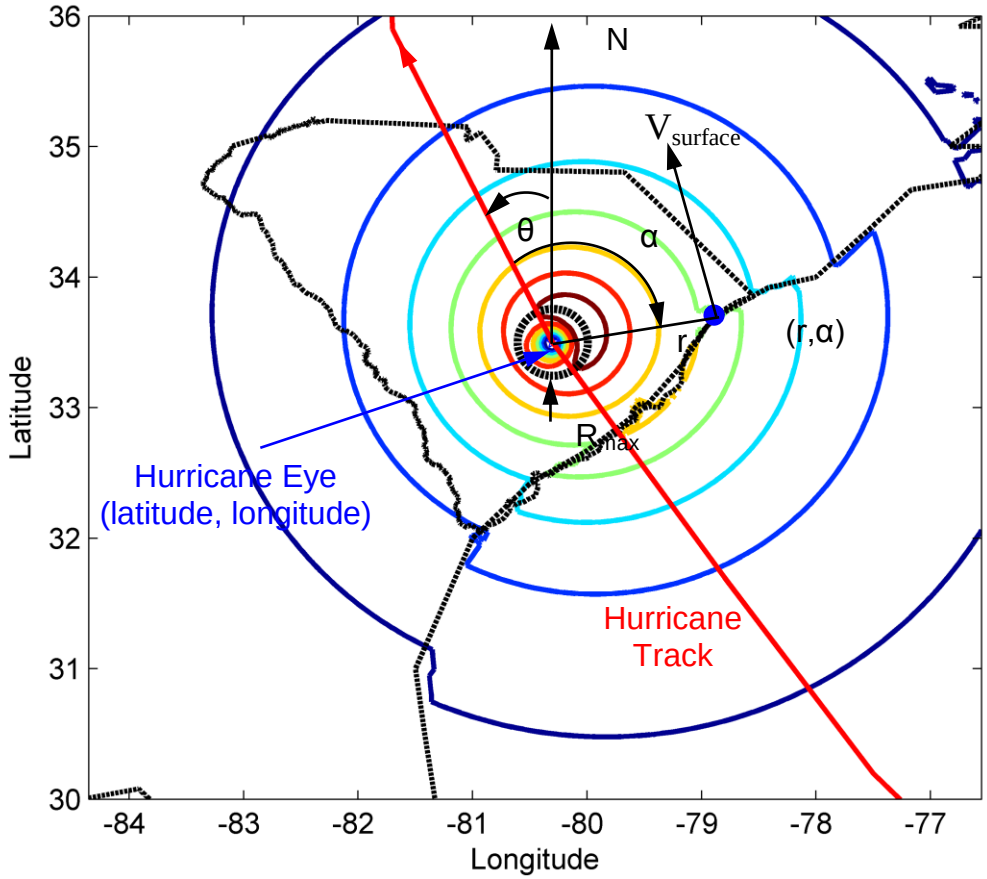


Figure 3.2: Illustration of wind field parameters, including latitude, longitude, heading angle (θ), radius of maximum wind ($R_{max}$) and etc.

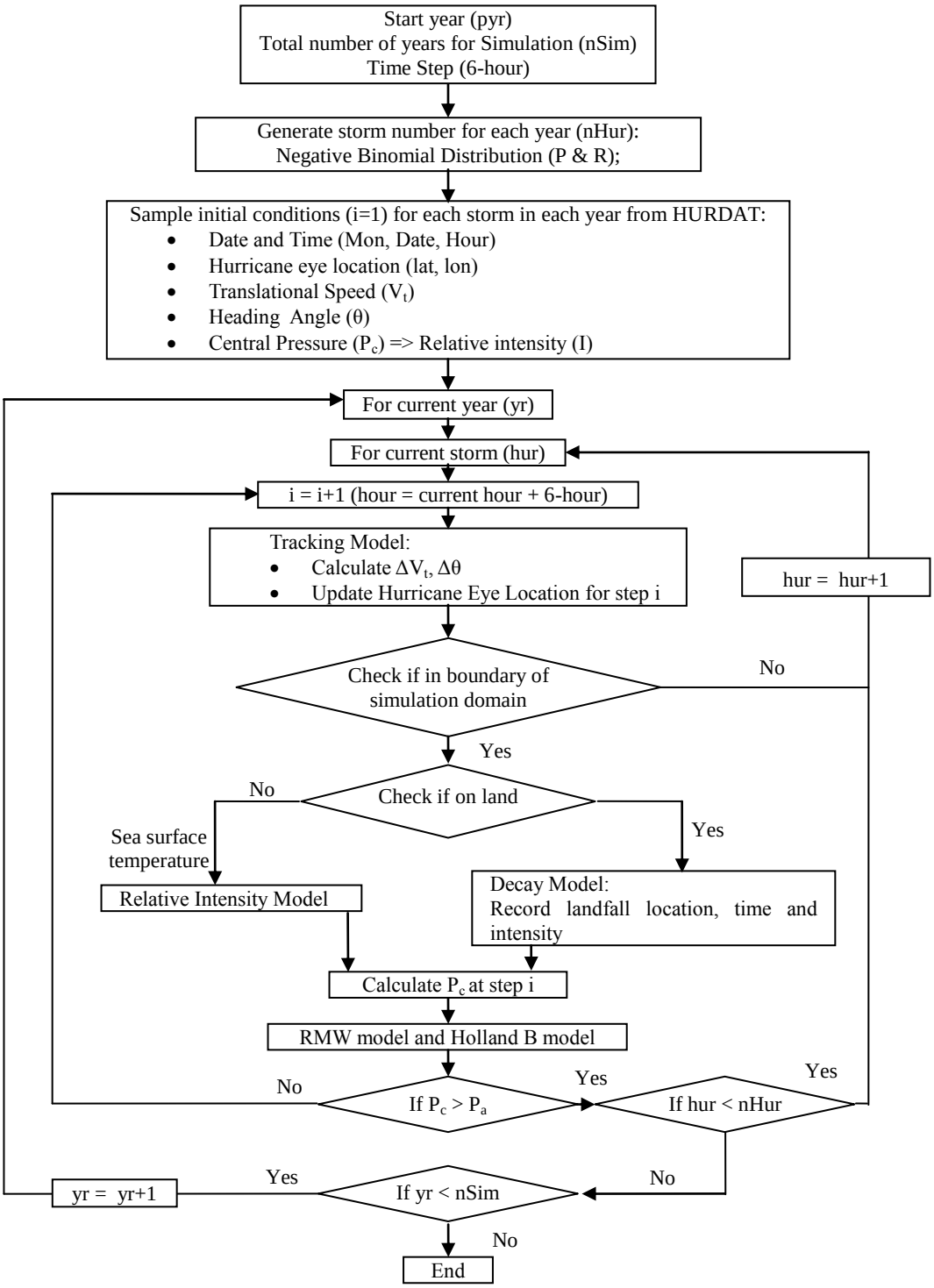


Figure 3.3: Simulation flowchart

## 3.1 Genesis Model

For each simulation year, the number of storms in that particular year is randomly generated using a negative binomial distribution. The mean ($\mu$) annual storm frequency from 1851 to 2012 is 10.74 storms/year and the standard deviation ($\sigma$) is 5.58 storms/year (Figure 3.4a). The parameters of the negative binomial distribution can be estimated using the method of moments as:

$$R = \frac{\mu^2}{\sigma^2 - \mu} \qquad P = \frac{\mu}{\sigma^2} \tag{4}$$

In this case, the parameters of the negative binomial distribution ($R$ and $P$) are estimated using maximum likelihood estimation on the historical records. The values of $R$ and $P$ are found as 6.39 and 0.37, respectively. Three realizations of storm frequency simulation from 1851 to 2012 using the fitted negative binomial distribution are plotted in Figure 3.4b with contrast of the mean and standard deviation from the historical record. Figure 3.5 shows that the negative binomial distribution fits reasonably well to the observed annual storm frequency data.

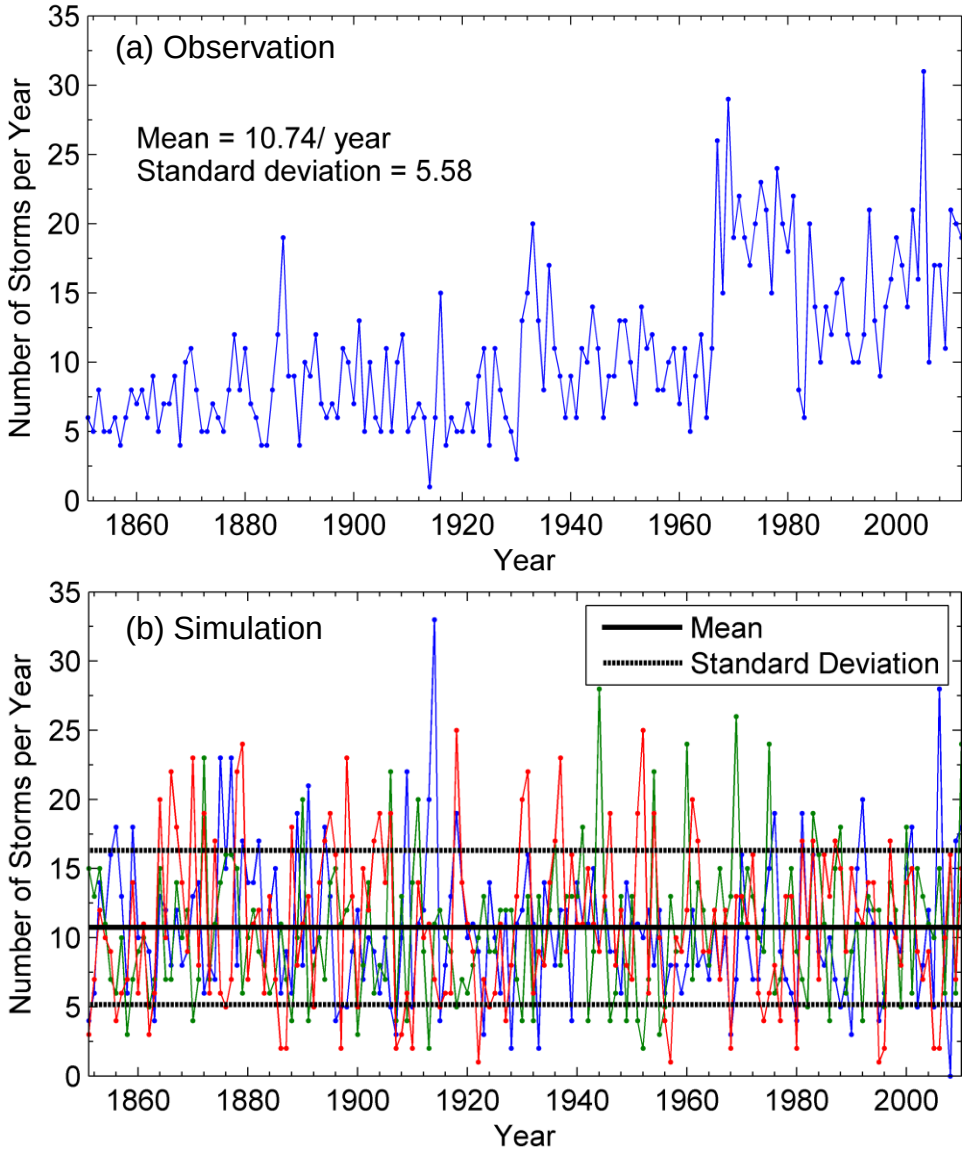


Figure 3.4: Number of storms per year from 1851 to 2012 and three sets of simulated storm numbers per year using negative binomial distribution. Each set of simulation is shown in a different color (red, green and blue).

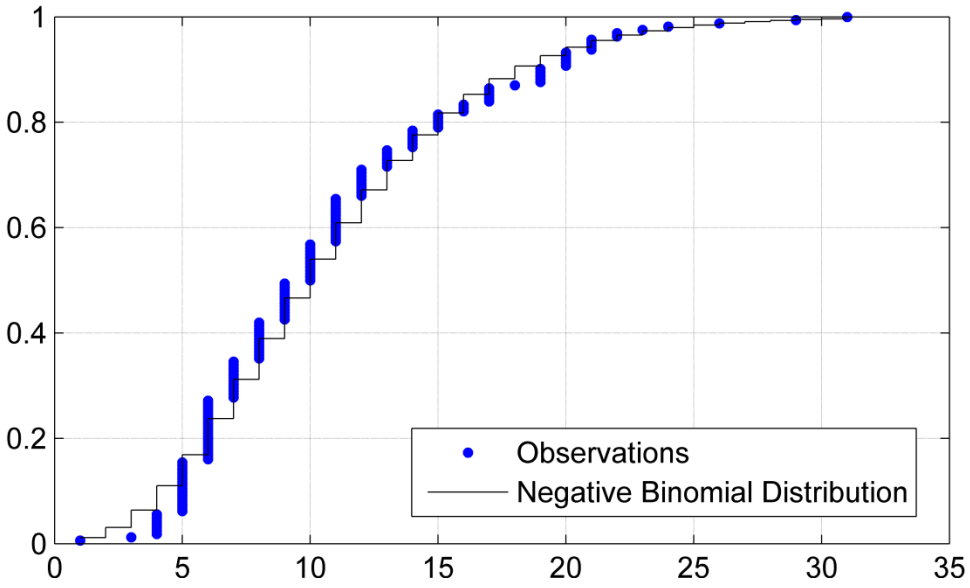


Figure 3.5: Cumulative distribution function of the number of storms per year.

## 3.2 Tracking Model

The movement of a storm is modeled using the weighted progressive equations of the change in forward speed ($V_t$) and heading angle ($\theta$):

$$\Delta \ln V_t = \ln V_{t(i+1)} - \ln V_{t(i)} = a_1 + a_2\psi + a_3\lambda + a_4 \ln V_{t(i)} + a_5\theta_i + \varepsilon_{V_t} \quad (5)$$

$$\Delta\theta = \theta_{i+1} - \theta_i = b_1 + b_2\psi + b_3\lambda + b_4 c_i + b_5\theta_i + b_6\theta_{i-1} + \varepsilon_\theta \quad (6)$$

where $a_1$-$a_5$ are the cell specific coefficients for the difference of logarithmic storm forward speed regression model; $b_1$-$b_6$ are the cell specific coefficients for the change in heading angle regression model; $\psi$ and $\lambda$ are the latitude and longitude of the storm eye, respectively; $V_{t(i)}$ is the forward speed at time step $i$; $\theta_i$ is the heading angle at time step $i$. The values of grid coefficients $a$ and $b$ depends on both the location in the simulation domain (i.e. cell location) and the storm heading direction (easterly or westerly). $\varepsilon_{V_t}$ and

$\varepsilon_\theta$ are the error terms which quantify the modeling errors (differences) between the regression models (i.e. Eqns. (5) and (6)) and the actual observations for forward speed and heading angle, respectively. A set of tracking models is developed respectively for easterly and westerly moving storms.

To obtain the coefficients $a_1$-$a_5$ and $b_1$-$b_6$ in Eqns. (5) and (6), least squares regression is performed using historical data of each grid. The least squares regression procedure is summarized in the following steps:

*Step 1: Assemble Grid Data*

Assemble the variables in Eqns. (5) and (6) from HURDAT by grids. The 6-hour records in HURDAT are grouped into 5° by 5° grids (Figure 3.1) based on the location of hurricane eye. For each 5° by 5° grid, the data are further divided into westward and eastward storms according to the heading angles. Figure 3.6 shows part of the assembled data for eastward movements of storms for cell 72 (see Figure 3.1). The unit for translational wind speed $V_t$ is in m/s. The units for other measurements (i.e. latitude, longitude and heading angle) are in terms of degrees. The heading angle is measured clockwise from the north for eastward storms (from 0° to 180°) and counter-clockwise from north for westward storms (from 0° to -180°).

*Step 2: Fit Regression Coefficients a and b*

Use least squares regression to fit the coefficients *a* and *b* (i.e. minimize the following functions to obtain the best-fit values for *a* and *b*):

$$\min \sum_{j=1}^{n_j} \left\{ \left( \ln V_{t_{i+1}} - \ln V_{t_i} \right) - \left( a_1 + a_2\psi + a_3\lambda + a_4 \ln V_{t_i} + a_5\theta_i \right) \right\}^2 \qquad (7)$$

$$\min \sum_{j=1}^{n_j} \left\{ \left( \theta_{i+1} - \theta_i \right) - \left( b_1 + b_2\psi + b_3\lambda + b_4 c_i + b_5\theta_i + b_6\theta_{i-1} \right) \right\}^2 \qquad (8)$$

where *i* is the time step number for the 6-hour record in HURDAT; *j* is the total number of 6-hour records found in the specified grid grouped by westward or eastward storm movements. The other notations are previously defined in Eqns. (5) and (6).

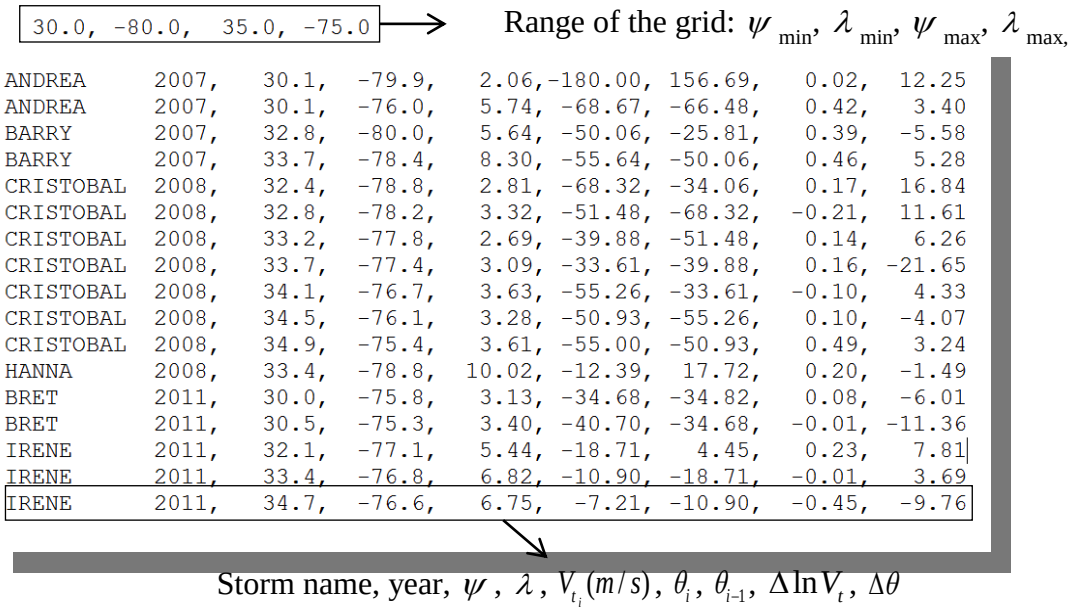


Figure 3.6: Example of assembled data in one cell.

*Step 3: Quantify Modeling Errors*

Once the *a* and *b* coefficients are obtained, the differences (errors) between the modeled values and the observations are calculated. The modeling errors for $\Delta \ln V_t$ and $\Delta\theta$ in cell 72 are shown in Figure 3.7a and b. As can be seen, both the storm

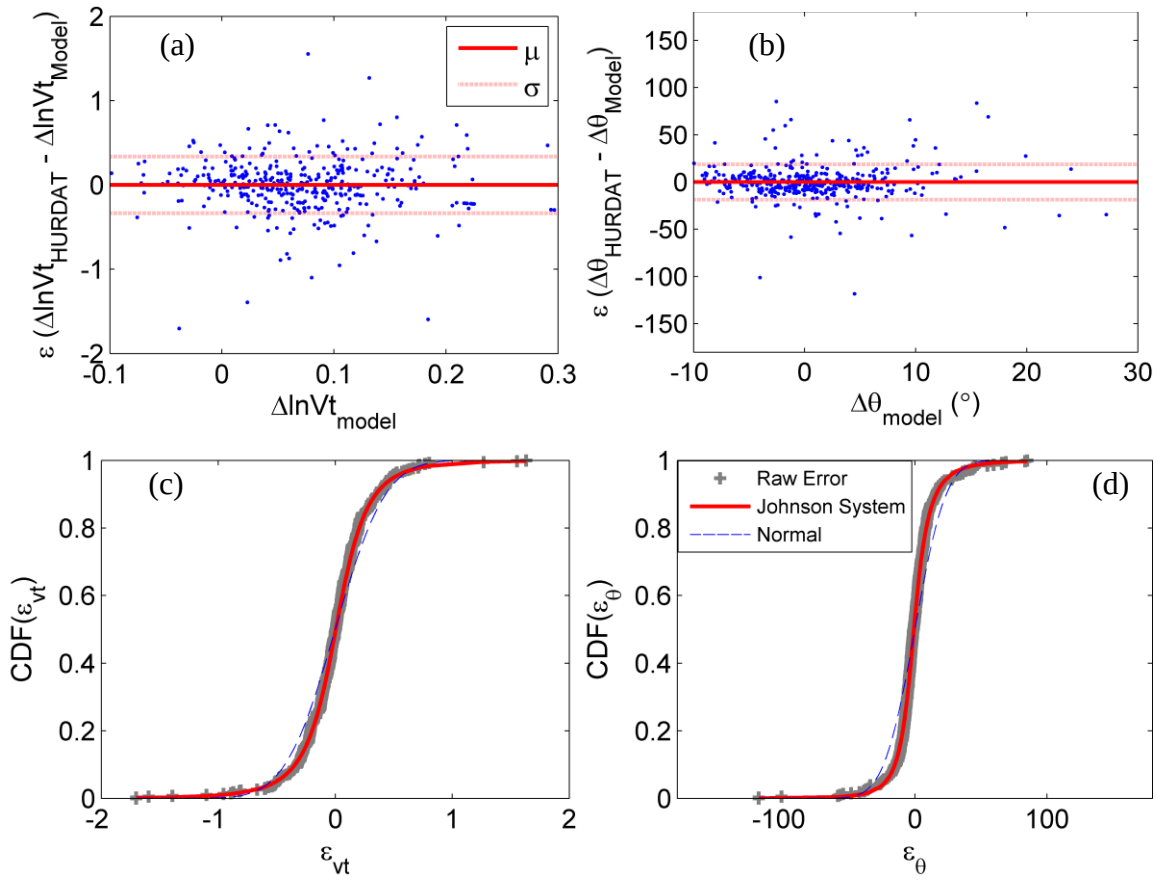


Figure 3.7: Tracking model errors for cell 72, (a) scatter plot of logarithmic modeling errors, (b) scatter plot of heading angle modeling errors, (c) CDF of forward speed modeling errors, and (d) CDF of heading angle modeling errors.

forward speed and heading angle model errors are scattered around zero, which indicate that the models are unbiased, and the scatter plots do not show any trend, which means the errors are randomly distributed. The cumulative distribution functions (CDFs) for the model errors along with the fitted Normal distribution and unbounded Johnson distribution CDFs are shown in Figure 7c and d. Both the CDFs of the fitted Normal and unbounded Johnson distributions match the empirical CDFs reasonably well. While both distributions fit the modeling errors well, it was determined that the unbounded Johnson distribution is the better model. This is

verified by the Kolmogorov-Smirnov test (K-S test) quantitatively: the critical value of K-S test for the data sample size (n=388) in cell 72 is 0.0685. For the modeling error of $V_t$, the K-S value is 0.091 for Normal distribution and 0.0256 for unbounded Johnson distribution; For the error in heading angle, K-S value is 0.1418 for the Normal distribution and 0.0224 for the unbounded Johnson distribution. Therefore, the modeling errors for tracking parameters were modeled using unbounded Johnson distribution. More details on the equation of unbounded Johnson distribution and the procedure to find the distribution parameters are given in the Appendix A.

Once the regression coefficients *a* and *b*, and the corresponding modeling errors are determined using the steps described above, changes in hurricane forward speed ($\Delta \ln V_t$) and heading direction ($\Delta\theta$) can then be calculated using Eqns. (5) and (6). Figure 3.8 shows example changes in hurricane forward speeds and heading angles for cell 72 computed using the tracking models (Eqns. (5) and (6)) and the initial values from HURDAT for all historical storms that passed through cell 72 as inputs. Note that the modeled data points shown in Figure 3.8a and b do not include the modeling errors in the calculation; hence, the HURDAT or observed data points are scattered around the model data. Figure 3.8c and d show examples of simulated changes in forward speed and heading angle with modeling errors sampled from the unbounded Johnson distribution. As can be seen, the dispersion of the modeling results matches well with the HURDAT observations after adding in the random errors. More plots of contrast between the modeled parameters and the observations in the same format of Figure 3.7 and 3.8 were made in other cells than cell 72. These plots are provided in Appendix B.

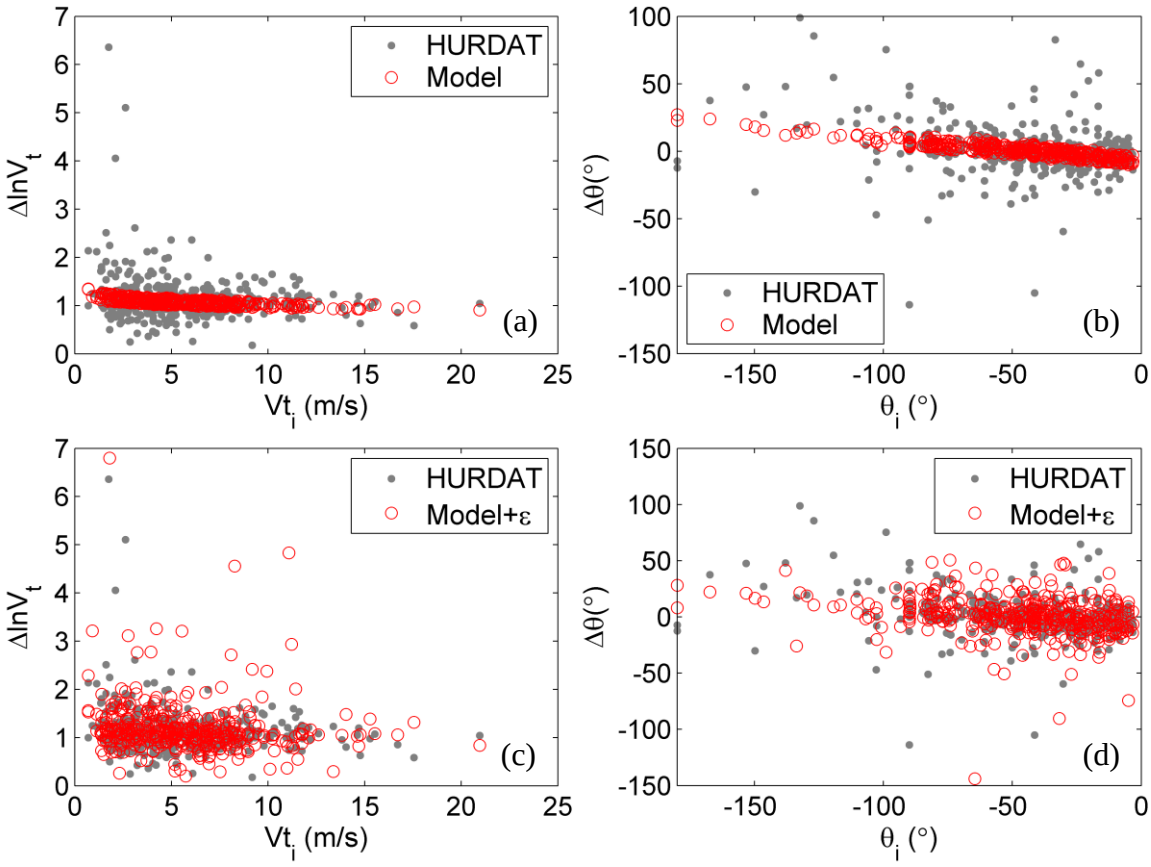


Figure 3.8: Comparisons between the outputs of tracking models and observations (HURDAT) for cell 72; (a) change in forward speed without modeling error, (b) change in heading angle without modeling error; (c) change in forward speed with modeling error, and (d) change in heading angle with modeling error.

Note that coefficients (*a* and *b*) and modeling error are only determined for those cells with 6 or more data points. This is because least squares regression cannot be performed to get reliable estimation of the coefficients when there are less than 6 data points. Hence, for those cells without sufficient records (less than 6 data points, shown in grey color in Figure 3.1), the coefficients and distribution parameters of modeling errors are copied from adjacent cells (shown in black color in Figure 3.1), if available, or the

closest neighboring cells. The criterions to copy the coefficients from one cell to another are illustrated in Appendix C.

## 3.3 Central Pressure Model

### 3.3.1 Relative Intensity Model

In the simulation framework, when the storm eye is on the ocean, the storm central pressure is converted into a transformed quantity, termed *relative intensity* (Darling 1991). The storm intensity model over the ocean is given by the following equation, which is a function of the SST (Vickery et al. 2000):

$$\ln\left(I_{i+1}\right) = c_o + c_1 \ln\left(I_i\right) + c_2 \ln\left(I_{i-1}\right) + c_3 \ln\left(I_{i-2}\right) + c_4 T_{s_{i+1}} + c_5 \left(T_{s_{i+1}} - T_{s_i}\right) + \varepsilon_I \qquad (9)$$

where $c_o$-$c_5$ are the cell specific intensity coefficients; $I_i$ is the relative intensity at step $i$; $T_{s_i}$ is the sea surface temperature (SST) at location $i$; $\varepsilon_I$ is the random error term.

The procedure to derive the coefficients in the relative intensity model is similar to that for the tracking models. The variables in Eqn. (9) were first grouped by cell numbers and heading directions (i.e. easterly or westerly movements). The $c$ coefficients were determined using least squares regression for those grids with at least 6 or more data entries (each data entry is for a 6-hour step). The modeling error, $\varepsilon_I$, quantified as the difference between the model predictions and the observations, was fitted into Normal and unbounded Johnson distribution.

Similar to the tracking models, for those cells without sufficient records (less than 6 data points), the fitted coefficients and modeling errors from adjacent cells are copied to those cells with insufficient data. It should be noted that there are more cells in the

simulation domain with insufficient data for fitting the coefficients for the intensity model than that of the tracking model. This is attributed to sparse central pressure records for those storms in the earlier years in HURDAT, due mainly to the limitation of monitoring technology.

The relative intensity is a function of central pressure and SST. The conversion from relative intensity to central pressure restricts the central pressure values within a reasonable domain (i.e. 863~1013mb). The procedure for performing the conversion of central pressure to relative intensity is discussed in Darling (1991). The SST data used in the intensity model of this study is obtained from the HadISST (Hadley Centre sea Ice and Sea Surface Temperature) dataset from years 1870 to 2013 (Met Office, Hadley Centre 2013). The monthly average SST data were used for the baseline model (i.e. without climate change). The monthly average temperatures were calculated by taking the mean of all the records in the same month from 1870 to 2013 with a resolution of 1° by 1° (Figure 3.9). The region covered by the SST maps in the simulation model is from 0° to 60° latitude and -110° to 0° longitude.

To examine the behavior of the central pressure model, the modeled central pressure in contrast with observations for various cells were plotted and provided in Appendix D. Along with the modeling estimations, the plots of modelling error are also provided to verify that the selected unbounded Jonson distribution is an appropriate type for modeling error of central pressure model.

### 3.3.2 Decay Model

Once a storm has made landfall, the central pressure deficit decay model (or filling rate model) is used to model the reduction in hurricane intensity (Vickery and Twisdale 1995, Vickery 2005). The filling rate model describes the decay of a storm (or rise in central pressure) as a function of time after landfall.

The central pressure decay model employed in this study is the model introduced in Vickery (2005). In this model, the decay rate of landfalling hurricanes is geographic dependent. For modeling purposes, Vickery (2005) subdivided the east coast of the United States (U.S.) into four different geographic regions: Gulf Coast, Florida, Mid-Atlantic Coast and New England Coast (Figure 3.10). For each region, the change in central pressure after landfall, $\Delta P_c$, with respect to the central pressure at landfall, $P_{co}$, is defined using the following equation:

$$\Delta P_c(t) = P_c(t) - P_{co} = (P_a - P_{co})\exp(at) \tag{10}$$

where $\Delta P_c(t)$ is the central pressure difference at hour $t$ after landfall $P_a$ is the ambient air pressure, and $a$ is the decay rate:

$$a = a_o + a_1(P_a - P_{co}) + \varepsilon_a \tag{11}$$

where $\varepsilon_a$ is a normally distributed error term with a mean of zero. $a_o$ and $a_1$ are the exponential filling rate constants that vary for different regions. The values of the decay constants and modelling error parameters are given in Table 3.1 where $N$ is the number of data used in model derivation (Vickery 2005).

Table 3.1: Decay constant $a$ and regression parameters (Vickery 2005).

| | | $a = a_o + a_1 \Delta p_{co}$ | | | |
|---|---|---|---|---|---|
| Landfall Region | N | $a_1$ | $a_o$ | $r^2$ | $\sigma_\varepsilon$ |
| Gulf Coast | 26 | 0.00068 | 0.0244 | 0.2683 | 0.0225 |
| Florida | 13 | 0.00116 | -0.0213 | 0.3149 | 0.0325 |
| Mid-Atlantic Coast | 13 | 0.00074 | 0.0128 | 0.3212 | 0.0174 |
| New England Coast | 6 | 0.00099 | 0.0034 | 0.5471 | 0.5471 |

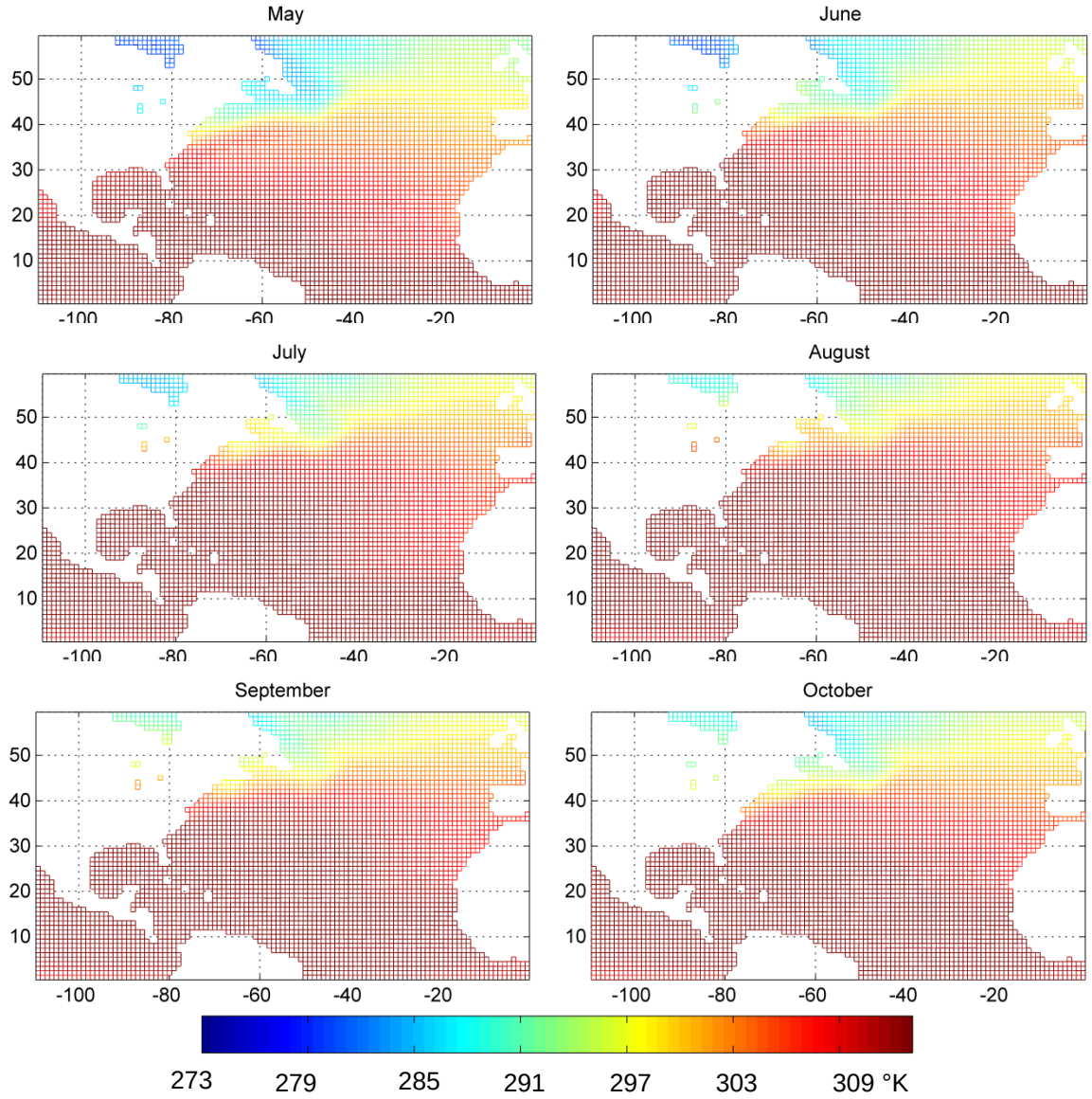


Figure 3.9: Monthly average SST from May to October (Met Office, Hadley Centre 2013).

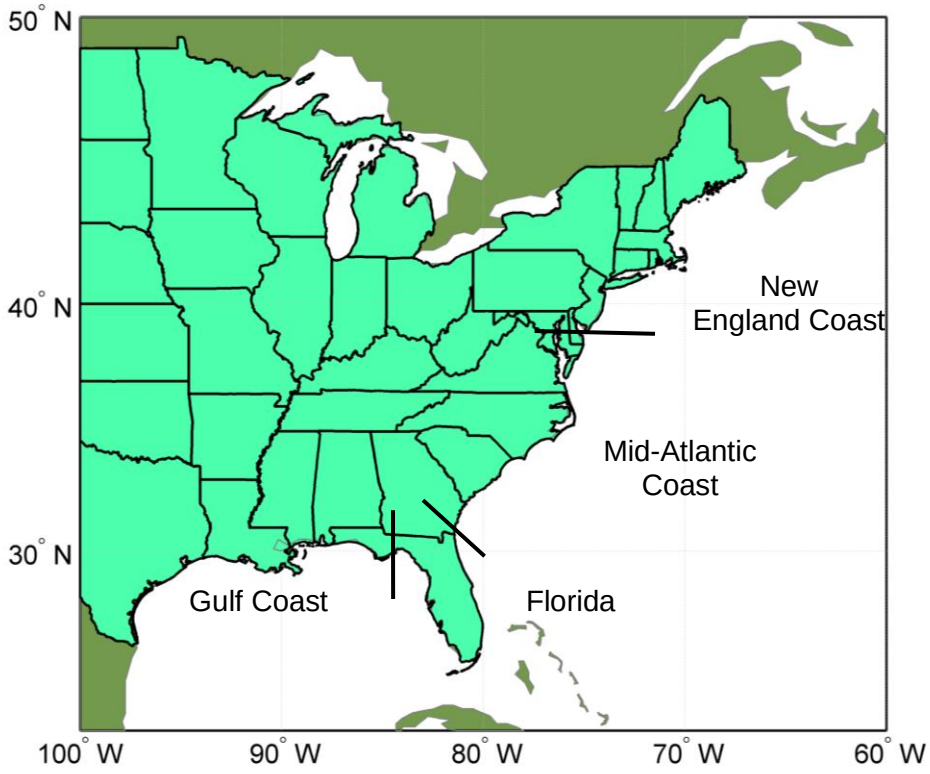


Figure 3.10: Geographic regions for decay model.

A storm is deemed dissipated when its central pressure is at or above the standard atmospheric pressure (1013 mbar). The simulation process of a storm is terminated when the particular storm has dissipated or has moved beyond the simulation domain.

## 3.4 Gradient Wind Speed

The following asymmetric wind field model was utilized to compute the gradient-level wind speeds, which occur around 500 to 2000 meters above the ground surface (Georgiou 1985, Georgiou et al. 1983):

$$V = \frac{1}{2}\left(c \cdot \sin\alpha - fr\right) + \sqrt{\frac{1}{4}\left(c \cdot \sin\alpha - fr\right)^2 + \frac{B\Delta p}{\rho}\left(\frac{R_{\max}}{r}\right)^B \exp\left[-\left(\frac{R_{\max}}{r}\right)^B\right]} \qquad (12)$$

where, $V$ = gradient wind speed; $\rho$ = air density; $\alpha$ = the angle (clockwise positive) from the storm forward direction to the location of interest; $r$ = distance from storm center to location of interest; $c$ = translational wind speed (storm forward speed); $R_{\max}$ = radius-to-maximum wind speed; $B$ = pressure profile parameter; $f$ is the Coriolis parameter and $f = 2\Omega \sin\phi$, where $\Omega$ is the rotation rate of the earth and $\phi$ is the latitude. One realization of gradient wind field negated using Eqn.(12) with input parameters from observation records is shown Figure 3.11.

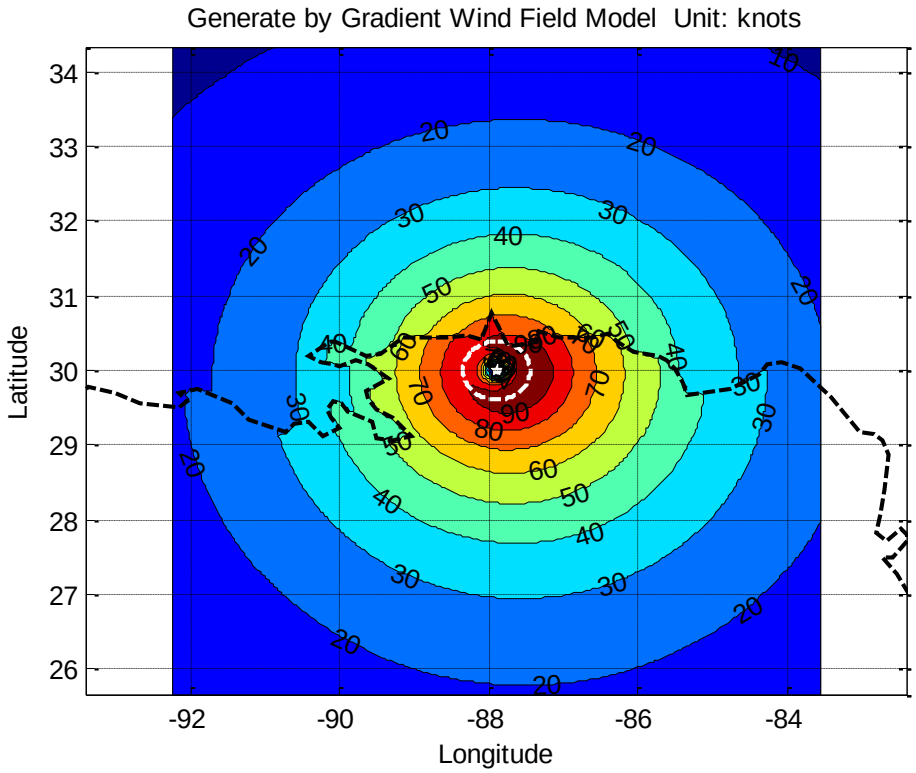


Figure 3.11: Gradient wind field generated using Eqn. (12) for 1-minuate sustained wind of Hurricane Ivan (2004) at 6:00 UTC on September 16th, 2004 (Dash line indicates the enclosure of $R_{max}$).

## 3.5 Empirical Model of Radius-to-maximum Wind Speed

The radius-to-maximum wind speed ($R_{max}$) and parameter $B$ is simulated using an empirical model (Vickery et al. 2009a; Vickery and Wadhera 2008). The radius-to-maximum wind speed (RMW or $R_{max}$) is determined using two empirical models. The equation for the Gulf of Mexico hurricanes is (Vickery and Wadhera 2008):

$$\ln R_{\max} = 3.858 - 0.000077\Delta p^2 + \varepsilon_R \tag{13}$$

where $\Delta p$ is the difference between the current central pressure and the atmospheric pressure $\left(P_c - P_a\right)$; $\varepsilon_R$ is the modeling error of the radius-to-maximum wind model. For the hurricanes in Gulf of Mexico, the standard deviation of the modelling error is given by the following equations:

$$\sigma_{\ln RWM} = 0.396, \Delta p \le 100 hPa \tag{14}$$

$$\sigma_{\ln RWM} = 1.424 - 0.01029\Delta p, 100\,\text{hPa} \le \Delta p \le 120 hPa \tag{15}$$

$$\sigma_{\ln RWM} = 0.19, \Delta p > 120 hPa \tag{16}$$

The $R_{max}$ model applied to all the other hurricanes is:

$$\ln R_{\max} = 3.015 - 0.0006291\Delta p^2 + 0.0337\psi + \varepsilon_R \tag{17}$$

where $\psi$ is the latitude of the storm center and the standard deviation of the modelling error is given as:

$$\sigma_{\ln RWM} = 0.448, \Delta p \le 87 hPa \tag{18}$$

$$\sigma_{\ln RWM} = 1.137 - 0.00792\Delta p, 87\,\text{hPa} \le \Delta p \le 120 hPa \tag{19}$$

$$\sigma_{\ln RWM} = 0.186, \Delta p > 120 hPa \tag{20}$$

## 3.6 Empirical Model of Parameter B

The parameter *B* describes the shape of the pressure field around the storm eye and the rate of the rise in pressure when moving away from the storm eye. A statistical model for parameter *B* is introduced in Vickery and Wadhera (2008) by analyzing the hurricane wind field data for historical storms with central pressures less than 980 mbar on the ocean:

$$B = 1.7642 - 1.2098\sqrt{A}, \sigma_B = 0.226 \tag{21}$$

The non-dimensional parameter *A* in Eqn. (21) which incorporates the effects of $R_{max}$, $\Delta p$, latitude and $T_s$ is defined as:

$$A = \frac{R_{\max} \bullet f}{\sqrt{2R_d \left(T_s - 273\right) \ln\left(1 + \frac{\Delta p}{p_c e}\right)}} \tag{22}$$

where *f* is the Coriolis parameter; $R_d$ is the gas constant for dry air as 287 J/(kg·K); $T_s$ is the sea surface temperature in degree Kelvin.

The modeling equation for parameter *B* after landfall is given as (Vickery et al. 2009a):

$$B(t) = B_o \exp(at) \tag{23}$$

$$a = 0.0291 - 0.0429 B_o, a \le -0.005 \tag{24}$$

where $B_o$ is the *B* value at landfall and *t* is the hour after landfall.

## 3.7 Boundary Layer Model

A hurricane boundary layer model (Vickery et al. 2009c) is used to convert the gradient wind speed from boundary layer height (around 500-1000 m) to the surface-level (10 m). In addition to the adjustment of height, transition and shift of the roughness regime from open water to overland is also considered in the boundary layer model. The hurricane boundary layer model is expressed in the following equation (Vickery et al. 2009c):

$$U(z) = \frac{u_*}{k}\left[\ln\left(\frac{z}{z_o}\right) - a\left(\frac{z}{H^*}\right)^n\right] \tag{25}$$

where $U(z)$ is the wind speed at height $z$ above the surface of the ground or the sea; $z$ in this application is taken as the standard observation height for surface wind which is 10m; $k$ is the von Kármán coefficient having a value of 0.4; $z_o$ is the surface roughness (m); $a$ and $n$ are 0.4 and 2 as given in Vickery et al. (2009c). $u_*$ is the friction velocity, which is related to the surface shear stress ($\tau$) via the following expression (Vickery et al. 2009c):

$$\tau = \rho u_*^2 = \rho C_d U_{10}^2 \tag{26}$$

where, $C_d$ is the drag coefficient and $U_{10}$ is the wind speed at 10m elevation or $U$(z=10m). $H$* is the boundary layer height parameter. For the hurricane boundary layer on the sea, $H$* is modeled using the following empirical equation (Vickery et al. 2009c):

$$H^* = 343.7 + 0.26 / I \tag{27}$$

For hurricane boundary layer on the land, it is determined by boundary layer height $H$ divided by 1.12 (Kepert 2001, Vickery et al. 2009c):

$$H = \sqrt{\frac{2K}{I}} \tan^{-1}\left(-1 - \frac{2}{\chi}\right), \chi = C_d V \sqrt{\frac{2}{KI}} \tag{28}$$

where $K$ is the turbulent diffusivity of momentum and taken as 75 $m^2/s$ (Kepert 2001, Vickery et al. 2009c); $I$ is the inertial stability and $V$ is the gradient wind speed (computed using Eqn.(12)). The equation for inertial stability $I$ is defined as (Kepert 2001, Vickery et al. 2009c):

$$I = \sqrt{\left(f + \frac{2V}{r}\right)\left(f + \frac{V}{r} + \frac{\partial V}{\partial r}\right)} \tag{29}$$

where $f$ is the Coriolis parameter; $r$ is the radial distance from the storm center. The sea surface drag coefficient $C_d$ at surface level is modeled as (Applied Research Associates 2008a):

$$C_{d10} = \left(0.49 + 0.065U(10)\right) \times 10^{-3}, C_{d10} \le C_{d_{\max}} \tag{30}$$

The maximum value of $C_d$ is limited to:

$$C_{d\max} = \left(0.0881r + 17.66\right) \times 10^{-4}, 0.0019 \le C_{d\max} \le 0.0025 \tag{31}$$

The drag coefficient on the land is taken as 0.0047 for open terrain.

By substituting Eqns. (26) to (31) into Eqn. (25) and evaluating it at z = 10m, the wind speed at 10m elevation $U(10)$ is the only unknown variable remains at both sides of Eqn. (25). The Matlab *fminsearch* function minimization algorithm (Lagarias et al. 1998) is used to solve for $U(10)$ in Eqn.(25).

Figure 3.12 shows the vertical wind profiles for wind speeds measured between 1200m and 10m elevations using dropsondes, grouped into 20-29, 30-39, 40-49, 50-59, 60-69 and 70-85 m/s bins, for storms with $R_{max}$ between 10-30km. The gradient wind speeds computed using the Georgious' wind field model (Eqn.(12)) are assumed to be at

an elevation of 1200m. The boundary layer model (Eqn.(25)) is calibrated for wind speeds measured at elevations between 1000m and 10m. To convert the gradient wind speed (at 1200m) to the top of the boundary layer model (i.e. 1000m), a factor of 1.15 was used for the adjustment of height from gradient level (1200m) to 1000m. The 1.15 factor is determined empirically by averaging the wind speeds at 1200m divided by that at 1000m for all bins shown in Figure 3.12. For validation purpose, Eqn. (25) was used to reproduce the wind profiles with $R_{max}$ from 10-30km and the boundary layer wind profiles are shown as green curves in Figure 3.12. The initial values to the boundary layer model (shown as "*" on x-axis in Figure 3.12) were found from Vickery et al. (2009c) and comparison was made between the modeled wind profile in this study and the observations in Vickery et al. (2009c). As can be seen, the model wind profiles match the measured wind profiles reported in Vickery et al. (2009c) reasonably well for heights between 10m and 1000m.

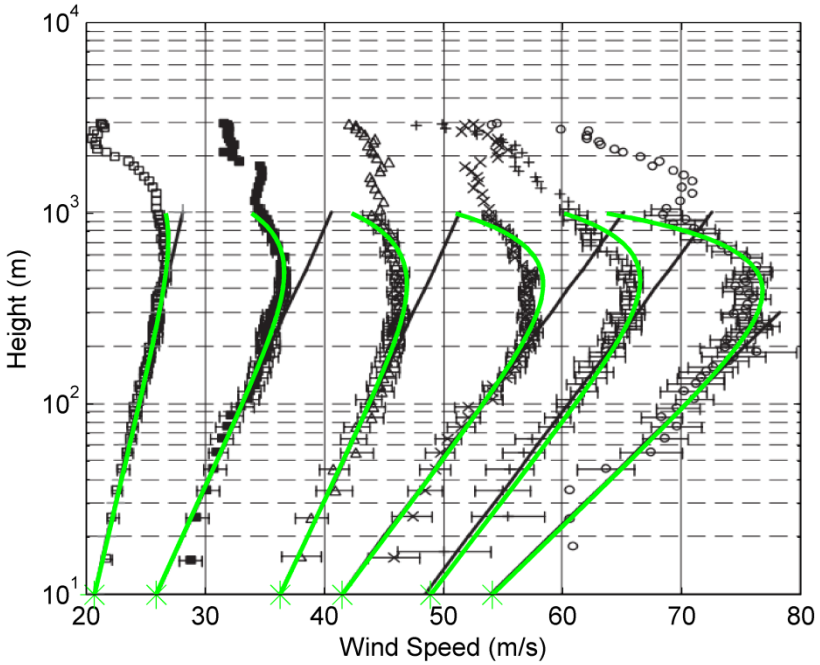


Figure 3.12: Mean and fitted logarithmic profiles near the $R_{max}$ (10-30 km) location in wind field. The scatter data are observations in the mean boundary layer bins (20-29, 30-39, 40-49, 50-59, 60-69 and 70-85 m/s) from Vickery et al. (2009c). Straight lines are least squares fits from 20-200m in Vickery et al. (2009c). The bold curved lines are the wind profiles computed in this study using Eqn. (25).

# CHAPTER FOUR: MODEL VALIDATION AND SENSITIVITY STUDY OF SIMULATION MODULES

## 4.1 Validation of Baseline Hurricane Simulation Results

### 4.1.1 Distribution of Hurricane Characteristic Parameters in Selected Grid

In the previous Chapter, the performance of simulation models was examined by reproducing historic hurricane events with initial observation as input to the models and sensitivity analysis on key parameters using one-at-a-time approach (Figure 3.8, Appendix B and Appendix D). In order to validate the results produced from the complete Monte Carlo simulation procedure, the statistics of simulated hurricanes were inspected cell by cell over the simulation domain (Figure 3.1). Three important characteristic parameters: heading angle ($\theta$), forwarding speed ($V_t$) and central pressure ($P_c$) were compared between the extracted values from HURDAT and those from the events of 1000 simulated years on the grid map (Figure 4.1). As shown in Figure 4.1, the figures in the right column show the predictions made at step *i* in the example cell (No. 95) versus the values from its previous steps (step *i-1*) that served as the input. The patterns in the figures are almost linear with the slope close to 1. It indicates the magnitude changes in the parameters are mostly not abrupt over 6-hour. The simulation models with progressive weighted functions (Eqns.(5), (6) *and* (9)) are proved to be able to represent this property of tropical storms by carrying information from previous steps into the prediction of the following steps. The figures in the left column show the distributions of key parameters in percentage. The range of the characteristic parameters

was divided into 4 bins and the percentages from both historical data and simulation results fallen into each bin were presented on the vertical axis. The distributions in cell 95 which contains large number of data points were demonstrated in Figure 4.1. In the simulation domain, cell 95 is located around the coastline of Carolinas. It can be observed that the pattern from the simulated data overlapped those from observations. Also, the percentages of parameters from both sources agree well with each other which indicate the hurricane simulation model is capable to represent the trend of hurricane observations. The inspections of the data in more cells are included in Appendix E.

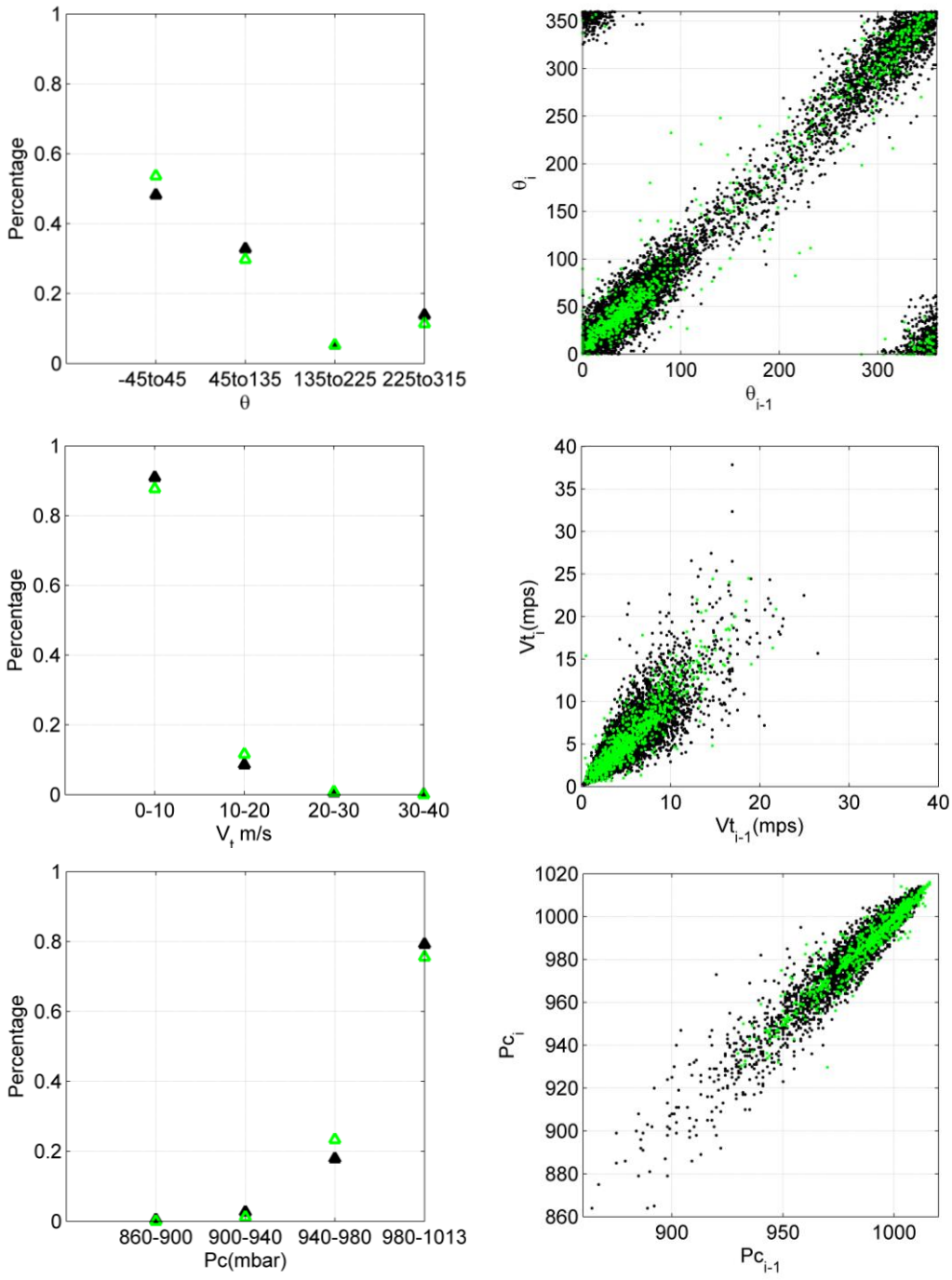


Figure 4.1: Statistics of hurricane parameters in cell 95. Figures on the left show the distributions of hurricane parameters in the cell. Figures on th right show the predictions made in the cell vs. values of previous step as input (Black dots represent simulated results; green ones represent observations).

### 4.1.2 Distribution of Hurricane Characteristic Parameters along the Coastline

To validate the simulation results especially in aspect of their impact to coastal regions, occurrence rate, forwarding wind speed, heading direction and central pressure of the landfalling and bypassing hurricanes (travelling alongshore) were inspected and compared with historical records. The key parameters from hurricane events travelling around the coastline were obtained from both simulation and historical database. The statistics of the parameters were assembled around the same 61 locations on the U.S. coast as shown in Figure 4.2. The range of search for sample data from the entire database is defined as 250 km around each milepost which is the same manner in dealing with Figure 4.11 and 4.15. From the comparison in Figure 4.3, it is found that the

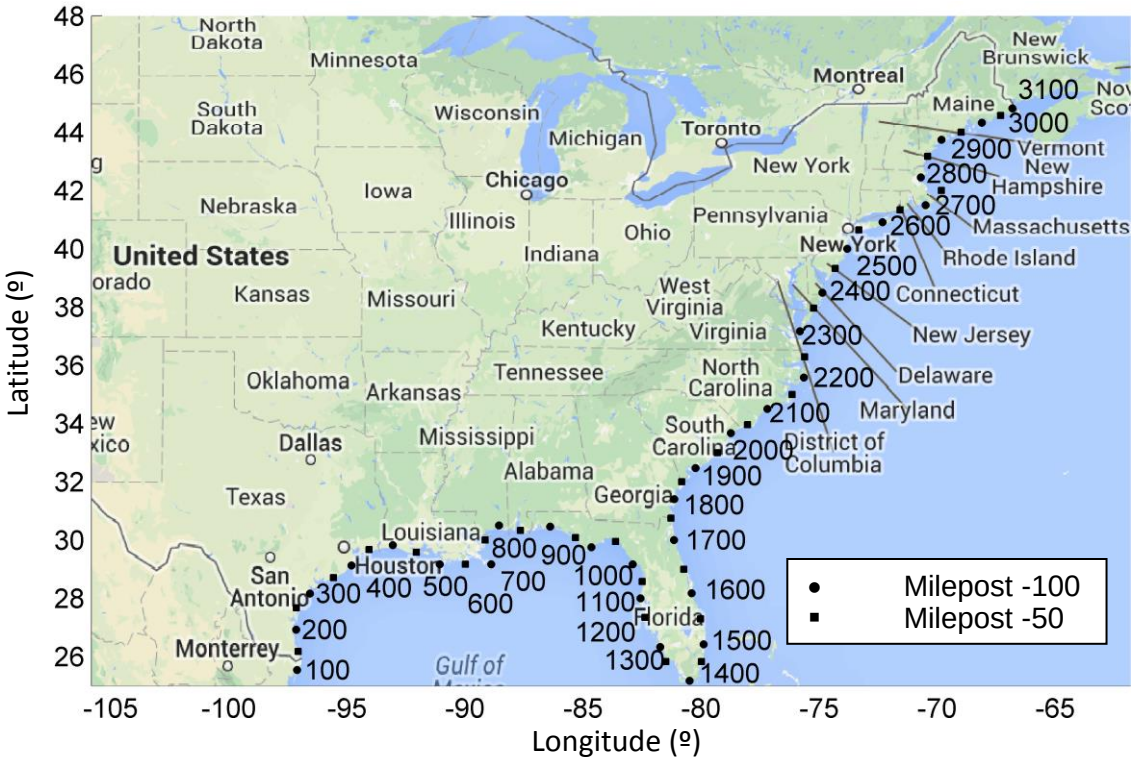


Figure 4.2: Milepost locations along the U.S. coastline.

statistics from simulation results agree reasonably to the levels in historical observation along the coastline. The mean values of the four parameters vary in the trend of the observed means along the mileposts. The spreads of these parameters also match well with that from the observed data, as the standard deviation values are close between the two data sets. The consistency in the mean levels and the dispersions indicates that the simulated statistics are representative of the observations.

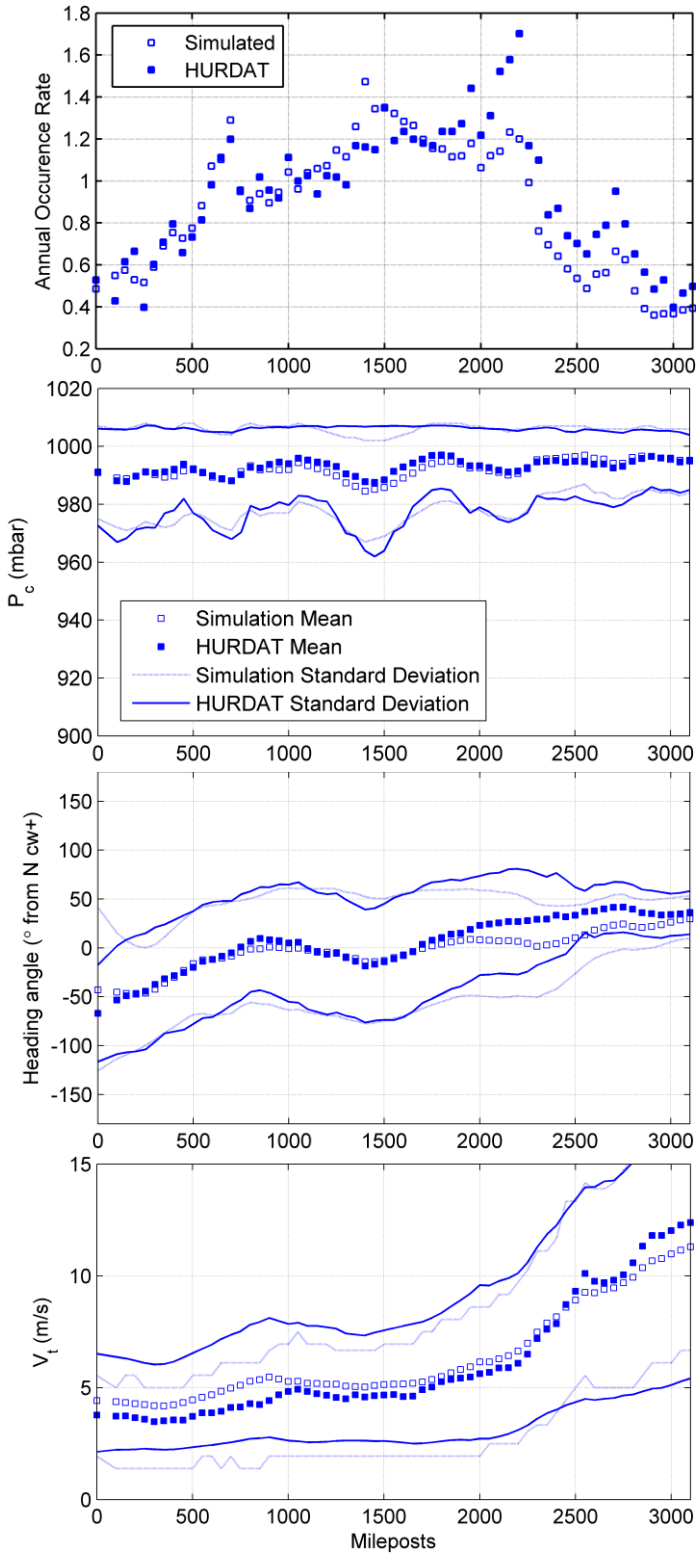


Figure 4.3: Statistics of hurricane parameters at mileposts along the coastline.

## 4.2 Assessment of Tracking Model

To inspect the simulated hurricane tracks qualitatively, storm tracks of 5-year simulations were sampled randomly from the simulated database and plotted in Figure 4.4. In comparison, the real tracks from years 2008 to 2012 are also plotted. Similar tracking patterns can be observed from the two plots, with the general westerly travelling

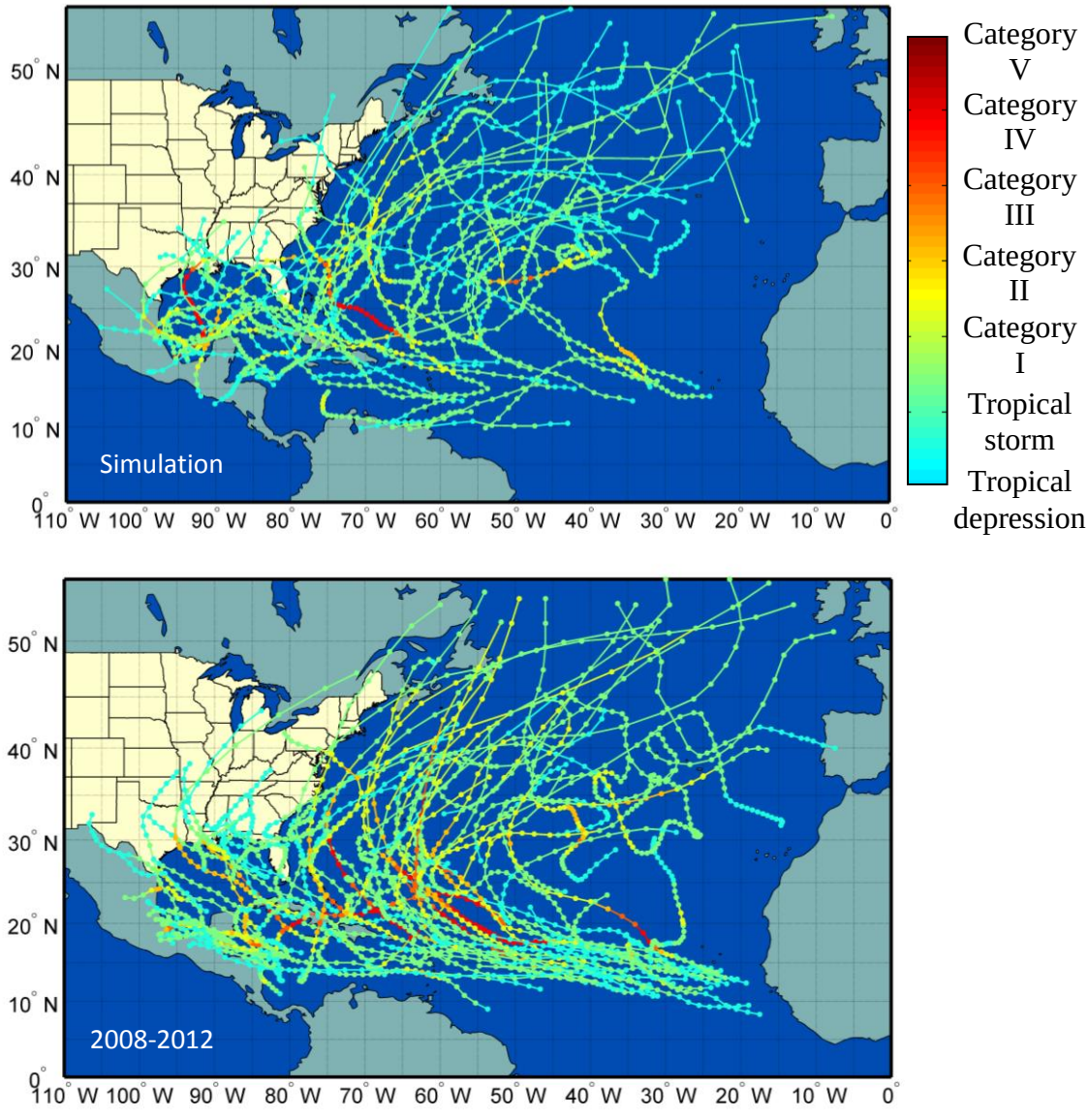


Figure 4.4: Simulated storm tracks of 5 years and real storm tracks from 2008 to 2012.

trends to the south of latitude of 30º and easterly travelling trends when storms travel further to the north.

To examine the performance of the tracking model, simulations were performed on the tracking model module in the simulation framework independently. The initial conditions of Hurricane Irene at UTC 00:00 on August 25th, 2011 were used as the input in the simulation. Synthetic hurricane tracks were generated for the next 72 hours (Figure 4.5). The initial location of hurricane eye, forward speed and heading direction of Hurricane Irene at UTC 00:00 on August 25th, 2011 were used as inputs for Eqns. (5) and (6) to simulate the storm forward speeds and heading direction for the next 72 hours. A

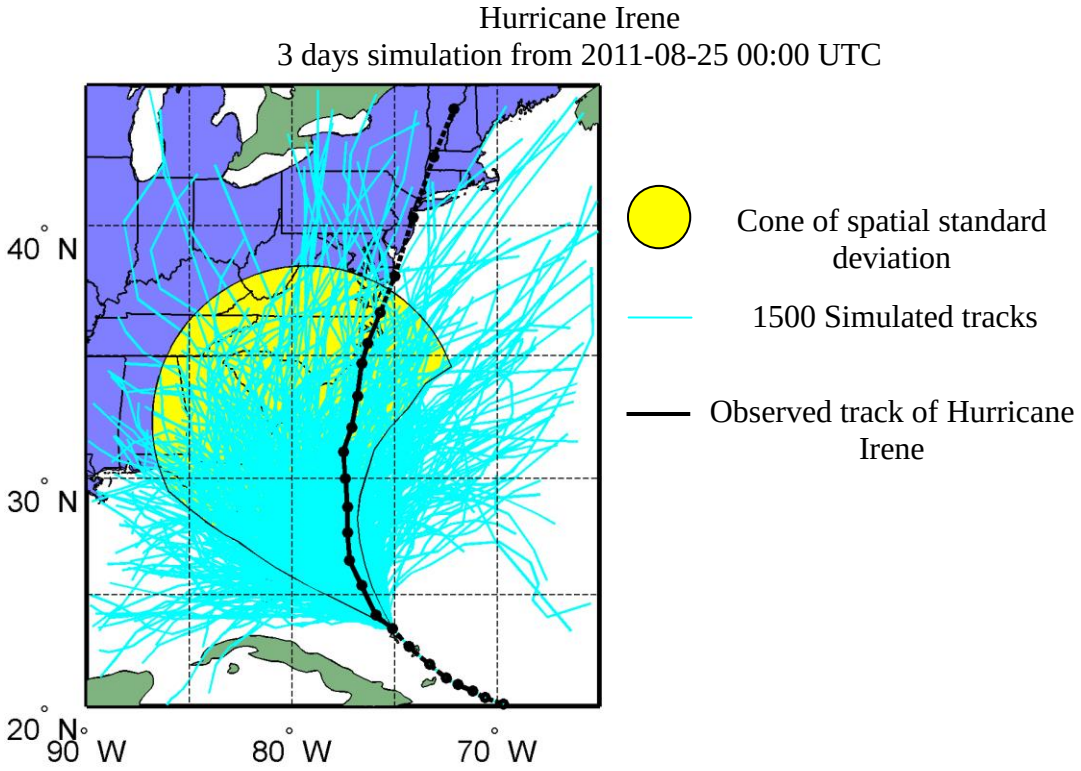


Figure 4.5: Simulation of storm tracks in 3 days with initial hurricane information of Hurricane Irene at 00:00 UTC, August 25th 2011.

convergence study was performed on the tracking model by simulating 3000 realizations of Hurricane Irene tracks. Note that Figure 4.5 includes 1500 of the 3000 simulated tracks. By calculating the spatial standard deviation of the simulations, it was determined that convergence of the spatial standard deviation cone occurred at around 1500 simulations (Figure 4.6). The simulated one spatial standard deviation cone is presented in Figure 4.5 along with the observed track of Hurricane Irene (solid black line). As shown in the Figure, the real track of Hurricane Irene lies inside the one standard deviation cone of the tracking model. More examples of tracking model assessment are given in Appendix H.

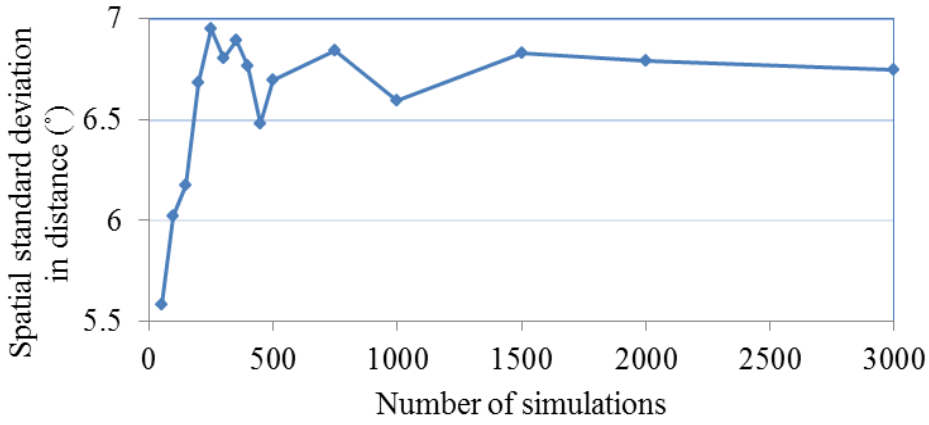


Figure 4.6: Number of storm track simulations versus spatial standard deviation of the 3-day out simulated storm locations of Hurricane Irene from UTC 00:00, August 25th 2011.

## 4.3 Assessment of Central Pressure Model

Similar to the tracking model, simulations on central pressure were performed using relative intensity model (Eqn. (9)) for storms on the sea and central pressure decay model (Eqns. (10) and (11)) for storms on land. The coefficients used in these models (i.e.

the *c* coefficients in the cells and decay rate) were determined based on the storm path and the central pressures are simulated based on the central pressures of previous steps. The example simulations were performed using the actual path and initial central pressures of three storms. The three events selected are Major Hurricane Katrina (2005), Hurricane Ophelia (2005) and Tropical Storm Arlene (2005). These three events occurred at different time during the same year (Figure 4.7) and represent different hurricane categories. The time histories of the simulated central pressures with 6-hour intervals are shown in Figure 4.8 and 4.9. The central pressure simulations based on tracking information of Hurricane Katrina were performed from August 24$^{th}$, 2005 when the storm

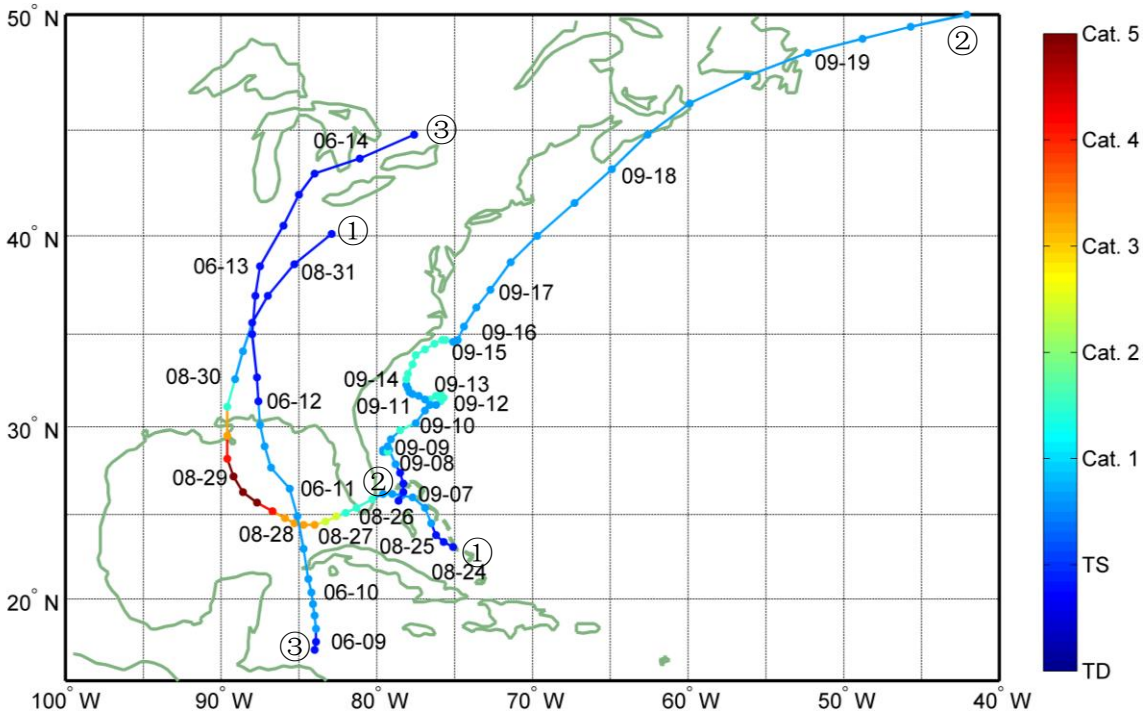


Figure 4.7: Storm tracks of ①Major Hurricane Katrina (2005), ②Hurricane Ophelia (2005) and ③Tropical Storm Arlene (2005). Colors indicate the intensity of storm.

track located on the ocean shortly after its formation (Figure 4.8). The relative intensity model (Eqn.(9)) was used to simulate the storm central pressure when the storm eye is on the sea surface. When the storm eye moved to the land, the model used to calculate central pressure is switched from the intensity model to the central pressure decay model (Eqns.(10) and (11)). For Hurricane Katrina, the decay model was employed for central pressure calculation of the 6-hour after its first landfall at UTC 00:00 on August 26$^{th}$ near South Florida and the central pressure calculations after the second landfall near Louisiana at UTC 12:00 August 31$^{st}$, 2005. Figure 4.8 includes 1000 simulations of the Hurricane Katrina's central pressure time histories. The mean, +/- one and two times of standard deviation of the simulated central pressure time histories based on the track of Hurricane Katrina are shown in Figure 4.10. It shows that both the mean and standard deviation converged at round 1000 or more simulations. From Figure 4.8, it can be seen that the central pressure of Hurricane Katrina actually dropped outside of the minus one standard deviation bound of simulation for large parts of the time history. This result is conceivable since Hurricane Katrina produced the third lowest central pressure measured at landfall in the history of hurricane record (Blake et al. 2011). The central pressure simulations based on tracking information of Hurricane Ophelia (2005) and Tropical Storm Arlene (2005) were performed using the same models (Figure 4.9). The highest intensity of Hurricane Ophelia during its life was category I. Unlike the case of Hurricane Katrina, it is found that the mean values of simulated central pressure for Hurricane Ophelia lie around the central pressure observations. And the observations are mostly enclosed in the bounds of simulation standard deviation. The central pressure observation

of Tropical Storm Arlena is found close to the upper bound (above mean) of simulation standard deviation. The intensity of Hurricane Arlena stayed at or below the tropical storm level of the Saffir-Simpson wind scale during its entire life. More assessments of central pressure simulation over time are given in Appendix I.

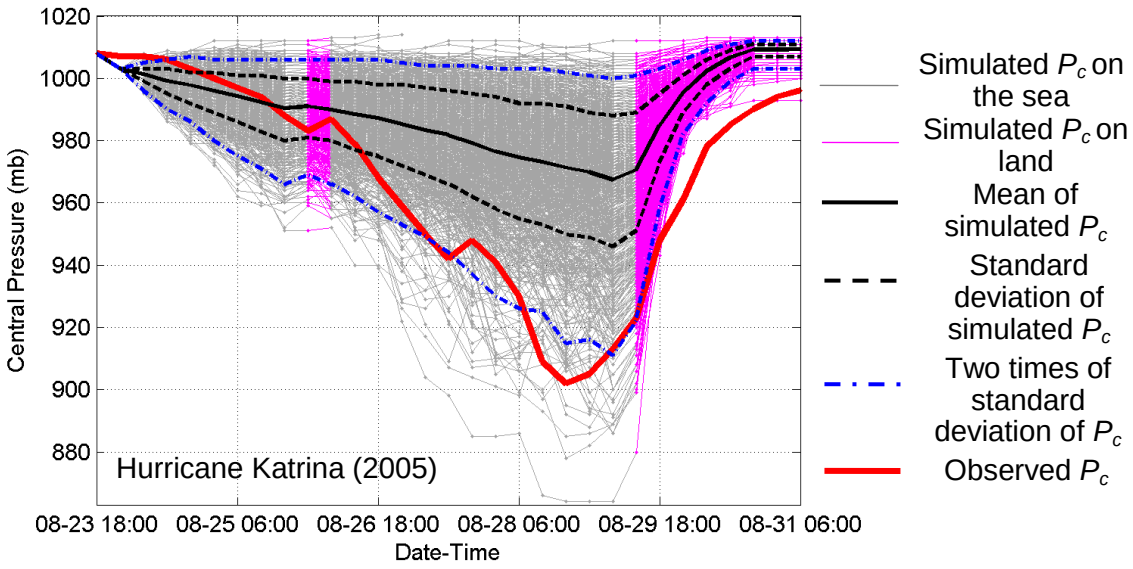


Figure 4.8: Time histories of the observed and simulated central pressures of Hurricane Katrina (2005).

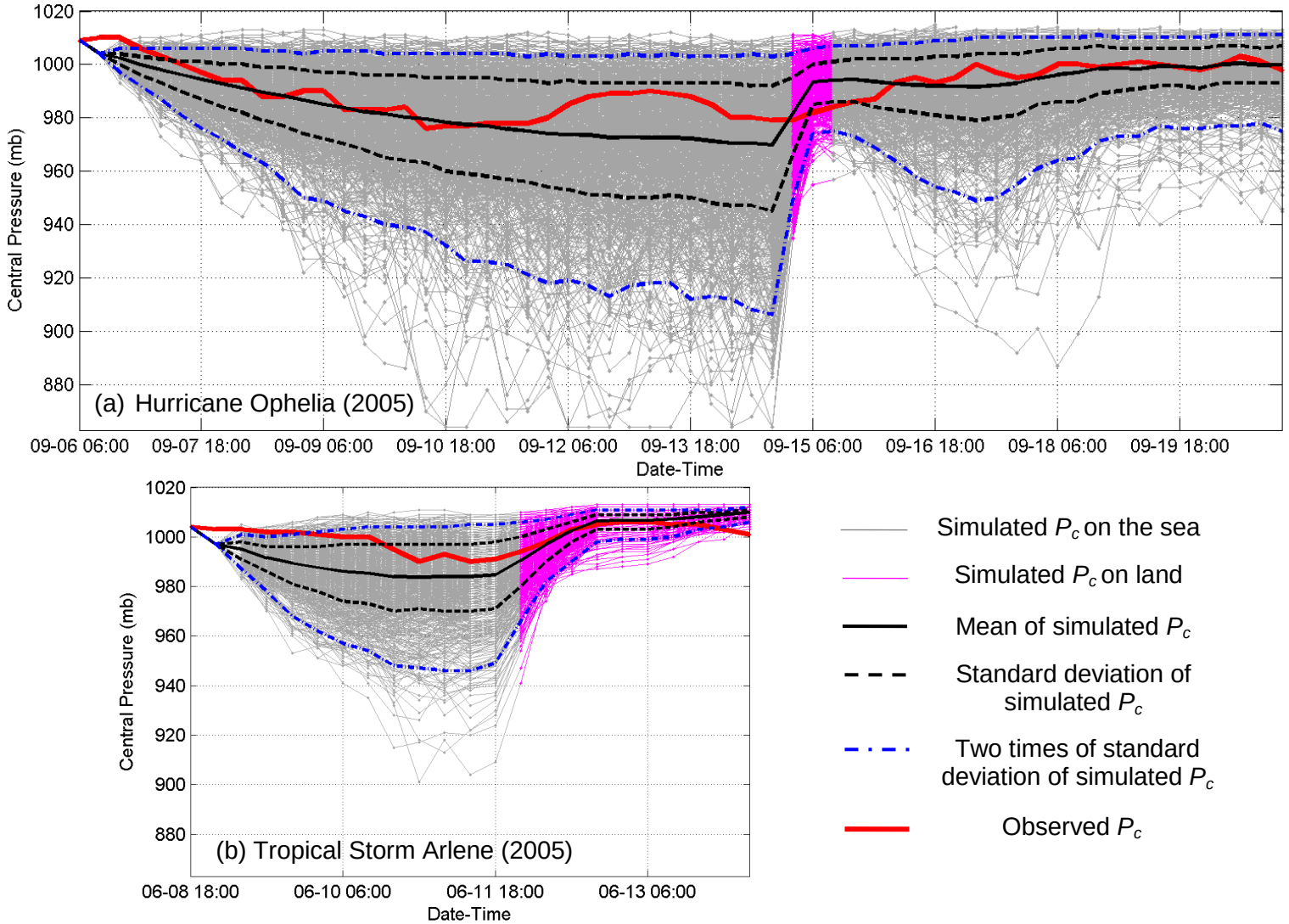


Figure 4.9: Time histories of the observed and simulated central pressures of (a) Hurricane Ophelia (2005) and (b) Tropical Storm Arlene (2005).

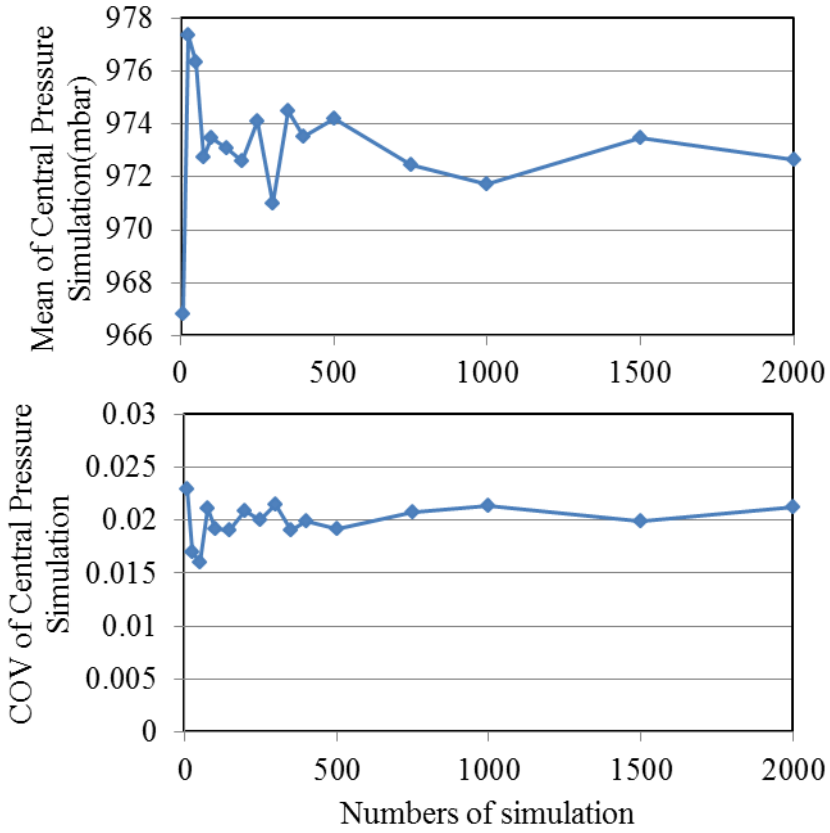


Figure 4.10: Convergence plot of simulated central pressures; (top) mean central pressure versus number of simulations, and (bottom) CoV of central pressure versus number of simulations.

## 4.4 Sensitivity Analysis of Sea Surface Temperature and Storm Formation Rate

For a complex mathematical model such as the stochastic hurricane simulation model discussed in Chapter Three, sensitivity analysis is an important parametric study technique for the model. It quantitatively examines the responses of the model to the change of individual inputs and is useful in model validation. In this study, the one-at-a-time approach was employed to perform sensitivity analysis and to test the changes in the

model response due to changes in the two climate change variables considered in this study, namely storm frequency and sea surface temperature.

The sensitivity analysis of storm frequency was performed by adjusting the statistical mean in the baseline storm genesis model by ±10% and ±20%. As mentioned in Chapter Three, the annual storm frequency of the baseline simulation model is generated using a negative binominal distribution which distribution parameters were fitted from historical records. In this sensitivity analysis, the distribution parameters (*R* and *P*, see Eqn.(4)) were re-calculated and adjusted by altering the mean value of storm number per year from the historical average (10.74 storms/year). The standard deviation was kept unchanged (5.58 storms/year). The ±10% change to historical average storm frequency produces about one more or fewer storm each year and ±20% means about two more or fewer storms each year. A simulation of 20,000 years was performed for each of the variations (i.e. +10%, -10%, +20% and -20%).

Sixty one markers spaced at 92.6 km (50 nautical miles) apart along the eastern coastline of the U.S., refer to as "mileposts" (Figure 4.2), are used to examine the simulation results. The annual occurrence rate or approaching rate of hurricanes for each milepost was computed by dividing the total number of storms observed within a radius of 250 km from individual mileposts by the total simulation years. In the same manner, the mean of central pressure for each milepost was calculated using the central pressure observed within the same search radius (i.e. 250 km).

### 4.4.1 Sensitivity Study of Storm Formation Rate

The simulation results of sensitivity analysis on storm formation frequency are shown in Figure 4.11. As expected, the annual storm occurrence rate along the coastline increases or reduces proportionally with the change in storm formation frequency. The maximum increase in storm occurrence rate compared to the baseline model is 0.29 storm/year (+1 storm for every 3.4 years) at milepost 1400 in Florida Peninsula for a +20% increase in mean annual storm formation rate (from 10.7 storms/year to 12.9 storms/year) and 0.14 storm/year (+1 storm for every 7.1 years) from mileposts 1400 to 2200 for a +10% increase in storm formation rate (from 10.7 storms/year to 11.8 storms/year). The mean increases for all 61 mileposts are 0.09 and 0.18 storm/year, respectively, for the two levels of formation frequency adjustments (i.e. +10% and +20%). This implies that there will be averagely one additional storm approaches any single location on the U.S. coastline every 6 to 11 years if the storm formation frequency is raised by 10% to 20%. For the segment of coastline that exposed to higher change of hurricane strike rate (i.e. Florida and Atlantic coast), there will be one more storm for every 3 to 7 years for a 10% to 20% increase in annual storm formation rate. It can also be observed from Figure 4.11 that the magnitudes of decreases in annual occurrence rates at mileposts when the mean storm formation rate was reduced by 10% and 20% largely symmetric to that when the storm formation rate was increased. The results in Figure 4.12 show that the storm occurrence rate along the coastline is directly proportional to the mean annual storm formation rate in the genesis model. This is expected and verified with the four mileposts selected in Figure 4.12 as milepost 700 in Gulf coast, milepost

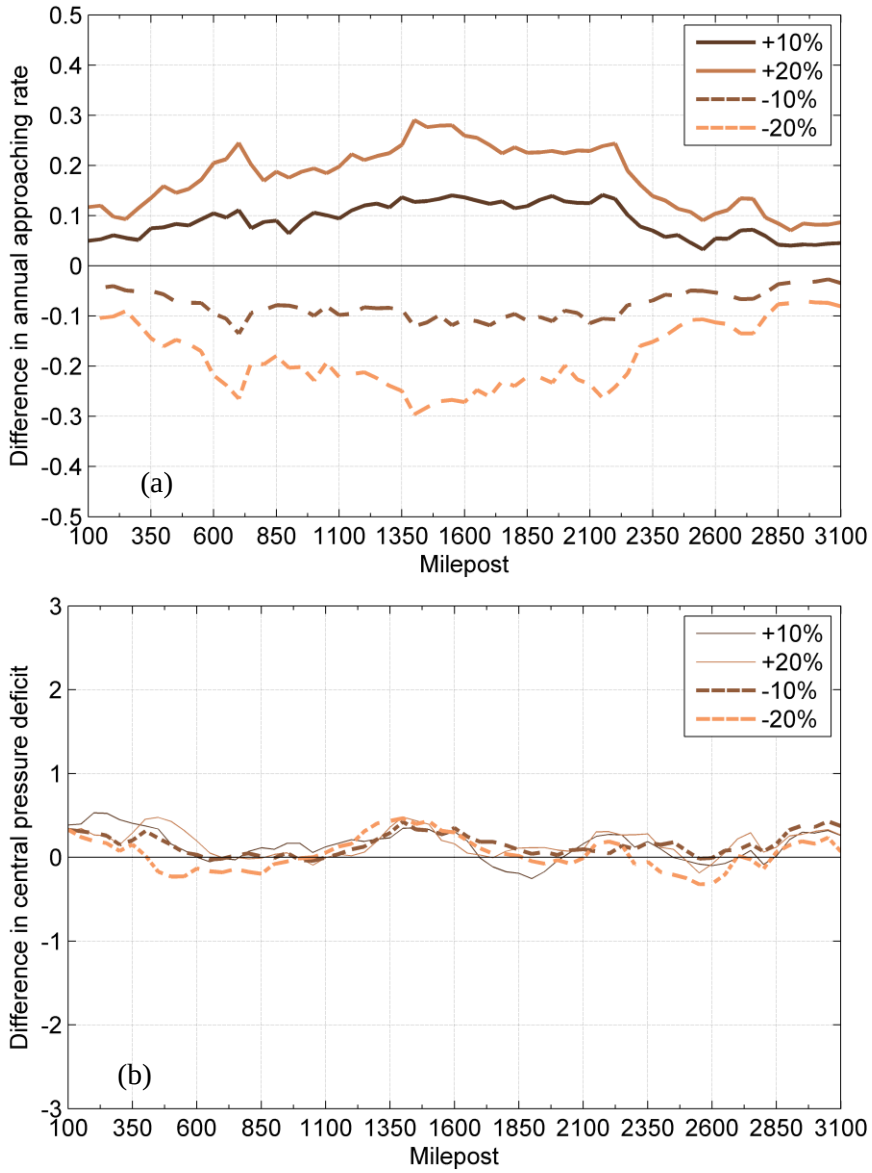


Figure 4.11: Difference of annual approaching rate and central pressure for synthetic hurricanes with ±10% and ±20% adjustment in formation frequency.

1400 on Florida Peninsula, milepost 1950 along the Mid-Atlantic coast and milepost 2550 on the New England coast. As the number of storms formed in Atlantic Basin increases or decreases, the probability and number of storms making landfall are also increased or decreased correspondingly.

The changes in mean central pressures at mileposts compared to that of the baseline model due to changes in storm formation rate are shown in Figure 4.11b. The maximum magnitude of change in the mean central pressure of storms for the four adjusted storm formation rates (i.e. ±10% and ±20%) is less than 0.5 mbar (0.007 psi). In this sensitivity study, the storm formation rate was varied while other parameters such as the sea surface temperature (SST) were kept constant. Since SST is the main factor that affects the storm intensity, while the storm formation rate was varied, the probability for a given storm to intensify or weaken when it travels over the Atlantic Ocean remained the same because the SST was kept constant. Therefore, the average storm intensities (or central pressures) observed at mileposts are expected to remain unchanged.

In addition to storm occurrence rate and central pressure, other parameters such as

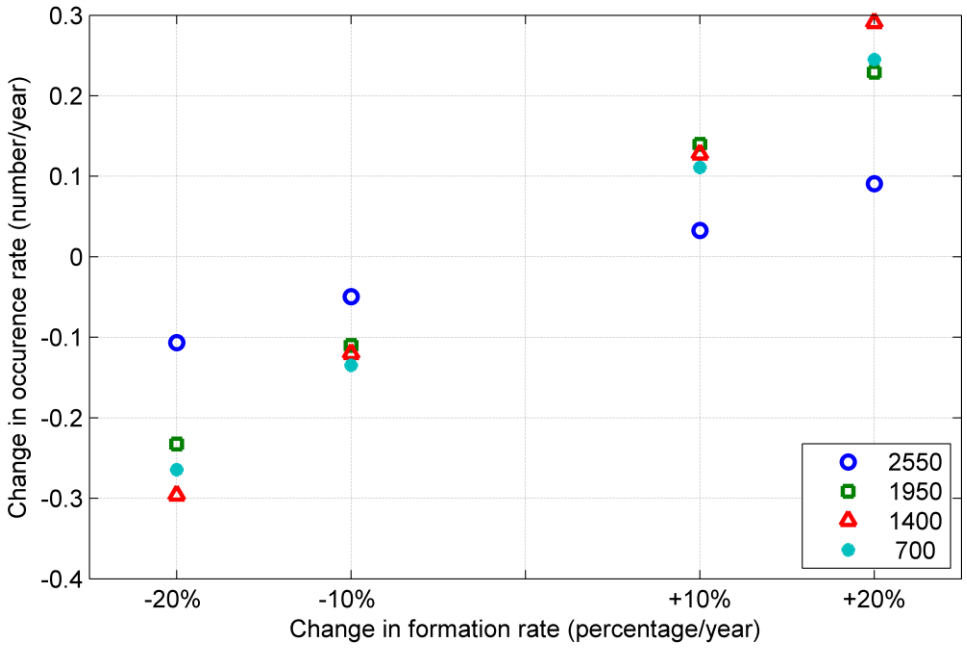


Figure 4.12: The changes in annual occurrence rate versus percentages of change in hurricane formation rate for milepost 700, 1400, 1950 and 2550.

the forward speed and approach angle at the mileposts were also examined and they were found to remain unchanged compared to that of the baseline model. More details about the changes in other parameters can be found in Appendix F.

Figure 4.13 shows the comparisons between the 10m gust wind speeds of the baseline model and the models with an adjusted storm formation rate. The 300-year, 700-year and 1700-year mean recurrence interval (MRI) wind speeds for the 61 mileposts are shown in Figure 4.13a, b and c, respectively. The 300-, 700-, and 1700-year MRIs were selected because these MRIs correspond to the ASCE 7-10 design wind speeds for design Risk Categories I, II and III&IV, respectively. In general, the wind speeds reduces as the storm formation rate reduces and vice versa; however, the differences are not significant. When the storm formation rate is adjusted to increase and more storms are formed in the Atlantic Ocean, the probability of rare (e.g. with a MRI of 1700 years) and intense storms with low landfalling central pressures increases slightly as well. It should be noted while the mean landfalling central pressures at mileposts remain more or less unchanged when the storm formation rate is adjusted upward or downward (see Figure 4.11), the central pressures of storms at the tail end of the distribution or extreme events (300-, 700- and 1700-year MRIs are considered as extreme events) may change based on the storm occurrence rate at mileposts.

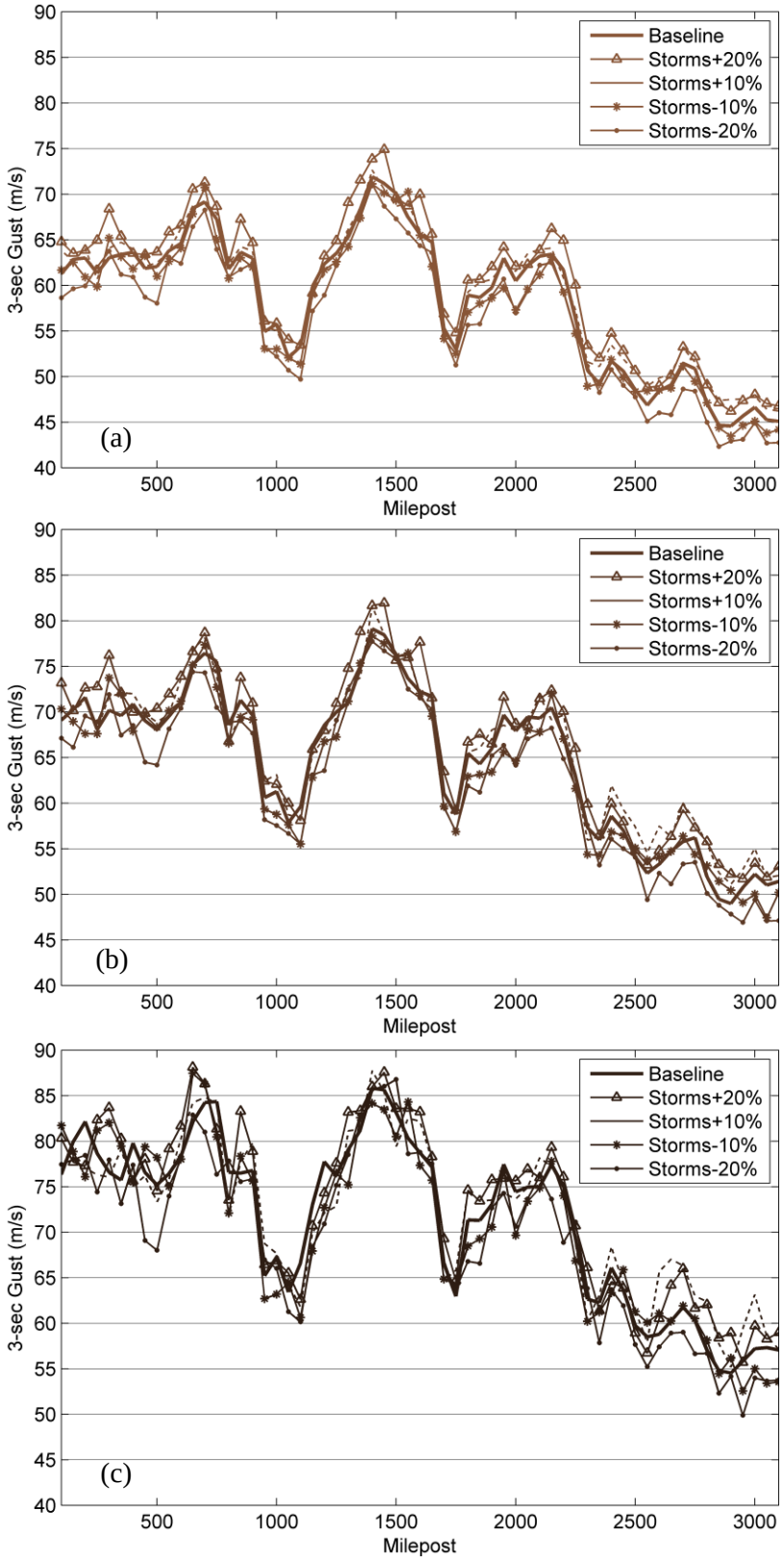


Figure 4.13: Comparisons of 10m-height gust of (a) 300, (b) 700 and (c) 1700-year MRI in formation rate variations.

### 4.4.2 Sensitivity Study of SST

The sensitivity analysis on SST was performed by adjusting the historical monthly mean SST of the baseline model by ±10% and ±20% (see Figure 4.14). The percentage changes were applied to the mean monthly SST in Celsius. For example, the highest temperature recorded in August in the 1° by 1° grid map is 30.3°C (303.5°K). For 10% and 20% increases in SST, the maximum values become 33.3°C and 36.4°C, respectively. Vice versa, for 10% and 20% decreases in SST, the peaks of SST in the basin are 27.3°C and 24.3°C, respectively. The SST maps of the adjusted SSTs for the month of August for the four cases considered are given in Figure 4.14. The adjusted SSTs for other months are provided in Appendix G.

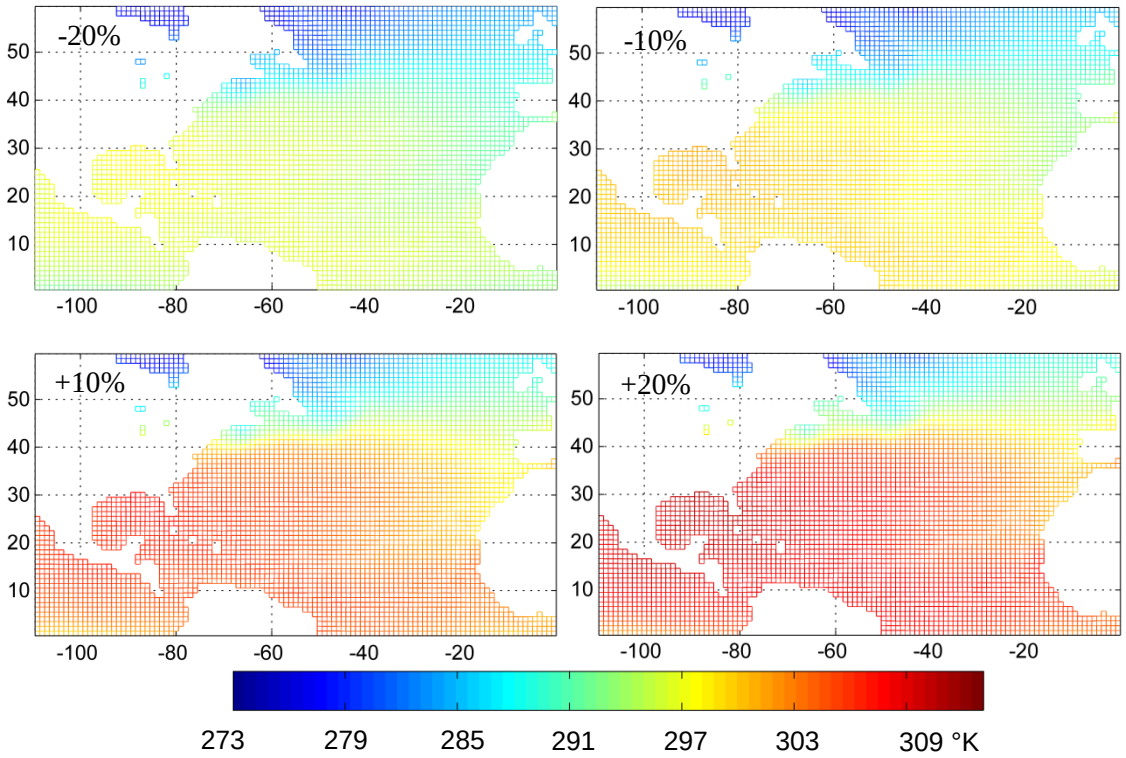


Figure 4.14: Grid maps of SST in August with adjustment of -20%, -10%, +10% and +20% based on the historical mean record.

The approaching rates and mean central pressures at mileposts were computed for 20,000 years of simulations for each case of increase or decrease of SST. The differences of storm occurrence rate and mean central pressures compared with the baseline model are shown in Figure 4.15.

For the two cases with increased SSTs (+10% and +20%), the storm approaching rate along the coastline barely changed which indicates that there no extra storms were

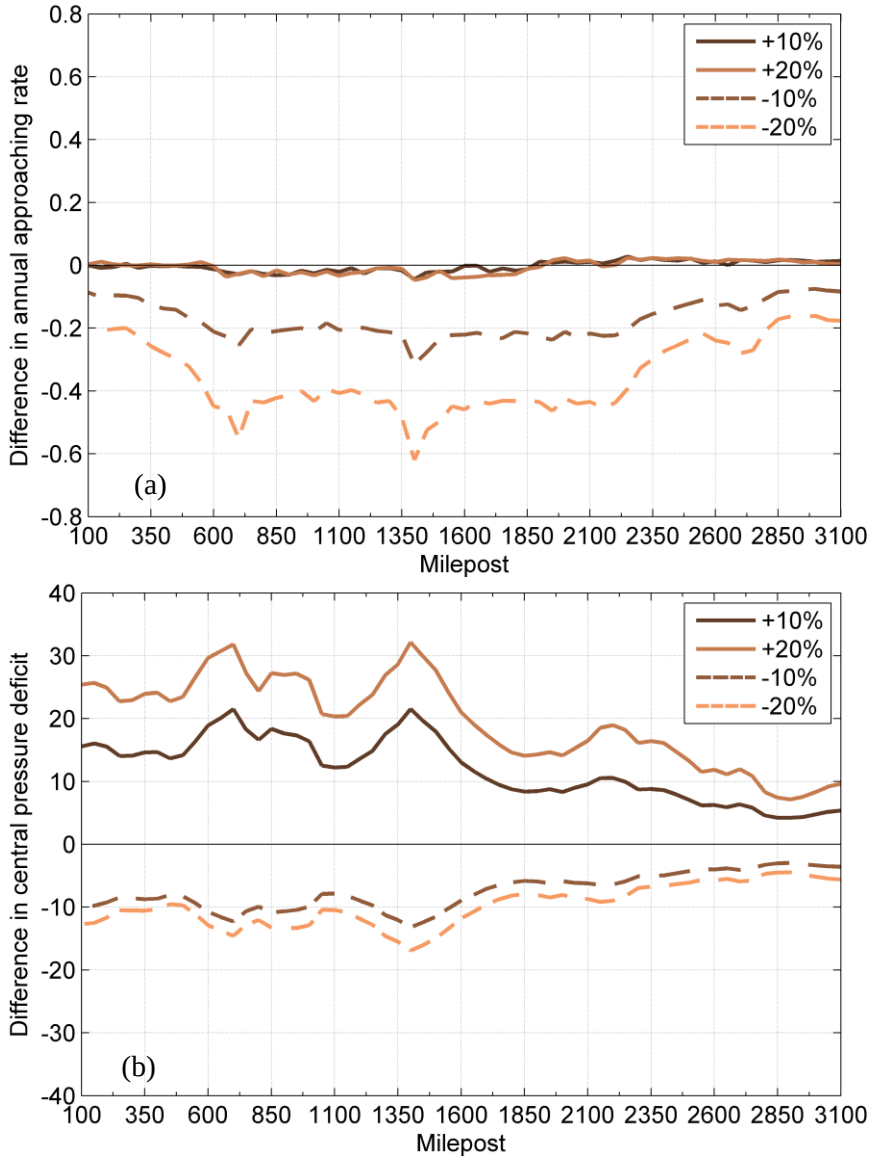


Figure 4.15: Difference of annual approaching rate and central pressure for synthetic hurricanes with ±10% and ±20% adjustment in SSTs.

observed at the coastline due to the increase in sea surface temperature (Figure 4.15a). On the contrary, the mean central pressure deficit increased significantly with the increase in SSTs (Figure 4.15b). The maximum and average increases in mean central pressure deficit were 32 mbar and 20 mbar, respectively, for a 20% increase in SST. At a lower level of increase in SST (+10%), the maximum and average increases in central pressure deficits were 22 mbar and 12 mbar, respectively. In other words, when the SST is increased, the approaching storm becomes more intense though the frequency (storm occurrence rate) remains unchanged.

For the two cases with decreased SSTs, both the storm approaching rates and mean central pressure deficits are reduced compared to the baseline model. The average decrease in approaching rate over the entire coast is 0.18 and 0.35 storms/year for a 10% and a 20% downward adjustments in SST, respectively, which translates to about one fewer storm to approach the coastline than the baseline model for every 6 or 3 years, respectively.

It is interesting to note that varying the SSTs results in asymmetrical responses of storm occurrence rate at coastline and more or less symmetrical responses for changes in central pressure deficits (Figure 4.15). In the hurricane simulation model, the storm path (tracking model) is not a function of the SST (see Eqns. (5) and (6)). Therefore, while increasing the SSTs causes the storms become more intense, the pattern of the storm paths remain unchanged and the chance for the intensified storms to approach the land stays the same. On the contrary, when the SSTs are reduced, the intensities of the storms are generally lower than that of the baseline model, making them more likely to dissipate

prior to reaching the land, hence, the decrease in the milepost approaching rates. The decreases in central pressure deficits for +10% and +20% SSTs are slightly lower than the counter parts for increases in SSTs. The downward adjustment of SSTs caused the mean central pressure to increase towards an asymptotical upper limit of 1013 mbar, the standard atmospheric pressure (Figure 4.16). On the other hand, upward adjustments of SSTs by 10% to 20% resulted in the mean central pressures to reduce but without the lower limit constraint. The lowest mean central pressure occurred at milepost 1400 when the SSTs were raised by 20%. This central pressure was still significantly higher than the lowest central pressure ever recorded for an Atlantic basin hurricane was 882 mbar (Hurricane Wilma in 2005).

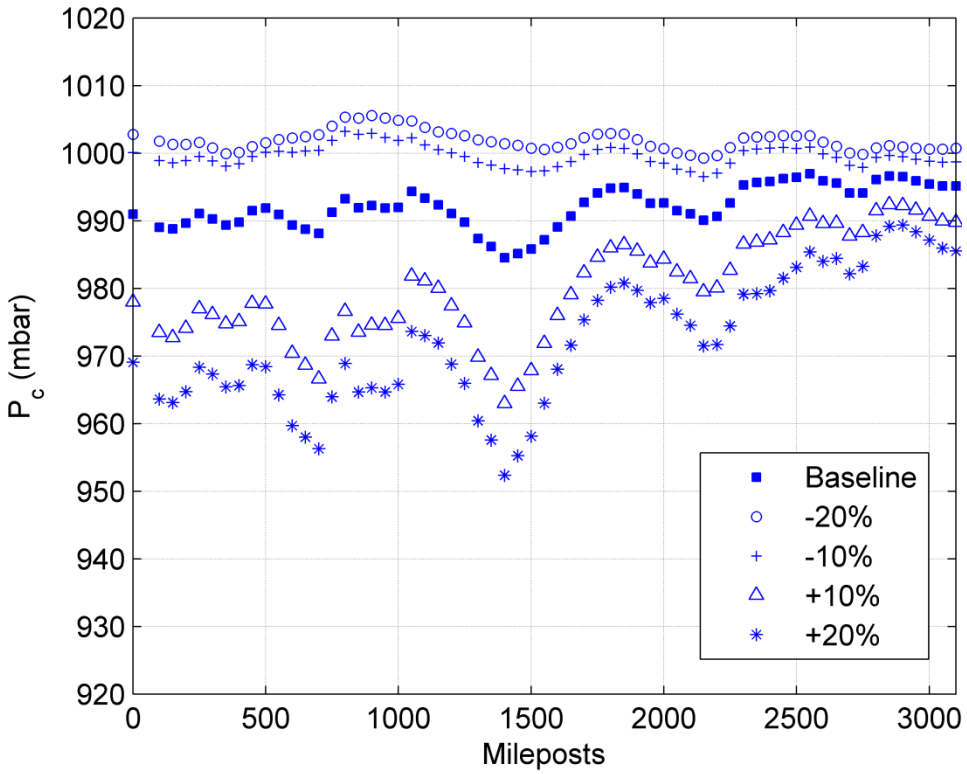


Figure 4.16: Mean central pressures from synthetic hurricanes with ±10% and ±20% adjustment in SSTs in comparison with that from the baseline case.

The changes in peak gusts along the coastline due to the adjustment of SSTs were examined and plotted in Figure 4.17. The gust wind speeds calculated from simulation with ±10% and ±20% change in SST were evaluated at MRI 300, 700 and 1700 years. For all three MRI levels, the wind speed levels are clearly distinct apart by the SST adjustment levels. The magnitudes of increase or decrease in wind speeds changed accordingly with the magnitude of SST adjustments. The maximum and average increase in wind speed for +20% SST adjustments is 39.7 m/s and 25.4 m/s for MRI 300 years, 35.6 m/s and 24.9 m/s for MRI 700 years, 31.6 m/s and 23.2 m/s for MRI 1700 years at milepost 700, respectively. On the other side, the decreased magnitudes in wind speed due to -20% SST adjustments are mostly symmetric along the coastline compared to the changes due to the upward adjustments. The maximum and average decrease in wind speed for -20% SST adjustments is 32.3 m/s and 20.5 m/s for MRI 300 years, 36.94 m/s and 22.1 m/s for MRI 700 years, 41.8 m/s and 23.7 m/s for MRI 1700 years at milepost 750, respectively. According to Saffir-Simpson hurricane scale, each hurricane category is approximately ranged 10 m/s apart. An increase or decrease of 20 m/s in wind speed will likely to result one or two levels of upgrade or degrade in hurricane category.

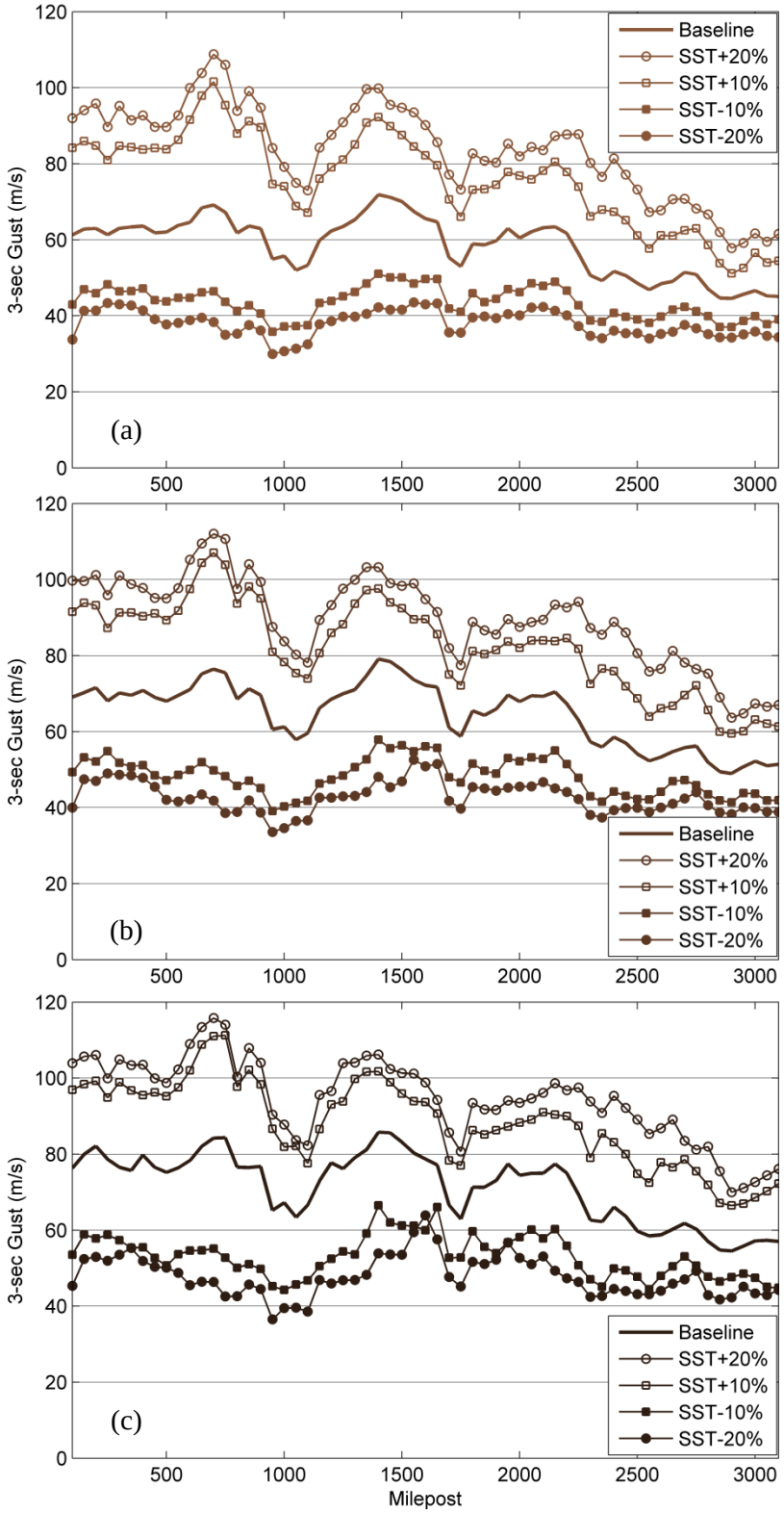


Figure 4.17: Comparisons of 10m gust of (a) 300-, (b) 700- and (c) 1700-year MRI in SST variations.

# CHAPTER FIVE: HURRICANE SIMULATION UNDER CLIMATE CHANGE SCENARIOS

The simulation framework introduced in Chapter Three (see Figure 3.3) was further developed to couple with climate change variables in order to produce simulation with climate change effects and to examine the influence of climate change on surface wind speed of coastal regions. Two climate change related factors were considered in this study: (1) annual storm formation rate, and (2) sea surface temperature.

In the baseline model, the mean and standard deviation of annual storm frequency, which are determined from historical hurricane records, are assumed constant over time. For hurricane simulation with climate change effects, annual storm frequency projection models are developed to simulate changes in storm formation rate over time. The projections of storm frequency over time are based on extrapolations of past annual storm formation rates. Specifically, mean and standard deviation of annual storm rate are modeled as functions of time in the projection models.

Sea surface temperature (SST) is one of the inputs in the relative intensity model (Eqn.(9)). Its changes over time are projected based on the global climate models (GCMs) under multiple future climate scenarios in the United Nations Intergovernmental Panel on Climate Change (IPCC) fifth assessment report (AR5). Combinations between the two projected climate change factors, namely storm formation rate and SST, are referred to herein as “Climate Change Cases”.

## 5.1 Projections of Annual Storm Frequencies

Two projection models were developed for annual storm formation rate: a linear moving average (LMA) mean model and an oscillating moving average (OMA) model. Figure 5.1 shows the mean storm formation rate as a function of time for the two annual storm frequency projection models. Also shown in the Figure is the mean storm formation rate used in the baseline model.

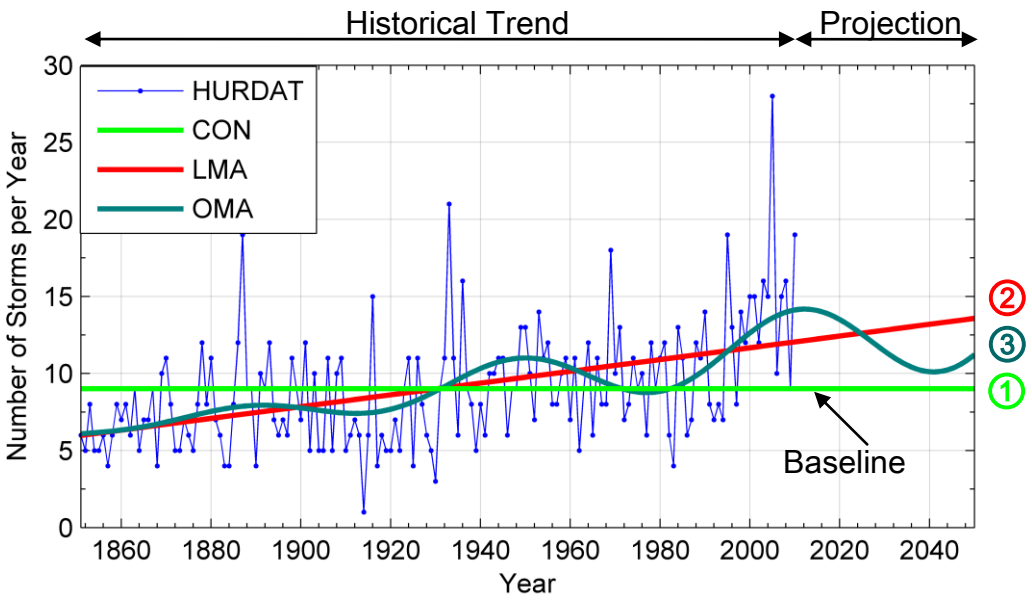


Figure 5.1: Annual storm frequency projection models.

### 5.1.1 Linear Moving Average (LMA) Model

An overall increasing trend of annual storm frequency can be seen in the past observations (Figure 5.2). In order to account for the increasing trend, a linear moving average (LMA) model is developed to project future storm frequencies. A least-squares regression line is fitted to the 20-year moving average storm frequencies and the fitted

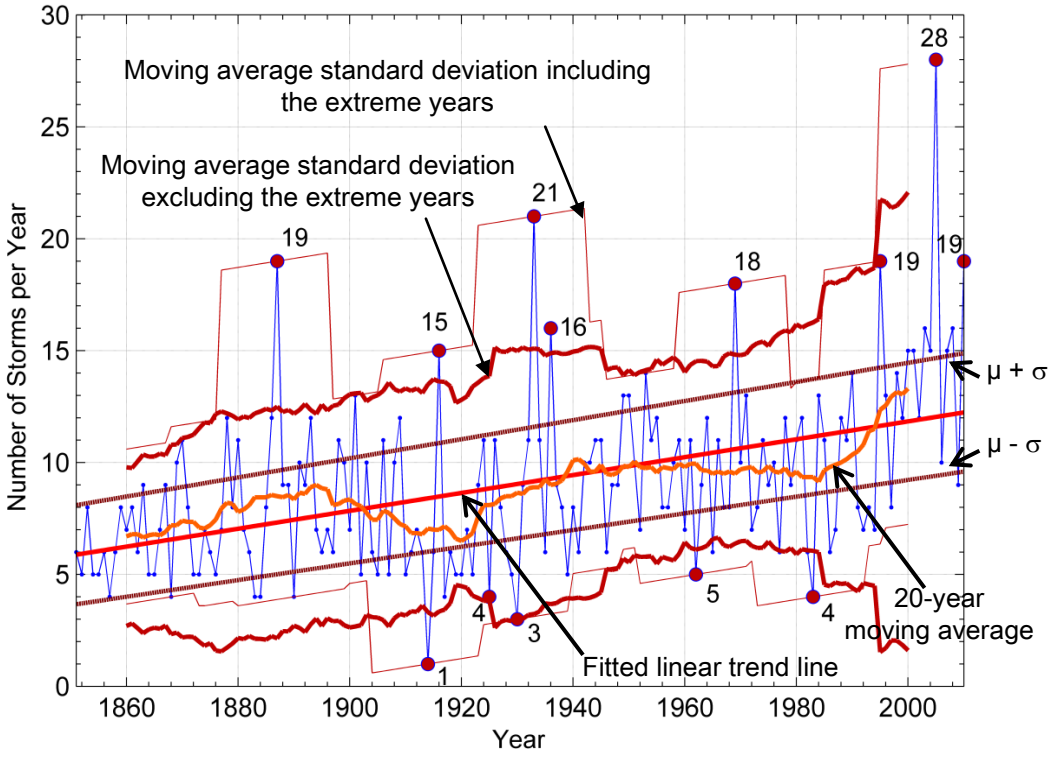


Figure 5.2: Linear moving average storm frequency model.

linear trend line is then used to characterize the mean annual storm frequency ($\mu$), as a function of year ($yr$) (see Figure 5.2). The twenty years period is chosen since it crosses both the active and inactive phases of a decadal oscillation cycle. Similarly, a linear trend line is used to model the 20-yr moving window standard deviation ($\sigma$) of the annual storm frequency.

From Figure 5.2, it can be seen that there were a number of years where the numbers of storms were exceedingly high. These extreme active hurricane seasons, identified as solid dots in Figure 5.2, reoccurred about every 18 years. These extraordinary years are defined as those data points that are more than $2\sigma$ (moving window standard deviation) away from the moving average. Note that once these

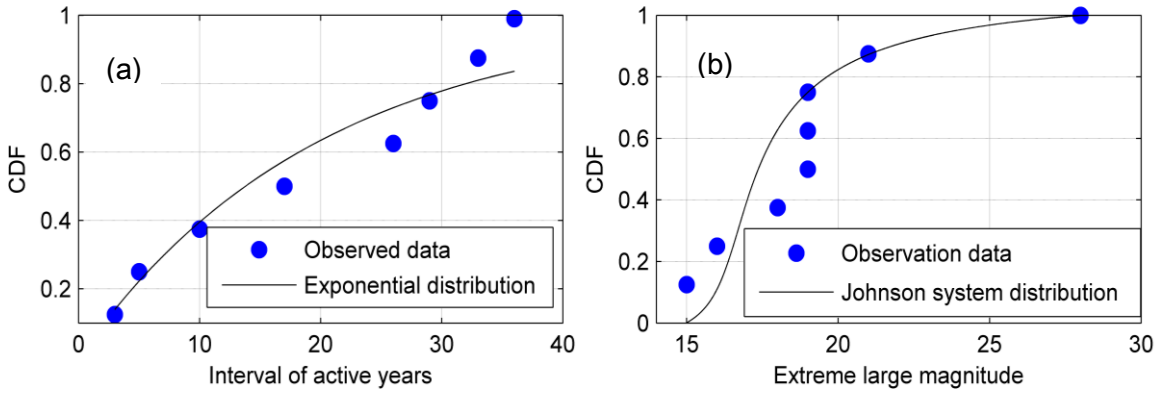


Figure 5.3: (a) CDF of inter-arrival time (year) of active hurricane seasons, (b) CDF of number of storms for active hurricane seasons.

"outliners" are identified, they are excluded from the moving window average and standard deviation calculations. A Bernoulli Pulse process is employed to simulate the extraordinary years. The inter-arrival years of the extreme active hurricane seasons are modeled using an exponential distribution (Figure 5.3a) and the magnitudes (i.e. the number of storms of active years) are modeled using the bounded Johnson distribution (Figure 5.3b). The equations and the procedures to fit distribution parameters for the bounded Johnson distribution are given in Appendix A. The percentile matching approach is used to estimate the four Johnson distribution parameters (Table 5.1). Based on the same methodology used to model the extreme active hurricane seasons, the inter-arrival years between two extreme inactive hurricane seasons are modeled using an exponential distribution (Figure 5.4a) and the magnitudes are modeled with a Poisson distribution (Figure 5.4b).

Table 5.1: Linear moving average annual storm frequency model parameters.

| Model Type | | Distribution | Parameters |
|---|---|---|---|
| Normal Years | | Negative Binominal | $\mu$ = 0.0382yr - 64.67<br>$\sigma$ = 0.0027yr - 2.78<br>(yr = [1851:2100]); |
| Extraordinary Years (Active) | Magnitude | Johnson | $\lambda$ = 0.75, $\gamma$ = -0.62<br>$\delta$ = 0.62, $\xi$ = 16.48 |
| | Inter-arrival Time | Exponential | $\mu$ = 17.57 |
| Extraordinary Years (Inactive) | Magnitude | Poisson | $\lambda$ =3.40 |
| | Inter-arrival Time | Exponential | $\mu$ = 17.25 |

In the LMA model simulation process, the annual storm frequencies for "normal years" are first sampled using the moving mean and standard deviation shown in Table 5.1. The negative binomial distribution parameters needed to generate the annual storm frequencies of normal years are computed by substituting the moving mean and standard deviation into Eqn. (4). Once the normal years are simulated, extraordinary years (active and inactive years) are simulated next using the Bernoulli Pulse process and they are used to replace the initially sampled normal years.

### 5.1.2 Oscillating Moving Average (OMA) Model

In order to account for the oscillating pattern of storm number over time, an oscillating moving average (OMA) model is developed to capture the alternate active and inactive phases of the decadal oscillation cycles. An equation with a sine function is utilized to fit the 20-year moving average storm frequencies (Figure 5.5). After excluding the extraordinary years, the standard deviation is found to be very close to a constant. Hence, the dispersion of the normal years is quantified using a constant value (2.53

storms/year) in the OMA model. The procedure to determine the extraordinary years is the same as the one used in the development of LMA model and the OMA model parameters for extraordinary years are given in Table 5.2. The period of the fitted OMA model is approximately 60 to 65 years from 1851 to 2012 (Figure 5.5) which is very close to the period of Atlantic Multi-decadal Oscillation (AMO) of 60 to 80 years determined by others (UCAR 2012; Schlesinger and Ramankutty 1994). The coincidence between the trends of SST in the North Atmosphere and the number of Atlantic tropical storms has been thoroughly investigated by many other studies, such as the aforementioned Holland and Webster (2007) and Vecchi and Knutson (2007). The significant correlation between SST and storm number since the latter half of the $19^{th}$ century was highlighted by both studies. In Vecchi and Knutson (2007), it specifically noted that the number of tropical storms exhibited a multi-decadal variability and co-varied with the multi-decadal variation of SST in the main development region of tropical storms. The consistency between the period of the OMA model in this study and the period of the AMO shows that the OMA model implicitly incorporate the effects of multi-decadal oscillation and the rise of SST.

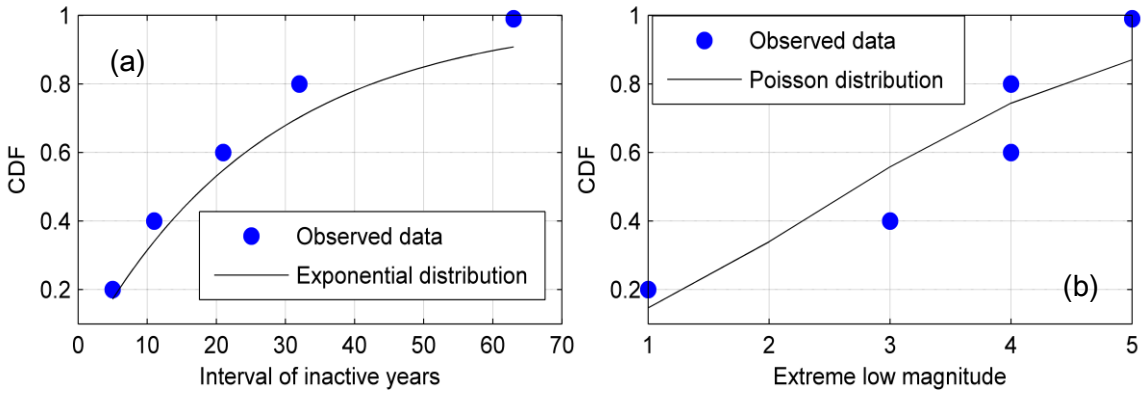


Figure 5.4: (a) CDF of inter-arrival time (year) of extreme inactive hurricane seasons, (b) CDF of number of storms for inactive hurricane seasons.

Table 5.2: Oscillating moving average annual storm frequency model parameters.

| Model Type | | Distribution | Parameters |
|---|---|---|---|
| Normal Years | | Negative Binominal | $\mu = 0.015x \cdot \sin(0.099x - 1.60) + 0.037x + 6.09$<br>$\sigma = 2.53$<br>(x = yr-1851, yr = 1851:2100) |
| Extraordinary Years (Active) | Magnitude | Johnson SB | $\lambda = 0.75,\ \gamma = -0.62$<br>$\delta = 0.62,\ \xi = 16.48$ |
| | Inter-arrival Time | Exponential | $\mu = 17.57$ |
| Extraordinary Years (Inactive) | Magnitude | Poisson | $\lambda = 3.40$ |
| | Inter-arrival Time | Exponential | $\mu = 17.25$ |

## 5.2 Climate Change Scenarios

Projections of hurricane activities were made up to year 2100 under six different speculated future climate scenarios, referred to as Cases, shown in Table 5.3. Each climate scenario considers the effects of changes in annual storm frequency and SST on the hurricane wind speeds along the U.S. eastern coastline. Scenarios 1 to 4 consider the

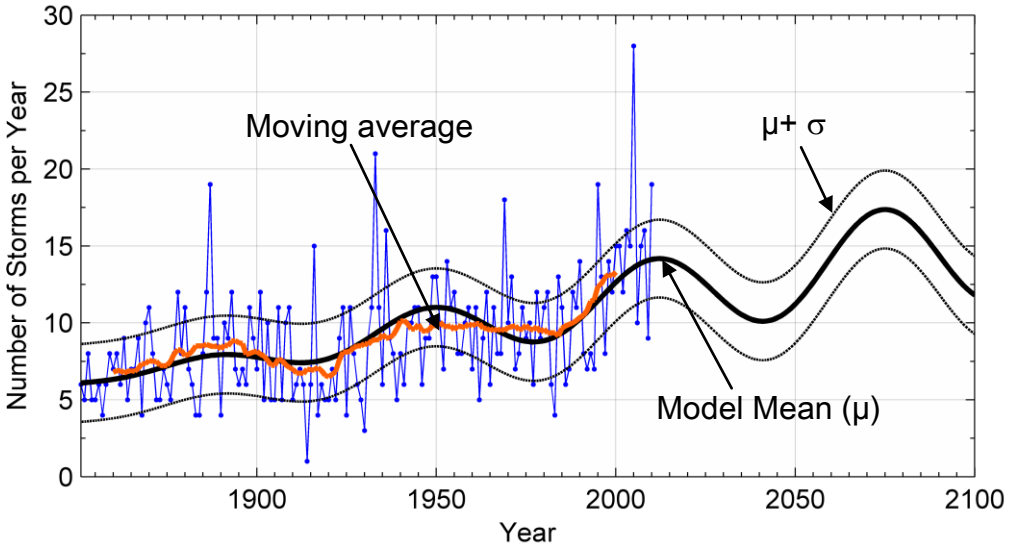


Figure 5.5: Oscillating moving average (OMA) storm frequency model.

effects of changes in storm frequency and SST jointly while scenarios 5 and 6 consider the effects of changes in SST and annual storm frequency independent of each other.

Table 5.3: Climate change scenarios.

| Climate Change Scenario | Annual Storm Frequency | Sea Surface Temperature |
|---|---|---|
| Case 1 | Oscillating Moving Average (OMA) | RCP 8.5 (CMIP5) |
| Case 2 | Oscillating Moving Average (OMA) | RCP 4.5 (CMIP5) |
| Case 3 | Oscillating Moving Average (OMA) | RCP 2.6 (CMIP5) |
| Case 4 | Linear Moving Average (LMA) | RCP 8.5 (CMIP5) |
| Case 5 | Constant (CON) | RCP 8.5 (CMIP5) |
| Case 6 | Oscillating Moving Average (OMA) | Historical Record (HadISST) |
| Baseline Model | Constant (CON) | Historical Record (HadISST) |

The SST projections were taken from the Coupled Model Intercomparison Project Phase 5 (CMIP5) simulations under initial conditions of the various IPCC RCP scenarios (Taylor et al. 2012). The SST projections were obtained from Climate Model 3 (CM3)

data from the Geophysical Fluid Dynamics Laboratory (GFDL) of NOAA under the *World Climate Research Programme* (GFDL 2014). Six simulated hurricane databases, each consists of 100,000 realizations for each year from 2006 to 2100, were produced for the six speculated future climate scenarios listed in Table 5.3. In addition, another 100,000-year simulation (total 200,000-year) was realized under the condition of 2050 and 2100 to inspect the hurricane risk of long recurrence intervals in the middle and by the end of the century.

## 5.3 Projection Results

### 5.3.1 Projections of Annual Storm Frequencies

Examples of simulated annual storm frequencies for three different projection models are shown in Figure 5.6. The trend lines from years 1851 to 2011 are plotted from the actual historical storm formation rates. The trend lines in light color ranged from 2006 to 2100 are projections. The bold line is the average number over 1000 realizations. The scattered data points in each of the sub-figure in Figure 5.6 show one example realization of the simulated annual storm frequencies. The simulation was set to start from 2006 in order to be consistent with the length of SST projections. As can be seen, all three storm frequency projection models produce plausible trends as extrapolations of historical records.

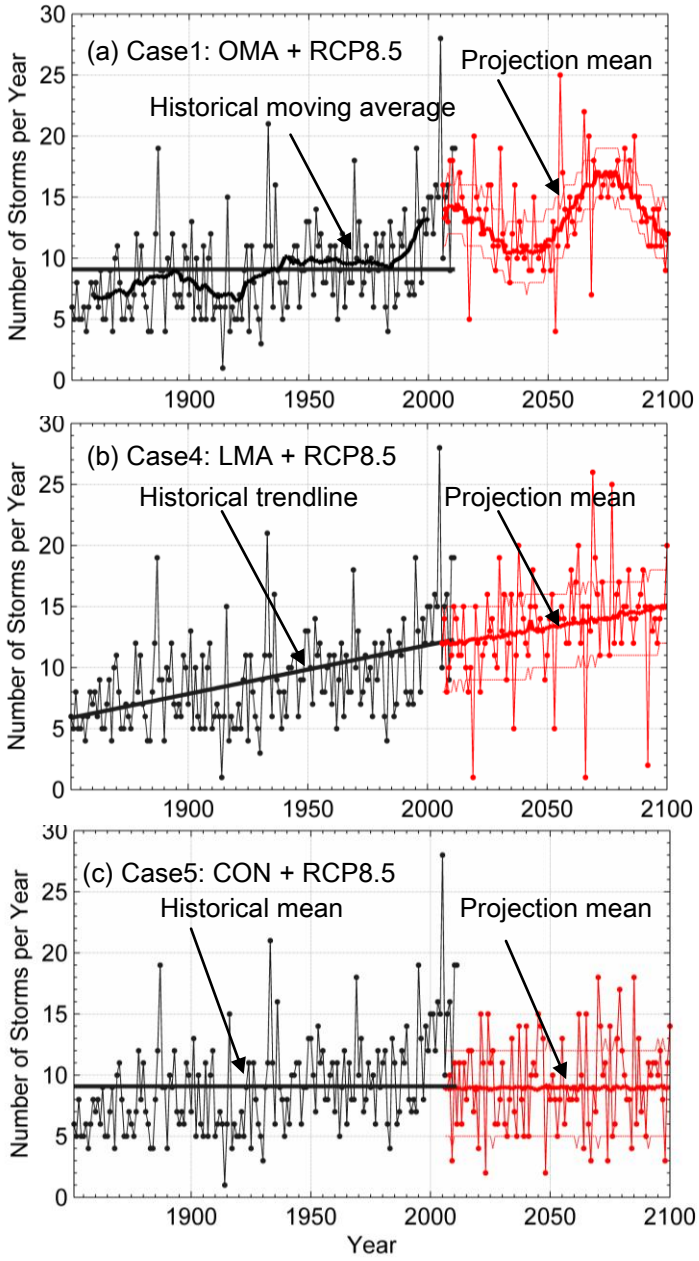


Figure 5.6: Example simulated storm frequencies. Black lines show historical observation from 1851 to 2012. Red lines show one simulation realization from each case from 2006 to 2100. (a) oscillating moving average model, (b) linear moving average model, and (c) constant storm frequency model.

### 5.3.2 Storm Occurrence Rate

The mean annual occurrence rates and central pressures along the coastline are also evaluated for the six future climate cases (Table 5.3) and compared to that of the baseline model (current climate). The differences in mean annual occurrence rates between each speculated future climate condition and the baseline model for years 2050 and 2100 are plotted in Figure 5.7, where a positive value indicates an increase in annual

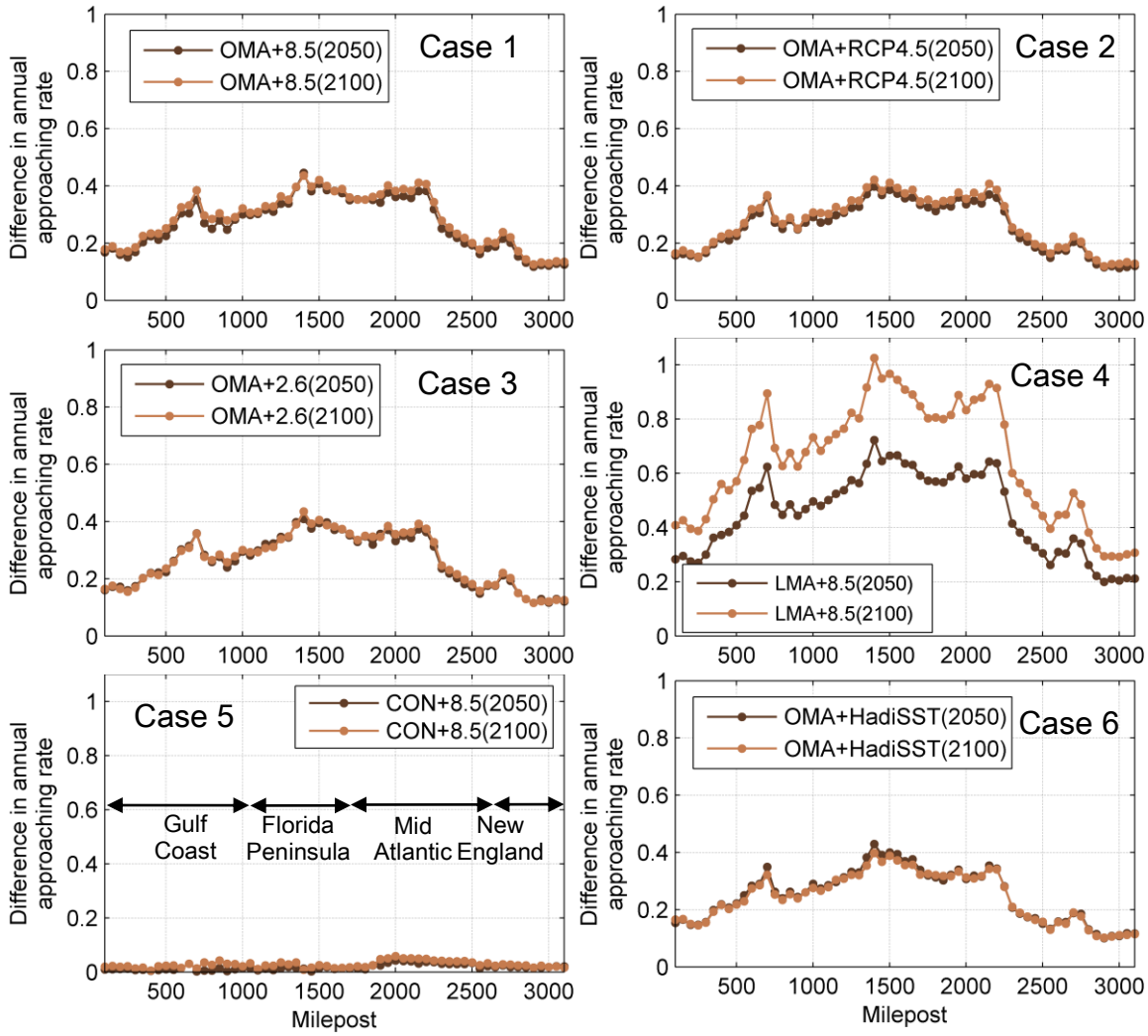


Figure 5.7: The difference of annual occurrence rate from the level of baseline simulation to that of future climate projections at the year of 2050 and 2100 along coastal locations (projection - baseline level).

occurrence rate.

Cases 1 to 3 consider the effects of changes in storm frequency and SSTs jointly. Based on the differences in annual occurrence rates in Figure 5.7, it can be observed that the annual storm rates do not vary significantly with the change in SSTs. For example, the annual occurrence rates for Cases 1, 2, 3 and 6, which are projected from the same storm frequency model (OMA) but different SSTs, are approximately the same at year 2050. The SSTs for Cases 1, 2 and 3 are derived based on the high emission (RCP 8.5), medium-low emission (RCP 4.5) and low emission (RCP 2.6) scenarios. Slight increases in annual occurrence rate can be seen from year 2050 to year 2100 for Cases 1 to 3. This is because both of these two years happened to lay on the dip parts of the oscillation, with mean storm number of 11.2 at 2050 and 11.8 at 2100. Case 1 (OMA + RCP8.5) presents the most notable increases (on average less than 0.03 storm/year). This is because, while the storm frequency model is the same for these three cases, among them Case 1 has the highest projected increases in SSTs at the end of the 21th century which means more intense storms (with low central pressures) are likely to form over the Atlantic basin. Compared to weaker storms, these high intensity storms generally have a higher chance to survive the journey and make landfall.

Case 6 (OMA + current SST), which assumes the future SSTs remain the same as the current climate, shows no noticeable differences in occurrence rates between years 2050 and 2100. Based on the OSM model, the Texas coastline and Gulf coast region may experience one extra storm every 5 to 10 years and the Southern Florida may see one extra storm every 2 to 3 years in 2050. Among all scenarios, Case 4 (LMA + RCP8.5)

has the most substantial increases in storm occurrence rates. If the linear increasing trend of storm frequency holds and the radiative forcing reaches the level of 8.5 Watt/$m^2$ in year 2100, Texas and Northeastern region of the U.S. may experience one extra storm every 2 to 3 years while Florida, South Carolina and North Carolina coastal regions may experience an extra landfall storm every 1 to 2 years.

### 5.3.3 Storm Intensity (Central Pressure)

Changes in central pressure deficits between the speculated future climate conditions and the current climate for years 2050 and 2100 are plotted in Figure 5.8. A positive change in central pressure deficit means the storm is more intense than that of the current climate. As can be seen, the change in central pressure deficit is proportional to the rises in radiative forcings and SSTs. Under the most dramatic radiative forcing level (RCP 8.5), the central pressure deficit of landfall storms increased by as much as 5 mbar and 20 mbar by years 2050 and 2100, respectively. In general, a drop of 20 mbar in central pressure may cause the storm intensity rating to increase by one category under the Saffir-Simpson scale. Case 4 (OMA+RCP8.5), which considers the effects of changes in storm frequency and SSTs jointly, and Case 5 (CON+RCP8.5), which considers only the effects of changes in SSTs, show nearly identical responses. This shows that the intensity of future landfall storms is sensitive to changes in SSTs (or radiative forcing) while changes in annual storm frequency have minimal impacts on the intensity of future storms. Under the RCP8.5 scenario, the average central pressure deficits for storms along the U.S. eastern coastline drops by 6.4 mbar and 15.4 mbar in years 2050 and 2100, respectively.

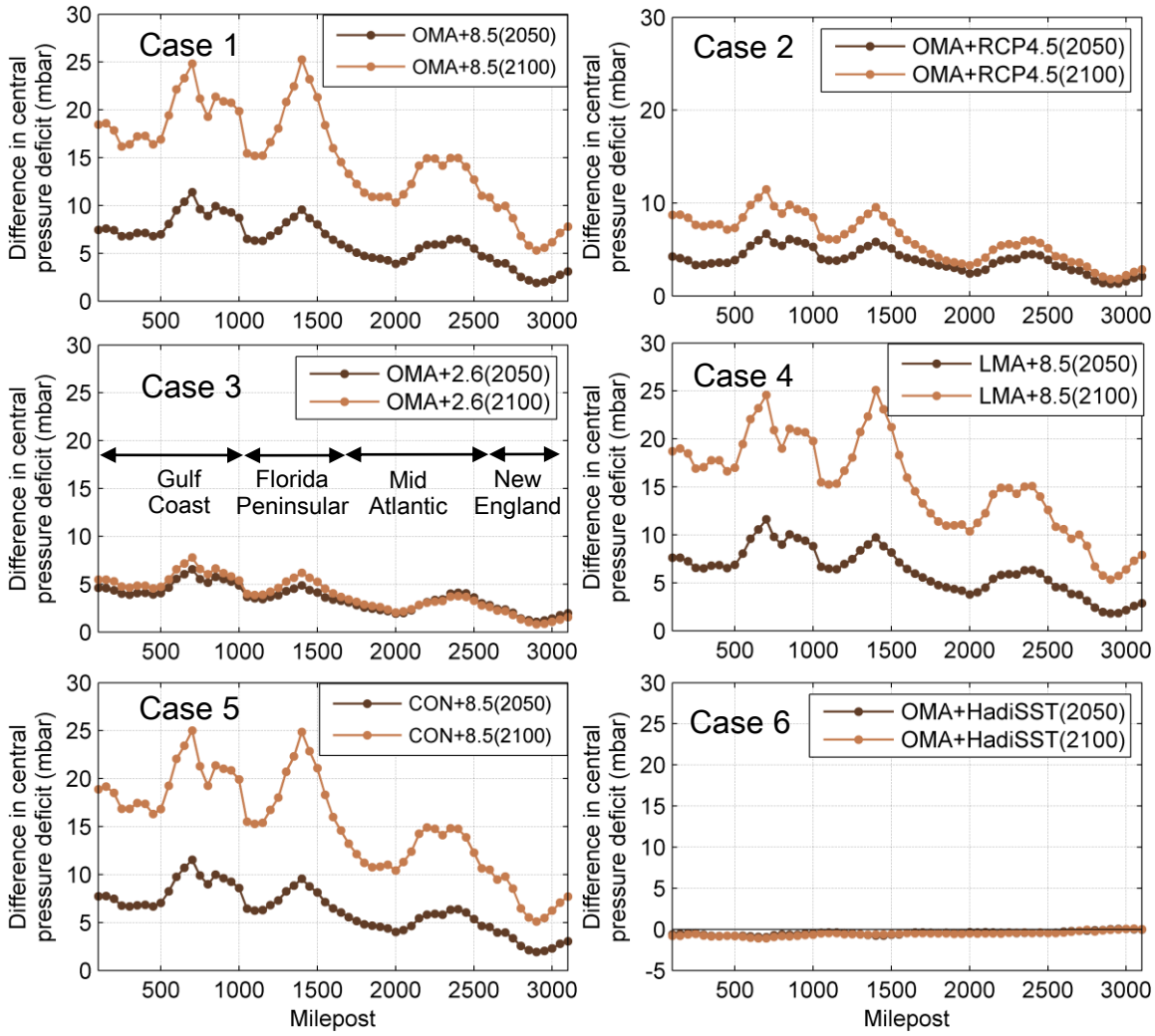


Figure 5.8: The difference of central pressure deficit from the level of baseline simulation to that of future climate projections at the year of 2050 and 2100 along coastal locations (projection - baseline level).

### 5.3.4 Surface Wind Speed

#### 5.3.4.1 Projected Wind Speeds for Selected Locations

To evaluate the impacts of climate change on future design wind speeds, the 3s surface wind gusts under different future climate scenarios for four selected sites are compared to the current ASCE 7-10 design winds. These four locations are:

(1) milepost 700 (Lat. 29.17˚, Lon. -89.08˚) in Louisiana (LA) in Gulf Coast,

(2) milepost 1400 (Lat. 25.17˚, Lon. -80.67˚) in Florida (FL),

(3) milepost 1950 (Lat. 33˚, Lon. -79.5˚) in South Carolina (SC), and

(4) milepost 2550 (Lat. 40.65˚, Lon. -73.5˚) in New York (NY).

The surface gust wind speeds are plotted as a function of MRI for years 2050 and 2100. The simulated wind speeds for the six speculated future climate cases are combined into four groups (Figure 5.9 to 5.12).

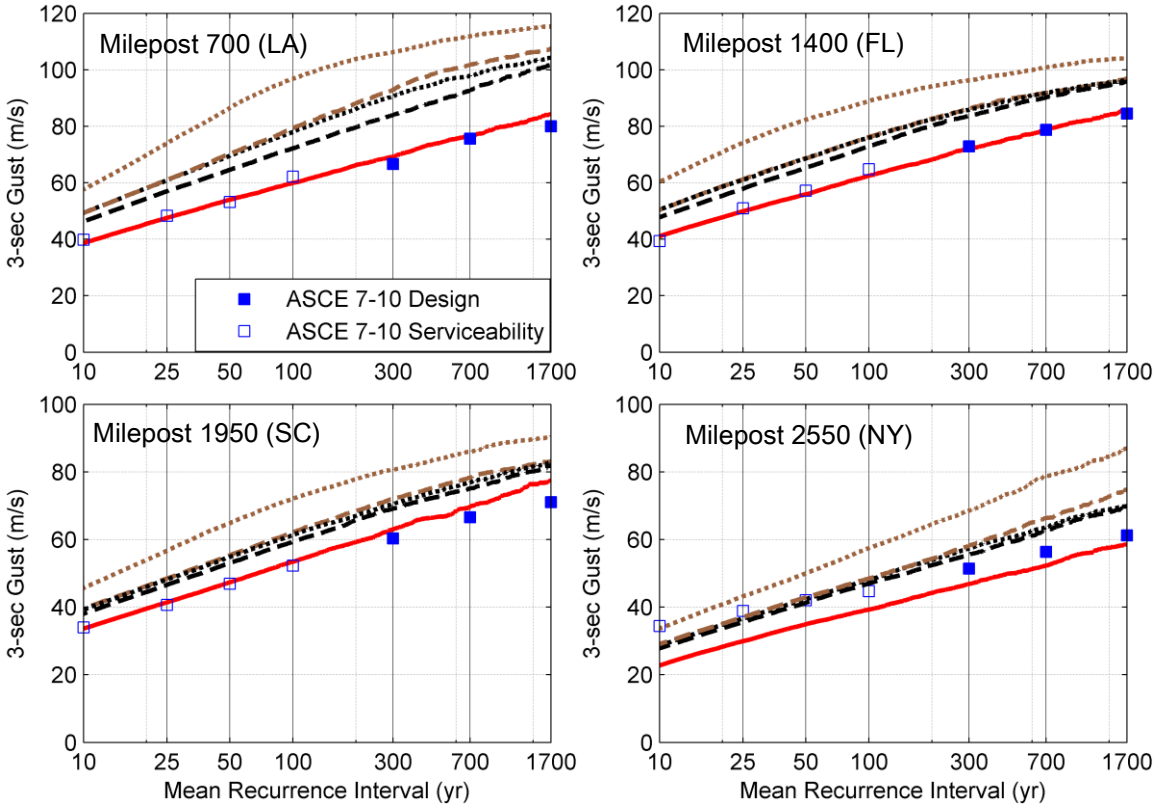


Figure 5.9: Projected future 10m-height gust wind speeds of Cases 1 (OMA+RCP 8.5) and 2 (OMA+RCP4.5) versus MRI for locations in Florida, Gulf Coast, South Carolina and New York. Brown dot lines show the gust winds in 2100 from Case 1; Brown dash lines show the gust winds in 2050 from Case 1; Black dot lines show the gust winds in 2100 from Case 2; Black dash lines show the gust winds in 2050 from Case 2; Bold red lines show the gust winds from baseline simulation; The squares show the gust wind from ASCE 7-10.

Comparing the wind speeds produced by Cases 1 to 3 (Figure 5.9 and 5.10) reveals that the largest increases in wind speeds at the end of the 21th century come from the RCP8.5 scenario (Case 1). This is expected as the RCP8.5 has the highest radiative forcing and the highest increases in SSTs. The average increases in Case 1 wind speeds across all MRIs for the four locations range from 15 m/s to 35 m/s in year 2100 and from 8 m/s to 24 m/s in 2050 with the milepost in Louisiana having the largest increase in wind speed (35 and 24 m/s for 2050 and 2100, respectively). This level of increase is

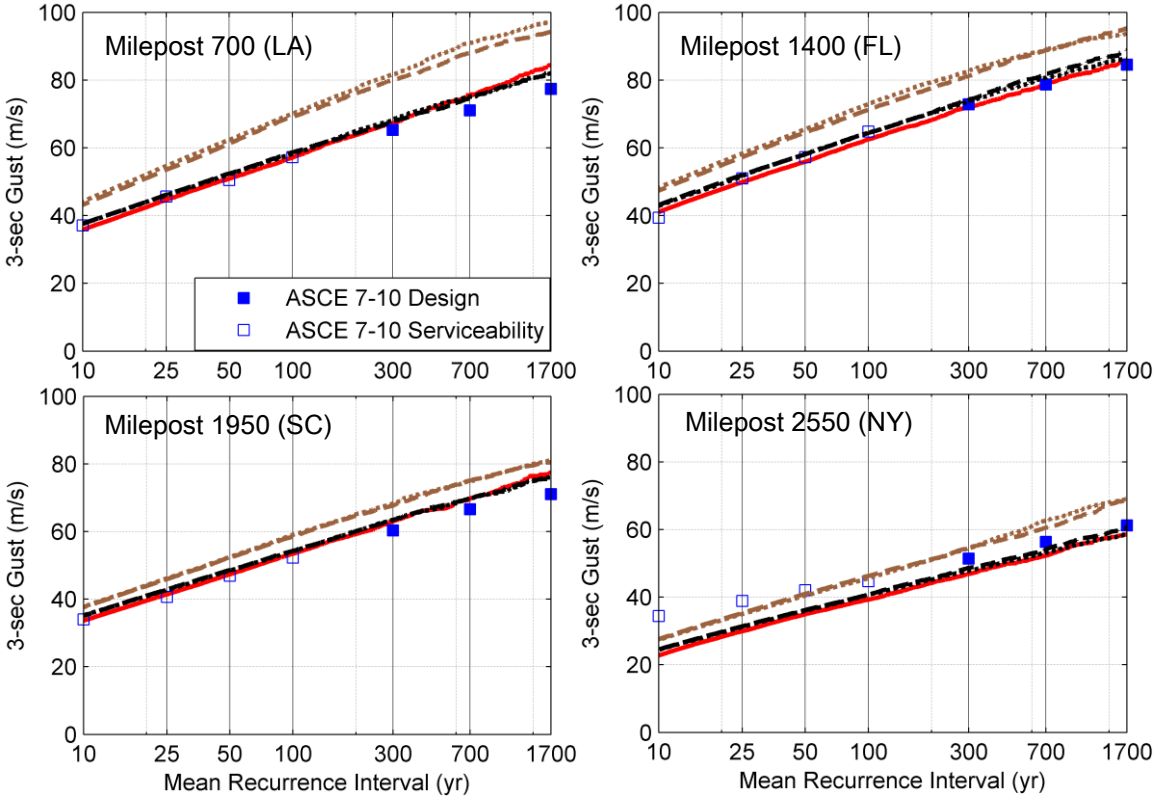


Figure 5.10: Projected future 10m-height gust wind speeds of Cases 3 (OMA +RCP2.6) and 6 (OMA+HadiSST) versus MRI for locations in Florida, Gulf Coast, South Carolina and New York. Brown dot lines show the gust winds in 2100 from Case 3; Brown dash lines show the gust wind in 2050 from Case 3; Black dot lines show the gust winds in 2100 from Case 6; Black dash lines show the gust winds in 2050 from Case 6; Bold red lines show the gust winds from baseline simulation; The squares show the gust wind from ASCE 7-10.

very significant. Under the OMA+RCP8.5 scenario (Case 1), the 1700-year MRI wind speeds for the coastal region of Louisiana increase from approximately 80 m/s to over 90 m/s and 100 m/s in years 2050 and 2100, respectively. Note that under the high emission scenario of Case 1 (RCP8.5), the increases in design wind speeds in year 2050 reach the same levels as that in year 2100 of Case 2 (RCP4.5) with medium emission (Figure 5.9).

For Case 3 (OMA+RCP2.6) and Case 6 (OMA+current SST) shown in Figure 5.10, differences in wind speeds at mid-century (2050) and end of the century (2100) are much smaller compared to those enhanced scenarios. The average increases in wind speeds for Case 3 range from 5 m/s to 17 m/s. The wind speed projections for Case 6, which considers only the changes in storm frequencies (SSTs remain unchanged), do not have noticeable differences between the mid-century and end-of-century wind speeds and that of the current design code winds. In other words, changes in annual storm frequency alone do not have significant effects on the design wind speeds.

The most significant increases in wind speeds among all the climate change scenarios considered in this study are found in Case 4 (LMA+RCP8.5), which assumes the linear increasing trend of annual storm frequency persists until the end of the century and the radiative forcing reaches the worst-case scenario (8.5 Watt/$m^2$). As shown in Figure 5.11, the wind speeds in years 2050 and 2100 are significantly higher than that of the baseline level. The average increases in wind speeds for the four mileposts under Case 4 range from 15 m/s to 24 m/s in year 2100, and 5 m/s to 12 m/s in year 2050. The projected increases in wind speeds at the end of the 21th century under Case 4 are slightly

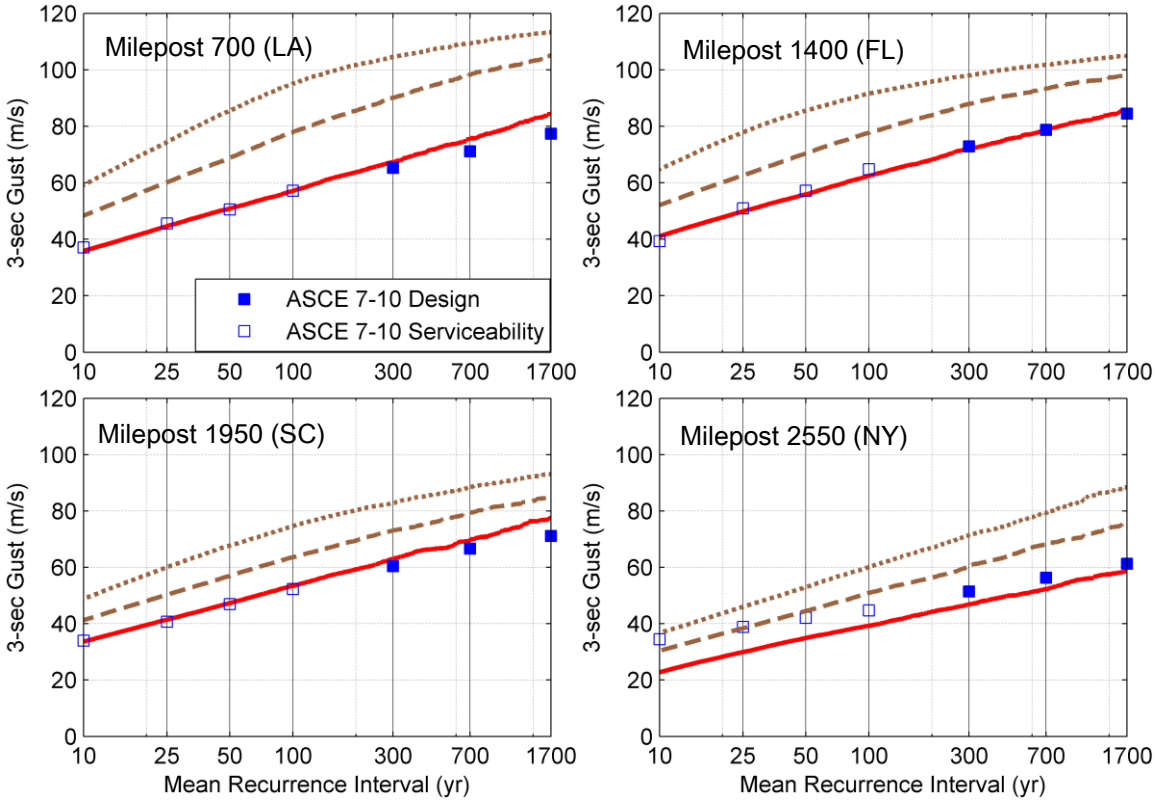


Figure 5.11: Projected future 10m-height gust wind speeds of Case 4 (LMA+RCP8.5) versus MRI for locations in Florida, Gulf Coast, South Carolina and New York. Brown dot lines show the gust winds in 2100 from Case 4; Brown dash lines show the gust wind in 2050 from Case 4; Bold red lines show the gust winds from baseline simulation; The squares show the gust wind from ASCE 7-10.

higher than that from Case 1. This is attributed to the annual storm spawn rates of Case 4 model higher than that of Case 1.

The results in Figure 5.12 from Case 5 (CON+RCP8.5) highlight the effects of changes in SSTs on wind speeds. Under Case 5 scenario, the projected median increase in global temperature is 4.6˚C by the end of the century while the annual storm frequency is assumed to remain unchanged. The average increases in wind speeds for the four sites range from 9 m/s to 19 m/s by the end of the century with Louisiana having the largest increase in wind speed (19 m/s at 1700-year MRI by year 2100). The projections in Case

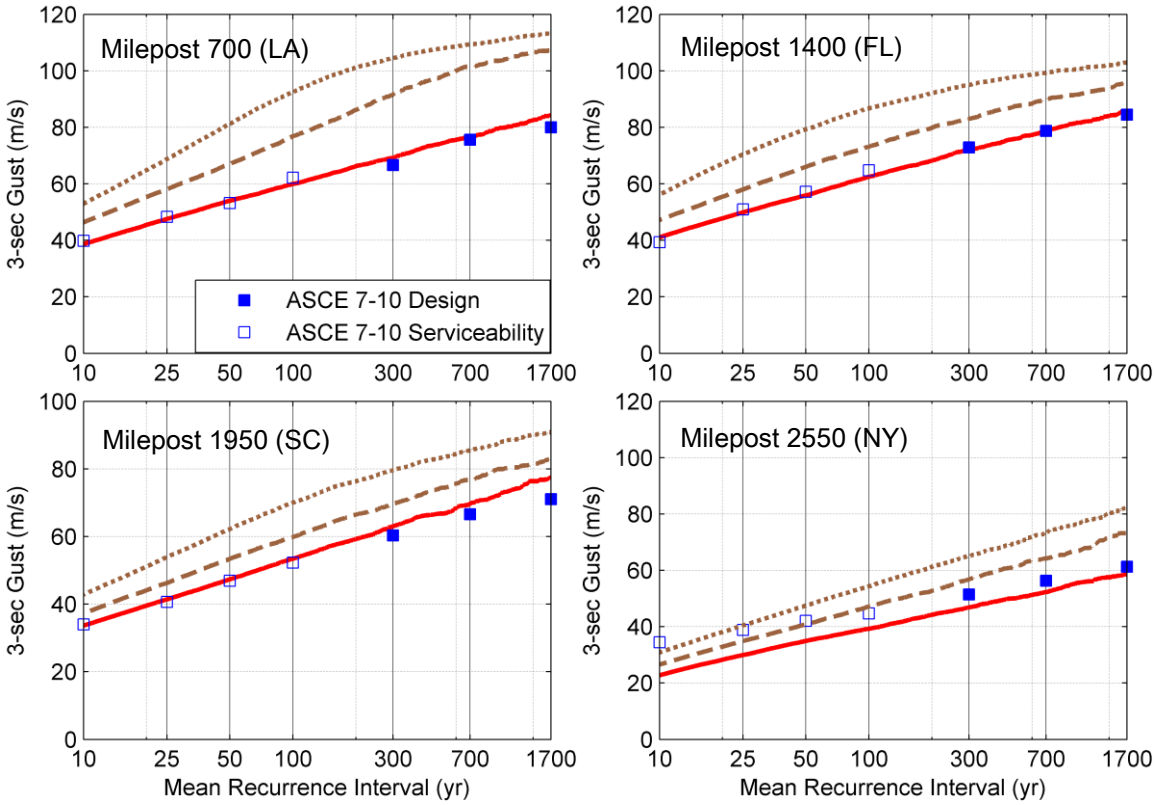


Figure 5.12: Projected future 10m-height gust wind speeds of Case 5 (CON+RCP8.5) versus MRI for locations in Florida, Gulf Coast, South Carolina and New York. Brown dot lines show the gust winds in 2100 from Case 5; Brown dash lines show the gust wind in 2050 from Case 5; Bold red lines show the gust winds from baseline simulation; The squares show the gust wind from ASCE 7-10.

5 reflect the worst case merely due to the increase in SST (i.e. exclude the influence from the frequency projection). It turns out that dramatic increases in future design wind speeds can still be observed which is a major concern for the safety of structures in the future.

#### 5.3.4.2 Projected 50-year MRI Wind Speed versus Time

Figure 5.13 provides an alternative way to examine the changes in wind speeds over time for different climate scenarios. The 50-year MRI wind speeds are plotted

against the projection years (2006 to 2100) for the four mileposts. To eliminate fluctuations from year to year, a 10-year moving window is used to smooth the 50-year MRI wind speed curves. As observed previously in Figure 5.9 and 5.12, Case 1 (OMA+RCP8.5) and Case 4 (LMA+RCP8.5) have the two highest wind speeds by the end of the century. These two cases also have the highest rates of increase in wind speeds over time (i.e. the steepest positive slope). Note that Case 4, which is based on the linear moving average (LMA) storm frequency model, shows a linear increasing trend in wind speeds while Case 1, which is based on the oscillating moving average (OMA) model, shows an overall increasing trend but with traces of Atlantic multi-decadal oscillation.

Note that for Case 3 (OMA+RCP2.6), the RCP2.6 scenario is referred to as a "peak and decline" pathway with the projected radiative forcing levels reaching a peak value of 3.1 Watt/$m^2$ by mid-century and then declining to 2.6 Watt/$m^2$ by the end of the century. The "peak and decline" of simulated 50-year MRI wind speeds for Case 3 is also reflected in Figure 5.13. Case 6 (OMA+current SST) presents the least significant changes in wind speeds compared to the other cases because it assumes the current SSTs remain unchanged through the end of the century. Although the SSTs remain constant under Case 6 scenario, the wind speeds still vary over time. The Case 6 50-year MRI wind speeds increase beyond the current level (baseline) and reach the peak around 2070 then decline back to the baseline level again by the end of the century (Figure 5.13). This "peak and decline" phenomenon is mainly attributed to the variation in annual storm frequency due to Atlantic multi-decadal oscillation. Note that the pattern of "increase and

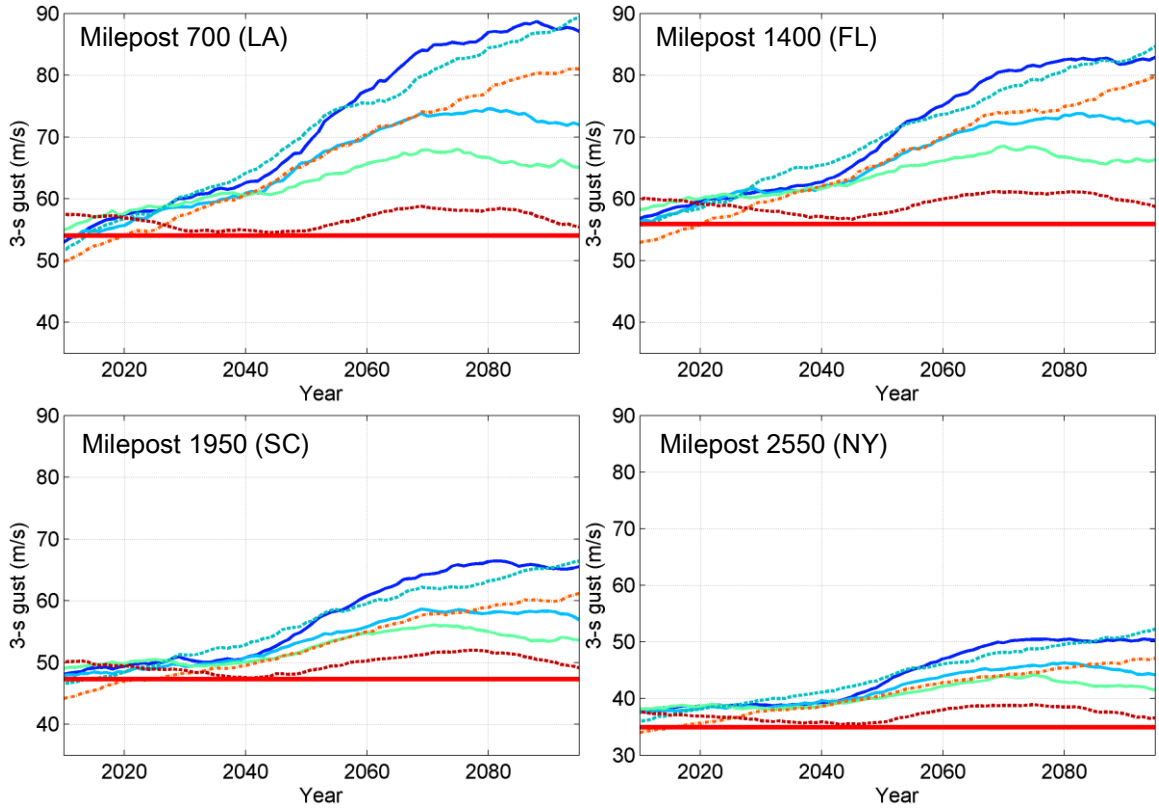


Figure 5.13: Projected 50-year MRI gust wind speeds over time for locations in Florida, Gulf Coast, South Carolina and New York. Solid dark blue lines show the gust winds from Case 1 (OMA + RCP8.5); Solid light blue lines show the gust winds from Case 2 (OMA + RCP4.5); Solid light green lines show the gust winds from Case 3 (OMA + RCP2.6); Dash blue lines show the gust winds from Case 4 (LMA + RCP8.5); Dash orange lines show the gust winds from Case 5 (CON + RCP8.5); Dash red lines show the gust winds from Case 6 (OMA + HasiSST); Bold red lines show the gust winds from baseline simulation.

decrease" in wind speeds of Case 6 also matches the pattern of annual storm frequency time history shown in Figure 5.6a.

#### 5.3.4.3 Projected Wind Speeds for All Mileposts

Figure 5.14 to 5.17 present the comparisons of 300-, 700- and 1700-year MRI wind speeds for all mileposts along the U.S. coastline for years 2050 and 2100 between

the climate change scenarios and the baseline model (current ASCE 7-10 strength-level design wind speeds).

Figure 5.14 and 5.15 present the wind speeds for cases simulated using the OMA storm frequency model (Cases 1, 2, 3 and 6) for years 2100 and 2050 respectively. The simulation results shown in these figures include the climate change effects. As shown in both Figures, the magnitude of increases in design wind speeds is proportional to the changes in radiative forcing levels. Under the highest IPCC radiative forcing scenario (RCP8.5, Case 1), the 300-, 700-, and 1700-year MRI wind speeds for Gulf coast and Florida increase by 13-17% and 25-30% beyond the current levels in years 2050 and 2100, respectively. Under the moderate (RCP4.5) and low (RCP2.6) radiative forcing scenarios (Cases 2 and 3), increases in design wind speeds for Gulf coast and Florida are estimated to be around 9-12% and 11-19% for Case 2 and 7-11% and 9-13% for Case 3 for years 2050 and 2100, respectively.

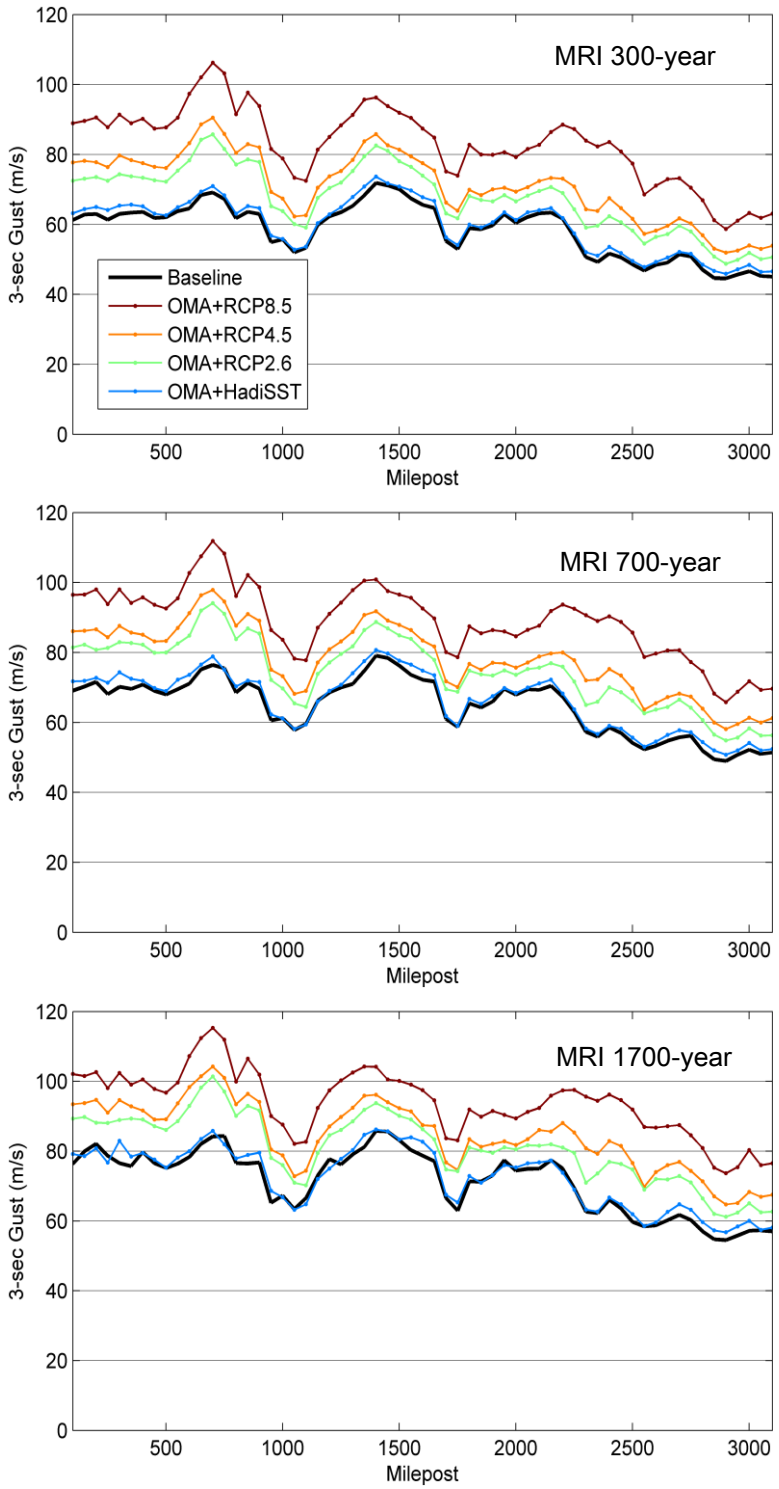


Figure 5.14: Projected gust wind speeds for (a) 300-year MRI, (b) 700-year MRI, and (c) 1700-year MRI for mileposts along the U.S. coastline in year of 2100.

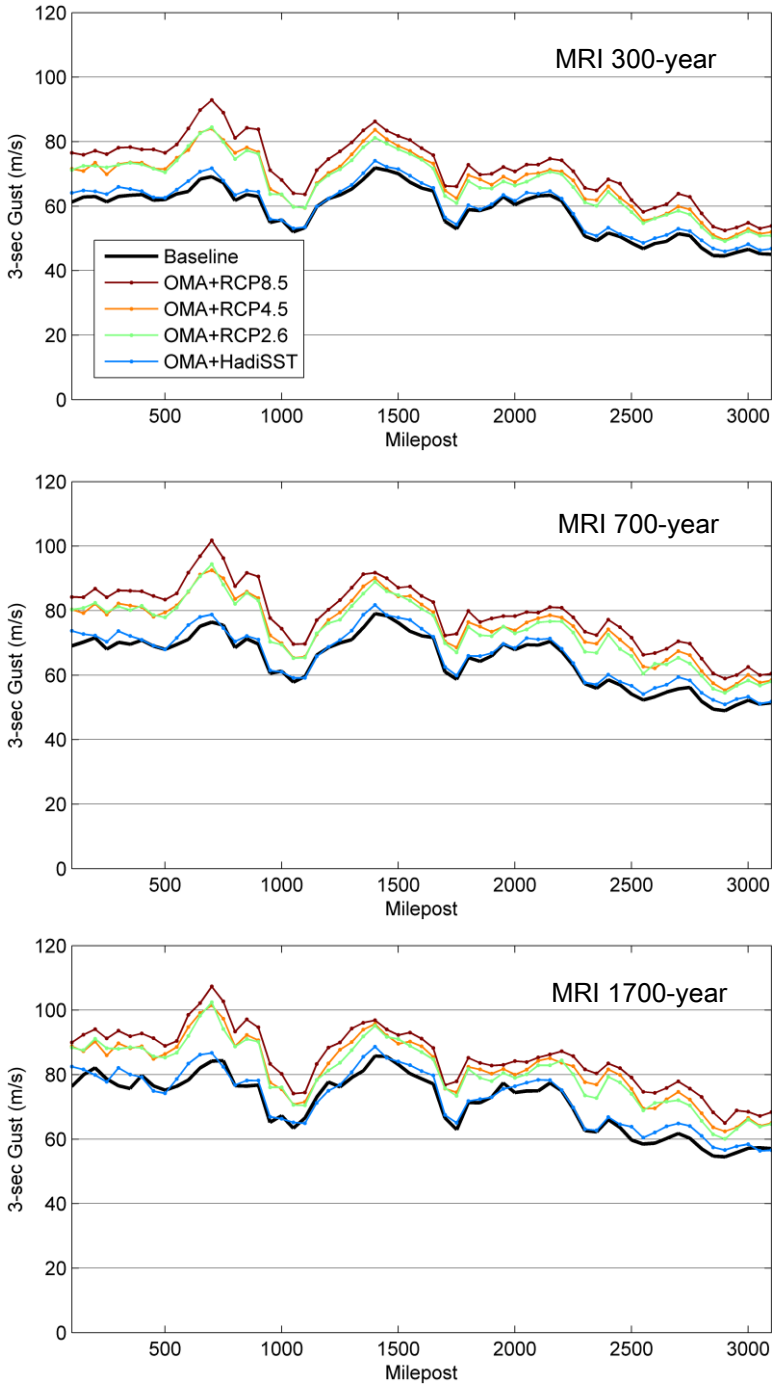


Figure 5.15: Projected gust wind speeds for (a) 300-year MRI, (b) 700-year MRI, and (c) 1700-year MRI for mileposts along the U.S. coastline in year of 2050.

Figure 5.16 shows the wind speeds for Case 4 (LMA+RCP8.5), which is the worst-case scenario among the six climate change cases considered in this study. Figure 5.17 presents the results of Case 5 (CON+RCP8.5), which considers only the changes in SSTs. If Cases 4 and 5 are realized in the future, the peak 1700-year MRI wind speeds in Gulf coast and Florida regions are expected to increase substantially. Under these two cases, the peak 1700-year MRI wind speeds may exceed 100 m/s in year 2100, which are more than 40% higher than the current ASCE 7-10 1700-year MRI wind speeds for these two regions. This level of increase is very drastic; however, it is not inconceivable. The peak 1-min sustained wind speed of Hurricane Wilma (2005) was reported at 160 knot (82 m/s), which is roughly equal to 100 m/s of 3s gust speed (NHC 2006).

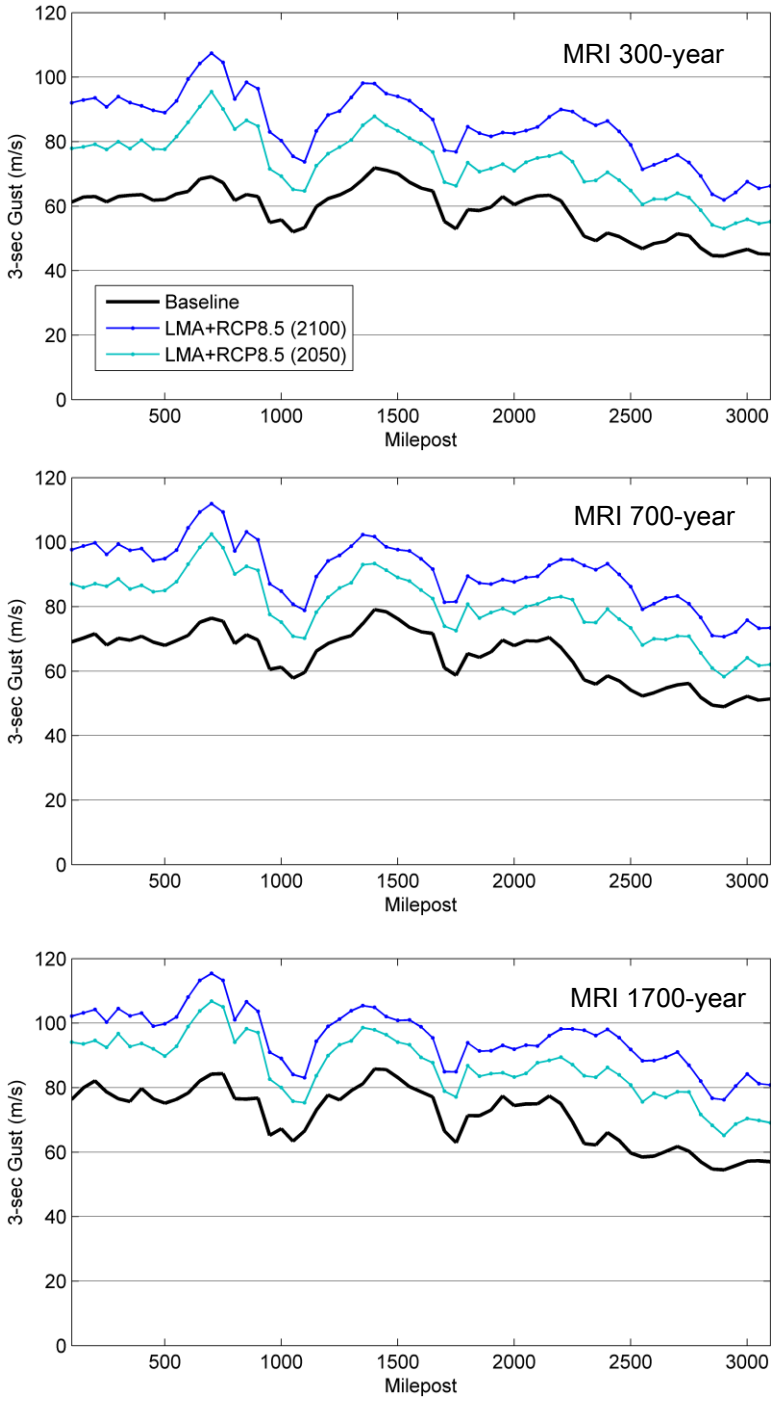


Figure 5.16: Projected 300-, 700- and 1700-MRI gust wind speeds for Case 4 (LMA+RCP8.5) for mileposts along the U.S. coastline.

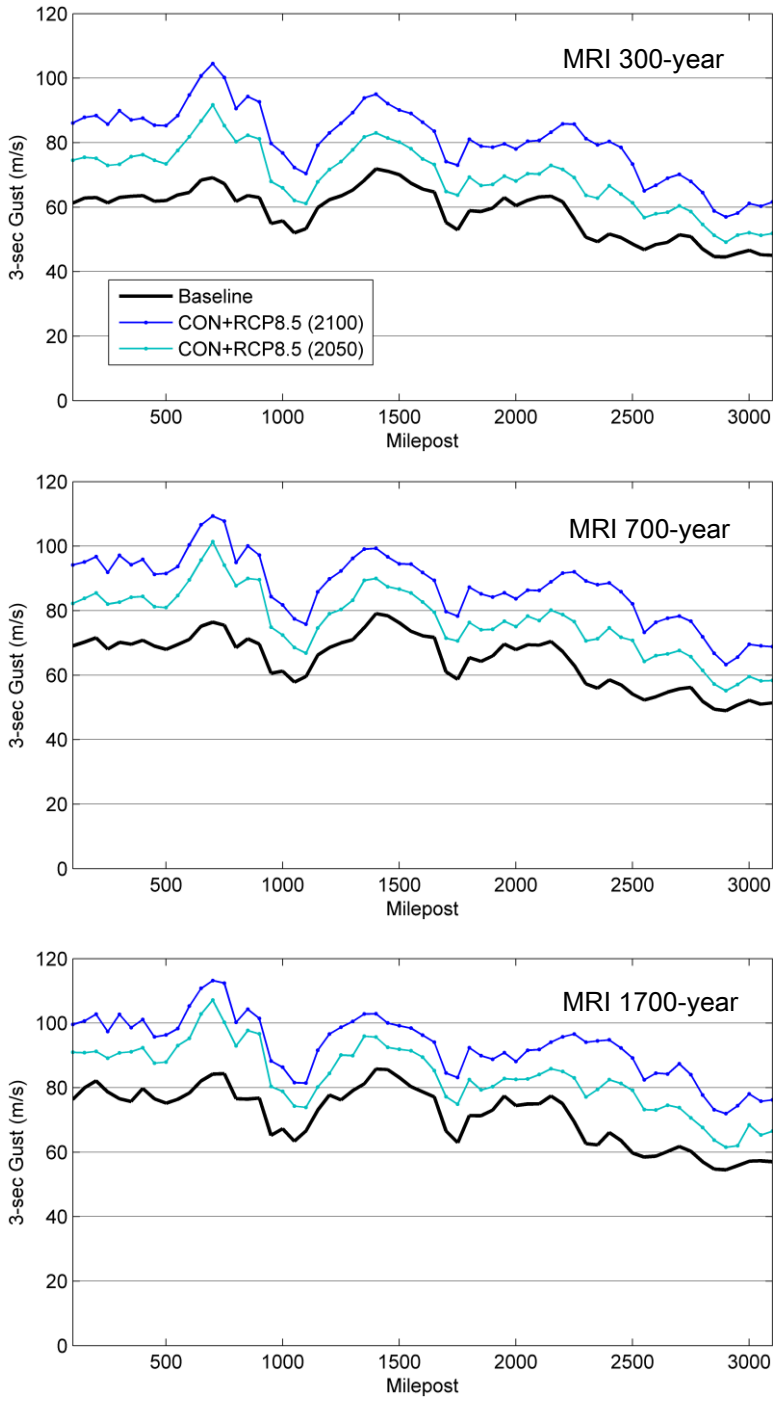


Figure 5.17: Projected 300-, 700- and 1700-MRI gust wind speeds for Case 5 (CON+RCP8.5) for mileposts along the U.S. coastline.

#### 5.3.4.4 Percentage Differences in Projected Wind Speeds

A summary of increases in design wind speeds compared to the baseline level is provided in Table 5.4. All statistics are grouped into four bins which correspond to four segments of the U.S. coastline: (1) Gulf Coast (MP 100-1050), (2) Florida Peninsula (MP 1100-1700), (3) Mid Atlantic (MP 1750-2550) and (4) New England (MP 2600-3100). The maximum increase, location of maximum increase and average increase for each region and the average of the entire coastline are summarized in Table 5.4. On average, the increase in New England region is lower than the other regions and is below the average of the entire coastline. On the other hand, design wind speeds in Gulf Coast, Florida and Mid-Atlantic are more sensitive to climate changes than New England, especially for Cases 1, 4 and 5 with high radiative forcing scenario (RCP 8.5). While the average percentage increase in design wind speeds within each speculated climate change scenario is about the same for all three MRIs, in general, the percentage increases in design wind speeds are slightly higher for ASCE 7-10 Risk Category I (MRI = 300 years) than Risk Categories III & IV (MRI = 1700 years).

Table 5.4: Increase in 3s gust surface wind speed for 300, 700 and 1700-year MRI from baseline to Case 1 - 6 at projection years of 2050 and 2100 along the U.S. coastline

| Future climate Case- Year | MRI | Increase in wind speed (m/s) | | | | | | | | |
|---|---|---|---|---|---|---|---|---|---|---|
| | | Gulf Coast | | Florida Peninsula | | Mid Atlantic | | New England | | All |
| | | Avg | Max /MP | Avg | Max /MP | Avg | Max /MP | Avg | Max /MP | Avg |
| **Case 1-2100** | 300 | 29 | 37/700 | 23 | 27/1350 | 25 | 33/2300 | 10 | 24/2650 | 24 |
| | 700 | 27 | 35/700 | 21 | 27/1300 | 25 | 33/2300 | 9 | 26/2600 | 24 |
| | 1700 | 24 | 31/700 | 19 | 24/1250 | 23 | 33/2300 | 8 | 28/2600 | 23 |
| **Case 1-2050** | 300 | 17 | 24/700 | 13 | 15/1350 | 13 | 17/2400 | 10 | 12/2700 | 13 |
| | 700 | 17 | 25/700 | 12 | 17/1350 | 14 | 19/2400 | 12 | 15/2700 | 14 |
| | 1700 | 16 | 23/700 | 11 | 15/1300 | 14 | 19/2500 | 13 | 16/2700 | 14 |
| **Case 2-2100** | 300 | 16 | 21/700 | 12 | 15/1350 | 11 | 16/2400 | 9 | 11/2650 | 13 |
| | 700 | 17 | 21/700 | 12 | 16/1350 | 12 | 17/2400 | 11 | 13/2650 | 13 |
| | 1700 | 16 | 20/600 | 10 | 15/1350 | 12 | 18/2300 | 12 | 16/2650 | 13 |
| **Case 2-2050** | 300 | 11 | 15/700 | 9 | 12/1350 | 10 | 14/2400 | 7 | 9/2650 | 10 |
| | 700 | 12 | 16/700 | 9 | 13/1350 | 10 | 16/2400 | 8 | 12/2700 | 10 |
| | 1700 | 12 | 17/700 | 9 | 13/1350 | 11 | 16/2450 | 10 | 13/2700 | 10 |
| **Case 3-2100** | 300 | 12 | 17/700 | 9 | 11/1350 | 8 | 11/2400 | 6 | 8/2700 | 9 |
| | 700 | 13 | 18/700 | 9 | 12/1350 | 9 | 12/2500 | 7 | 11/2700 | 10 |
| | 1700 | 12 | 17/700 | 8 | 11/1350 | 9 | 15/2500 | 9 | 13/2600 | 10 |
| **Case 3-2050** | 300 | 11 | 15/700 | 8 | 10/1350 | 8 | 13/2400 | 6 | 8/2650 | 9 |
| | 700 | 12 | 18/700 | 8 | 11/1350 | 9 | 14/2400 | 7 | 10/2600 | 9 |
| | 1700 | 11 | 18/700 | 7 | 11/1350 | 9 | 14/2500 | 9 | 12/2600 | 9 |
| **Case 4-2100** | 300 | 31 | 38/700 | 25 | 30/1350 | 27 | 36/2300 | 21 | 25/2650 | 27 |
| | 700 | 29 | 36/700 | 23 | 28/1300 | 26 | 35/2350 | 24 | 28/2650 | 26 |
| | 1700 | 26 | 31/700 | 20 | 25/1250 | 25 | 35/2300 | 26 | 30/2600 | 24 |
| **Case 4-2050** | 300 | 18 | 26/700 | 14 | 17/1350 | 14 | 19/2400 | 11 | 14/2600 | 15 |
| | 700 | 19 | 26/700 | 14 | 18/1350 | 15 | 21/2400 | 13 | 17/2600 | 15 |
| | 1700 | 17 | 23/700 | 12 | 17/1350 | 15 | 21/2500 | 15 | 19/2600 | 15 |
| **Case 5-2100** | 300 | 27 | 35/700 | 21 | 26/1350 | 23 | 31/2300 | 16 | 20/2650 | 22 |
| | 700 | 26 | 33/700 | 20 | 25/1300 | 23 | 32/2350 | 19 | 23/2600 | 23 |
| | 1700 | 23 | 29/700 | 18 | 23/1250 | 22 | 32/2350 | 21 | 26/2600 | 21 |
| **Case 5-2050** | 300 | 14 | 23/700 | 10 | 13/1350 | 10 | 15/2400 | 7 | 9/2600 | 11 |
| | 700 | 16 | 25/700 | 10 | 15/1350 | 11 | 17/2500 | 9 | 13/2600 | 12 |
| | 1700 | 15 | 23/700 | 10 | 15/1350 | 12 | 19/2500 | 10 | 14/2650 | 12 |
| **Case 6-2100** | 300 | 2 | 3/250 | 1 | 3/1300 | 1 | 2/2400 | 1 | 2/2850 | 1 |
| | 700 | 2 | 4/300 | 1 | 3/1300 | 1 | 2/2100 | 2 | 3/2850 | 1 |
| | 1700 | 1 | 6/300 | 1 | 4/1600 | 1 | 2/1750 | 2 | 3/2700 | 1 |
| **Case 6-2050** | 300 | 2 | 3/600 | 1 | 2/1400 | 1 | 2/2050 | 2 | 2/2800 | 1 |
| | 700 | 2 | 5/100 | 1 | 4/1350 | 1 | 3/2500 | 2 | 4/2700 | 1 |
| | 1700 | 1 | 6/100 | 1 | 4/1350 | 1 | 4/2500 | 2 | 4/2800 | 1 |

# CHAPTER SIX: HURRICANE ENSEMBLE SELECTION

Using the hurricane simulation framework presented in Chapter Three, a synthetic hurricane database containing 200,000 hurricane seasons[2] was generated. The database contains more than 2,000,000 simulated full-track hurricanes. Due to high computation demand of analyses such as storm surge simulation and regional loss estimation, it is not feasible to analyze every hurricane in the database. This Chapter presents methodologies for selecting: (1) a reduced set of hurricane events to represent the true hazard, and (2) hurricane ensembles for specific return periods or hazard levels.

## 6.1 Reduced Hurricane Database Selection using Inverse Cumulative Distribution Function Method

The complete hurricane database can be used to represent the true hurricane hazard. However, high computational demand of certain analyses that require the time history of full-track hurricanes (e.g. storm surge simulation) often limits one from utilizing the entire database due to time constraint. A reduced database with less number of events but still represents the same hazard of the original database is a solution to the computational limitations. The reduced database can be generated using the inverse Cumulative Distribution Function (CDF) method.

The *inverse CDF method,* also known as the *inverse transform sampling,* is employed to sample individual or group of events from the CDF composed of all the candidate events. For illustration purpose, the development of a reduced hurricane

[2] A hurricane season year is from June to November.

database containing 1000 events from the original database consisting of 100,000 years of simulation with more than 120,000 events at milepost 1400 in Florida (Figure 4.2) is given here as an example (Figure 6.1). The procedure is as following:

1) Create the CDF of 3s-gust surface wind at milepost 1400 by evaluating all the hurricane events that approach within 250km from milepost 1400 during the 100,000 simulated years (Figure 6.1).
2) Divide the cumulative probability (y-axis) into 1000 bins uniformly and locate the values of the mid-point in these bins (e.g. 0.0005, 0.0015 … 0.9995) on the y-axis.
3) Use the mid-point values on the y-axis of the CDF curve (i.e. cumulative probability values) to identify the wind speeds and hurricane events associated with these cumulative probability values from the hurricane database.

Figure 6.1 shows both the CDF curves produced using the full database and the

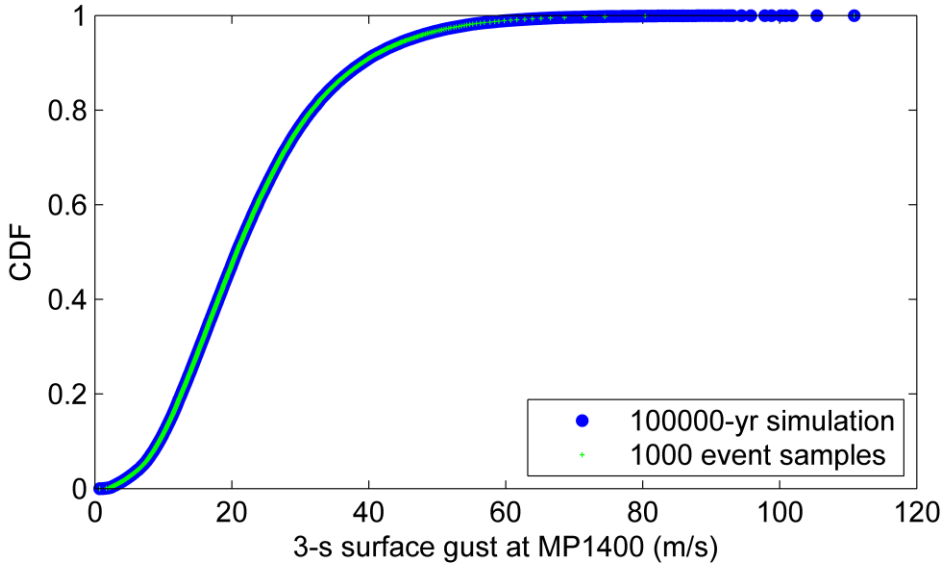


Figure 6.1: The cumulative distribution function of 3s-gust wind at milepost 1400 in Florida.

reduced database. As can be seen, the CDF of the reduced database is nearly identical to the CDF of the full database.

## 6.2 Mean Recurrence Interval of Wind Speed

The mean recurrence interval (MRI) of a given wind speed, *V*, at a particular site can be computed using the following equation:

$$MRI\left(v_i > V\right) = \frac{1}{\lambda P\left(v_i > V\right)} = \frac{Y}{n} \tag{32}$$

where $P\left(v_i > V\right)$ is the probability of the peak surface wind speed of storm *i*, ($v_i$), greater than a given threshold wind speed, *V*; $\lambda$ is the mean annual occurrence rate of storms at the site; *n* is the total number of storms having wind speed $v_i$ larger than *V* and *Y* is the number of simulation years.

The region of interest can be defined either as a single site (a point) or an area. As a statistical measurement, MRI at a single site represents the point risk, which is useful for design and safety analysis of individual building (Vickery et al. 2009a). One application of the point probability is the development of the wind hazard map in Vickery et al. (2000) and Vickery et al. (2009a). If the wind speeds appearing anywhere within a given region are taken into account in the determination of MRI, the MRI level in such case refers to the areal risk within the given range. Areal risk is useful for risk assessment of a system expanded in a large area, such as the transmission lines or a portfolio of buildings (Vickery et al 2009a).

Table 6.1 summarizes the applications of synthetic hurricane database related to quantifications of MRI. Each application is labeled with a letter (A, B or C) which indicates the type of study domain and a roman number (I, II or III) which indicates the type of application (hazard level quantification, hurricane ensemble selection and etc.). For the type of study domain, a point site (A) is defined with a pair of latitude and longitude; circular area domain (B) is defined by the center of the study domain (latitude and longitude) and a radius (also called the scan circle); irregular area (C), typically used to define a county, several combined coastal counties or even several states, is defined using vectors of latitude and longitude. Descriptions and examples for these applications are given below.

Table 6.1: Applications of wind speed calculation and quantification of MRI

| Application / Domain | Hazard Level/ Return Period Quantification (I) | Hurricane Ensemble Selection (II) | MRI Determination for Individual Event (III) |
|---|---|---|---|
| Point Site (A) | A-I | A-II | A-III |
| Circular Area (B) | B-I | - | B-III |
| Irregular Area (C) | C-I | C-II | C-III |

### 6.2.1 Development of MRI-curve (A-I) and Hurricane Selection for Point Site (A-II)

In this study, hurricane wind speeds were evaluated and their associated MRIs were determined at 61 point locations (mileposts) along the U.S. coastline (Figure 4.2). The wind speed used here refers to the 3-s gust surface wind (10 m height) occurred at each site. To search for the events that produce significant winds at each site, the

proximity of storm tracks to the site is first checked. The hurricane events with track segment lying within a circle of 250 km radius centered at each site were selected as the candidate events. Then, the wind speeds of these candidate events were evaluated at a 15-min interval along the track segment in the circle. The storm locations and hurricane parameters were interpolated from 6-hour to 15-min time steps. The interpolated hurricane parameters were then used for wind speed calculations. On the completion of wind speed calculations for all candidate events in the database, the maximum wind of each candidate event was assembled into a vector and sorted on the MRI-curve for the specific site. The referring MRIs for these wind speeds were determined using Eqn. (32). The peak wind speeds of candidate events were rank ordered and Eqn. (32) was used to compute the MRI of peak wind speed associated with each event.

The curves of wind speeds versus MRIs which are derived from 100,000 years of simulation without climate change are plotted in Figure 6.2 for four locations. The four locations are (1) milepost 700 in Louisiana (LA), (2) milepost 1400 in Florida (FL), (3) milepost 1950 in South Carolina (SC), and (4) milepost 2550 in New York (NY). Three MRIs (300, 700 and 1700 years) are highlighted on the Figure. These three MRIs correspond to the ASCE 7-10 design level wind speeds for Occupancy Categories I, II and III & IV, respectively. For comparison purpose, the ASCE 7-10 wind speeds were extracted from the design wind speed database website maintained by the Applied Technology Council (ATC 2013) and are shown as rectangular markers in Figure 6.2.

The wind speeds for MRIs of 300, 700 and 1700 years at all 61 milepost locations are plotted in Figure 6.3 (bold gray line) and are compared to those from ASCE 7-10

(thin red line). The simulation result in this study agrees well with the current design code. Four peaks can be observed from the wind speed versus milepost plots of both sources: (1) around the mouth of the Mississippi River in Louisianan (MP 700); (2) at the very tip of South Florida (MP1400); (3) around Myrtle Beach area near the boundary between the Carolinas (MP 2000); and (4) around Cape Cod area in Massachusetts (MP 2700). The fluctuation of wind speeds is consistent with the changing of central pressure along the coastline (Figure 4.3). The largest difference between the wind speeds of this study and that of the ASCE 7-10 is about 8m/s (<15% difference) ,which occurs at milepost 2700 in northeastern U.S.

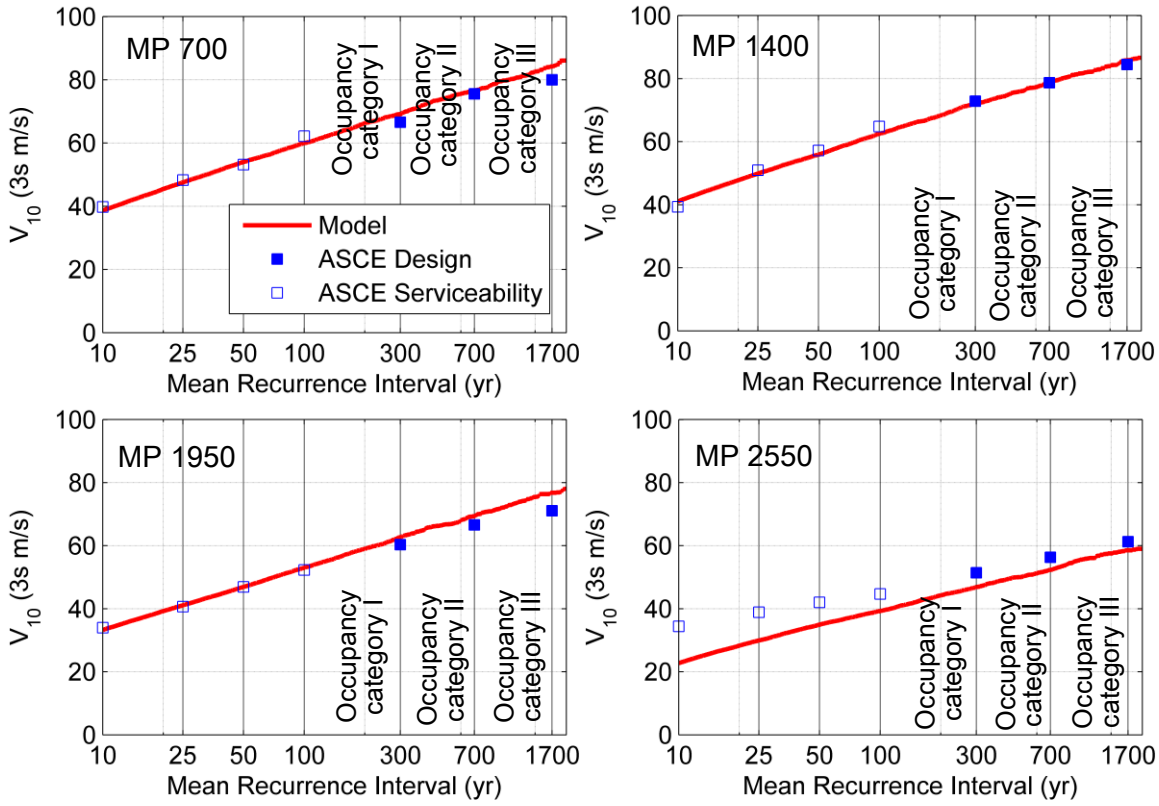


Figure 6.2: 3-s gust at 10m-height versus MRI levels at selected locations along coastline, including MP 700 in Louisiana, MP 1400 in Florida, MP 1950 in South Carolina and MP 2550 in New York.

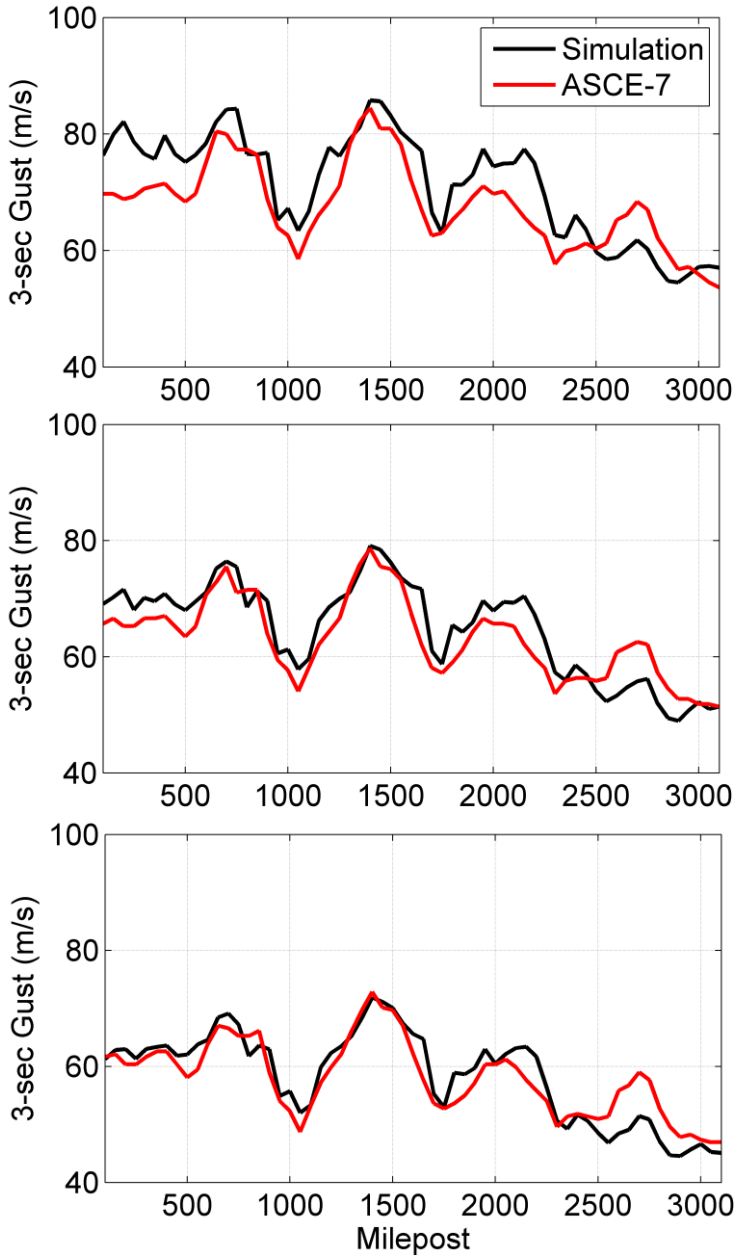


Figure 6.3: Wind speeds of 300, 700 and 1700-year MRI at 10m-height for locations along the coastline

The slight differences in wind speeds between ASCE 7-10 and this study are likely attribute to the different methods and algorithms employed in the simulation that developed for ASCE 7-10 (Vickery et al. 2009a) and the ones used in this study. For example, different wind field models were used to characterize the wind field. The

evaluation of wind speed from hurricane parameters involves the gradient wind field model, radius of maximum wind speed model, Holland *B* model and all other components in the simulation framework. All these differences in the modeling of hurricane parameters might lead to inexact results between different studies.

For any given MRI for a given site, its corresponding hazard level in terms of wind speed can be found from the MRI curve for the specific site (i.e. the bold lines in Figure 6.2). Using the MRI curve shown in Figure 6.2, the specific hurricane event that produced the MRI wind speed at the site can be extracted from the hurricane database. This extracted event with complete time history information of the track is regarded as the event that represents the risk of the given MRI in terms of extreme wind for the specific site. In practice, it usually requires more than one hurricane event of a certain MRI level in order to quantify the event-to-event uncertainty. To obtain more events of the same MRI, multiple sets of hurricane databases or sub-database must be prepared. In this way, one event of desired hazard level can be selected from each hurricane database and create an ensemble of full-track hurricane events to quantify the hurricane hazard at a specific hazard level or for a specific MRI. An example of hurricane ensemble selection procedure using multiple databases is performed for milepost 1400 for MRIs ranged from 10 to 1700 years. The MRI curves from five sets of database each containing 20,000 years of events for milepost 1400 were plotted in Figure 6.4. From Figure 6.4, it can be seen that the wind speed versus MRI curves between the five sets of 20,000-year simulations are nearly identical, in particular for short MRIs.

Figure 6.5 to 6.8 show the tracks of hurricane ensembles selected for MRIs of 10, 25, 50, 100, 300, 700, and 1700 years for milepost 1400 in Florida. Ten hurricane events were selected for each hazard level (MRI) from a master database consisting of 200,000 years of simulated events. The master database was divided into ten sub-databases each contains 20,000 years of simulation and a full-track hurricane was selected from each sub-database. The arrows in the Figure 6.5 to 6.8 show the travel direction of the selected storms and the red dots show the locations where maximum wind speeds were observed at the site of interest (i.e. milepost 1400 in this example). As can be seen, the selected storms cover different scenarios in which the storm tracks approach the site from different directions (east, west, north and south). As the hazard level or MRI increases, the proximity of the selected tracks to the site also reduces. This is expected as peak wind speed typically increases as a storm gets closer to the site. The selected hurricane ensembles can be used in hurricane loss analysis to consider event-to-event uncertainty. Hurricane loss assessment using hurricane ensembles will be presented in Chapter Seven.

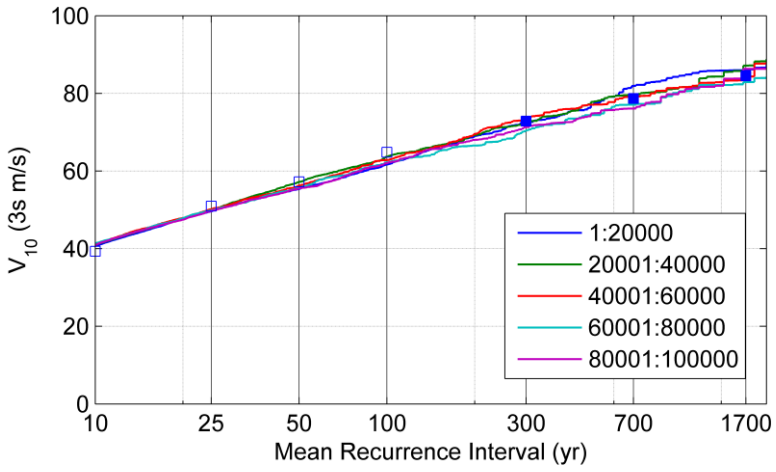


Figure 6.4: MRI-curves from 5 sets of 20,000-year simulation at milepost 1400 in Florida.

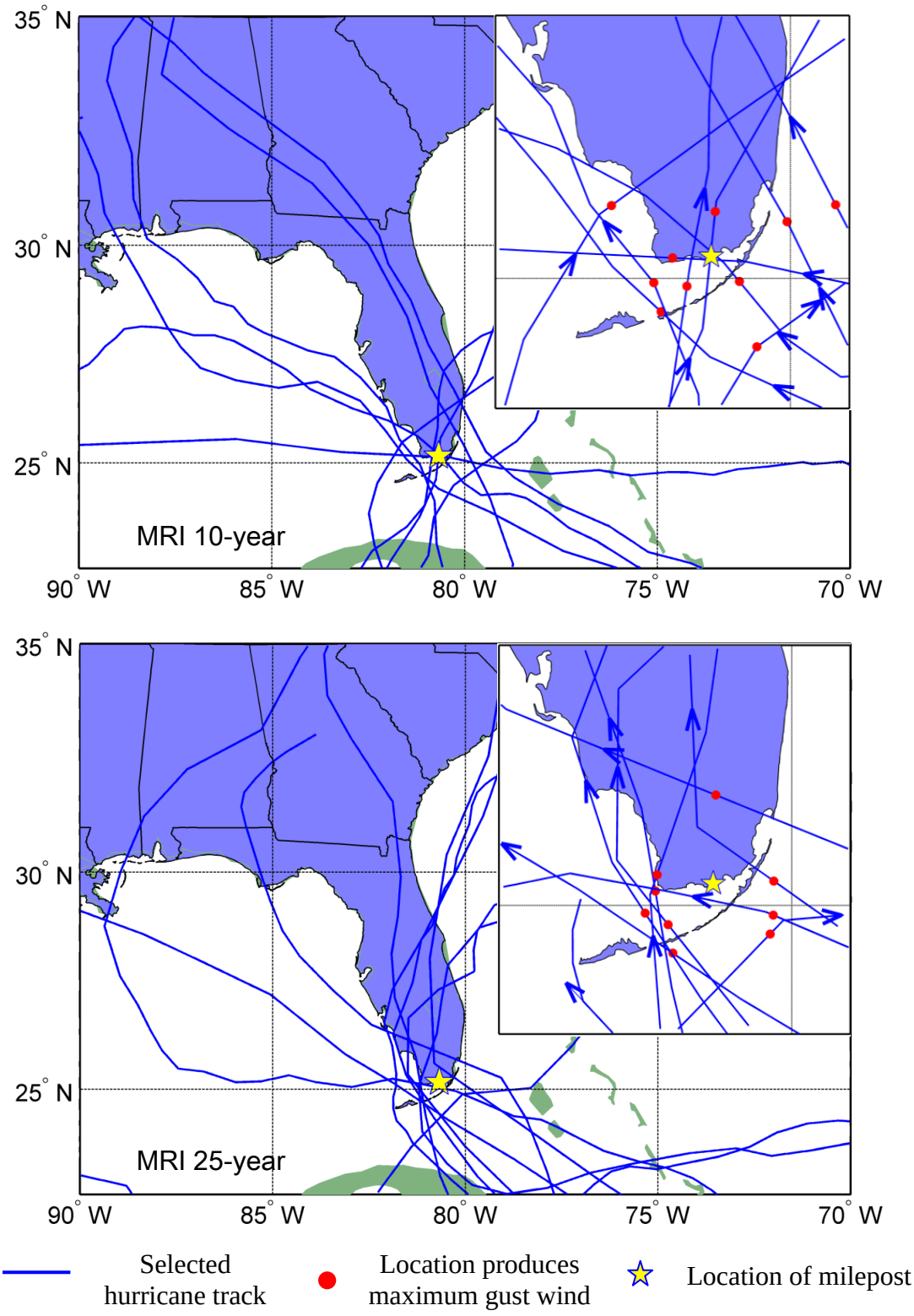


Figure 6.5: Selected hurricane events for MRIs of 10 and 25-year.

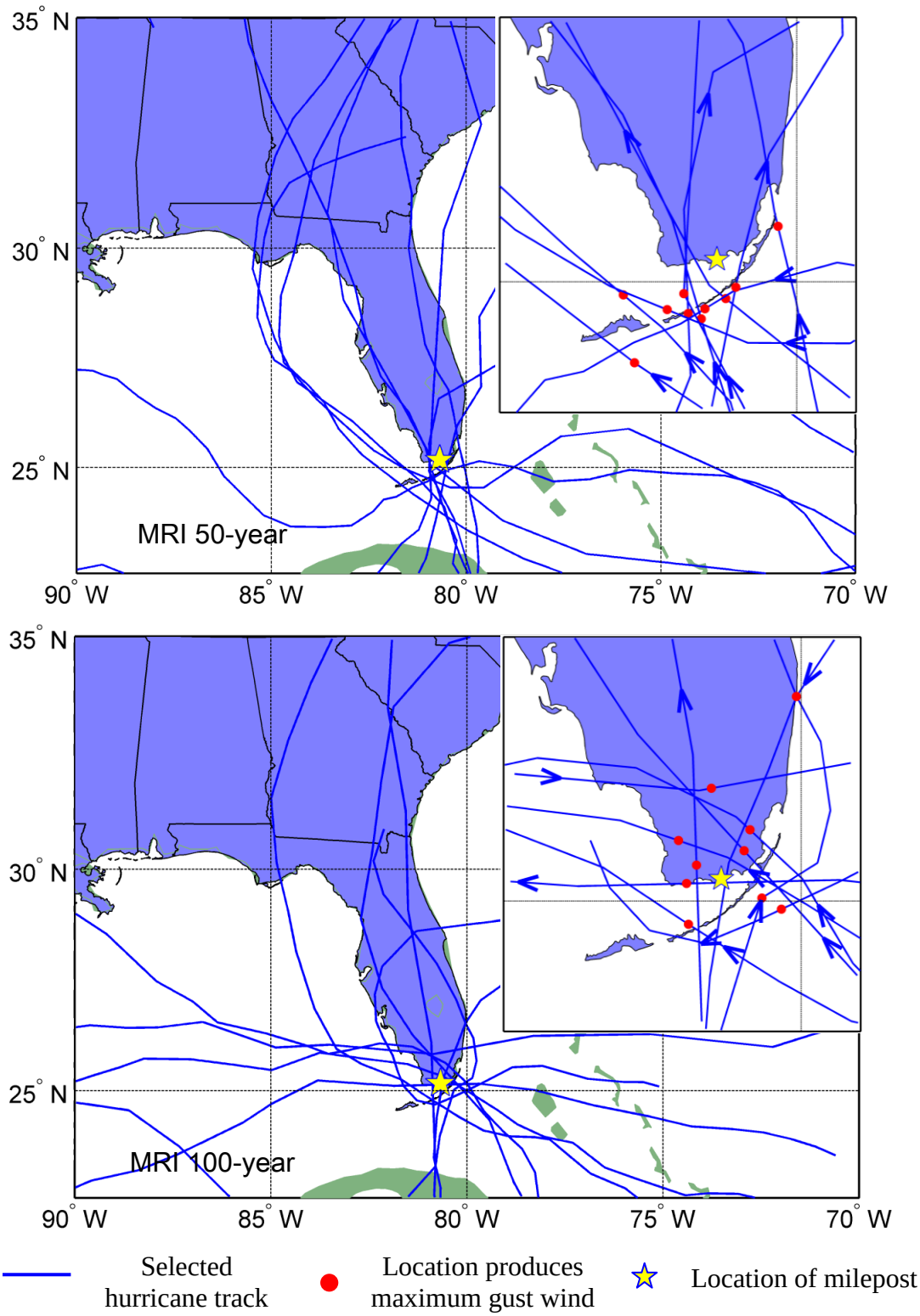


Figure 6.6: Selected hurricane events for MRIs of 50 and 100-year.

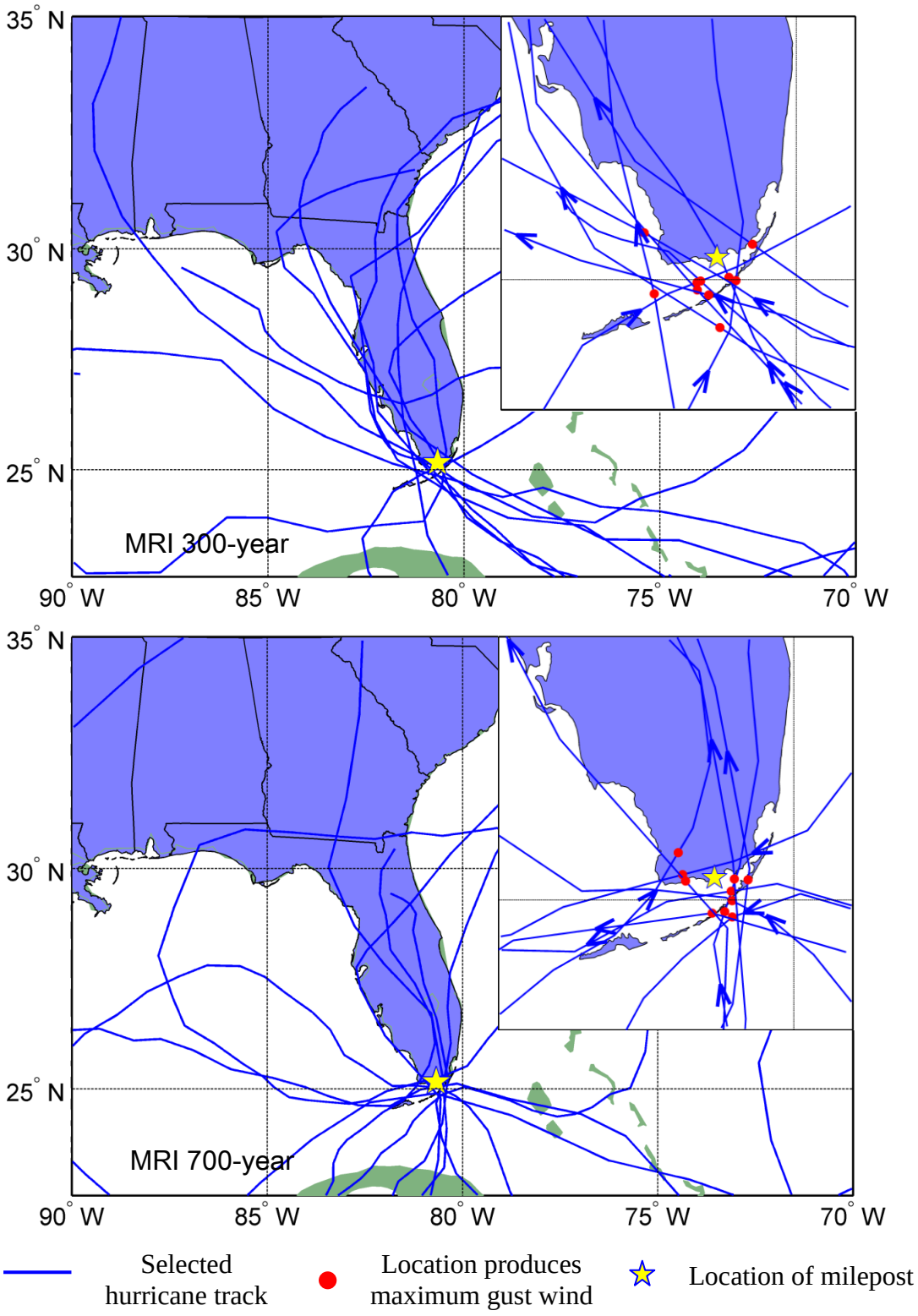


Figure 6.7: Selected hurricane events for MRIs of 300 and 700-year.

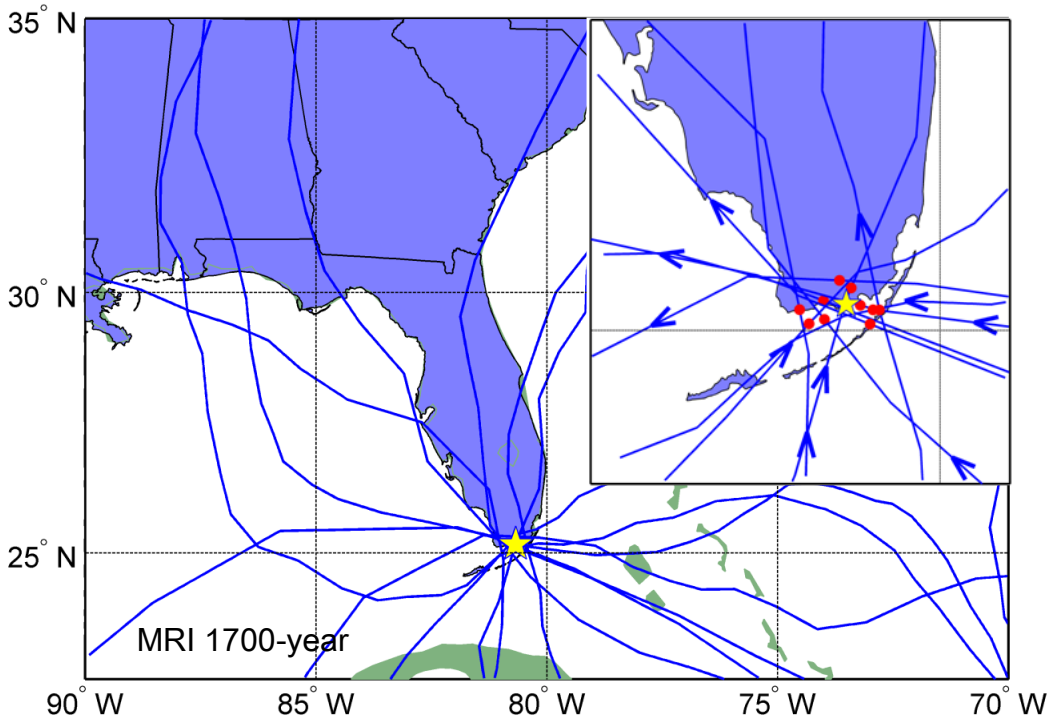


Figure 6.8: Selected hurricane events for MRI of 1700-year.

### 6.2.2 Circular Areal Wind Speed MRI Estimation (B-I)

The method to determine an areal MRI using extension from a point MRI in the area was first proposed by Neumann (1987). It can be used for a circular area with radius less than 111km (60 nautical miles) or an area approximately circular (i.e. the length and width are approximately the same) with equivalent radius less than the same threshold. There are several steps to extend the point probability into an areal one. To determine the circular areal probability, scan circles were drawn with uniformly increased radii that enclosed small to relatively larger areas from the center point of the area, i.e. radii from 9.3 to 130 km (5 to 70 nautical miles) with increment of 18.5 km (10 nautical miles). Then, the MRI curves were developed again with only those storms that cross the scan circles. Each curve represents the probabilities within a different range of radius.

Equivalent radius of the original area was used to find or interpolate the appropriate scan circle that can represent the MRIs for the extended area with the given hazard level. Details in the evaluation procedures can be found in Neumann (1987).

One application of circular areal MRI estimation is provided in NOAA Technical Memorandum NWS NHC-6 (Blake et al., 2007) on the estimation of MRIs for hurricane (>33m/s) and major hurricane (>49m/s) passing within 92.6 km (50 nautical miles) around locations on the U.S. coast. The MRIs for hurricanes and major hurricanes from 100,000 simulated years were estimated and the results are plotted in the same format as the MRI plots on pages 25 and 26 in NOAA Technical Memorandum NWS NHC-6 (Figure 6.9). This technical report is available on NOAA NHC website (http://www.nhc.noaa.gov/pdf/nws-nhc-6.pdf)

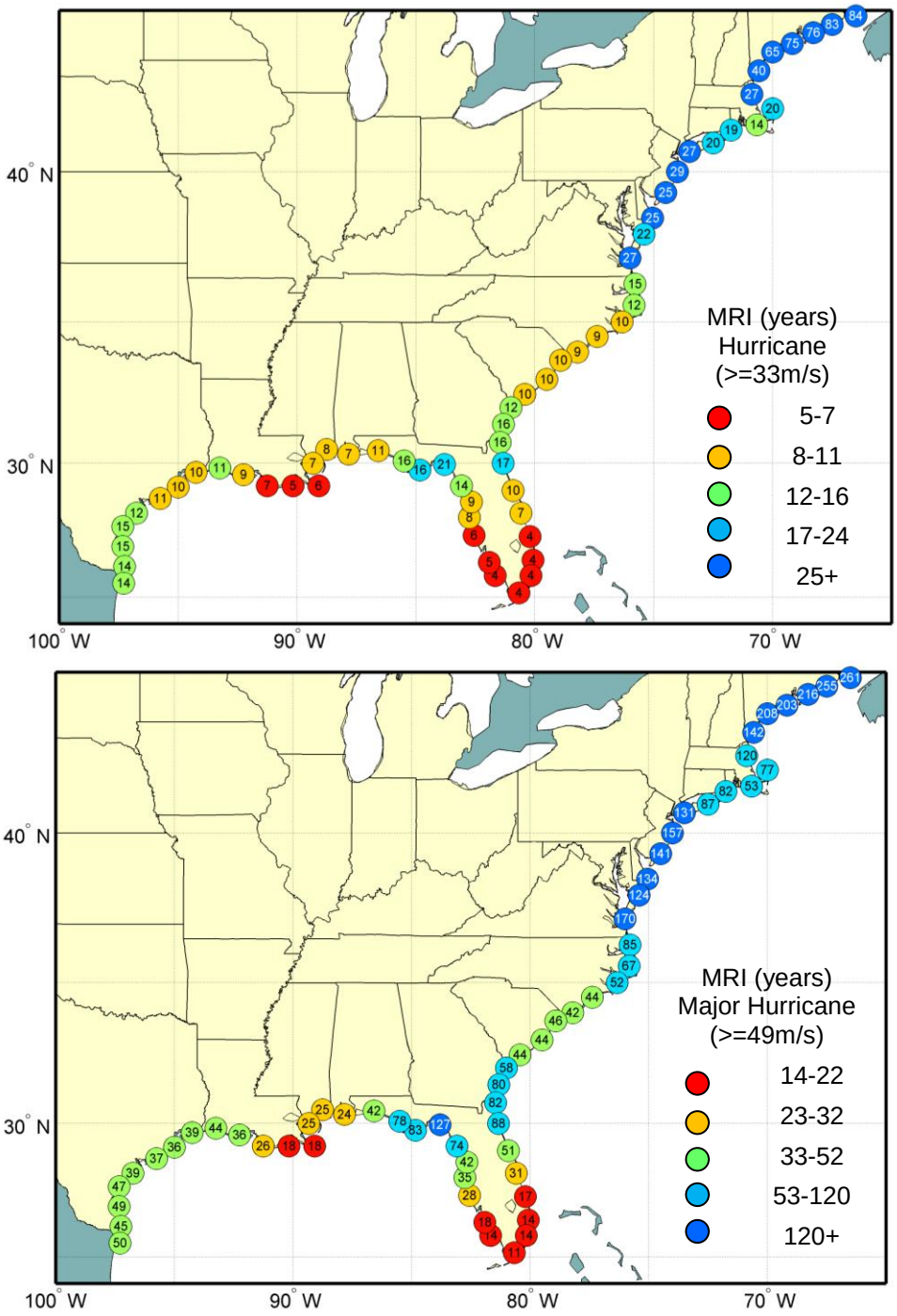


Figure 6.9: Estimated MRI in years for hurricanes (sustain wind > 33m/s) and major hurricanes (sustain wind > 49m/s) passing with 92.6 km (50 n mi) of various locations on the U.S. Coast.

### 6.2.3 Application of MRI Estimation for a Large Area (C-I and C-III)

To estimate the MRIs for a large irregular area, a set of grids is defined for the area and wind speeds are evaluated at the joints of the grids. Unlike the MRI curve developed for a single location (see Section 6.2.1), the dots on the MRI curve for a large irregular area are the maximum wind speeds produced by hurricane events over the entire grid coverage. The value on the curve stands for the probability of recurrence of certain wind speed at everywhere in the region covered by the grids. An application of MRI estimation with area-wide grids can be found in Vickery et al. (2009a) for the populated areas of Miami-Dade and Broward counties in Florida. In Vickery et al. (2009a), the study region was covered with 0.05˚ by 0.05˚ grids and a 20,000-year simulation was performed to evaluate the MRI levels up to 1,000 years.

For illustration purpose, the method for estimating the MRIs in an irregular area (C-III) was employed to determine the return period of Hurricane Katrina (2005) with respect to the Gulf Coast region (see Figure 6.10a). Since the Gulf Coast region is much larger than the two counties investigated in Vickery et al. (2009a), instead of covering the entire region with grids, a set of grids with 0.054˚ by 0.054˚ resolution were constructed within boxes along the track. The box is a square with 5˚ by 5˚ size and was generated around the location of hurricane eye at every 15 minutes. The distance of 2.5˚ (278km) from the hurricane center to the four edges of the box is long enough to enclose the major portion of the wind field that produces significant wind speeds. This is because the mean of $R_{max}$ for hurricanes is 47 km and the standard deviation is 27 km (Hsu and Yan, 1998). If the box overlaps any portion of the Gulf Coast region, wind speeds were evaluated on

the grids within the overlapped region. The maximum wind speed in the boxes during all 15-min intervals was recorded as the maximum wind produced by the event and marked as a dot on the MRI curve.

According to the MRI curve for the Gulf Coast region in Figure 6.10, the return period of Hurricane Katrina which produced 1-min maximum sustained wind of 65 m/s is

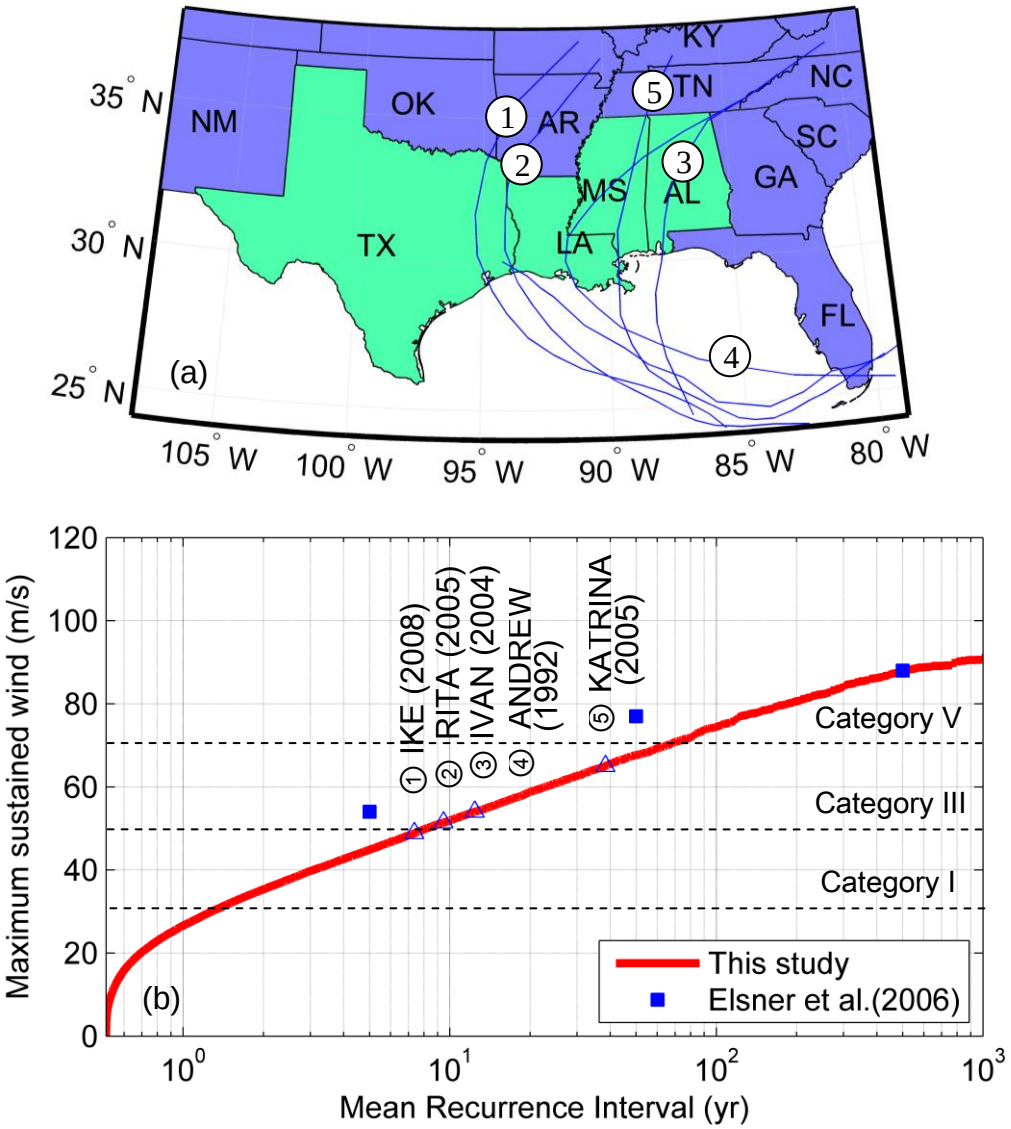


Figure 6.10: (a) Gulf Coast region. (b) MRI curve from hurricane winds in the Gulf Coast region.

38 years. Elsner et al. (2006) also made the return period estimation for Hurricane Katrina in the same region and found that the 95% confidence limit ranges from 10 to 50 years. The MRI of Katrina estimated in this study with respect to the Gulf Coast is within the confidence range and slightly higher than the mean estimation of 21 years by Elsner et al. (2006). The complete MRI curve for the Gulf Coast region is presented in Figure 6.10b with more comparisons to the estimations in Elsner et al. (2006). Their estimations of wind speeds for 5-year, 50-year and 500-year MRIs for the Gulf Coast region were given as 54, 77 and 88 m/s, respectively, shown as the solid squares in Figure 6.10b. These values for the same MRI levels in this study were found to be 45, 68, and 88 m/s from the MRI curve. Besides Hurricane Katrina, four other historical hurricanes that made landfall in the Gulf Coast region were marked as triangles in Figure 6.10b. These hurricanes are Hurricane Ike (2008), Hurricane Rita (2005), Hurricane Ivan (2004) and Hurricane Andrew (1992). According to Black et al. (2007), they were all ranked as the top ten costliest mainland hurricanes in the U.S. Their MRIs were quantified using the maximum sustained winds observed at landfall moments from the NOAA hurricane reports (National Hurricane Center 2014). The MRI for Hurricane Ike is 7 years with wind speed of 49 m/s (95 knot); MRI for Hurricane Rita is 9 years with wind speed of 51 m/s (100 knot); and for both Hurricane Ivan and Andrew, the MRI is 12 years with wind speed of 54 m/s (105 knot).

### 6.2.4 MRI Estimation for a Given Storm Track on Coastal Locations (A-III and C-III)

On a MRI curve, wind speeds are paired with MRIs. Therefore, the MRI curves for single sites (e.g. Figure 6.2) can be used to estimate the MRIs of hurricane events for point locations along the coast if the wind speed distributions at these locations are known. The MRIs of Hurricane Irene (2011) at point locations along the coastline (milepost 1950-3100) were evaluated using winds produced during its landfalls at North Carolina and New Jersey (Figure 6.11). The wind speeds at the milepost locations were calculated using hurricane parameters from HURDAT and the NOAA–HRD hurricane wind analysis (H*Wind) database (Powell et al. 1998). The critical wind speeds for the

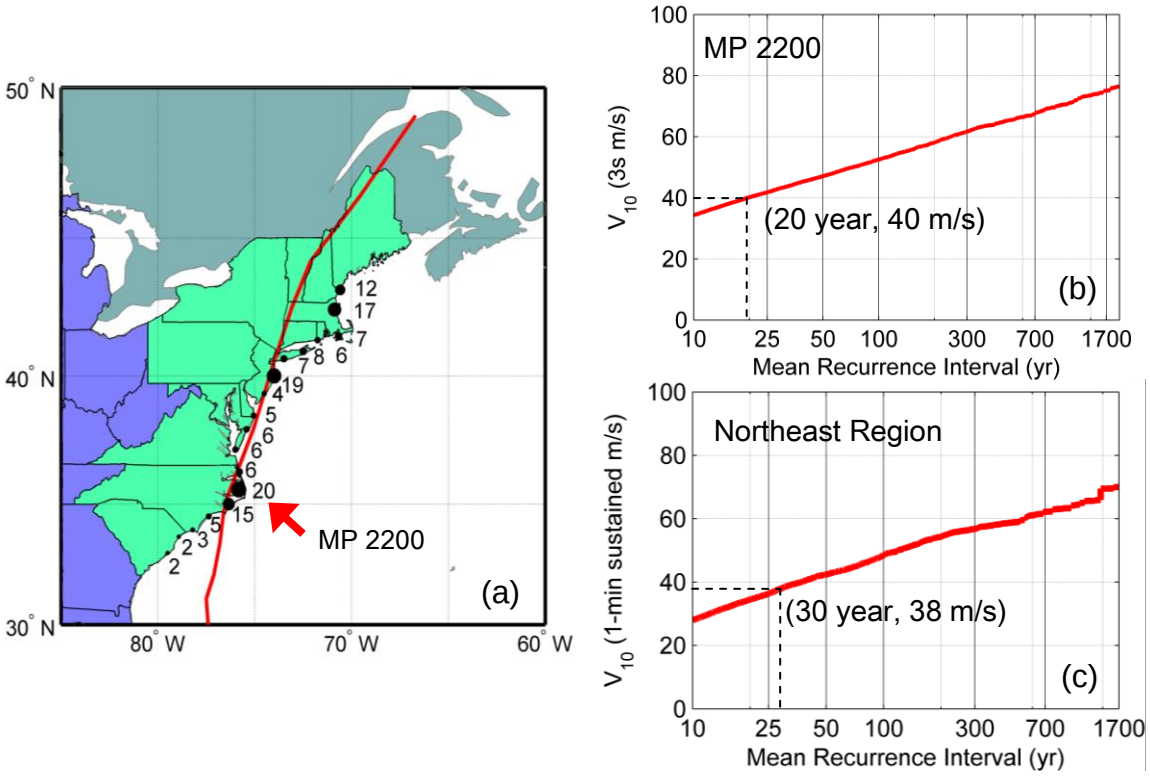


Figure 6.11: MRIs of Hurricane Irene (2011) on coastal locations and the Northeast region.

locations may occur at different time due to the movement of hurricane center and the change in hurricane intensity. The largest MRI found among the locations is 20 years at milepost 2200 with 10m-height gust wind of 40 m/s, which occurred after its landfall moment in North Carolina. The MRI curve for the Northeast region was developed to quantify the MRI of Hurricane Irene with respect to individual point sites in the region (see application C-III in Table 6.1). The Northeast region includes all the coastal states to the north of South Carolina on the U.S. Atlantic coast. Though Pennsylvania and Vermont have no coastlines, they are also included as shown in Figure 6.11a. The maximum sustained wind observed during the life of Hurricane Irene in the Northeast region is found to be 38 m/s (75 knot) in NOAA hurricane report (National Hurricane Center 2014). The MRI from the curve for that level of sustained wind is 30 years as shown in Figure 6.11c.

# CHAPTER SEVEN: PROJECTION OF REGIONAL HURRICANE LOSS

In this Chapter, the impact of hurricane events under climate change effects is quantified in terms of loss and compared with that from the events representing current climate condition. In addition to the hazard level, different vulnerability and exposure conditions were compared in the study regions as summarized in Table 7.1. Combinations of different hazard, vulnerability and exposure levels are referred as loss estimation cases. In the four loss estimation cases applied in this study, two hazard levels were employed: hurricane events from the non-climate change conditions (baseline simulation) and those from one of the worst case climate change scenarios (Climate Change Case 1 in Table 5.3). These two hazard levels were then coupled with two building vulnerability levels: the current existing building condition (no-retrofit) and buildings with improved configurations in resisting high wind load (retrofitted). The four cases were applied to four coastal cities from the Gulf Coast, Florida, Mid-Atlantic Coast and Northeast Coast. The details of building vulnerability and exposure information for these locations are explained in the following sections.

The estimated losses in this Chapter refer to the direct property damage losses, which include the estimated costs to repair or replace the damaged buildings and their contents, due to the selected hurricane events from Chapters Three and Five. The loss estimation in this study is realized using the loss estimation model in the Hazards United States – Multi Hazards (HAZUS-MH) software, which was developed by the Federal Emergency Management Agency (FEMA) and the National Institute of Building Sciences (FEMA 2014). The loss estimation in this Chapter only includes the calculation

using the hurricane module in HAZUS, so only damages due to high winds (i.e. building envelope damage, debris impacts, etc.) were considered. The losses due to flood, storm surge, hurricane-induced tornado and other indirect causes were not included in this study.

Table 7.1: Regional loss estimation cases.

| Loss estimation cases | Hazard | Vulnerability | Exposure |
|---|---|---|---|
| Case I | No climate change | Non-retrofitted structures | Four coastal regions (Miami, New Orleans, Charleston, and New York City) |
| Case II | No climate change | Retrofitted structures | Four coastal regions (Miami, New Orleans, Charleston, and New York City) |
| Case III | Climate Change Case 1 (Oscillating frequency + high emission level = OMA+ RCP8.5) in 2100 | Non-retrofitted structures | Four coastal regions (Miami, New Orleans, Charleston, and New York City) |
| Case IV | Climate Change Case 1 (Oscillating frequency + high emission level = OMA + RCP8.5) in 2100 | Retrofitted structures | Four coastal regions (Miami, New Orleans, Charleston, and New York City) |

## 7.1 Selected Coastal Regions for Hurricane Loss Estimation

### 7.1.1 New Orleans

The City of New Orleans is the largest city in Louisiana and a major port of the U.S. coast. The New Orleans metropolitan area (New Orleans-Metairie-Kenner) is the 3rd largest metropolitan statistical area on the Gulf Coast and is the 46th largest in the U.S. (U.S. Census Bureau 2010). The New Orleans surrounding area was struck by many destructive hurricanes in the past. It is stated by King (2006) that “on average, one major storm crosses within 185 km (100 nautical miles) of New Orleans every decade”. Table

7.2 lists 7 historical hurricanes that affected New Orleans area. It includes Hurricane Katrina (2005), which is the costliest hurricane in the record (Blake et al. 2011); and Hurricane Camille (1969), which was the strongest landfalling tropical cyclone in the world. This record stood until 2013 when Typhoon Haiyan made landfall at the Central Philippines with a greater intensity (Smith 2013).

Table 7.2: Historical hurricanes in New Orleans area.

| Name | Year | Category at landfall (kt) | Damage ($) | Fatality (in U.S.) | Landfall location | Minimum pressure at landfall (mbar) |
|---|---|---|---|---|---|---|
| Isaac | 2012 | 70 | 2.35 billion | 5 | Port Fourchon, LA | 966 |
| Katrina | 2005 | 105 | 108 billion | 1833 (1577 in Louisiana) | Buras, LA | 928 |
| Cindy | 2005 | 65 | 320 million | 1 | Grand Isle, LA | 991 |
| Florence | 1988 | 85 | 2.5 million | 1 | Southeastern Louisiana | 984 |
| Bob | 1979 | 65 | 20 million | 1 | Grand Isle, LA | 986 |
| Camille | 1969 | 165 | 1.42 billion | 259 | Bay St Louis, MS | 905 |
| Betsy | 1965 | 120 | 1.42 billion | 81 | Grand Isle, LA | 948 |

*Damage values are given in USD in the year the hurricane occurred (not adjusted by inflation);
*All data in the Table were cited from NHC hurricane reports if no further reference is noted.

### 7.1.2 Miami

The City of Miami is located in the southeast of Florida on the Atlantic coast. It is ranked as the 7th in the U.S. and 33rd among global cities for its influence in the aspects of finance, commerce, culture, education and etc. The Miami-Fort Lauderdale-West Palm Beach metropolitan statistical area expended from the City of Miami is ranked as the 8th

populated statistical areas in the U.S. (U.S. Census Bureau 2010). Miami is exposed to the highest level of hurricane threat, as it is located close to the coastal segment that is mostly struck by hurricanes along the entire U.S. coastline. The historical hurricanes occurred in this area had great impact to the development of the City. The Great Miami Hurricane in 1926 slowed down the development of the City during the 1930s from its prosperity in the 1920s. Hurricane Andrew (1992) left widespread destructions and aftermath in social effects during the 1990s (Sainz 2002; Garrison et al. 1995). Under the influence of Hurricane Andrew, stricter building codes were proposed and drafted in 1996 by the Florida Building Code Commission (Florida Department of Business and Professional Regulation 2004). After that, the new Florida Building Code, which was assessed to effectively reduce the damage from the hurricane hazard, was established in 1998 and put into effect on 2002 (Sims 2012; Cox et al. 2006). Table 7.3 tabulates 7 historical hurricanes that affected Miami area, including Hurricane Andrew which produced the third highest wind speed at landfall in the record, and the Great Miami Hurricane which caused even more losses than Hurricane Katrina (2005) after adjusted for inflation, population and wealth (National Hurricane Center 2012; Blake et al. 2011).

Table 7.3: Historical hurricanes in Miami area.

| Name | Year | Category at landfall (kt) | Damage ($) | Fatality (in U.S.) | Landfall location | Minimum pressure at landfall (mbar) |
|---|---|---|---|---|---|---|
| Wilma | 2005 | 105 | 20.6 billion | 5 | Cape Romano, FL | 950 |
| Katrina | 2005 | 70 | 108 billion (523 million in Florida) | 1833 (14 in Florida) | Broward/Miami-Dade County line, FL | 984 |
| Irene | 1999 | 70 | 800 million | 8 (indirect) | Cape Sable, FL | 987 |
| Andrew | 1992 | 125 | 26 billion | 26 (39 indirect) | Homestead, FL | 922 |
| Frances | 2004 | 90 | 9 billion | 6 (41 indirect) | Hutchinson Island, FL | 960 |
| Jeanne | 2004 | 105 | 6.9 billion | 4 | Stuart, FL | 950 |
| Great Miami Hurricane | 1926 | 126[1] | 164,839 billion[2] (normalized in 2010 inflation, population and wealth) | 373[1] | Between Coral Gables and South Miami1 | 930[1] |

[*]Damage values are given in USD in the year the hurricane occurred (not adjusted by inflation);
[*]All data in the Table were cited from NHC hurricane reports if no further reference is noted.
[1]National Hurricane Center (2012)
[2]Blake et al (2011)

### 7.1.3 Charleston

The City of Charleston is located around the geographical midpoint of South Caroline's coastline. It is the second largest city in South Carolina and the county seat of Charleston County. It is adjacent to the third largest city in South Carolina, North Charleston, which is also included in the Charleston County. The Charleston-North Charleston metropolitan statistical area is ranked as the 78th populated statistical area in

the U.S. Among the historical hurricanes that struck Charleston area, the most well know event is Hurricane Hugo (1989), which made landfall as category IV hurricane. Hurricane Hugo's landfall occurred with the high tide during the autumnal equinox (South Carolina State Climatology Office 2014). It damaged three-quarters of the homes in Charleston's historic district and made 60,000 people homeless within the week after the hit. Besides Hurricane Hugo which is the 12$^{th}$ intense hurricanes in the history, Hurricane Gracie (1959) that made landfall near Charleston ranks 43th on the list of the most intense mainland hurricanes in the U.S. (Blake et al. 2011). The list of historical hurricanes that approached Charleston is provided in Table 7.4.

Table 7.4: Historical hurricanes in Charleston area.

| Name | Year | Category at landfall (kt) | Damage ($) | Fatality (in U.S.) | Landfall location | Minimum pressure at landfall (mbar) |
|---|---|---|---|---|---|---|
| Gaston | 2004 | 65 | 130 million | 8 | Awendaw, SC | 985 |
| Charley | 2004 | 70 | 15 billion (in 2011 USD) | 10 | Cape Romain, SC | 992 |
| Hugo | 1989 | 120 | 7 billion | 20 | Sullivan's Island, SC | 934 |
| Bob | 1985 | 65 | 20 million[1] | 5 | Beaufort, SC | 1003 |
| Gracie | 1959 | 104 | 14 million | 22 | Edisto Island, SC | - |

*Damage values are given in USD in the year the hurricane occurred (not adjusted by inflation);
*All data in the Table were cited from NHC hurricane reports if no further reference is noted.
[1]Cocke (1995)

### 7.1.4 New York

The City of New York is the most densely populated major city in the U.S. (U.S. Census Bureau, 2010). The New York-Newark-Jersey City metropolitan statistical area,

which doubles the population in the statistical area ranked in the third place, extended from the New York City is the most populated statistical area in the U.S. New York City sits by one of the largest natural harbors in North America. It consists of five boroughs, namely the Bronx, Brooklyn, Manhattan, Queens and Staten Island. According to historical hurricane statistics, tropical storm and hurricane events rarely occurred around New York (less than 1 event approached within 250km per year, Figure 4.3) compared to other parts along the U.S. coast. However, in consideration of the great population density, hurricane and hurricane induced hazards hold great threats to the City. In addition to the population, the warming SST and northerly pattern shift of tropical storm tracks in the North Atlantic Ocean due to climate change (Mudd et al. 2012; Bengtsson et al. 2006) are likely to increase the risk of hurricane strike to the City. One recent example that caused the disastrous consequence in New York City is Hurricane Sandy (2012). The destructive storm surge induced by Hurricane Sandy caused large part of the City and the surrounding area out of power for several days and part of the public transportation systems were not functional (Blake et al. 2012). Hurricane Sandy has prompted the discussion about stronger defense on the shoreline, such as seawalls, in order to protect the City from such disastrous consequence in the future (Eshelman 2012). Other hurricanes affected the New York City area in the past are listed in Table 7.5.

Table 7.5: Historical hurricanes in New York City area.

| Name | Year | Category at landfall (kt) | Damage ($) | Fatality (in U.S.) | Landfall location | Minimum pressure at landfall (mbar) |
|---|---|---|---|---|---|---|
| Sandy | 2012 | 70 | At least 50 billion | 72 | Brigantine, NJ | 945 |
| Irene | 2011 | 55 | 15.8 billion | 41 | Coney Island, Brooklyn, NY | 965 |
| Bob | 1999 | 100 | 1.5 billion | 15 | Block Island, RI | 950 |
| Gloria | 1985 | 75 | 1 billion | 11 | Western Long Island, NY | 961 |
| Belle | 1976 | 65 | 100 million | 5 (indirect)[1] | Long Island, NY | 980 |
| Donna | 1960 | 87 | 3.35 billion | 50 | Long Island, NY | - |
| Carlo | 1954 | 109 | 462 million | 72 | Eastern Long Island, NY | 960 |

*Damage values are given in USD in the year the hurricane occurred (not adjusted by inflation);
*All data in the Table were cited from NHC hurricane reports if no further reference is noted.
[1]Associated Press. (1976).

## 7.2 Methodology and Application of HAZUS Program

HAZUS-MH program employs a system of methodology called "hazard-load-resistance-damage-loss" in its hurricane loss estimation module (FEMA 2012). There are five key components in the modeling framework: hurricane hazard model, surface roughness model, wind load model, damage model and loss model (Vickery et al 2006a; Vickery et al 2006b). The modeling and simulation techniques that were used to develop the damage states and loss functions in HAZUS are involved with the concepts of structural reliability and probabilistic tools. To determine the damage state of the entire building, the damage condition on each building component/element (e.g. roof coverings, roof-to-wall connections, openings and etc.) is evaluated. The failure probability of the

single element is determined by the integration of the resistance of the element and the demand from the wind hazard:

$$P_f = P(R - S < 0) = \int_{-\infty}^{\infty} F_R(x) f_s(x) dx \tag{33}$$

where $R$ is the structural resistance; $S$ is the hazard demand; $F_R$ is the cumulative distribution function of resistance smaller than the load effect $x$; and $f_s$ is the probability density function of load effect $x$. In other words, the failure or damage probability is the probability that the wind load effect (e.g., pressure or impact) is greater than the resistance of the element.

On completion of examining the damage on each element, their consequences are assembled and treated as probabilistically independent events to determine the overall failure probabilities of the building systems. Damage state is assessed based on the percentages of damage in the building systems and the degrees of function losses. Damage state categories include no damage or very minor damage, minor damage, moderate damage, severe damage and destruction.

The following steps were conducted in the application of HAZUS program to calculate losses, from selecting hurricane events to exporting the loss estimation results:

1) Define the region of study

HAZUS performs loss estimation on multiple categories of regions: census tract, county and state. All the information required for damage and loss estimation, such as population, exposure values, loss functions and etc., are prepared in advance in HAZUS and extracted according to the selection of regions. The data are assembled from the

census block level, which contains information from the 2000 Census Bureau data (FEMA 2012).

2) Import the hazard scenario into the selected study region in HAZUS

Hazard scenario refers to the hurricane event which contains the time history of the key hurricane parameters. The key parameters are in similar format as those recorded in HURDAT.

3) Evaluate wind speeds

Wind speeds due to the imported event are calculated in the selected region using the built-in wind speed model and the surface roughness information.

4) Loss estimation using fast running damage and loss functions

Fast running damage and loss functions for different building types are saved in the HAZUS database to quickly evaluate damage and loss from wind speeds. There are thousands of loss functions available in HAZUS. Each of them corresponds to a structural type and a specific combination of building configurations. For example, Figure 7.1 shows a typical loss function of a one-story wood single-family house (WSF1). Using loss function, the loss ratio can be easily obtained by giving wind speed. The value of direct economic loss equals to the product of loss ratio and the total building exposure value. In addition to the loss functions for damage on the exterior of the building (Figure 7.1), the loss functions for damages on building contents are also available in the same format. In parallel, wind speeds are applied to the wind born debris model to estimate the glazing damage due to the missile impact.

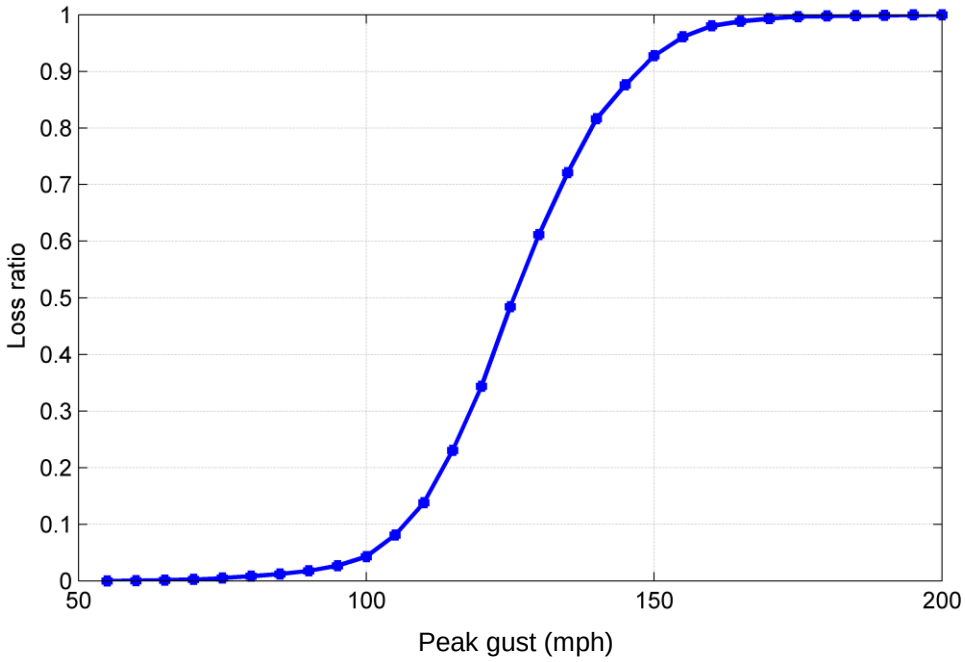


Figure 7.1: Loss function of single-family, one-story, wood, residential building (WSF1) (FEMA 2012).

Based on the framework of the "hazard-load-resistance-damage-loss" methodology, the mitigation module in HAZUS allows users to adjust for the mitigation ratio in building configurations and assess the reduced loss in the study region (FEMA 2012; Vickery et al 2006b). Changes due to the adoption of the mitigation will reflect accordingly on the damage state functions and loss functions. The mitigation options for residential building, which is the major building type in the four selected regions, include installation of window protections (i.e. shutters), upgrade of roof-to-wall connections (i.e. from toe-nails to straps), upgrade of roof deck attachment and installation of secondary water resistance.

1) Installation of window protections

Shutter is a type of opening protection and serves as the minimal level of mitigation compared to other types of opening protection. Opening protections like shutters have significant effect on building damage and loss mitigation. Generally, it contributes in two ways: *1*. It prevents the breach of building envelope occurring with broken window or door. Once breaches are formed, the positive pressure from inside of the building becomes additional load on the building envelope and puts the building into overload situation. *II*. It reduces the building content loss due to water intrusion when the openings fail. At least, functional shutters can protect the openings as rain screens and reduce the water leakage into the building (Applied Research Associates 2008b). In the existing building configuration profiles, only a small portion of the residential buildings in the four regions have equipped with shutters. In the mitigation cases, all residential buildings were modified to install shutters and the reduction in loss was investigated.

2) Upgrade of roof-to-wall connections

In the loading path of the structure, roof-to-wall strap as one of the types of roof-to-wall connections transfers the uplift load from the roof to the wall. It strengthens the building's integrity against wind load on the building envelope. In the mitigation cases of this study, the toe-nails as a type of roof-to-wall connection of low efficiency were replaced by metal straps in all residential buildings. Testing results showed that both the typical design strength and the ultimate strength of straps are over twice as those of the toe-nails (FEMA 2012; Applied Research Associates 2008b).

3) Upgrade of roof deck attachment

The mechanisms to fasten the roof deck to roof frame and prevent roof deck from uplift failure in high winds are the nail fasteners. The resistance of a nail is determined by the nail size, type, spacing, and penetration depth into the truss or rafter (Applied Research Associates 2008b). In the mitigation cases of this study, retrofits on the roof deck attachment were applied by upgrading the nails to 8d at 6”/6” spacing from the existing types including 6d at 6”/12” and 8d at 6”/12”. Studies indicated that the uplift capacity of 8d nails is doubled of that from 6d nails at the same spacing (FEMA 2012). It is beneficial for the building performance against high winds.

4) Installation of secondary water resistance

Secondary water resistance prevents rain from entering the interior of the house once the roof cover fails (Applied Research Associates 2008b). It is a layer of protection sealed on the roof deck and there are a variety of products of this kind. In the mitigation cases, secondary water resistance was applied to all residential buildings while it was rarely applied to the existing buildings in the four regions.

## 7.3 Configurations of Regional Vulnerability and Exposure in HAZUS Program

### 7.3.1 New Orleans

For loss estimation purpose, the Orleans Parish, which is coterminous with the City of New Orleans, was selected as the enclosure to quantify the damages and losses (Figure 7.2). The Orleans Parish is 350 square miles in size and contains 181 census tracts based on the built-in inventory data in HAZUS. This region contains a population of 484,674 people (2000 Census Bureau data). There are approximately 172,000 buildings in this region with a total building replacement value of 35 billion dollars (in

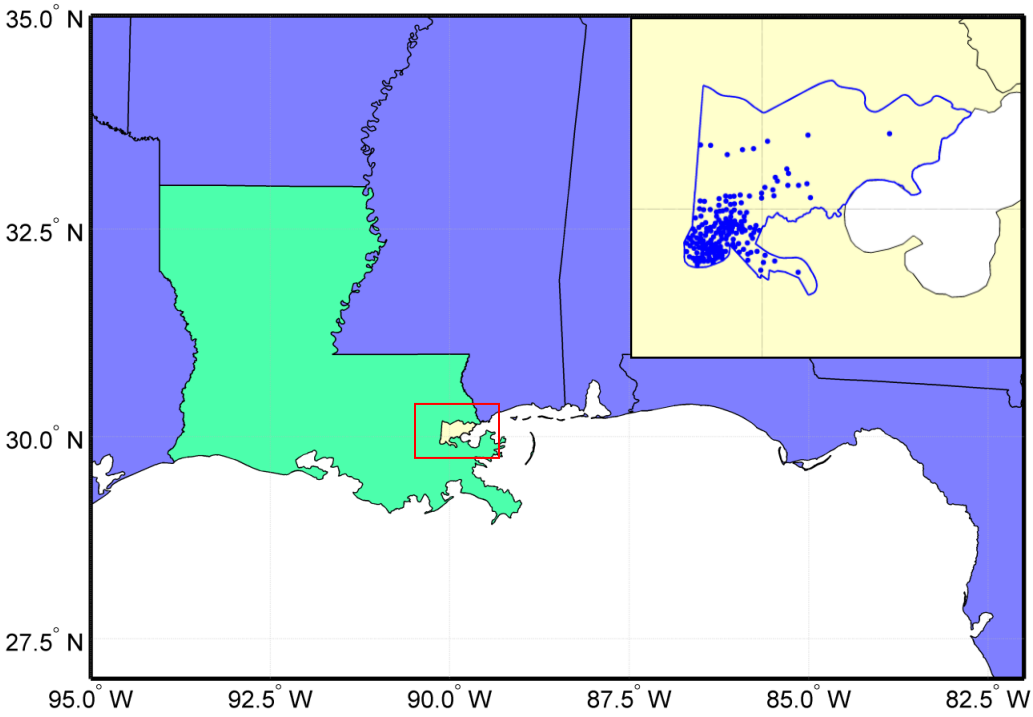


Figure 7.2: Region of the Orleans County in the loss estimation study and locations of census tracts.

2006 USD). About 93% of the buildings are residential buildings (Table 7.6). In the mitigation cases, retrofits were applied to residential buildings including single-family dwellings, multi-family dwellings, manufactured homes and residential engineered buildings. In the group of residential buildings, the most common specific building types are wood one-story single family house, wood two-or-more-story single family house and wood multi-unit two-story house (Table 7.7). The configurations of these three types of buildings before and after retrofit are given in Appendix J.

Table 7.6: Building number counts in occupancy classes of Orleans Parish

| Occupancy | Number Counts | Percentage of Total building (%) |
|---|---|---|
| Residential | 159,652 | 92.6 |
| Commercial | 9,272 | 5.4 |
| Industrial | 1,537 | 0.9 |
| Agriculture | 174 | 0.1 |
| Religion | 1,076 | 0.6 |
| Government | 368 | 0.2 |
| Education | 391 | 0.2 |

Table 7.7: Main building types for the region of Orleans Parish

| Building Type Code | Description | Number Counts | Percentage of Total building (%) |
|---|---|---|---|
| WSF1 | Wood, Single-Family, One-Story | 68616 | 39.8 |
| WSF2 | Wood, Single-Family, Two or More Stories | 40301 | 23.4 |
| WMUH2 | Wood, Multi-Unit Housing, Two Stories | 19308 | 11.2 |

- List all building types that occupy more than 75% of total building counts.

### 7.3.2 Miami

Miami Dade County was selected as the enclosure to quantify the damages and losses (Figure 7.2) on the Atlantic coast of Florida. The area of Miami Date County is 1,983.7 square miles and contains 347 census tracts based on the built-in data in HAZUS. There is a population of 2,253,362 people (2000 Census Bureau data). There are about 776,000 buildings in this region with the total building replacement value of 150 billion dollars (in 2006 USD). About 88% of the buildings are residential buildings (Table 7.8). In the mitigation cases, retrofit was applied to residential buildings. The mostly seen building types that belong to residential use are masonry one-story single-family house, wood one-story single-family house, masonry two or more stories single-family house, wood multi-unit two stories house and wood two or more stories single-family house

(Table 7.9). The configurations of these types of building before and after retrofit are listed in Appendix J.

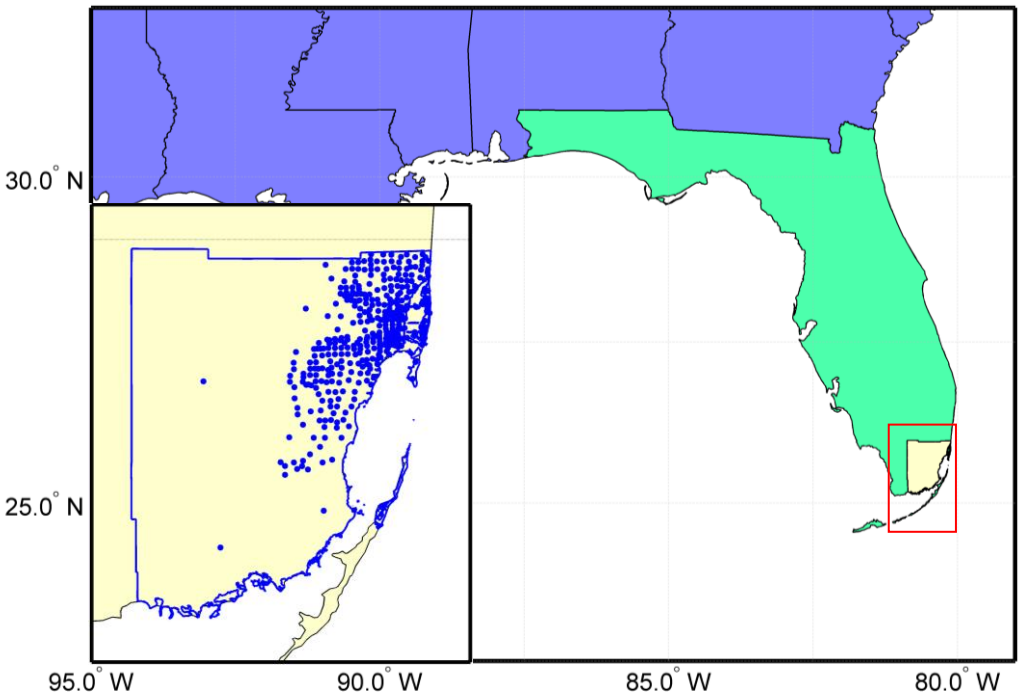


Figure 7.3: Region of the Miami Dade County in the loss estimation study and locations of census tracts.

Table 7.8: Building number counts in occupancy classes of Miami, FL

| Occupancy | Number Counts | Percentage of Total building (%) |
|---|---|---|
| Residential | 581279 | 87.6 |
| Commercial | 59787 | 9 |
| Industrial | 13421 | 2 |
| Agriculture | 2932 | 0.4 |
| Religion | 4137 | 0.6 |
| Government | 772 | 0.1 |
| Education | 1414 | 0.2 |

Table 7.9: Main building types for the region of Miami, FL

| Building Type Code | Description | Number Counts | Percentage of Total building (%) |
|---|---|---|---|
| MSF1 | Masonry, Single Family, One Story | 277883 | 41.9 |
| WSF1 | Wood, Single Family, One Story | 83693 | 12.6 |
| MSF2 | Masonry, Single Family, Two or More Stories | 56929 | 8.6 |
| WMUH2 | Wood, Multi-Unit Housing, Two Stories | 36012 | 5.4 |
| WSF2 | Wood, Single Family, Two or More Stories | 35874 | 5.4 |
| SECBL | Steel, Engineered Commercial Building, Low-Rise (1-2 Stories) | 28603 | 4.3 |

- List all building types that occupy more than 75% of total building counts.

### 7.3.3 Charleston

Charleston County which encloses the 2nd and 3rd largest city in South Carolina was selected to quantify the damages and losses (Figure 7.4). The area of Charleston County is 943.25 square miles and contains 78 census tracts based on the built-in data in HAZUS. There is a population of 309,969 people (2000 Census Bureau data). There are about 136,000 buildings in this region with the total building replacement value of 23 billion dollars (in 2006 USD). About 91% of the buildings are residential buildings (Table 7.10). In the mitigation cases, retrofit was applied to residential buildings. The mostly seen specific building types that belong to residential use are wood one-story single-family house, wood two or more stories single-family house , wood multi-unit two stories house, Manufactured home (1976 HUD) and masonry one-story single-family house (Table 7.11). The configurations of these types of building before and after retrofit are listed in Appendix J.

Table 7.10: Building number counts in occupancy classes of Charleston, SC

| Occupancy | Number Counts | Percentage of Total building (%) |
|---|---|---|
| Residential | 124,449 | 91.2 |
| Commercial | 8,042 | 5.9 |
| Industrial | 2,202 | 1.6 |
| Agriculture | 475 | 0.3 |
| Religion | 739 | 0.5 |
| Government | 226 | 0.2 |
| Education | 276 | 0.2 |

Table 7.11: Main building types for the region of Charleston, SC

| Building Type Code | Description | Number Counts | Percentage of Total building (%) |
|---|---|---|---|
| WSF1 | Wood, Single Family, One Story | 51835 | 38 |
| WSF2 | Wood, Single Family, Two or More Stories | 30443 | 22.3 |
| WMUH2 | Wood, Multi-Unit Housing, Two Stories | 9379 | 6.9 |
| MH76HUD | Manufactured Home, 1976 HUD | 7273 | 5.3 |
| MSF1 | Masonry, Single-Family, One-Story | 5722 | 4.2 |

- List all building types that occupy more than 75% of total building counts.

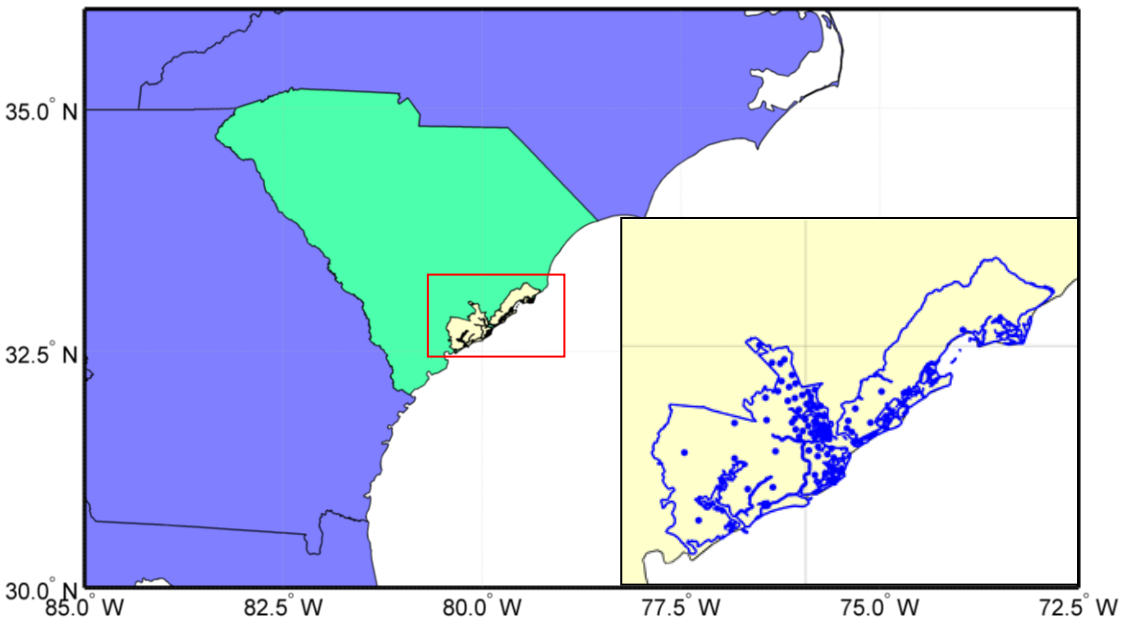


Figure 7.4: Region of the Charleston County in the loss estimation study and locations of census tracts.

### 7.3.4 New York

The City of New York is composed of five boroughs: the Bronx, Brooklyn, Manhattan, Queens and Staten Island. Each borough has the same boundary as a county in the New York. These five counties together were defined as the region of study in HAZUS (Figure 7.5). The area of New York City is 304.47 square miles and contains 2,216 census tracts based on the built-in data in HAZUS. The population in this region is 8,008,278 people (2000 Census Bureau data). There are about 3,021,000 buildings in this region with the total building replacement value of 650 billion dollars (in 2006 USD). About 86% of the buildings are residential buildings (Table 7.12). In the mitigation cases, retrofit was applied to residential buildings. The mostly seen specific building types that belong to residential use are wood one-story single-family house, wood two or more

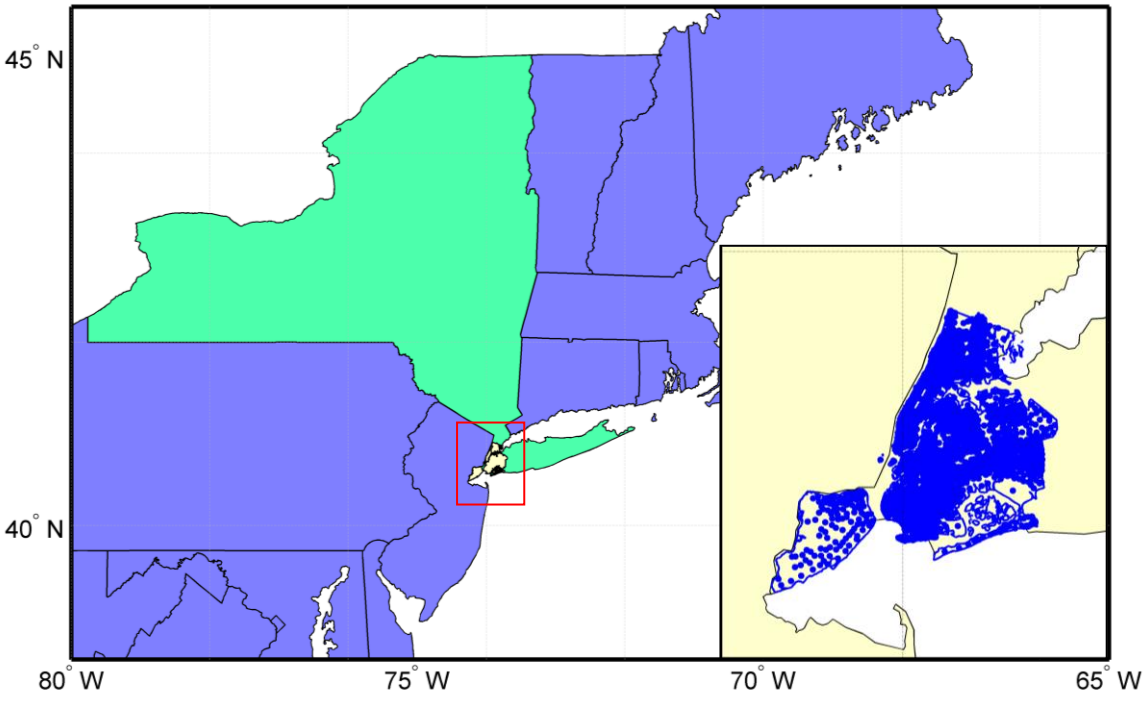


Figure 7.5: Region of the New York City in the loss estimation study and locations of census tracts.

stories single-family house, wood multi-unit two stories house, wood multi-unit three or more stories house, masonry multi-unit two stories house and steel low-rise engineered commercial building (Table 7.13). The configurations of these types of building before and after retrofit are listed in Appendix J.

Table 7.12: Building number counts in occupancy classes of New York City

| Occupancy | Number Counts | Percentage of Total building (%) |
|---|---|---|
| Residential | 931389 | 86.4 |
| Commercial | 104190 | 9.7 |
| Industrial | 23890 | 2.2 |
| Agriculture | 2932 | 0.4 |
| Religion | 4137 | 0.6 |
| Government | 772 | 0.1 |
| Education | 1414 | 0.2 |

Table 7.13: Main building types for the region of New York City

| Building Type Code | Description | Number Counts | Percentage of Total building (%) |
|---|---|---|---|
| WSF1 | Wood, Single Family, One Story | 270496 | 25.1 |
| WSF2 | Wood, Single Family, Two or More Stories | 187916 | 17.5 |
| WMUH2 | Wood, Multi-Unit Housing, Two Stories | 157631 | 14.7 |
| WMUH3 | Wood, Multi-Unit Housing, Three or More Stories | 62553 | 5.8 |
| MMUH2 | Masonry, Multi-Unit Housing, Two Stories | 61793 | 5.7 |
| SECBL | Steel, Engineered Commercial Building, Low-Rise (1-2 Stories) | 54125 | 5 |
| WMUH1 | Wood, Multi-Unit Housing, One Story | 50893 | 4.7 |

- List all building types that occupy more than 75% of total building counts.

## 7.4 Hurricane Event Selection for Loss Estimation

In order to perform loss estimation with hurricane events for various MRI levels, two synthetic hurricane databases each containing 200,000-year events were prepared using the simulation model discussed in Chapter Three and Five for no climate change scenario and Climate Change Case 1 in 2100 (Table 7.1), respectively. The 200,000-year simulations were divided into 10 bins, each of which contains 20,000-year simulaitons. Hurricane events representing 50, 100, 300, 700 and 1700 years MRI hazard levels were selected from each bin. Thus, for each MRI level there are 10 events from no climate change case and Climate Change Case 1, respectively. Based on the hurricane event selection methodology introduced in Chapter Six, a weighted MRI (WMRI) technique was developed to select events with regional effect on each census tract in the region. In Pei et al. (2013), the WMRI for each event is calculated from the MRI of a point and weighted using the factor of population at that point:

$$WMRI_i = \sum_{j=1}^{m} \frac{P_j}{\Sigma P} MRI_{i,j} \tag{34}$$

where $WMRI_i$ is the weighted MRI value of candidate hurricane $i$; $P_j$ is the population of point $j$; $\Sigma P$ is the total population of all the point locations; and $m$ is the total number of points in the loss estimation domain. On top of the conventional definition for MRI or return period, which describes the likelihood of occurrence for events above certain threshold (i.e., wind speed, ground acceleration), the impact on regions with large population is emphasized and the importance of potential fatality loss is highlighted in the quantification of MRI. In other words, the criterion to estimate the hazard level is not

limited to one single quantity but to consider the impact of the event. The WMRI describes the likelihood of events holding certain level of impact to the region of study. In order to emphasize the effect of the exposure to economic loss, the population term in Eqn.(34) is replaced by exposure *E* (building replacement value) at every census tract:

$$WMRI_i = \sum_{j=1}^{m} \frac{E_j}{\Sigma E} MRI_{i,j} \tag{35}$$

For each event, its resultant wind speed is evaluated at every census tract in the study region (i.e. Figure 7.2 to 7.5). For each census tract, the MRI curves were developed using the procedure introduced in Chapter Six and a MRI value was assigned to each hurricane event affecting the region. It should be noted that, the MRI values resulted from the same event may be found different at different locations. These point MRIs at the census tracts were put into Eqn. (35) to evaluate the weight MRI for the entire region. The events that produced WMRI of 50, 100, 300, 700 and 1700 years were selected for the four coastal regions. Ten events were selected for each WMRI level from the baseline case and Climate Chang Case 1, respectively.

As mentioned above, HAZUS, which is a complete risk assessment package, includes a wind speed calculation component. To validate the consistency between wind speeds from HAZUS and the wind speeds from the simulation program, comparisons on the maximum wind speeds produced by the two models in the selected regions were plotted in Figure 7.6 and 7.7. The wind speeds calculated using HAZUS model were used for loss estimation and the wind speeds evaluated in the simulation program were used to calculate WMRI. The consistency between the two sets of wind speeds is critical to

ensure the events selected by wind speeds would represent the same level of impact in loss estimation. The $R^2$ values between the two sets of wind speeds were evaluated for each region. The $R^2$ here refers to the coefficient of determination between the wind field model used in this study and that of the HAZUS:

$$R^2 = 1 - \frac{\sum_i \left( v_{HAZUS_i} - v_{model} \right)^2}{\sum_i \left( v_{HAZUS_i} - \bar{v}_{HAZUS} \right)^2} \tag{36}$$

All the $R^2$ values for both sets of events from baseline simulation and climate change case are higher than 0.8, which indicates a good agreement between two different wind speed models.

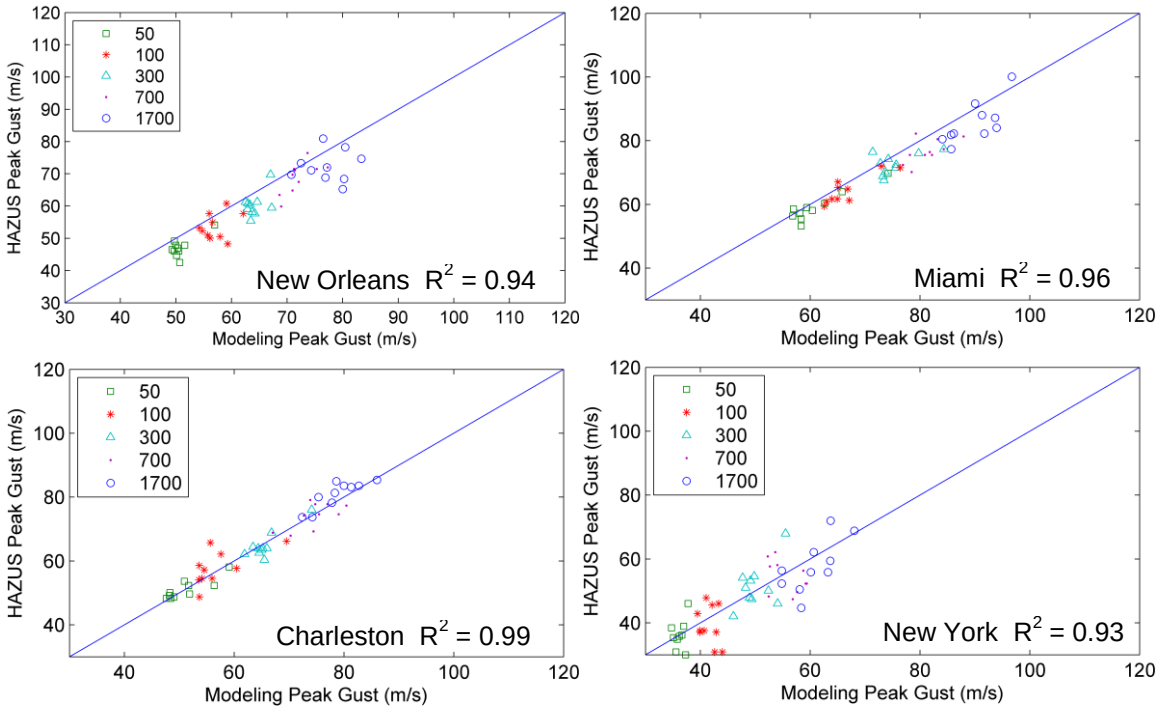


Figure 7.6: Maximum surface winds from baseline simulation model versus wind speeds from HAZUS.

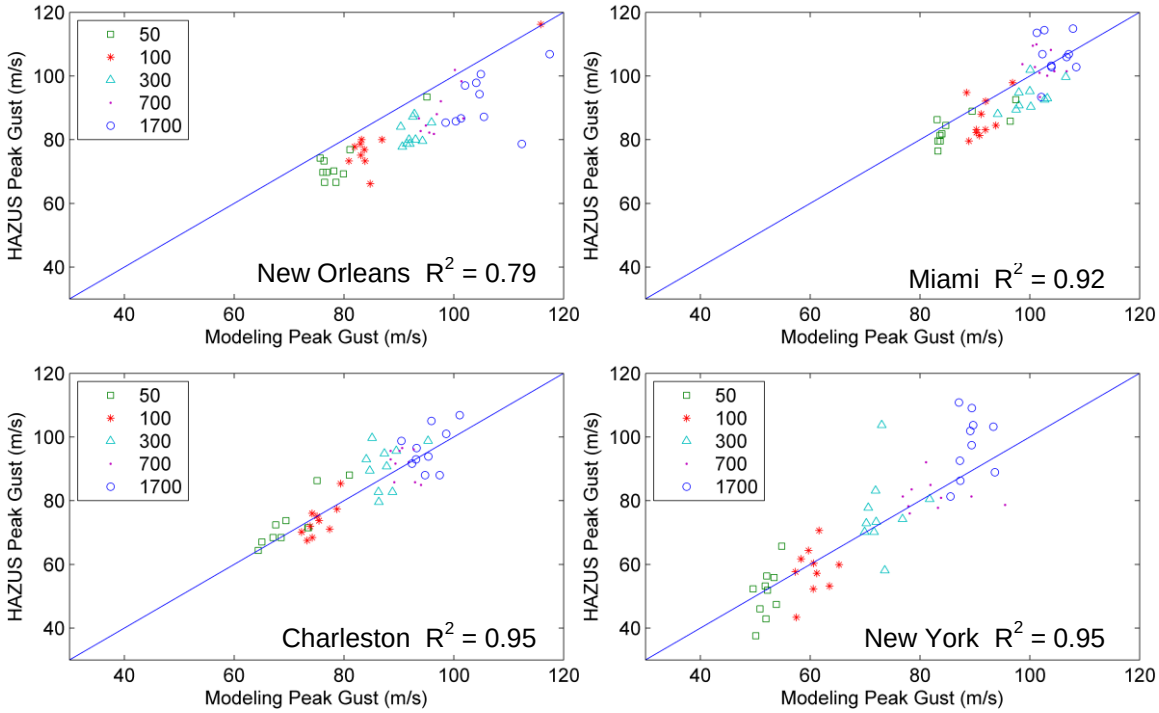


Figure 7.7: Maximum surface winds from simulation model with climate change scenario versus wind speeds from HAZUS.

## 7.5 Hurricane Induced Loss Estimation Results

The loss estimation results from the four coastal regions were evaluated in HAZUS based on the four cases defined earlier (see Table 7.1). The losses in Figure 7.8 to 7.11 are direct property losses which refer to the replacement values of the damaged parts. From the loss estimation results, it can be concluded that:

1) As expected, the mean values of property losses in all four regions increase with the increase of MRIs. This is because the higher the MRI ranked, the more rarely the event is likely to occur, and the more severe impact the event can pose to the region of study.

2) For the comparisons between the retrofitted and non-retrofitted cases no matter with or without climate change, it is obvious that the retrofit configurations efficiently reduced the amounts of damages produced by the same events in all MRI levels. The percentages of damages reduced due to retrofits on the structures were calculated and listed in Table 7.14. The percentages of damages reduced in the non-climate change case were found first increased with the rise of MRIs and then decreased after reaching the peak at the MRI of 300 years for all the four coastal areas expect New York. It indicates that the effect of retrofit is most efficient for 300-year MRI events. This phenomenon is subject to the difference of building behavior between the original and the retrofitted configurations against wind pressure. In other words, it is determined by the shapes of loss functions which describe the structural behaviors against extreme wind

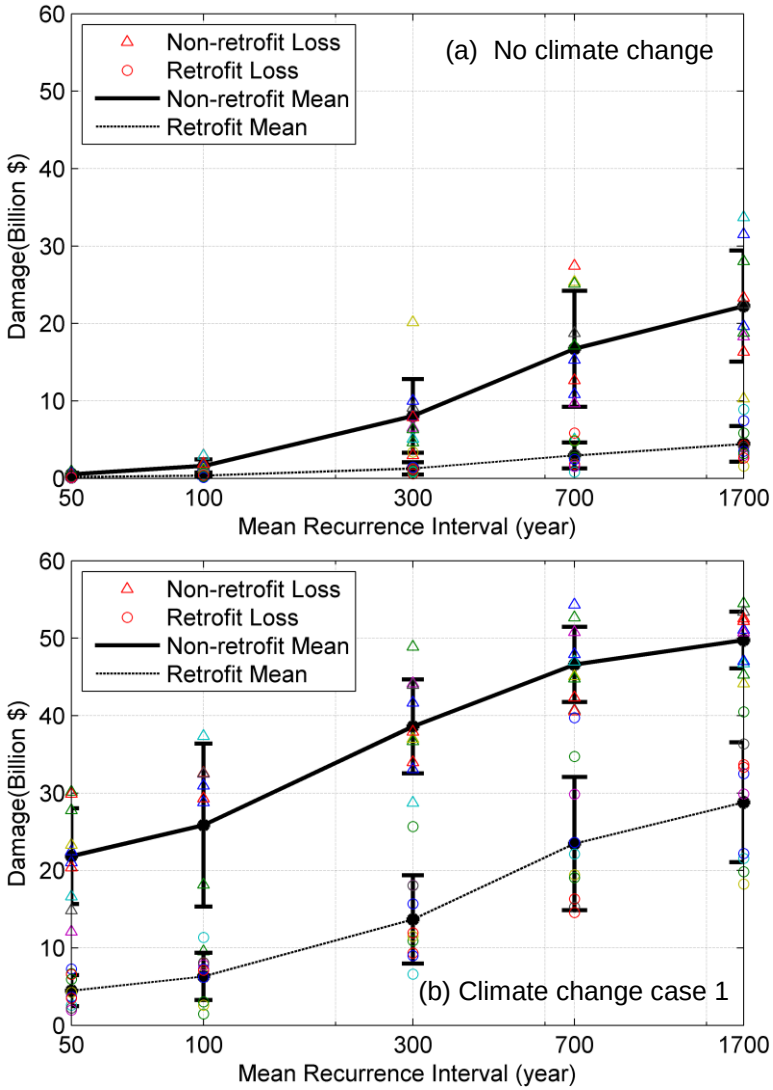


Figure 7.8: Direct property damage losses in Orleans Parish from baseline and Climate Change Case 1 simulation.

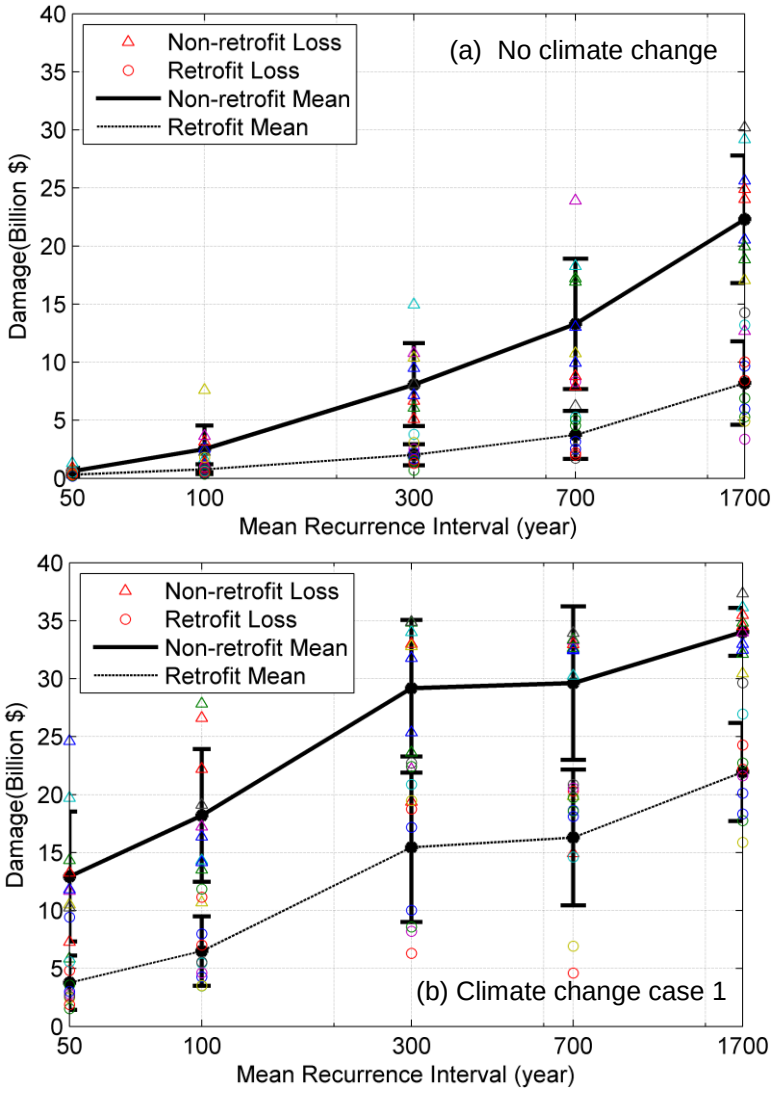


Figure 7.9: Direct property damage losses in Charleston County from baseline and Climate Change Case 1 simulation.

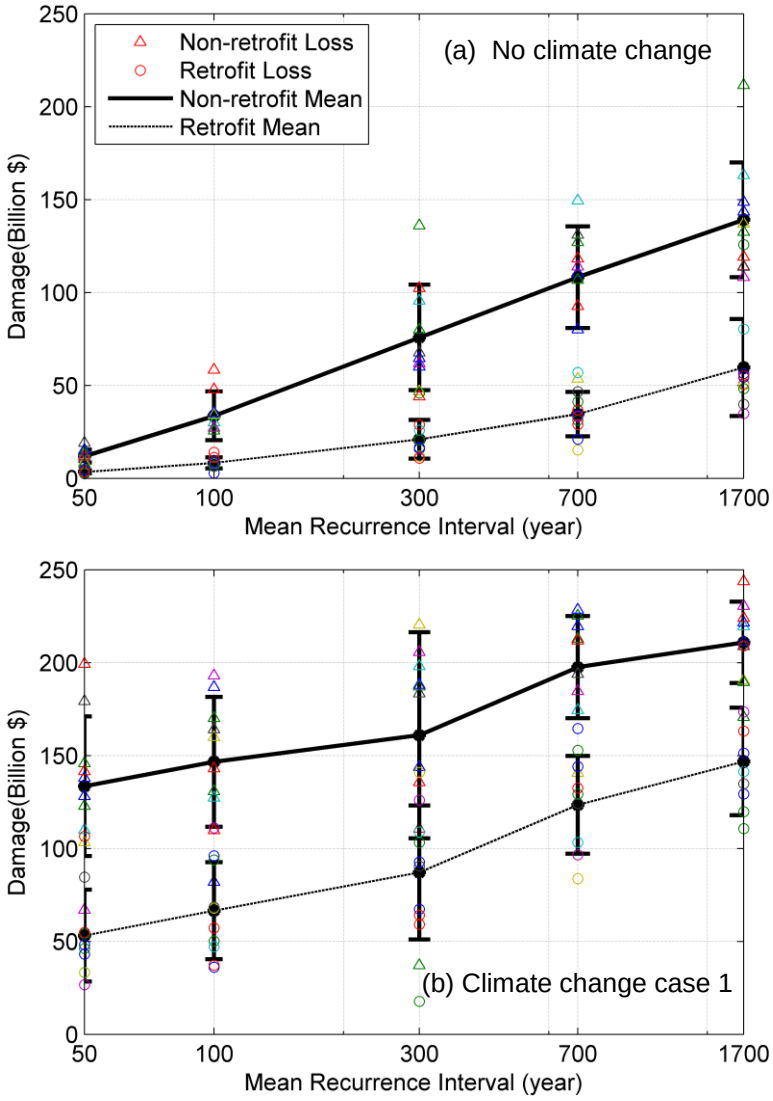


Figure 7.10: Direct property damage losses in Miami Dade County from baseline and Climate Change Case 1 simulation.

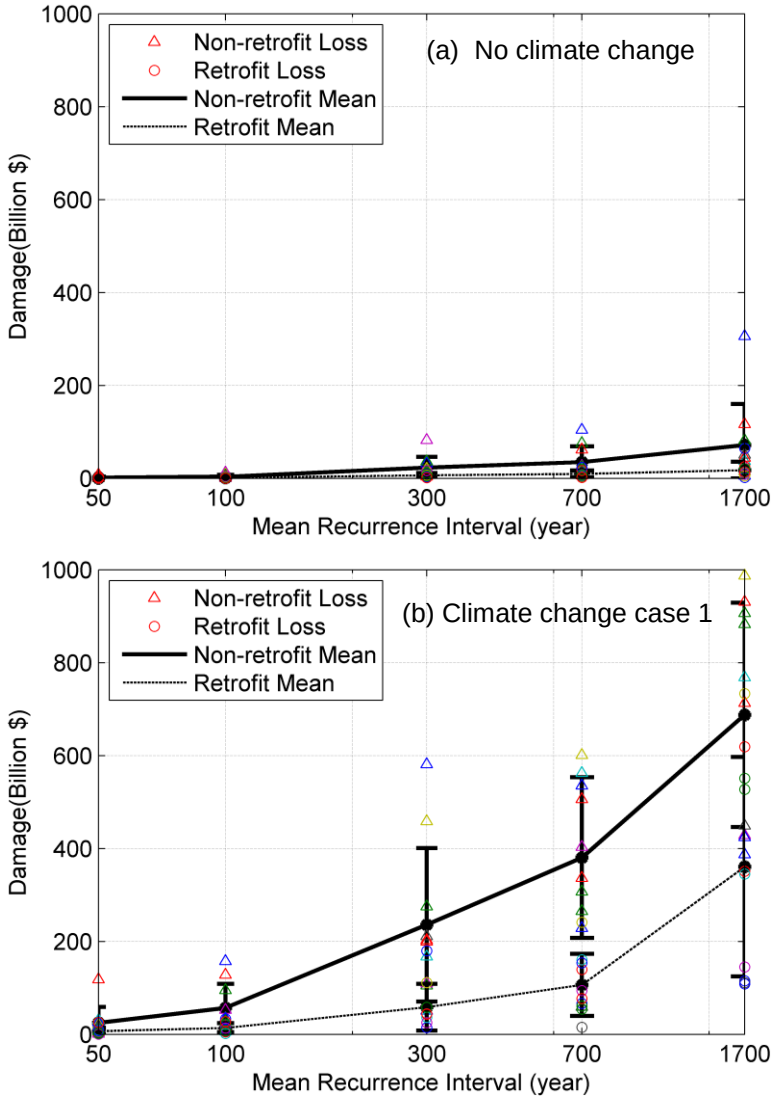


Figure 7.11: Direct property damage losses in New York City from baseline and Climate Change Case 1 simulation.

pressure before and after retrofit is applied. A more detailed explanation is given in Figure 7.12. Figure 7.12 provides the typical loss functions for one-story (WSF1) and two-story single-family wood residential buildings (WSF2) before and after the retrofit is applied. To examine the effect of retrofit, the changes in loss ratio for the non-climate change case are presented on Figure 7.12. Take New Orleans as an example. It is found from Figure 7.6 that the average values of the maximum wind speeds are 50 m/s (114 mph), 58 m/s (130 mph), 65 m/s (145 mph), 74 m/s (166 mph) and 81 m/s (181 mph) for 50, 100, 300, 700 and 1,700-year MRIs, respectively, in New Orleans for the non-climate change case. The loss ratios for these wind speeds were found from the loss curves for both non-retrofit and retrofitted cases. Shown as vertical distances between the loss curves, the largest decrease in loss ratio from the original structure to the retrofitted structure occurred at around 700-year and 300-year MRIs for WSF1 and WSF2, respectively. As two types of the most common buildings in New Orleans (63% of total building counts, see Table 7.6), the loss curves for WSF1 and WSF2 are representative for the building behaviors in this region. Thus, the dramatic decrease in the loss curves implies the effective increase in the resistance against wind pressure; and the increased resistance further results in the reduction in damage and loss. This is consistent with the percentage of loss reduced in Table 7.14 for the non-climate change case in New Orleans that the greatest reduction in loss was caused by the hurricane with a 300-year MRI. The loss functions also explain the percentages of reduction in New York. These percentages increase with MRIs and are in a different trend with those from the other three regions. This is because the wind speeds from the no-climate change case for all MRI levels in

New York are lower than the wind speed corresponding to the maximum difference between the loss curves (i.e. 160 mph for WSF1 and 145 mph for WSF2 in Figure 7.13). The variation of the reduced percentage loss in the climate change case can also be explained in the same way by examining the shapes of the loss functions.

Table 7.14: Percentage of damage reduced due to the retrofit configurations.

| Location | Loss estimation case | Percentage of damage reduced for MRIs (%) | | | | |
|---|---|---|---|---|---|---|
| | | 50 | 100 | 300 | 700 | 1700 |
| New Orleans | Non-climate change | 67.5 | 77.6 | 84.2 | 82.4 | 80 |
| | Climate Change Case II | 79.5 | 75.6 | 64.6 | 49.6 | 42.1 |
| Miami | Non-climate change | 70.8 | 75.3 | 72.4 | 68.1 | 57.1 |
| | Climate Change Case II | 60.2 | 54.6 | 45.9 | 37.5 | 30.4 |
| Charleston | Non-climate change | 49.3 | 69.1 | 74.8 | 71.9 | 63.2 |
| | Climate Change Case II | 70.8 | 64.3 | 47 | 45 | 35.5 |
| New York | Non-climate change | 65.9 | 64.7 | 71.2 | 72.6 | 75.5 |
| | Climate Change Case II | 72.4 | 75.7 | 75.3 | 72 | 47.5 |

Table 7.15: Times of increase in loss from non-climate change case to Climate Change Case 1.

| Location | Loss estimation case | Times of increase in loss due to climate change | | | | |
|---|---|---|---|---|---|---|
| | | 50 | 100 | 300 | 700 | 1700 |
| New Orleans | No-retrofit | 41.3 | 15.2 | 3.8 | 1.8 | 1.2 |
| | Retrofit | 25.6 | 16.7 | 9.8 | 7.0 | 5.5 |
| Miami | No-retrofit | 10.2 | 3.4 | 1.1 | 0.8 | 0.5 |
| | Retrofit | 14.3 | 7 | 3.2 | 2.6 | 1.5 |
| Charleston | No-retrofit | 20 | 6.2 | 2.6 | 1.2 | 0.5 |
| | Retrofit | 11.1 | 7.3 | 6.6 | 3.4 | 1.7 |
| New York | No-retrofit | 17.6 | 15.9 | 9.3 | 9.9 | 8.6 |
| | Retrofit | 14 | 10.7 | 7.8 | 10.1 | 19.5 |

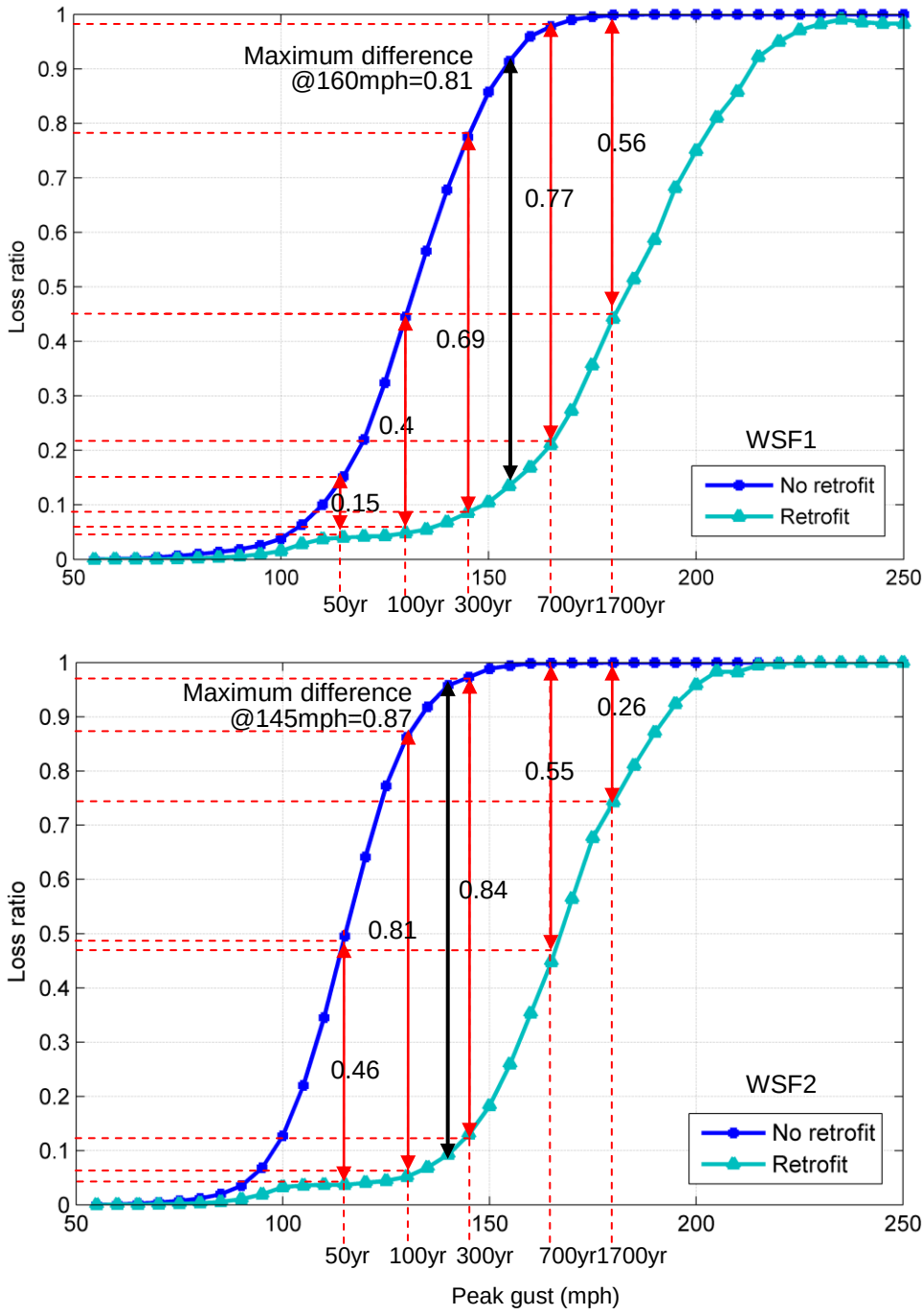


Figure 7.12: Loss function of single-family one-story wood residential building (WSF1) and single-family two-story wood residential building (WSF2).

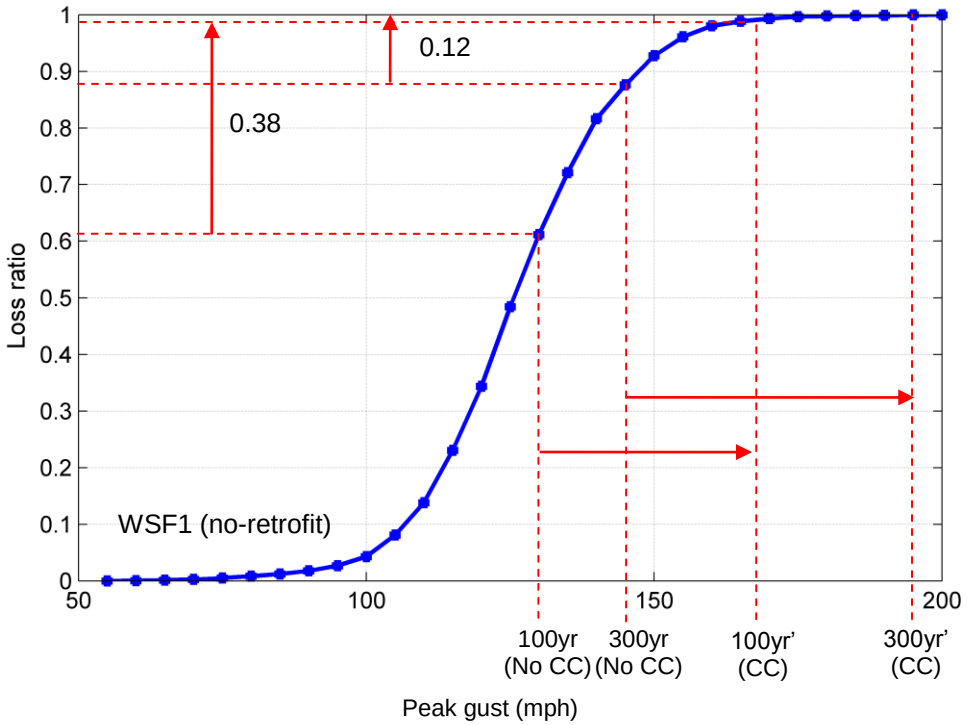


Figure 7.13: Loss function of single-family one-story wood residential building (WSF1).

3) For the comparison between the same building vulnerability levels, the events from Climate Change Case 1 (Figure 7.8b to 7.11b) produced larger damage than the events from the non-climate change case (Figure 7.8a to 7.11a). As the damage ratio is proportional to wind pressure on building envelope, the events from climate change case, which are more intensive in wind speed, resulted in more destructive consequences than those events from the non-climate change case. The times of amplifications in loss from no-climate change case to climate change case are listed in Table 7.15 (loss value in climate change case / loss value in no-climate change case -1). In Table 7.16, the direct property losses were divided by the total building exposure values in the regions. Dramatic increase (shown as "difference" in Table 7.16) in losses (30% to 80%) was

caused by climate change effect, as the loss ratios are apparently higher in climate change cases than no climate change cases. The magnitude of difference in loss ratio is proportional to the difference in the wind speed and it is determined by the shape of the loss function. As shown in Figure 7.13, the increases in loss ratio for MRIs of 100 years and 300 years with and without climate change effect are determined for WSF1 in Charleston County.

Table 7.16: Direct economic loss in percentage of total exposure.

| Location | Loss estimation case | | Percentage of total exposure (%) | | | | |
|---|---|---|---|---|---|---|---|
| | | | 50 | 100 | 300 | 700 | 1700 |
| New Orleans | No-retrofit | Non-CC | 1.5 | 4.5 | 22.9 | 47.6 | 63.3 |
| | | CC | 62.2 | 73.6 | 109.9 | 132.7 | 141.7 |
| | | **Difference** | **60.7** | **69.1** | **87** | **85.1** | **78.3** |
| | Retrofit | Non-CC | 0.5 | 1 | 3.6 | 8.4 | 12.7 |
| | | CC | 12.7 | 18 | 39 | 66.8 | 82 |
| | | **Difference** | **12.3** | **16.9** | **35.3** | **58.4** | **69.4** |
| Miami | No-retrofit | Non-CC | 7.9 | 22.3 | 50.4 | 71.9 | 92.4 |
| | | CC | 88.6 | 97.4 | 106.9 | 131.2 | 140.1 |
| | | **Difference** | **80.7** | **75.1** | **56.5** | **59.3** | **47.7** |
| | Retrofit | Non-CC | 2.3 | 5.5 | 13.9 | 22.9 | 39.6 |
| | | CC | 35.3 | 44.2 | 57.8 | 82 | 97.5 |
| | | **Difference** | **33** | **38.7** | **43.9** | **59** | **57.9** |
| Charleston | No-retrofit | Non-CC | 2.7 | 10.9 | 34.9 | 57.6 | 96.7 |
| | | CC | 56 | 78.9 | 126.5 | 128.4 | 147.5 |
| | | **Difference** | **53.4** | **68** | **91.5** | **70.8** | **50.9** |
| | Retrofit | Non-CC | 1.4 | 3.4 | 8.8 | 16.2 | 35.6 |
| | | CC | 16.3 | 28.2 | 67 | 70.7 | 95.2 |
| | | **Difference** | **15** | **24.8** | **58.2** | **54.5** | **59.6** |
| New York | No-retrofit | Non-CC | 0.2 | 0.5 | 3.5 | 5.4 | 11 |
| | | CC | 3.8 | 8.7 | 36.3 | 58.5 | 105.8 |
| | | **Difference** | **3.6** | **8.2** | **32.8** | **53.2** | **94.8** |
| | Retrofit | Non-CC | 0.1 | 0.2 | 1 | 1.5 | 2.7 |
| | | CC | 1.1 | 2.1 | 9 | 16.4 | 55.5 |
| | | **Difference** | **1** | **1.9** | **8** | **14.9** | **52.8** |

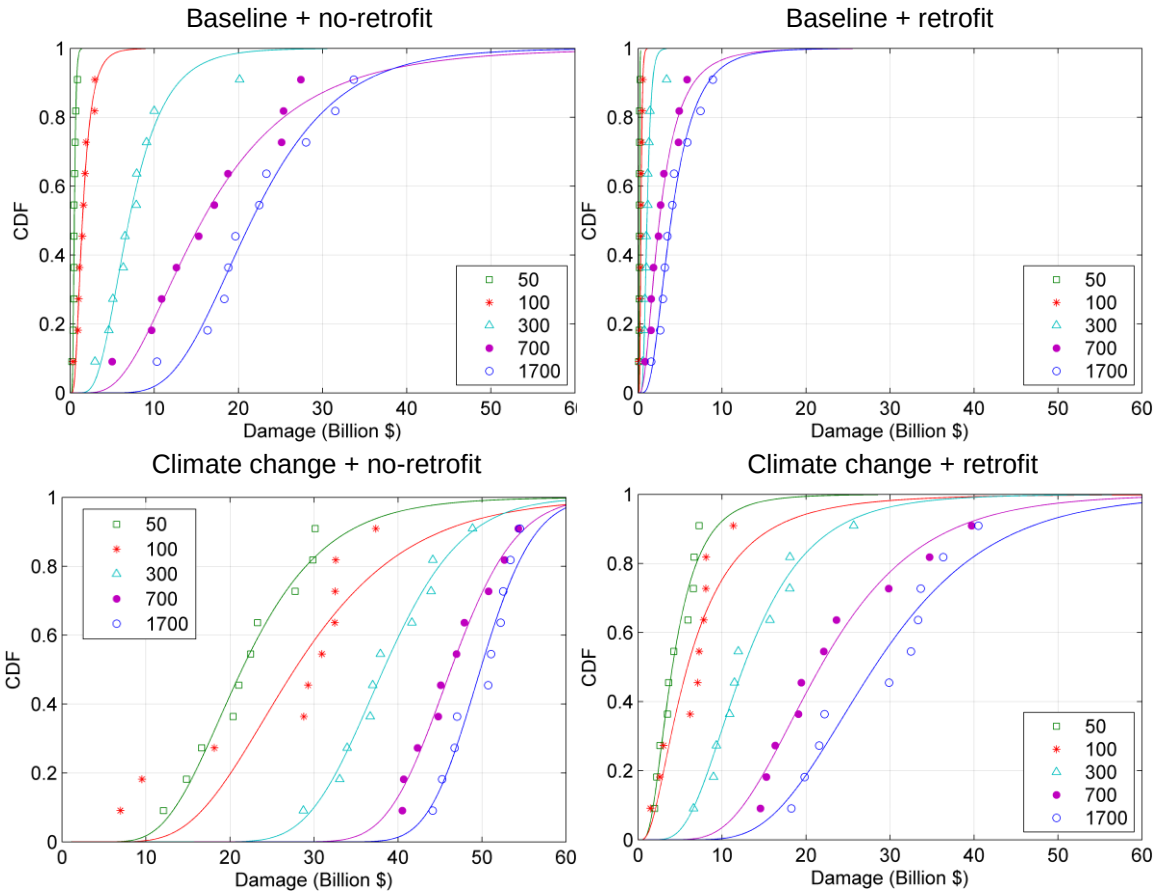


Figure 7.14: CDFs of direct property loss in Orleans Parish, LA.

4) The empirical CDF curves of losses in the four coastal regions are given in Figure 7.14 to 7.17 for the four loss estimation cases. Each set of loss data with a specific MRI level is fitted into a lognormal distribution and the fitted CDF curve is plotted on the top of the scatters of loss data. The fitting technique used to evaluate the best fit lognormal distribution parameters is the least squares fitting between the empirical cumulative functions and the fitted cumulative function. In general, the CDF curves agree with the observations from the previous loss plots (Figure 7.8 to 7.11). As the MRI levels increase, the locations of the curves shift to the right on the damage axis for all cases. It indicates that more enhanced consequences were found correspondingly with the rise of

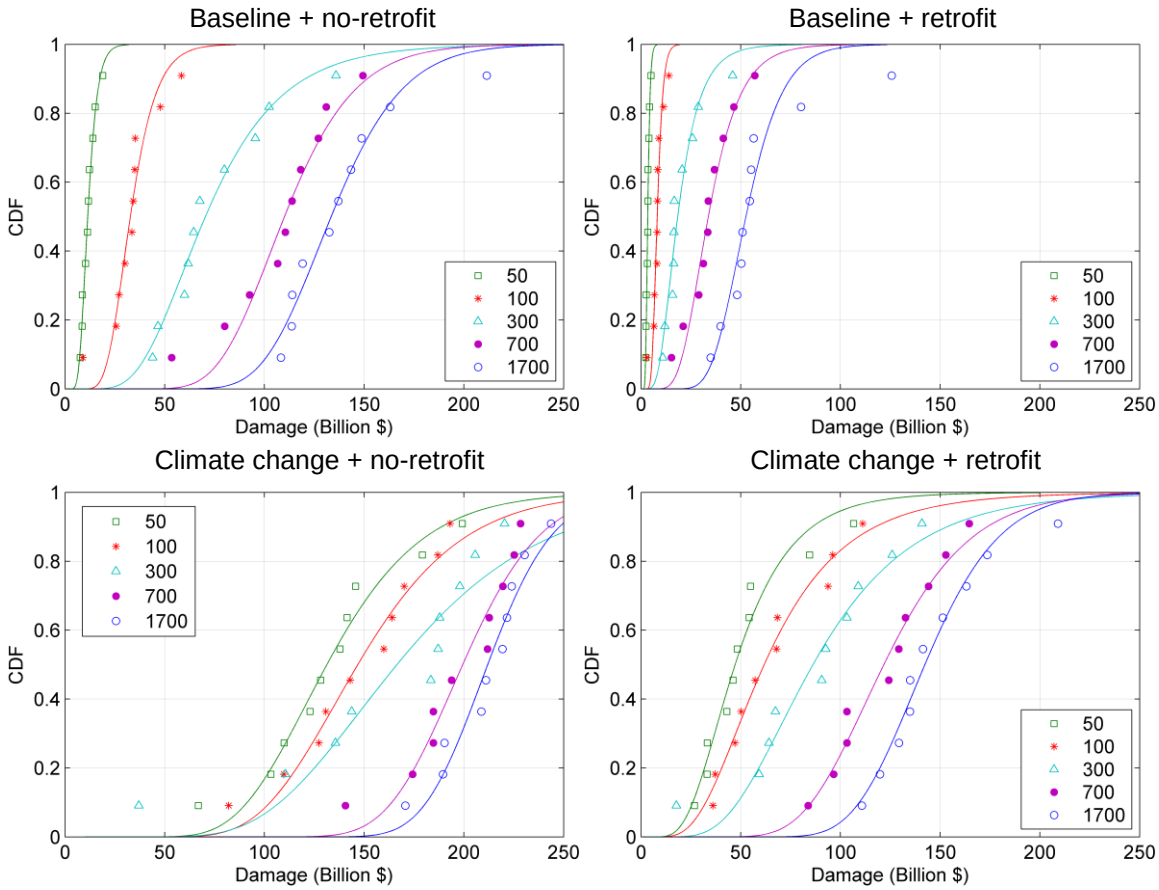


Figure 7.15: CDFs of direct property loss in Miami Dade County, FL.

hazard level. It is also observed that the incline of CDF curve changed gradually from vertical to flat with the rise of MRI levels in all cases in New York and all cases except for climate change with no-retrofit in the other three regions. The incline of the CDF curve suggests the spread of the data. The more inclined curves at higher MRIs indicate higher spread and larger standard deviation in loss data. Exceptions are found in the case of climate change with no-retrofit buildings in those regions other than New York. In these cases, the CDF curves of 700 years and 1700 yeas MRI are less inclined compared to those lower MRI curves which indicate smaller spread in the data. In this case of climate change (severe hazard demand) with no-retrofit buildings (lower capacity against

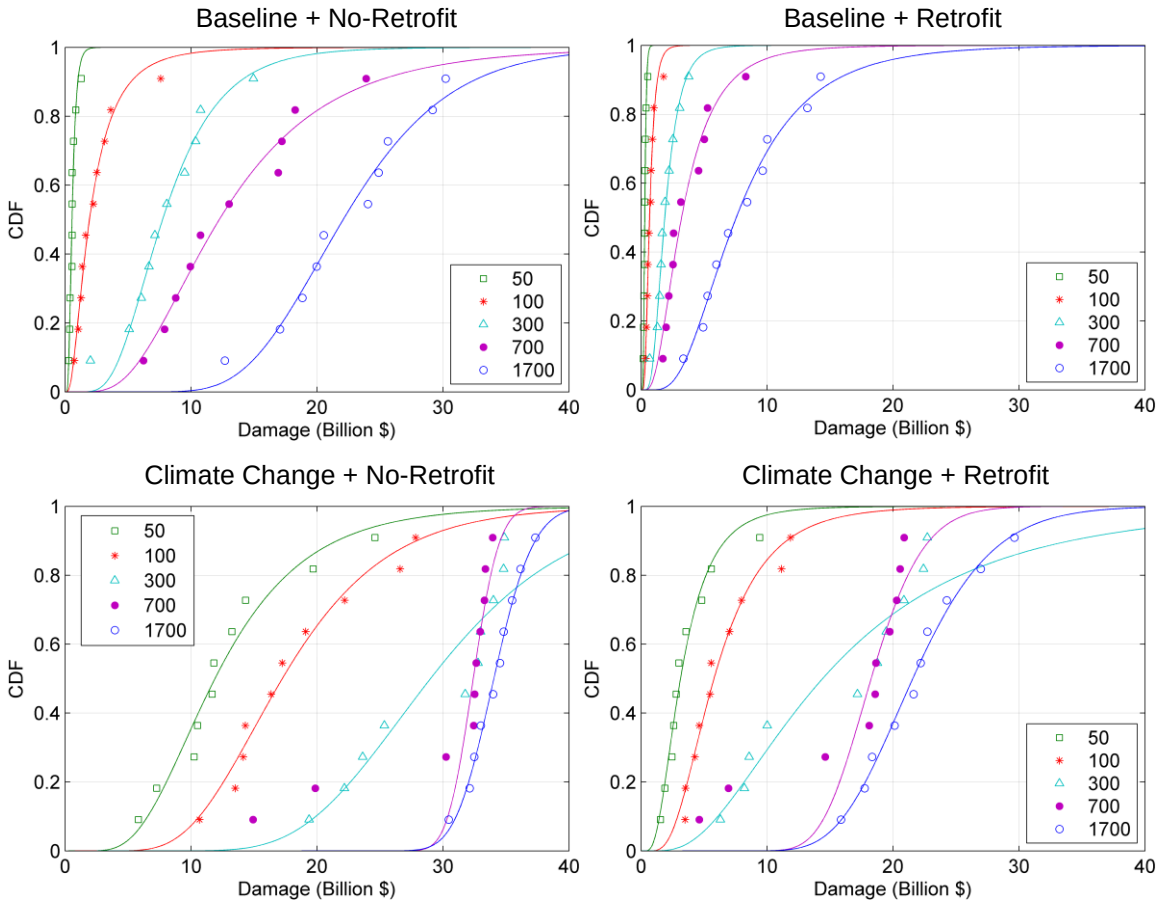


Figure 7.16: CDFs of property damage loss in Charleston County, SC.

hazard), property damage has almost reached its upper limit of the total exposure in the region when an event of 700-year MRI or higher occurs. It can be verified by the data in Table 7.16 which presents the percentage of loss over the exposure value. The percentages of loss in MRI 700 and 1700 years are 132.7% and 141.7% in New Orleans, 131.2% and 140.1% in Miami, 128.4% and 147.5% in Charleston. The percentages are higher than 100% because the total exposure values only include the replacement value of the exterior of the building and the total estimated loss includes damage from both exterior and interior of the building. In the loss estimation process, the loss function of building interior was used to evaluate the damages inside and the total value of contents

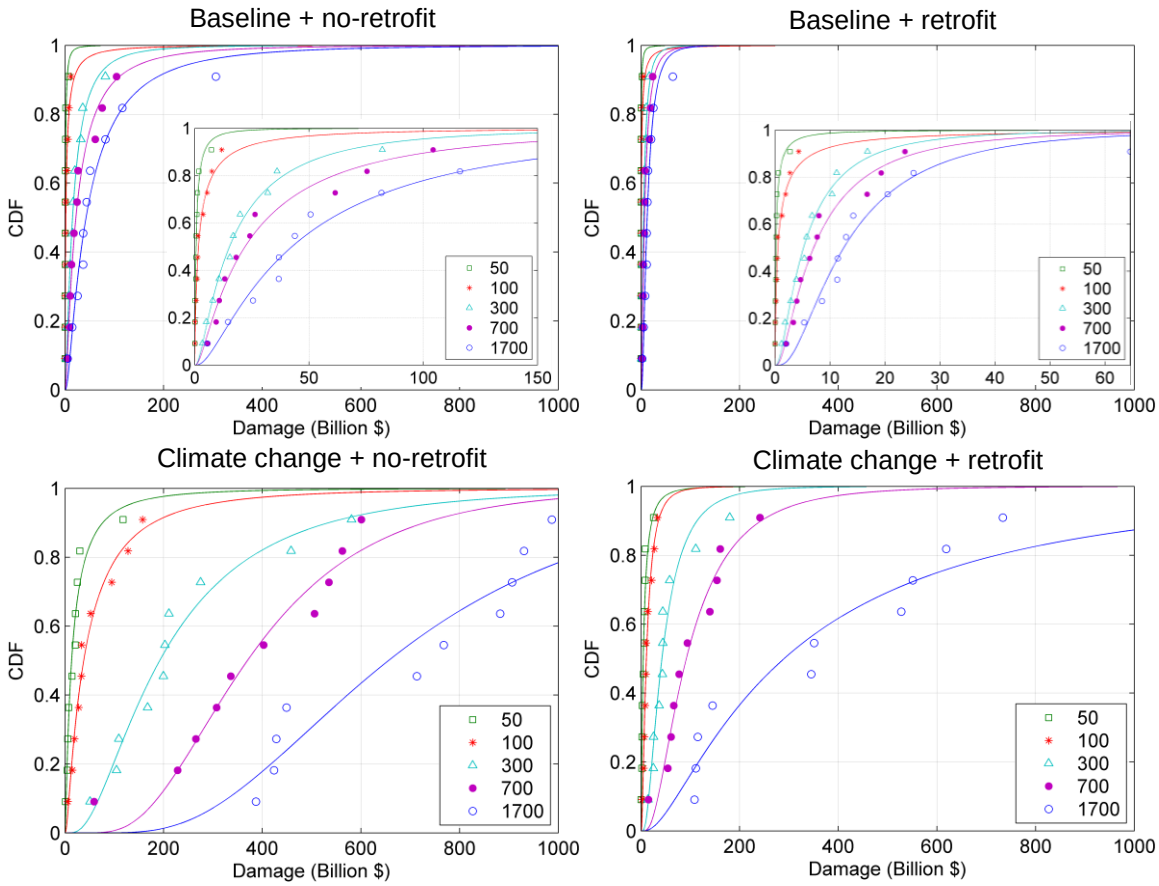


Figure 7.17: CDFs of property damage loss in New York City.

was assumed proportional to the replacement value of the exterior of the building. For example, the content value is assumed to be 50% of the building replacement value for residential building. This ratio is different for other types of building as the build-in assumptions in HAZUS. Therefore, the loss percentage of 130% and higher is very close to the upper limit of total damage that could take place in the region as in the case of climate change with no-retrofit buildings.

5) An alternative way to examine the results from different cases is the PDF curve. The PDFs of loss in the Orleans Parish from 50-1700 years MRI events are given in Figure 7.18 and 7.19. By plotting the PDF curves from the four loss estimation cases

together on the same scale, it is clear to compare the degree of destruction from the four cases. The advantage of retrofitted configurations as mitigation to wind hazard is proved by the left-ward shift of the curve from the no-retrofit case to the retrofit one under the same hazard level. Also, the generally smaller spread of retrofit PDF curves than the no-retrofit ones indicate that the performance of the buildings is not only stronger but also more certain with retrofit configurations. By comparing the locations of the curve for no-climate change with no retrofit and curve for climate change with retrofit (the two middle curves in Figure 7.19), it warns us that more severe damage due to hurricane hazard is expected than current level if the global climate changes as the prediction of Climate Change Case 1 by the end of the century, even if all the current common retrofit configurations have been applied. In the consideration of reducing hurricane-induced loss or at least preventing more destructive consequence, it is critical to realize that climate change effect is posing higher risk to the coastal environment. In the consideration of the worst case scenario from climate change, more efficient retrofit configurations are needed to provide higher strength against wind speed in structural design. Higher design wind speed than current level for all risk categories will help improve the performance of buildings against the challenge of more intense wind from climate change effect.

6) The relationships between the wind speeds from the selected hurricanes and the induced losses were inspected and compared. The maximum wind speeds, which served as the input to quantify the direst property losses, from events for 50, 100, 300, 700 and 1700-year MRIs were obtained from the HAZUS program. In Figure 7.20, the maximum wind speeds were plotted against the losses, which are the responses to the

hazards in the regions. The sub-figures in left column present the results from the case without climate change effect; and those in the right column are from the Climate Change Case 1. It can be observed that the range of wind speeds from MRIs of 50 to 1700 years (2% to 0.06% annual exceedance probability) shift up in the climate change case in comparison with the no climate change case. For the losses in either case, different ranges of the estimated losses are observed between the current building condition and the retrofitted one, even though the same hazard level was applied as the input. The losses in the retrofitted cases shift to the left compared to the cases without retrofit, which indicates reductions in the direct property losses. Besides the reduction in the loss value, the spread of the losses changed before and after the retrofit was applied to the regions. The range of the losses is much narrower in the retrofitted case on the sub-plots in Figure 7.20. It indicates that the response to the hazard in term of loss became more robust due to the retrofit of the building in the regions. It is consistent with what the PDF curves have implied in Figure 7.18 and 7.19.

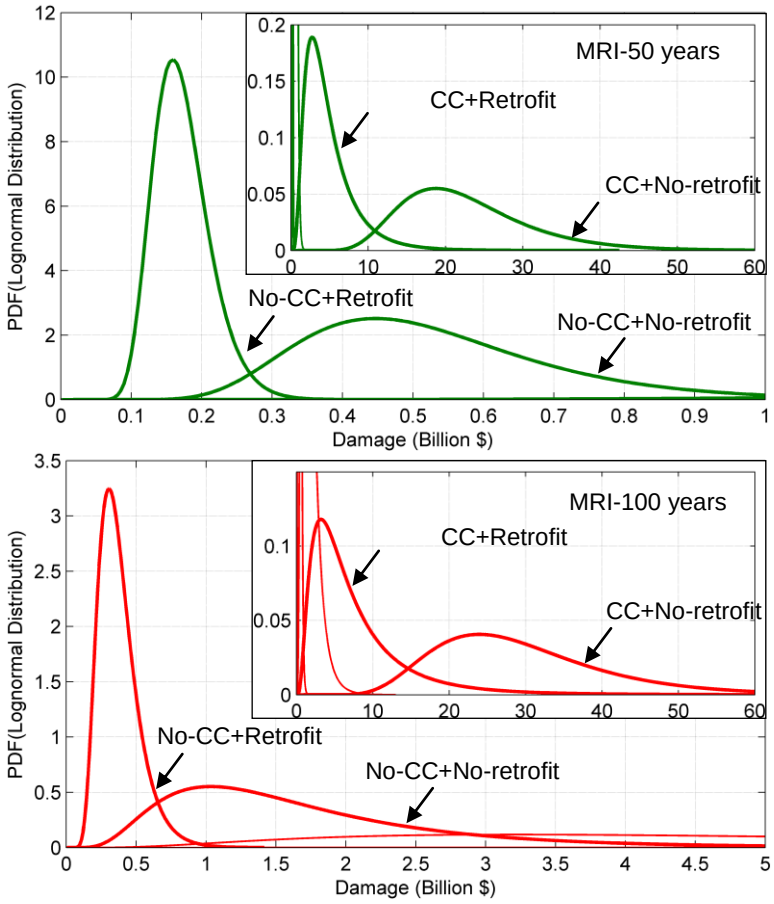


Figure 7.18: PDFs of property damage loss for 50 years and 100 years MRI events in Orleans Parish.

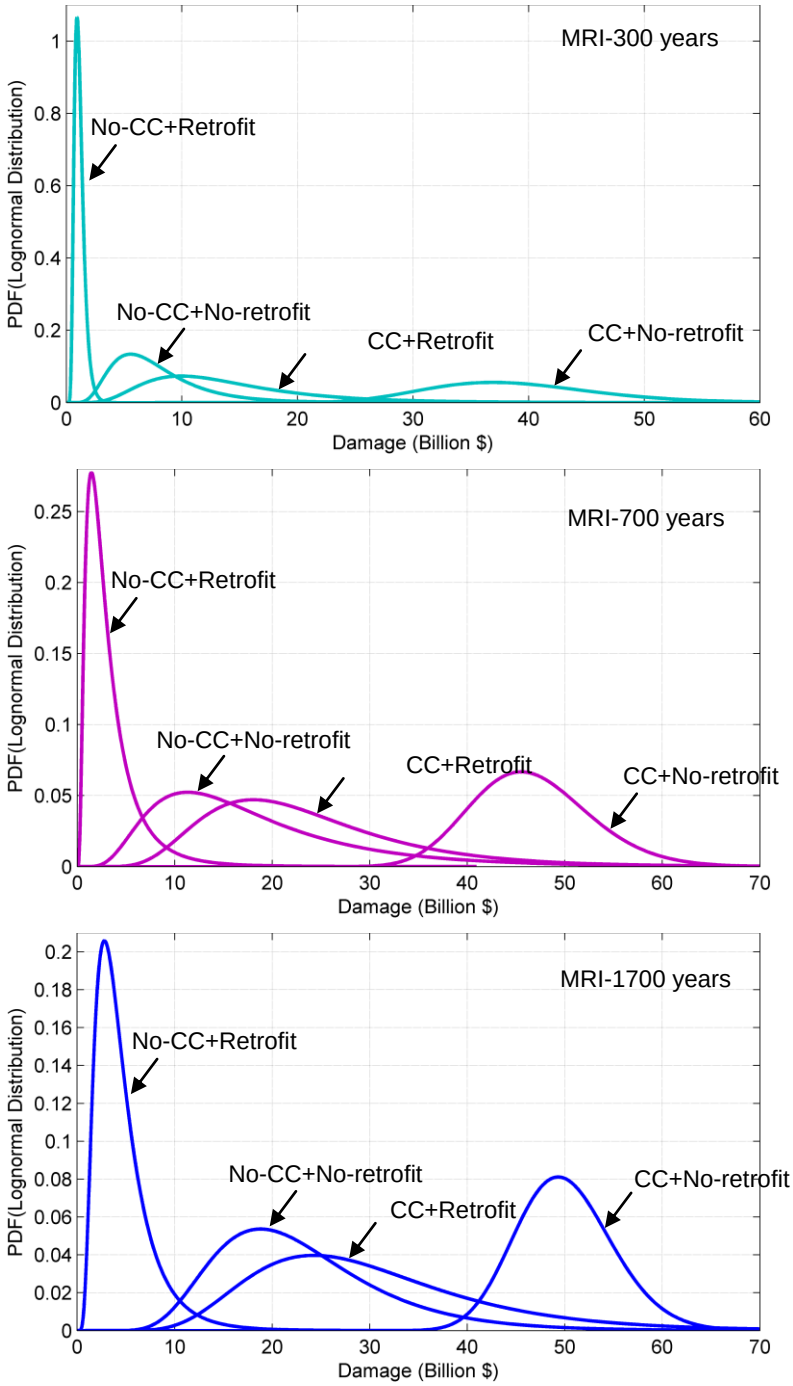


Figure 7.19: PDFs of property damage loss for 300 years, 700 years and 1700 years MRI events in Orleans Parish.

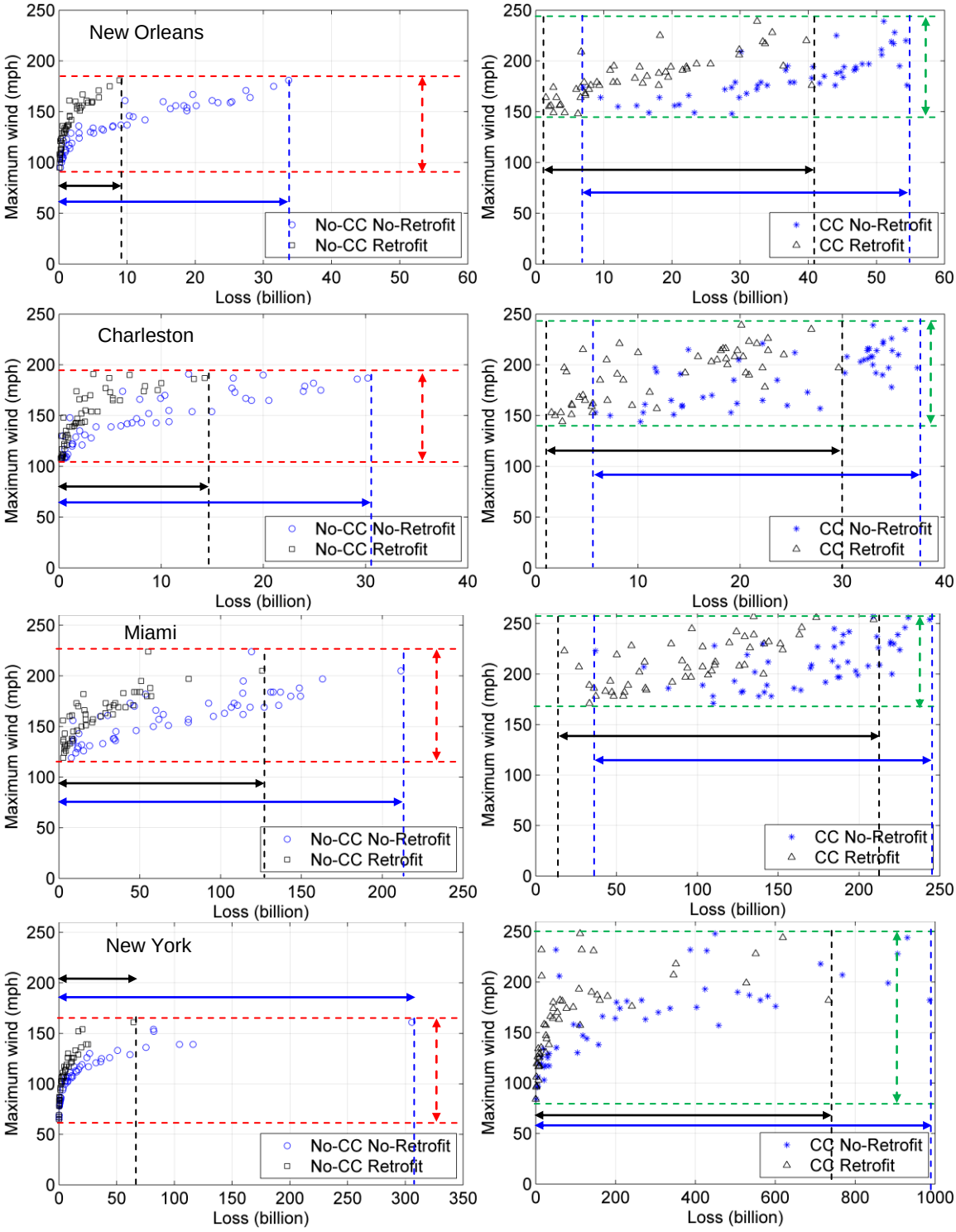


Figure 7.20: Loss versus maximum wind speed in the selected coastal counties.

## 7.6 Probabilistic Model of Hurricane Loss Estimation for Specified MRI

In this section, the relationship between hurricane induced losses and the MRIs is quantified. Hurricane induced losses are projected from the MRIs and modeled over the complete range of exceedance probability from the five known MRIs and the associated the losses estimated using HAZUS.

Assuming the losses due to the events of the same MRI are lognormally distributed (as indicated in Figure 7.14 to 7.17), the lognormal mean ($\mu_{LN}$) and lognormal standard deviation ($\beta_{LN}$) of the losses can be evaluated at each MRI level. The lognormal means obtained from the losses of 10 events at each MRI were plotted in Figure 7.21 and the lognormal standard deviations were in Figure 7.22 for all four loss estimation cases. As can be seen, the lognormal mean increases with the increase of MRI levels which reflect the general increasing trend of loss values. The lognormal standard derivations were found distributed in a constant range across all MRI levels from 50 to 1700 years. It indicates that although the amount of loss increases with the MRIs, the uncertainty in loss value and the potential loss range keeps constant over the MRI levels.

These pairs of lognormal distribution parameters ($\mu_{LN}$ and $\beta_{LN}$) and MRI levels are used to develop the loss estimation models for the four regions (Table 7.17). The loss value for a given MRI is modeled by a lognormal distribution of which parameters $\mu_{LN}$ is linearly interpolated between the mean values of the nearest two known MRIs and $\beta_{LN}$ is sampled from the range in Figure 7.22. The sampling from the lognormal distribution saved the time and effort of hurricane selection and loss calculation in HAZUS. Its

advantage as a probabilistic model includes the inherent uncertainty of the losses in the model as well.

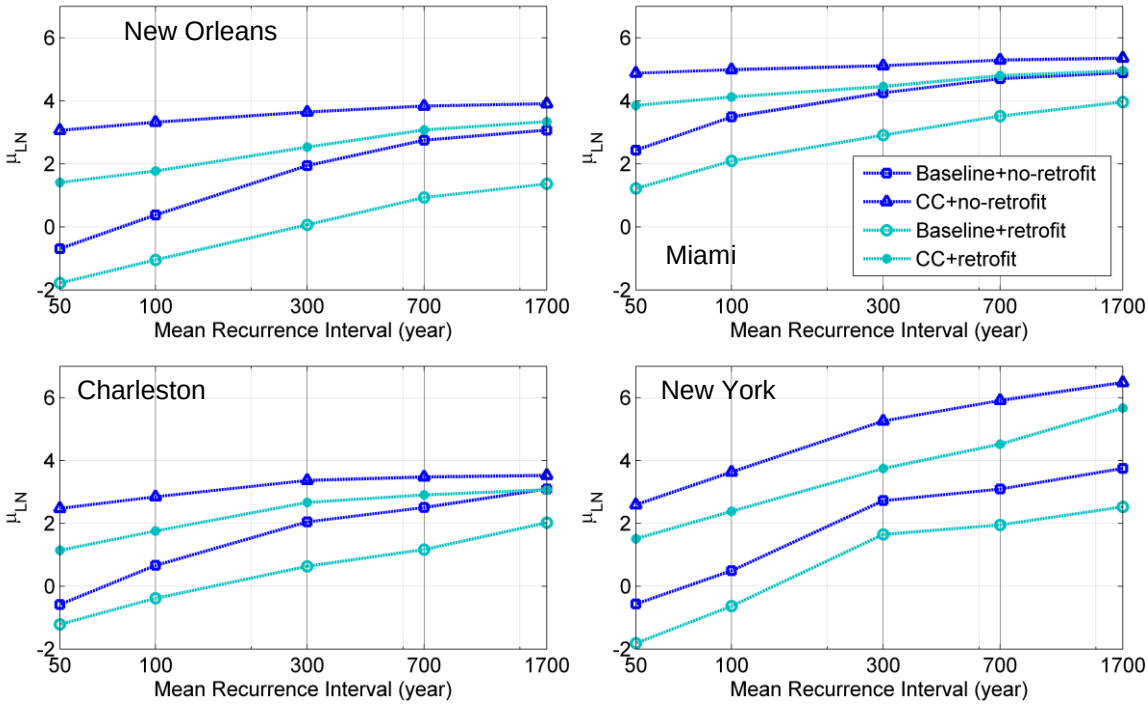


Figure 7.21: Lognormal means of losses versus MRIs in the selected regions.

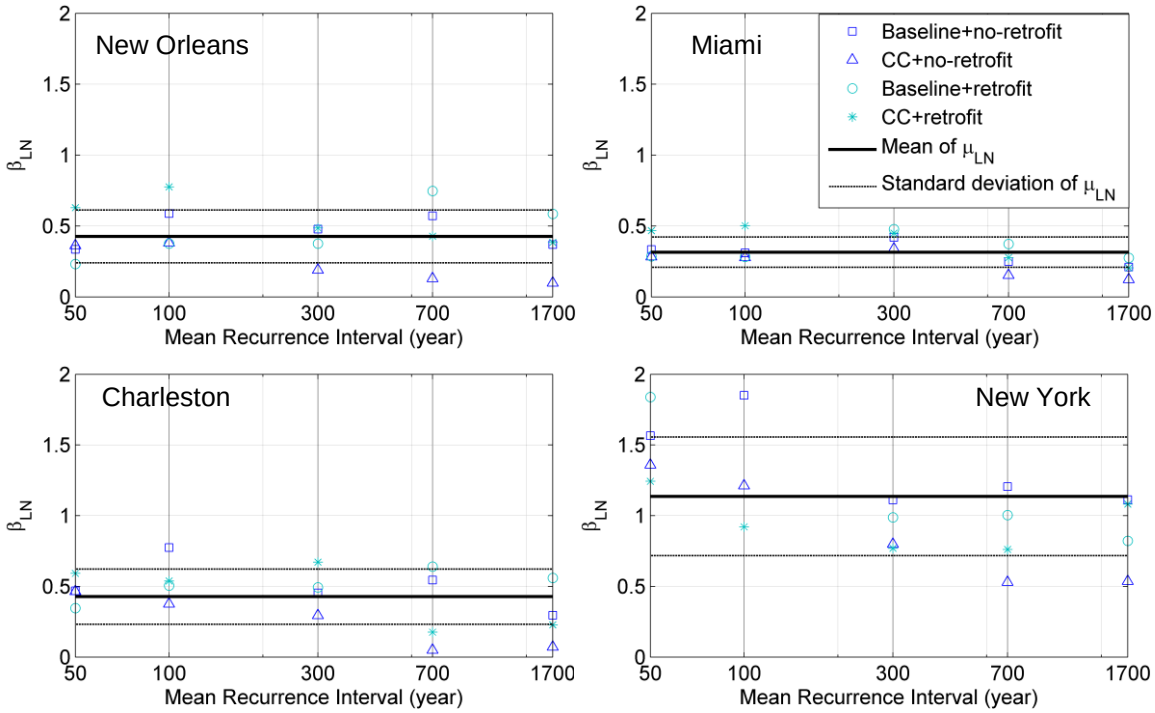


Figure 7.22: Lognormal standard deviations of losses versus MRIs in the selected regions.

Table 7.17: The fitted lognormal distribution parameters for losses of multiple MRI levels

| Region | MRI | $\mu_{LN}$ | | | | $\beta_{LN}$ | |
|---|---|---|---|---|---|---|---|
| | | No-CC No-Retrofit | No-CC Retrofit | CC No-Retrofit | CC Retrofit | Mean | COV |
| New Orleans | 50 | -0.69 | 3.06 | -1.78 | 1.41 | 0.43 | 0.44 |
| | 100 | 0.38 | 3.32 | -1.05 | 1.77 | | |
| | 300 | 1.94 | 3.64 | 0.07 | 2.53 | | |
| | 700 | 2.75 | 3.83 | 0.93 | 3.08 | | |
| | 1700 | 3.07 | 3.91 | 1.37 | 3.34 | | |
| Miami | 50 | 2.43 | 4.88 | 1.22 | 3.85 | 0.31 | 0.34 |
| | 100 | 3.49 | 4.99 | 2.09 | 4.12 | | |
| | 300 | 4.25 | 5.11 | 2.91 | 4.46 | | |
| | 700 | 4.70 | 5.30 | 3.52 | 4.80 | | |
| | 1700 | 4.89 | 5.36 | 3.96 | 4.96 | | |
| Charleston | 50 | -0.59 | 2.48 | -1.21 | 1.14 | 0.43 | 0.46 |
| | 100 | 0.66 | 2.85 | -0.38 | 1.76 | | |
| | 300 | 2.05 | 3.37 | 0.63 | 2.67 | | |
| | 700 | 2.50 | 3.48 | 1.17 | 2.91 | | |
| | 1700 | 3.09 | 3.53 | 2.02 | 3.07 | | |
| New York | 50 | -0.57 | 2.59 | -1.81 | 1.51 | 1.14 | 0.37 |
| | 100 | 0.49 | 3.63 | -0.63 | 2.39 | | |
| | 300 | 2.72 | 5.26 | 1.65 | 3.75 | | |
| | 700 | 3.09 | 5.91 | 1.95 | 4.52 | | |
| | 1700 | 3.75 | 6.49 | 2.53 | 5.67 | | |

# CHAPTER EIGHT: CONCLUSIONS AND RECOMMENDATIONS

## 8.1 Summary and Conclusion

In order to examine the influence of climate change on future hurricane activities and the associated hurricane losses in coastal environment, a hurricane simulation program was developed and the simulated hurricanes were utilized to perform loss assessments. The hurricane simulation program was coded using Matlab based on the methodology introduced in Vickery et al. (2000). The simulated hurricanes without considering climate change were validated by comparing the simulation results to historical observations. A baseline synthetic hurricane database containing 200,000 simulated hurricane seasons was generated in this study. The baseline model does not include climate change effects such as potential rise in future sea surface temperature.

To project potential changes in future hurricane activities, modifications were made to the baseline hurricane simulation model which assumes the current climate condition remains unchanged in the future. Two climate related changes were considered in this study, namely changes in sea surface temperature and annual storm frequency. Six speculated climate change scenarios derived from the United Nations Intergovernmental Panel on Climate Change (IPCC) Representative Concentration Pathway (RCP) scenarios were investigated. In the climate change scenarios, the projected sea surface temperatures (SSTs) based on three future greenhouse gas emission levels (RCPs 2.6, 4.5 and 8.5) along with three annual storm frequency projection models were utilized to simulate future hurricanes. The projected future design wind speeds under the speculated climate

change scenarios were compared to those in the current design code (ASCE 7-10). It is found that the design wind speeds for Occupancy Category II (700 years MRI) buildings, which were developed based on the current climate condition, may increase by as much as 46% in Gulf Coast by the end of the century under the most drastic climate change scenario (increase in storm frequency plus radiative forcing reaches 8.5 Watt/$m^2$ by year 2100). Changes in annual storm frequency and SSTs both contribute to the observed increases in design wind speeds with the rise in SSTs having the most influence on design wind speeds. In general, the increases in design wind speeds in Gulf Coast, Florida and Mid Atlantic coast are higher than that in the New England coast. Since the wind pressure exerted on a building envelope is directly proportional to the square of wind speed, the observed levels of wind speed changes might bring significant increase in future hurricane risk to coastal regions.

The simulated hurricane events generated from both the baseline and the climate change cases for 50, 100, 300, 700 and 1,700-year MRIs were imported into the HAZUS-MH program to perform loss estimations. These loss estimations were performed for four different regions (New Orleans, LA, Miami, FL, Charleston, SC and New York, NY). To consider event-to-event uncertainty, a methodology to select hazard-consistent hurricane events was developed and ensembles of full-track hurricanes, with each ensemble contains 10 events, were selected to characterize the wind hazards associated with MRIs of 50, 100, 300, 700 and 1700 years for the four regions.

In addition to consider changes in wind hazards (i.e. with and without climate change), changes in building resistances (with and without wind retrofits) were also

considered in loss estimation study. The HAZUS-MH wind retrofits were applied to residential buildings to provide higher resistance against high wind. To provide bounds to losses, it was assumed either none of the residential buildings were retrofitted or 100% of the residential buildings were retrofitted with all wind retrofit options available in the HAZUS-MH program (e.g. secondary water resistance and better roof-to-wall attachment).

Both effects due to climate change and the adoption of wind hazard mitigation were examined in terms of property losses for the four study regions. The losses produced by the events from climate change case 1 (increase in storm frequency plus radiative forcing reaches 8.5 Watt/$m^2$ by year 2100) are larger than the losses due to the hurricane events of current climate condition. The most dramatic increases in losses due to climate change were observed for 300- and 700-year MRI storms. This is because the loss ratio for non-retrofitted buildings under a 300- to 700-year storm typically falls on high-slope or loss-sensitive region of the S-shape loss function (near the lower plateau of the S-shape loss function), in which a slight increase in wind hazard due to climate change will cause the loss ratio to increase significantly (i.e. the loss ratio shifts from the lower plateau to the upper plateau on the S-shape loss function).

For the comparisons between the retrofitted and non-retrofitted cases, no matter with or without climate change, it was observed that existing common wind retrofit technologies are effective in reducing the impacts or losses due to climate change. The wind hazard mitigation is most efficient to reduce losses caused by 300 to 700-year MRI storms. It should be noted that retrofitted buildings not only reduce the losses due to

climate change but also the variability in the loss values. In other words, implementing retrofit is a win-win strategy irrespective of whether the future hurricane wind hazard is rising or keeps stationary.

## 8.2 Recommendations for Future Research

In seek of more comprehensive and accurate ways to quantify climate change effect and future hurricane risk, the following recommendations are made for further work in this direction:

1) Two climate change effects, namely change in sea surface temperature and change in annual storm frequency, were specifically considered in current study to simulate future hurricane events. While these two climate change factors are among the most important factors that affect the storm intensity and frequency, other factors such as changes in storm tracks (or travel patterns) and genesis locations should also be considered. A recent study by Bengtsson et al. (2006) indicates that the point where hurricanes or tropical cyclones hit their peak intensity may have shifted towards the poles in both hemispheres due to climate change. A shift in the tracks or travel patterns of tropical cyclones may change the chance of tropical cyclones strike the coastal regions (Mudd et al. 2012; Bengtsson et al. 2006). In addition, the storm genesis locations may change due to changes in SST. The track patterns and genesis locations may affect the landfall rate of hurricanes.

2) The losses estimated for the four study regions considered only the damages due to extreme wind pressure. To obtain a more accurate and comprehensive

estimate of the full impact of climate change, other types of hurricane induced hazards, such as storm surge and heavy rains should also be included in loss estimation. In particular, for coastal and waterfront communities, the largest contributor to losses may come from hurricane induced storm surge. The effects of changes in building portfolios and population in the coastal regions are not projected and considered in the quantification of future hurricane risk in this study. These social factors may have significant impacts on the exposure conditions and capitals, and hence should be considered in future study to accurately quantify the potential losses due to climate change.

3) The hurricane simulation program developed in this study is a statistically parameterized model, which relies on historical data. The hurricane simulation model for long-term risk assessment will be improved from the current statistically parameterized model to a model that is able to couple with the NOAA Numerical Weather Prediction (NWP) model. In this way, the model will become more flexible to consider the variation from climate conditions in simulate future storms and not limit to the length of historical records as a disadvantage. Also, the hybrid simulation model utilizing the NWP model may be able to simulate the change in storm paths.

# REFERENCES

ATC. (2013). “Applied Technology Council - windspeed by location.” <https://www.atcouncil.org/windspeed/> (Mar. 4, 2014).

Applied Research Associates. (2008a). “Methodology used to produce the new Caribbean Basin Wind Hazard Maps.” <http://www.paho.org/disasters/index.php?option=com_content&task=view&id=963&Itemid=911> (Apr. 19, 2014).

Applied Research Associates. (2008b). “2008 Florida residential wind loss mitigation study.” <http://www.floir.com/siteDocuments/ARALossMitigationStudy.pdf> (Mar. 23, 2014).

ASCE. (2010). *Minimum Design Loads for Buildings and Other Structures: ASCE Standard 7-10*. ASCE Publications, New York, USA.

Associated Press. (1976). “Hurricane Belle at Long Island Beach.” *Pittsburgh Post Gazette*, <http://news.google.com/newspapers?id=lOUNAAAAIBAJ&sjid=jW0DAAAAIBAJ&pg=6152,733776>.

Bengtsson, L., Hodges, K. I., and Roeckner, E. (2006). “Storm tracks and climate change.” *Journal of Climate*, 19(15), 3518–3543.

Bister, M., and Emanuel, K. A. (1998). “Dissipative heating and hurricane intensity.” *Meteorology and Atmospheric Physics*, 65(3-4), 233–240.

Bjarnadottir, S., Li, Y., and Stewart, M. G. (2011). “A probabilistic-based framework for impact and adaptation assessment of climate change on hurricane damage risks and costs.” *Structural Safety*, 33(3), 173–185.

Blake, E. S., Landsea, C. W., and Gibney, E. J. (2011). *The deadliest, costliest, and most intense United States tropical cyclones from 1851 to 2010 (and other frequently requested hurricane facts). NOAA Technical Memorandum NWS NHC-6*, NOAA Technical Memorandum NWS NHC-6, Miami, FL, USA.

Camargo, S. J., Sobel, A. H., Barnston, A. G. and Emanuel, K. (2007). “Tropical cyclone genesis potential index in climate models.” *Tellus A*, 59(4), 428–443.

CCSP. (2008). *Weather and Climate Extremes in a Changing Climate. Regions of Focus: North America, Hawaii, Caribbean, and U.S. Pacific Islands. A Report by the U.S. Climate Change Science Program and the Subcommittee on Global Change Research.* [Karl, T.R., Meehl, G.A., Miller, C.D., Hassol, S.J., Waple, A.M. and Murray, W.L. (eds.)]. Department of Commerce, NOAA's National Climatic Data Center., Washington, DC, USA.

Cocke, K. E. (1995). "Department of the Army Historical Summary Fiscal Year 1985." <http://www.history.army.mil/books/DAHSUM/1985/> (Mar. 21, 2014).

Conway, E. (2008). "What's in a Name? Global Warming vs. Climate Change." *NASA*, <http://www.nasa.gov/topics/earth/features/climate_by_any_other_name.html> (Mar. 4, 2014).

Cook, R., Griffis, L., Vickery, P., and Stafford, E. (2011). "ASCE 7-10 wind loads." *Structures Congress 2011*, 1440–1453.

Cox, R. F., Issa, R. R., and Ligator, J. (2006). "Top ten Florida residential building code violations." <http://www.floridabuilding.org/FBC/publications/CodeViolationsFinalReport4.pdf > (Mar. 21, 2014).

Darling, R. W. R. (1991). "Estimating probabilities of hurricane wind speeds using a large-scale empirical model." *Journal of Climate*, 4(10), 1035–1046.

Ellingwood, B. R. and Tekie, P. B. (1999). "Wind load statistics for probability-based structural design." *Journal of Structural Engineering*, American Society of Civil Engineers, 125(4), 453–463.

Elsner, J. B., Jagger, T. H., and Tsonis, A. A. (2006). "Estimated return periods for Hurricane Katrina." *Geophysical Research Letters*, 33(8), L08704.

Emanuel, K. (2013). "Downscaling CMIP5 climate models shows increased tropical cyclone activity over the 21st century." *Proceedings of the National Academy of Sciences of the United States of America*, 110(30), 12219–12224.

Emanuel, K. (2011). "Global warming effects on U.S. hurricane damage." *Weather, Climate, and Society*, 3(4), 261–268.

Emanuel, K. (2007). "Environmental factors affecting tropical cyclone power dissipation." *Journal of Climate*, 20(22), 5497–5509.

Emanuel, K., Ravela, S., Vivant, E., and Risi, C. (2006). "A statistical deterministic approach to hurricane risk assessment." *Bulletin of the American Meteorological Society*, 87(3), 299–314.

Emanuel, K. (2005). "Increasing destructiveness of tropical cyclones over the past 30 years." *Nature*, Nature Publishing Group, 436(7051), 686–688.

Emanuel, K. (2000). "A statistical analysis of tropical cyclone intensity." *Monthly Weather Review*, 128(4), 1139–1152.

Emanuel, K. (1987). "The dependence of hurricane intensity on climate." *Nature*, Nature Publishing Group, 326(6112), 483–485.

Eshelman, R. S. (2012). "Adaptation: Political support for a sea wall in New York Harbor begins to form." *eenews.net*, <http://www.eenews.net/stories/1059972561> (Mar. 21, 2014).

FEMA. (2014). "Hazus Software | FEMA.gov." <http://www.fema.gov/hazus-software> (Mar. 20, 2014).

FEMA. (2012). "Hazus 2.1 Technical and User's Manuals | FEMA.gov." <https://www.fema.gov/media-library/assets/documents/24609?id=5120> (Apr. 17, 2014).

Florida Department of Business and Professional Regulation. (2004). "History of the Florida Building Commission." <http://www.floridabuilding.org/fbc/information/building_commission.htm> (Mar. 21, 2014).

Garrison, C. Z., Bryant, E. S., Addy, C. L., Spurrier, P. G., Freedy, J. R., and Kilpatrick, D. G. (1995). "Posttraumatic stress disorder in adolescents after Hurricane Andrew." *Journal of the American Academy of Child and Adolescent Psychiatry*, 34(9), 1193–201.

Geerts, B., and Linacre, E. (1998). "What are general circulation models (GCM) ?" <http://www-das.uwyo.edu/~geerts/cwx/notes/chap12/nwp_gcm.html> (Mar. 4, 2014).

Georgiou, P. N. (1985). "Design wind speeds in tropical cyclone-prone regions." PHD Dissertation. University of Western Ontario, London, Ontario, Canada.

Georgiou, P. N., Davenport, A. G., and Vickery, B. J. (1983). "Design wind speeds in regions dominated by tropical cyclones." *Journal of Wind Engineering and Industrial Aerodynamics*, 13(1), 139–152.

GFDL. (2014). “GFDL’s Data Portal.” <http://nomads.gfdl.noaa.gov:8080/DataPortal/cmip5.jsp> (Jul. 20, 2014).

Gillett, N. P., Stott, P. A., and Santer, B. D. (2008). “Attribution of cyclogenesis region sea surface temperature change to anthropogenic influence.” *Geophysical Research Letters*, 35(9), L09707.

Goldenberg, S. B., Landsea, C. W., Mestas-Nunez, A. M. and Gray, W. M. (2001). “The recent increase in Atlantic hurricane activity: causes and implications.” *Science*, 293(5529), 474–9.

Holland, G. J. and Webster, P. J. (2007). “Heightened tropical cyclone activity in the North Atlantic: natural variability or climate trend?” *Philosophical Transactions of the Royal Society A: Mathematical, Physical and Engineering Sciences*, 365(1860), 2695–2716.

Hsu, S. A., and Yan, Z. (1998). “A Note on the Radius of Maximum Wind for Hurricanes.” *Journal of Coastal Research*, Vol. 14(2), 667–668.

Huang, Z., Rosowsky, D. V., and Sparks, P. R. (2001). “Long-term hurricane risk assessment and expected damage to residential structures.” *Reliability Engineering & System Safety*, 74(3), 239–249.

Huang, Z., Rosowsky, D. V., and Sparks, P. R. (1999). “Event based hurricane simulation for the evaluation of wind speeds and expected insurance losses.” *Proceedings of the 10th International Conference on Wind Engineering*, Copenhagen, Denmark.

Huang, Z. (1999). “Stochastic models for hurricane hazard analysis. PHD Dissertation.” Department of Civil Engineering, Clemson University.

IPCC. (2014). “Publications and Data - Intergovernmental Panel on Climate Change.” <http://www.ipcc.ch/publications_and_data/publications_and_data_reports.shtml> (Jul. 6, 2014).

IPCC. (2013). *Climate Change 2013: The Physical Science Basis. Contribution of Working Group I to the Fifth Assessment Report of the Intergovernmental Panel on Climate Change*. [Stocker, T.F., D. Qin, G.-K. Plattner, M. Tignor, S.K. Allen, J. Boschung, A. Nauels, Y. Xia, V. Bex and P.M. Midgley (eds.)]. Cambridge University Press, Cambridge, United Kingdom and New York, NY, USA, pp1535.

IPCC. (2012). *Managing the Risks of Extreme Events and Disasters to Advance Climate Change Adaptation: A Special Report of Working Group of the I and II of the Intergovernmental Panel on Climate Change*. [Field, C.B., V. Barros, T.F. Stocker, D. Qin, D.J. Dokken, K.L. Ebi, M.D. Mastrandrea, K.J. Mach, G.-K. Plattner, S.K. Allen, M. Tignor, and P.M. Midgley (eds.)]. Cambridge University Press, Cambridge, UK, and New York, NY, USA, pp582.

IPCC. (2007a). *Climate Change 2007: The Physical Science Basis. Contribution of Working Group I to the Fourth Assessment Report of the Intergovernmental Panel on Climate Change.* [Solomon, S., D. Qin, M. Manning, Z. Chen, M. Marquis, K.B. Averyt, M. Tignor and H.L. Miller (eds.)]. Cambridge University Press, Cambridge, UK and New York, NY, USA, pp996.

IPCC. (2007b). *Climate Change 2007: Impacts, Adaptation and Vulnerability. Contribution of Working Group II to the Fourth Assessment Report of the Intergovernmental Panel on Climate Change.* [Parry, M.L., Canziani, O.F., Palutikof, J.P., van der Linden, P.J. and Hanson, C.E. (eds.)]. Cambridge University Press, Cambridge, UK and New York, NY, USA, pp976.

IPCC. (2007c). *Climate Change 2007: Mitigation. Contribution of Working Group III to the Fourth Assessment Report of the Intergovernmental Panel on Climate Change.* [Metz, B., Davidson, O.R., Bosch, P.R.,Dave, R., Meyer, L.A. (eds.)]. Cambridge University Press, Cambridge, UK and New York, NY, USA, pp851.

IPCC. (2000). *Special Report on Emissions Scenarios: A Special Report of Working Group III of the Intergovernmental Panel on Climate Change [Nakicenovic, N. and Swart, R. (eds.)]*. Cambridge University Press, Cambridge, UK, and New York, NY, USA, pp570.

Irish, J. L., and Resio, D. T. (2010). "A hydrodynamics-based surge scale for hurricanes." *Ocean Engineering*, 37(1), 69–81.

Jagger, T. H., and Elsner, J. B. (2006). "Climatology models for extreme hurricane winds near the United States." *Journal of Climate*, 19(13), 3220–3236.

Jain, V. K. and Davidson, R. A. (2007). "Application of a regional hurricane wind risk forecasting model for wood-frame houses." *Risk Analysis*, 27(1), 45–58.

Jarvinen, B. R., Neumann, C. J., and Davis, M. A. S. (1984). *A tropical cyclone data tape for the North Atlantic Basin, 1886-1983: contents, limitations, and uses. Tech. Memo. NWS NHC 22*. U.S. Dept. of Commerce, National Oceanic and Atmospheric Administration, National Weather Service, Washington, D.C.

Johnson, N. L. (1949). “Systems of frequency curves generated by methods of translation.” *Biometrika*, 36(1-2), 149–176.

Kepert, J. (2001). “The dynamics of boundary layer jets within the tropical cyclone core. Part I: Linear theory.” *Journal of the Atmospheric Sciences*, 58(17), 2469–2484.

King, H. (2006). “Rebuild New Orleans - Flooding, Safety & Subsidence.” *Geology.com*, <http://geology.com/articles/rebuilding-new-orleans.shtml> (Mar. 20, 2014).

Knutson, T. R., McBride, J. L., Chan, J., Emanuel, K., Holland, G., Landsea, C., Held, I., Kossin, J. P., Srivastava, A. K., and Sugi, M. (2010). “Tropical cyclones and climate change.” *Nature Geoscience*, Nature Publishing Group, 3(3), 157–163.

Knutson, T. R., Delworth, T. L., Dixon, K. W., Held, I. M., Lu, J., Ramaswamy, V., Schwarzkopf, M. D., Stenchikov, G., and Stouffer, R. J. (2006). “Assessment of twentieth-century regional surface temperature trends using the GFDL CM2 coupled models.” *Journal of Climate*, 19(9), 1624–1651.

Lagarias, J. C., Reeds, J. A., Wright, M. H., and Wright, P. E. (1998). “Convergence properties of the Nelder-Mead simplex method in low dimensions.” *SIAM Journal on Optimization*, Society for Industrial and Applied Mathematics, 9(1), 112–147.

Landsea, C. W., Franklin, J., and Beven, J. (2013). “The revised Atlantic hurricane database (HURDAT2).” <http://www.aoml.noaa.gov/hrd/hurdat/newhurdat-format.pdf> (Mar. 4, 2014).

Landsea, C. W. (2007). “Counting Atlantic tropical cyclones back to 1900.” *Eos, Transactions American Geophysical Union*, 88(18), 197–208.

Landsea, C. W., Anderson, C., Charles, N., Clark, G., Dunion, J., Fernandez-Partagas, J., Hungerford, P., Neumann, C., and Zimmer, M. (2004). “The Atlantic Hurricane Database Re-analysis Project: Documentation for 1851-1910 Alterations and Additions to the HURDAT Database.” *Hurricanes and Typhoons: Past, Present and Future*, Columbia University Press, New York, 177–221.

Lee, K. H., and Rosowsky, D. V. (2007). “Synthetic hurricane wind speed records: development of a database for hazard analyses and risk studies.” *Natural Hazards Review*, American Society of Civil Engineers, 8(2), 23–34.

Legg, M. R., Nozick, L. K., and Davidson, R. A. (2010). “Optimizing the selection of hazard-consistent probabilistic scenarios for long-term regional hurricane loss estimation.” *Structural Safety*, 32(1), 90–100.

Lin, N., Emanuel, K. A., Smith, J. A., and Vanmarcke, E. (2010). "Risk assessment of hurricane storm surge for New York City." *Journal of Geophysical Research*, 115(D18), D18121.

Liu, F., and Pang, W. (2013). "Projections of Future US Design Wind Speeds due to Changes in Hurricane Frequency and Sea Surface Temperature." *Journal of Wind Engineering and Industrial Aerodynamics*. Submitted.

Lorenz, E. N. (1967). *The Nature and Theory of the General Circulation of the Atmosphere*. World Meteorological Organization, 161.

Mann, M. E. and Emanuel, K. A. (2006). "Atlantic hurricane trends linked to climate change." *Eos, Transactions American Geophysical Union*, 87(24), 233–241.

Met Office, Hadley Centre. (2013). "Met Office HadISST 1.1 (Global sea-Ice coverage and Sea Surface Temperature) (1870-Present) Dataset." <http://badc.nerc.ac.uk/view/badc.nerc.ac.uk__ATOM__dataent_hadisst> (Mar. 4, 2014).

Moss, R. H., Edmonds, J. A., Hibbard, K. A., Manning, M. R., Rose, S. K., van Vuuren, D. P., Carter, T. R., Emori, S., Kainuma, M., Kram, T., Meehl, G. A., Mitchell, J. F. B., Nakicenovic, N., Riahi, K., Smith, S. J., Stouffer, R. J., Thomson, A. M., Weyant, J. P., and Wilbanks, T. J. (2010). "The next generation of scenarios for climate change research and assessment." *Nature*. 463(7282), 747–56.

Mudd, L., Wang, Y., Letchford, C. and Rosowsky, D. (2014). "Assessing climate change impact on the U.S. East Coast hurricane hazard: temperature, frequency, and track." *Natural Hazards Review*, American Society of Civil Engineers, 15(3), 04014001.

Mudd, L., Wang, Y., Letchford, C. and Rosowsky, D. V. (2013a). "Assessing climate change impact on the US east coast hurricane hazard, III: sea temperature, hurricane frequency, and hurricane track." The 12th Americas Conference on Wind Engineering, Seattle, Washington, USA.

Mudd, L., Wang, Y., Rosowsky, D. V. and Letchford, C. (2013b). "Assessing climate change impact on the US east coast hurricane hazard, II: sea temperature and hurricane frequency." 11th International Conference on Structural Safety & Reliability, Columbia University New York, NY, USA.

National Climatic Data Center (NCDC). (2014). "Global Surface Temperature Anomalies | Monitoring References." National Climatic Data Center (NCDC), <https://www.ncdc.noaa.gov/monitoring-references/faq/anomalies.php> (Mar. 4, 2014).

National Hurricane Center. (2014). “NHC Data Archive.” <http://www.nhc.noaa.gov/data/#tcr> (Mar. 21, 2014).

National Hurricane Center. (2012). “Hurricanes in History.” <http://www.nhc.noaa.gov/outreach/history/> (Mar. 21, 2014).

National Research Council. (2010). *Advancing the Science of Climate Change*. The National Academies Press, Washington, DC, USA.

Neumann, C. J. (1987). *The National Hurricane Center Risk Analysis Program (HURISK). NOAA Technical Memorandum NWS NHC 38*. National Oceanic and Atmospheric Administration. Washington, DC.

NHC. (2006). “Tropical Cyclone Report Hurricane Wilma.” *National Hurricane Center*, National Hurricane Center. Miami, FL, USA, <http://www.nhc.noaa.gov/pdf/TCR-AL252005_Wilma.pdf>.

Nishijima, K., Maruyama, T., and Graf, M. (2012). “A preliminary impact assessment of typhoon wind risk of residential buildings in Japan under future climate change.” *Hydrological Research Letters*, 6, 23–28.

Pei, B., Pang, W., Testik, F. Y., Ravichandran, N., and Liu, F. (2014). “Mapping Joint Hu rricane Wind and Surge Hazards for Charleston, South Carolina.” *Nat. Hazards*, DO I 10.1007/s11069-014-1185-5

Pei, B., Pang, W., Testik, F. Y., and Ravichandran, N. (2013). “Selection of Hurricane Scenarios for Combined Wind and Flood Loss Estimation.” The 12th Americas Conference on Wind Engineering, Seattle, Washington, USA.

Peterka, J. A., and Shahid, S. (1998). “Design gust wind speeds in the United States.” *Journal of Structural Engineering*, American Society of Civil Engineers, 124(2), 207–214.

Pielke Jr, R. A., Gratz, J., Landsea, C. W., Collins, D., Saunders, M. A., and Musulin, R. (2008). “Normalized hurricane damage in the United States: 1900–2005.” *Natural Hazards Review*, American Society of Civil Engineers, 9(1), 29–42.

Rappaport, E. N. (2000). “Loss of life in the United States associated with recent Atlantic tropical cyclones.” *Bulletin of the American Meteorological Society*, 81(9), 2065–2073.

Rogelj, J., Meinshausen, M., and Knutti, R. (2012). “Global warming under old and new scenarios using IPCC climate sensitivity range estimates.” *Nature Climate Change*, Nature Publishing Group, 2(4), 248–253.

Powell, M. D., Houston, S. H., Amat, L. R. and Morisseau-Leroy, N. (1998). "The HRD real-time hurricane wind analysis system." *Journal of Wind Engineering and Industrial Aerodynamics*, 77-78, 53–64.

Russell, L. R. (1971). "Probability Distributions for Hurricane Effects." *Journal of the Waterways, Harbors and Coastal Engineering Division*, American Society of Civil Engineers, 97(1), 139–154.

Sainz, A. (2002). "Ten years after Hurricane Andrew, effects are still felt." <http://www.latimes.com/news/weather/sfl-1992-ap-mainstory,0,5535248,full.story#axzz2wYxJ5r8O> (Mar. 21, 2014).

Schlesinger, M. E., and Ramankutty, N. (1994). "An oscillation in the global climate system of period 65–70 years." *Nature*, 367(6465), 723–726.

Sims, D. (2012). "Strong building codes work only if they are enforced." *Sun-Sentinel.com*, <http://articles.sun-sentinel.com/2012-08-21/news/fl-codes-oped0822-20120821_1_code-officials-codes-work-codes-and-standards> (Mar. 21, 2014).

Smith, A. (2013). "8 most powerful storms on record to make landfall." *NBC News.com*, <http://www.nbcnews.com/news/us-news/8-most-powerful-storms-record-make-landfall-v21372026> (Mar. 20, 2014).

South Carolina State Climatology Office. (2014). "Hurricanes and tropical storms affecting South Carolina." <http://www.dnr.sc.gov/climate/sco/Tropics/hurricane_tracks_affecting_sc.php> (Mar. 21, 2014).

Taylor, K. E., Stouffer, R. J. and Meehl, G. A. (2012). "An overview of CMIP5 and the experiment design." *Bulletin of the American Meteorological Society*, American Meteorological Society, 93(4), 485–498.

UCAR. (2012). "Atlantic Multi-decadal Oscillation (AMO)." <http://www.cgd.ucar.edu/cas/catalog/climind/AMO.html> (Jul. 22, 2014).

U.S. Census Bureau. (2010). "American FactFinder - Results." <http://factfinder2.census.gov/faces/tableservices/jsf/pages/productview.xhtml?pid=DEC_10_NSRD_GCTPL2.US24PR&prodType=table> (Mar. 20, 2014).

van Vuuren, D. P., Edmonds, J., Kainuma, M., Riahi, K., Thomson, A., Hibbard, K., Hurtt, G. C., Kram, T., Krey, V., Lamarque, J.-F., Masui, T., Meinshausen, M., Nakicenovic, N., Smith, S. J., and Rose, S. K. (2011). "The representative concentration pathways: an overview." *Climatic Change*, 109(1-2), 5–31.

Vecchi, G. A., and Knutson, T. R. (2008). "On estimates of historical North Atlantic tropical cyclone activity." *Journal of Climate*, 21(14), 3580–3600.

Vickery, P. J., Wadhera, D., Twisdale, L. A., and Lavelle, F. M. (2009a). "U.S. hurricane wind speed risk and uncertainty." *Journal of Structural Engineering*, American Society of Civil Engineers, 135(3), 301–320.

Vickery, P. J., Masters, F. J., Powell, M. D., and Wadhera, D. (2009b). "Hurricane hazard modeling: The past, present, and future." *Journal of Wind Engineering and Industrial Aerodynamics*, 97(7), 392–405.

Vickery, P. J., Wadhera, D., Powell, M. D. and Chen, Y. (2009c). "A hurricane boundary layer and wind field model for use in engineering applications." *Journal of Applied Meteorology and Climatology*, 48(2), 381–405.

Vickery, P. J. and Wadhera, D. (2008). "Statistical models of Holland pressure profile parameter and radius to maximum winds of hurricanes from flight-level pressure and H*Wind data." *Journal of Applied Meteorology and Climatology*, 47(10), 2497–2517.

Vickery, P. J., Lin, J., Skerlj, P. F., Twisdale, L. A., and Huang, K. (2006a). "HAZUS-MH hurricane model methodology. I: hurricane hazard, terrain, and wind load modeling." *Natural Hazards Review*, American Society of Civil Engineers, 7(2), 82–93.

Vickery, P. J., Skerlj, P. F., Lin, J., Twisdale, L. A., Young, M. A., and Lavelle, F. M. (2006b). "HAZUS-MH hurricane model methodology. II: damage and loss estimation." *Natural Hazards Review*, American Society of Civil Engineers, 7(2), 94–103.

Vickery, P. J. (2005). "Simple empirical models for estimating the increase in the central pressure of tropical cyclones after landfall along the coastline of the United States." *Journal of Applied Meteorology*, 44(12), 1807–1826.

Vickery, P. J., Skerlj, P. F., and Twisdale, L. A. (2000). "Simulation of hurricane risk in the U.S. using empirical track model." *Journal of Structural Engineering*, American Society of Civil Engineers, 126(10), 1222–1237.

Vickery, P. J. and Twisdale, L. A. (1995). "Wind-field and filling models for hurricane wind-speed predictions." *Journal of Structural Engineering*, American Society of Civil Engineers, 121(11), 1700–1709.

Wang, Y., and Rosowsky, D. V. (2012). "Joint distribution model for prediction of hurricane wind speed and size." *Structural Safety*, 35, 40–51.

Weart, S. R. (2003). *The discovery of global warming*. Harvard University Press, 228.

Wing, A. A., Sobel, A. H., and Camargo, S. J. (2007). "Relationship between the potential and actual intensities of tropical cyclones on interannual time scales." *Geophysical Research Letters*, 34(8), L08810.

Yeo, D., Lin, N. and Simiu, E. (2014). "Estimation of hurricane wind speed probabilities: application to New York City and other coastal locations." *Journal of Structural Engineering*, American Society of Civil Engineers, 140(6), 04014017.

# APPENDICES

APPENDIX A

Parameters Estimation for Johnson System Distribution

The Johnson System Distribution refers to a family of distributions that are flexible to convert wide varieties of data populations into Normal distribution. To characterizing data populations with different properties and shapes, there are four different transformation functions in the Johnson's family: (1) lognormal system (SL), (2) unbounded system (SU), (3) bounded system (SB), and (4) normal system (SN). Three of the four transformations (SU, SB, and SL) can be expressed using the following general transformation equation (Johnson 1949):

$$z = \gamma + \delta \times f\left(\frac{\varepsilon - \xi}{\lambda}\right) \tag{A.37}$$

where $\varepsilon$ is the data population to be estimated using the Johnson Distribution. $z$ is the standard normal random variable and $f(.)$ is one of the three transformations. $\gamma$ and $\delta$ are the shape parameters, $\lambda$ is the scale parameter and $\xi$ is the location parameter.

There are three applications of Johnson System distribution in this study: the modeling error of tracking model (section 3.2), the modeling error of relative intensity model (section 3.3.1) and the model of storm numbers in the extreme active season (section 5.1). The modeling errors are lack of bounds in the physical manner. It has been determined that the unbounded system is the best transformation for modeling the error distribution. The transformation equation for the Johnson SU distribution is:

$$z = \gamma + \delta \times \log\left\{\left(\frac{\varepsilon - \xi}{\lambda}\right) + \left[\left(\frac{\varepsilon - \xi}{\lambda}\right)^2 + 1\right]^{\frac{1}{2}}\right\}, \quad -\infty < \varepsilon < +\infty \tag{A.38}$$

For the modeling of number of storms in the active seasons, it involves complex natural procedures and seems impossible to go infinity due to the limitations in the environment. Thus, as mentioned in section 5.1.1, it is found that the bounded Johnson distribution (SB) is the most appropriate form for the model of storm numbers in extreme active seasons. The transformation equation for the bounded Johnson distribution is (Johnson 1949):

$$z = \gamma + \delta \times \log\left\{\frac{x-\xi}{\xi+\lambda-\varepsilon}\right\},\ \xi < \varepsilon < \xi + \lambda \tag{A.39}$$

where x is the number of storms of the extreme active hurricane seasons. z is the standard normal random variable. $\gamma$ and $\delta$ are the shape parameters, $\lambda$ is the scale parameter and $\xi$ is the location parameter.

To solve for the four Johnson distribution parameters, the percentile matching approach is used. The percentile matching method involves estimating the four required parameters by matching four selected quantiles of the standard normal distribution to the corresponding quantiles of the target population distribution (i.e. the error distribution). The steps for percentile matching are given below:

(1) Select four target quantiles of the standard normal distribution. In this study, the quantiles are selected as $\{z_1 = -1.5, z_2 = -0.5, z_3 = 0.5, z_4 = 1.5\}$.

(2) Determine the cumulative properties from the standard normal distribution $\{\Phi(z_1) = 0.07, \Phi(z_2) = 0.31, \Phi(z_3) = 0.69, \Phi(z_4) = 0.93\}$ of the quantiles selected in step (1) as shown in Figure A.1a.

(3) Use cumulative percentile values determined ($\Phi(z_i)$) in step (2) and the inverse of the empirical cumulative density function to determine the corresponding quantiles of the modeling error, $\varepsilon_i = F^{-1}\left(\Phi(z_i)\right)$.

(4) Substitute the standard normal quantile values selected in step (1) (i.e. z = {-1.5, -0.5, 0.5, 1.5}) and the corresponding modeling error quantiles ($\varepsilon_i$) determined in step (3) into Eqn. (A.38) or (A.39). This results in four equations and four unknowns (i.e. the Johnson distribution parameters: $\gamma$, $\delta$, $\lambda$, and $\xi$). Solving for these four equations simultaneously yields the solutions for the Johnson distribution parameters.

Consider the modeling error of translational wind speed ($V_t$) in Cell 72 as an example. Using the four target quantiles of the standard normal distribution listed in Step (1) (z = {-1.5, -0.5, 0.5, and 1.5}), the corresponding percentiles or cumulative probabilities are 0.07, 0.32, 0.69 and 0.93, respectively (Figure A.1a). The modeling errors at the target percentiles determined directly from the empirical CDF are -0.435, -0.109, 0.117, and 0.436, accordingly (Figure A.1b). Using the percentile matching procedure, the Johnson distribution parameters for the Gulf Coast filling rate modeling error are $\gamma$ = 0.017, $\delta$ = 1.114, $\lambda$ = 0.243, and $\xi$ 0.008.

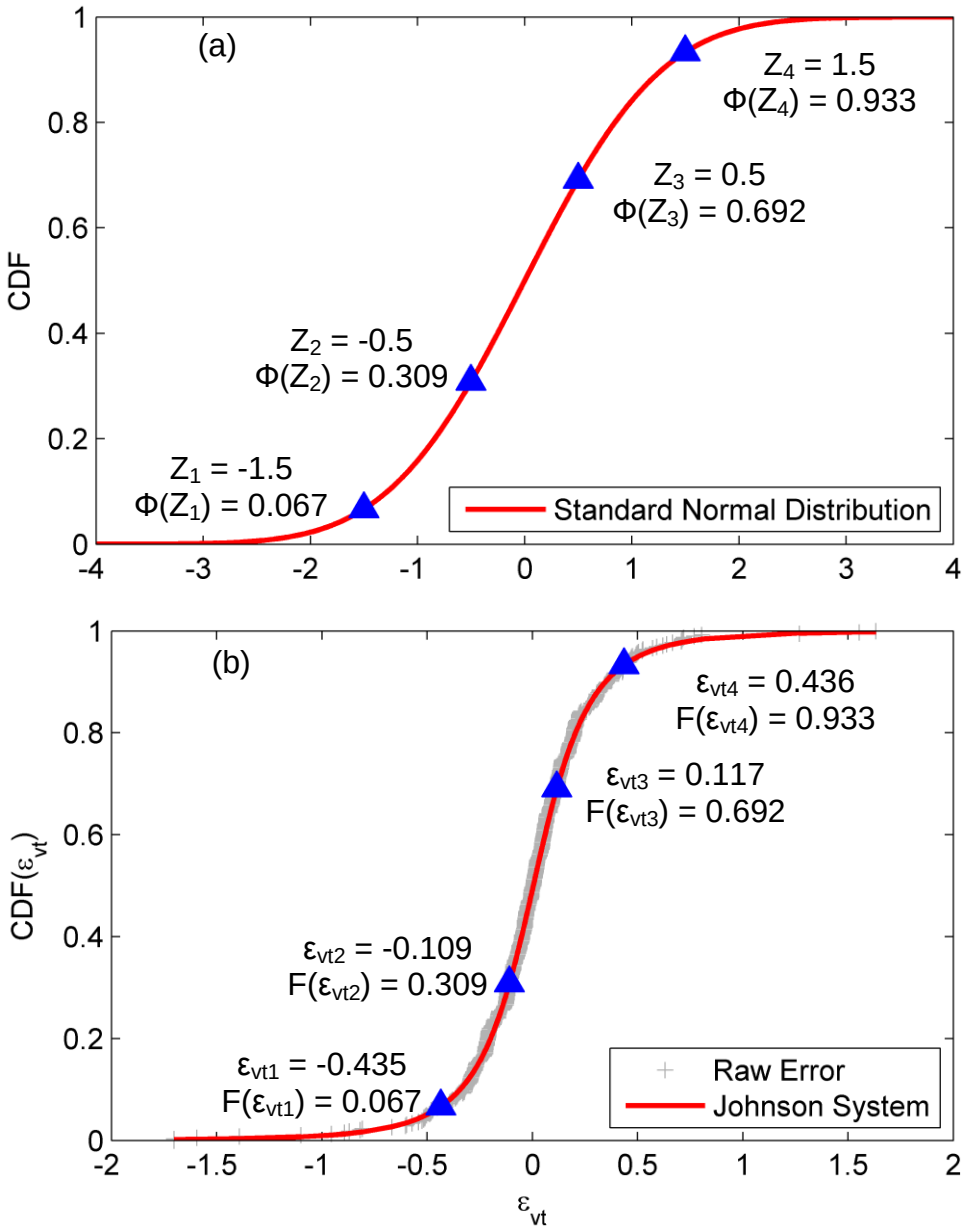


Figure A. 1: (a) Standard normal distribution, and (b) modeling error and Johnson SB distribution fit for the Gulf Coast model.

# APPENDIX B

## Tracking Model Plots for Selected Cells

The Plots of Tracking model for each cell include (1) scatter plot of logarithmic modeling errors; (2) scatter plot of logarithmic heading angle modeling errors; (3) CDF of forward speed modeling errors; (4) CDF of heading angle modeling errors; (5) change in forward speed without modeling error; (6) change in heading angle without modeling error; (7) change in forward speed with modeling error, and (8) change in heading angle with modeling error.

Cell 69, 70, 71, 72 (in Figure 3.1), 73, 95,118 and 141 are selected out of the total 220 cells in this session since they are the cells cover the coastline of the U.S. from the Gulf Coast to the New England Coast.

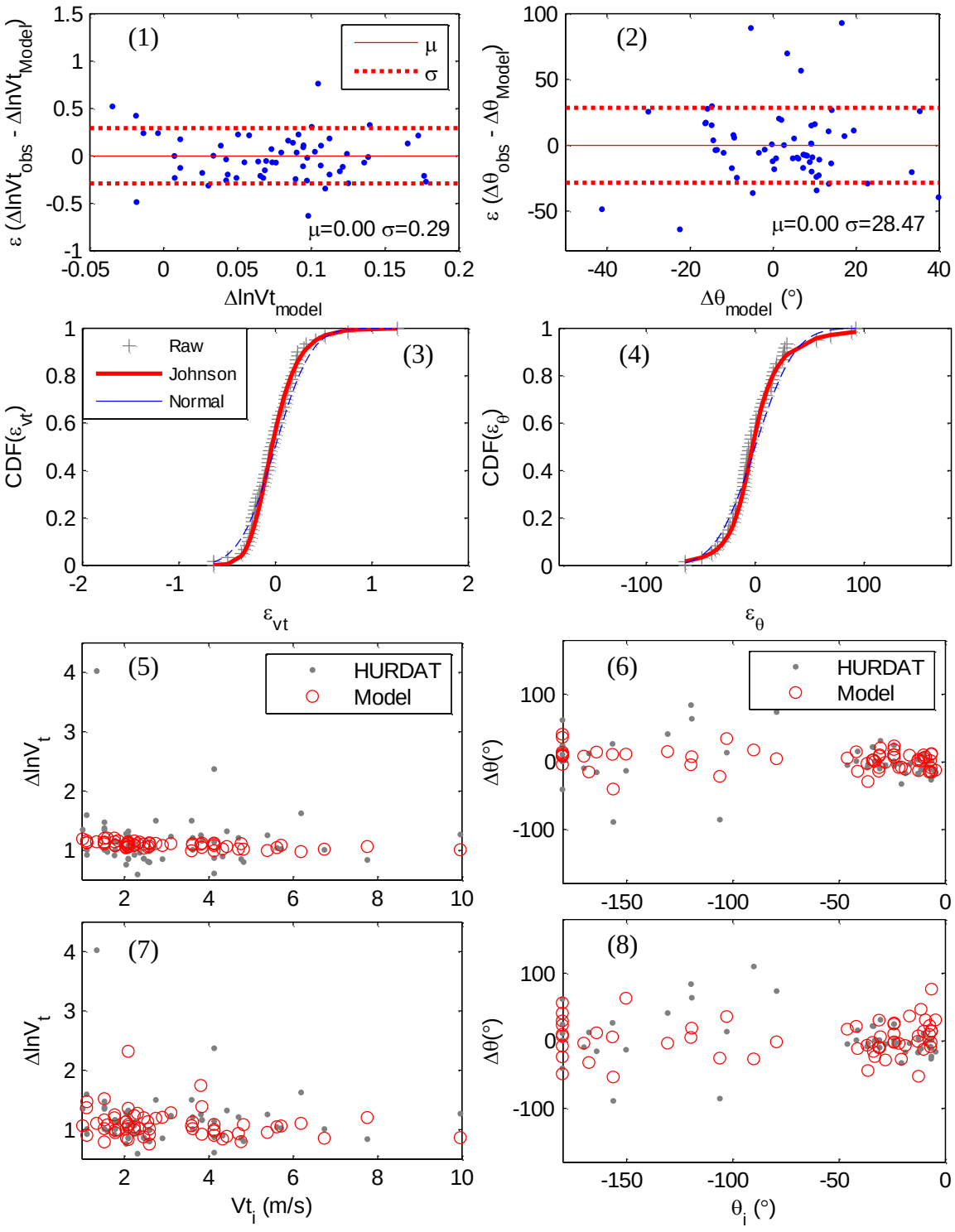


Figure B. 1: Tracking model information of Cell 69.

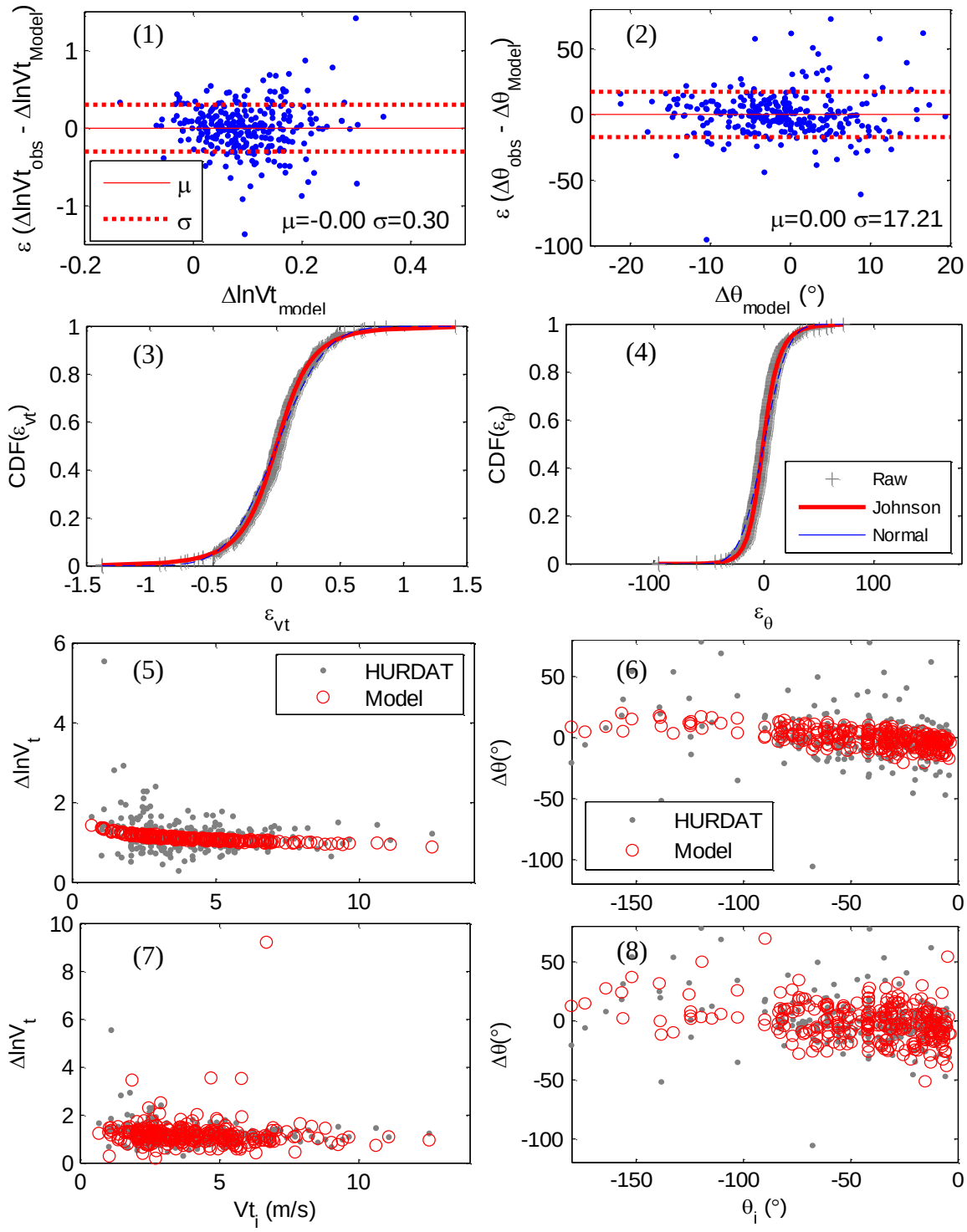


Figure B. 2: Tracking model information of Cell 70.

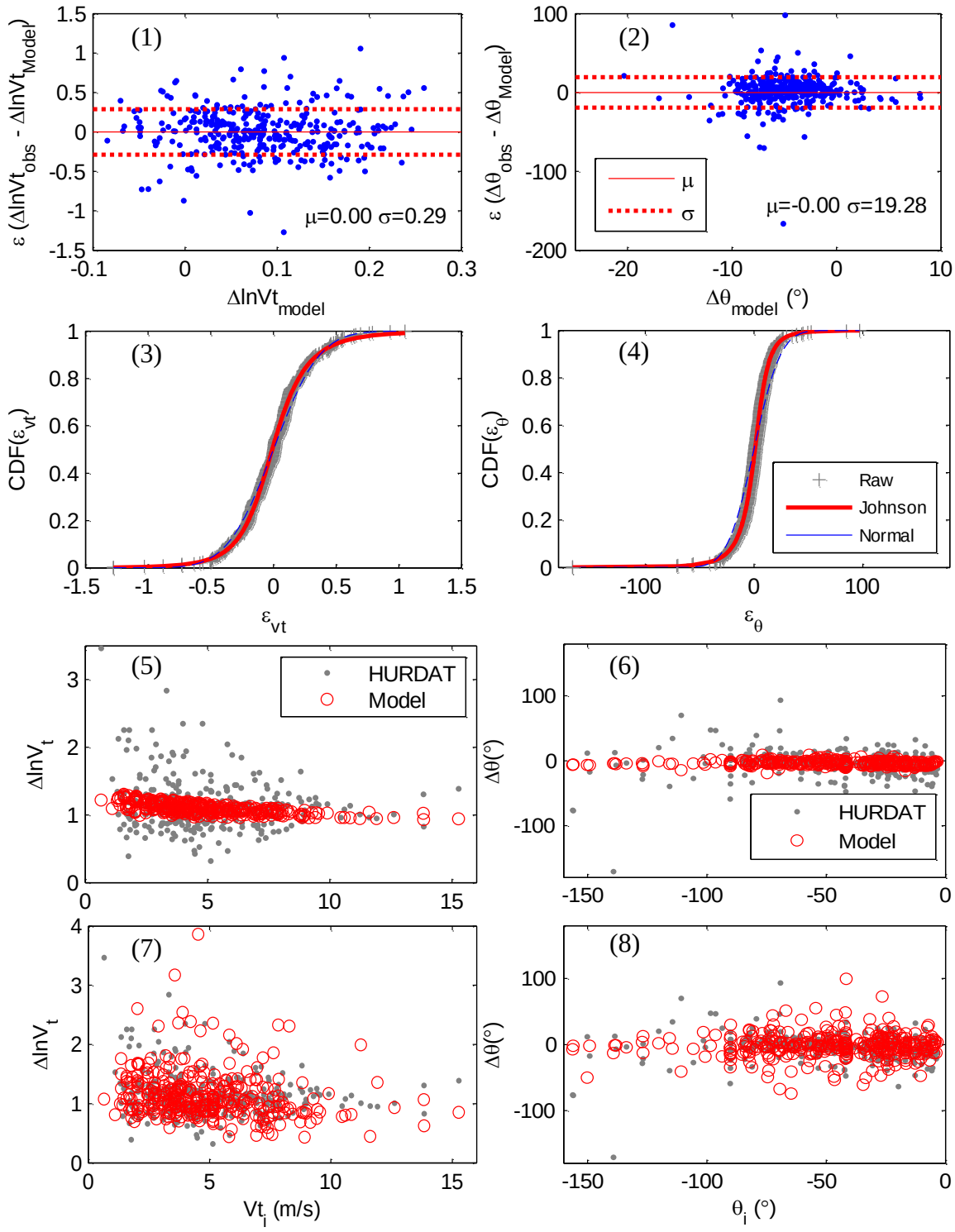


Figure B. 3: Tracking model information of Cell 71.

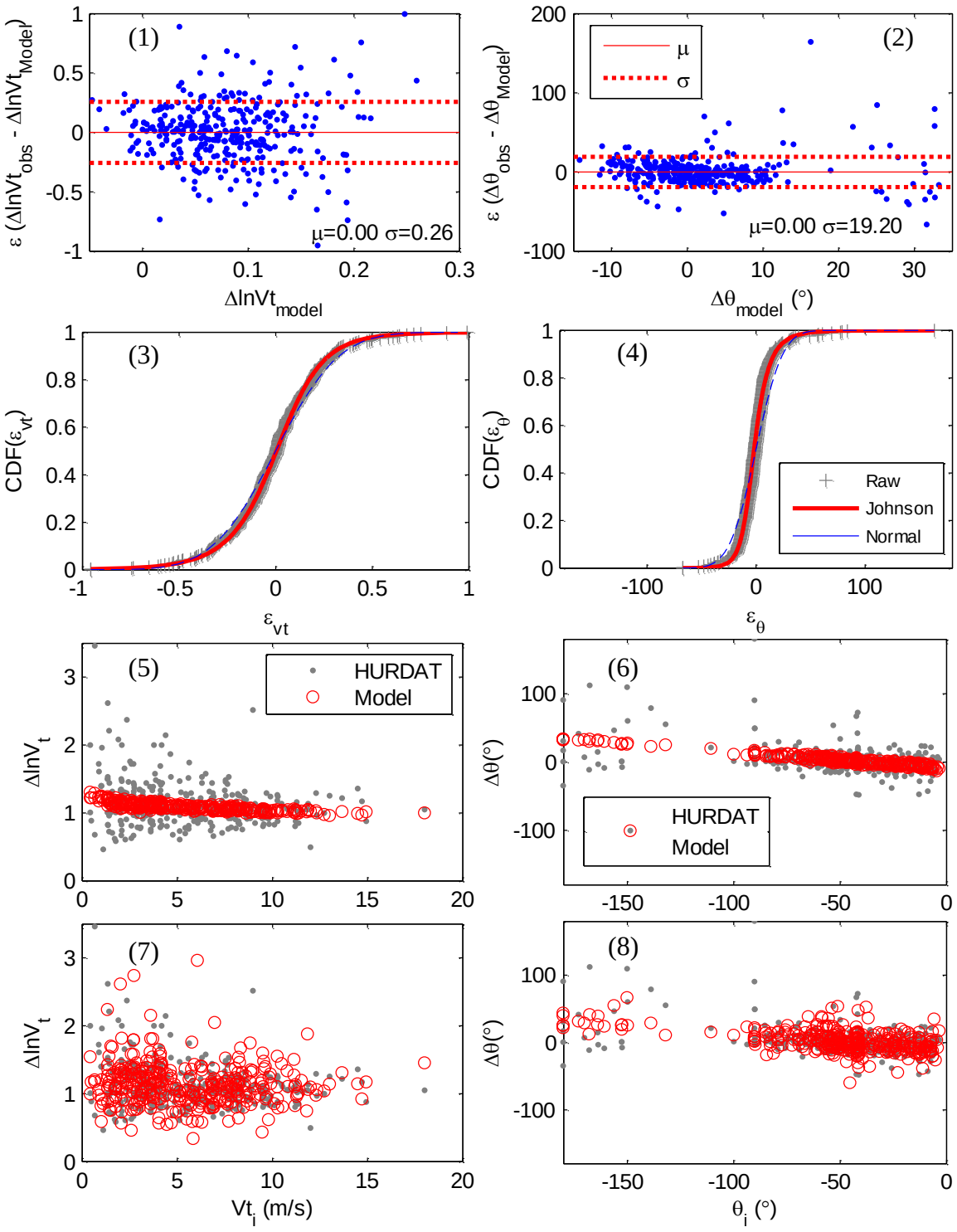


Figure B. 4: Tracking model information of Cell 73.

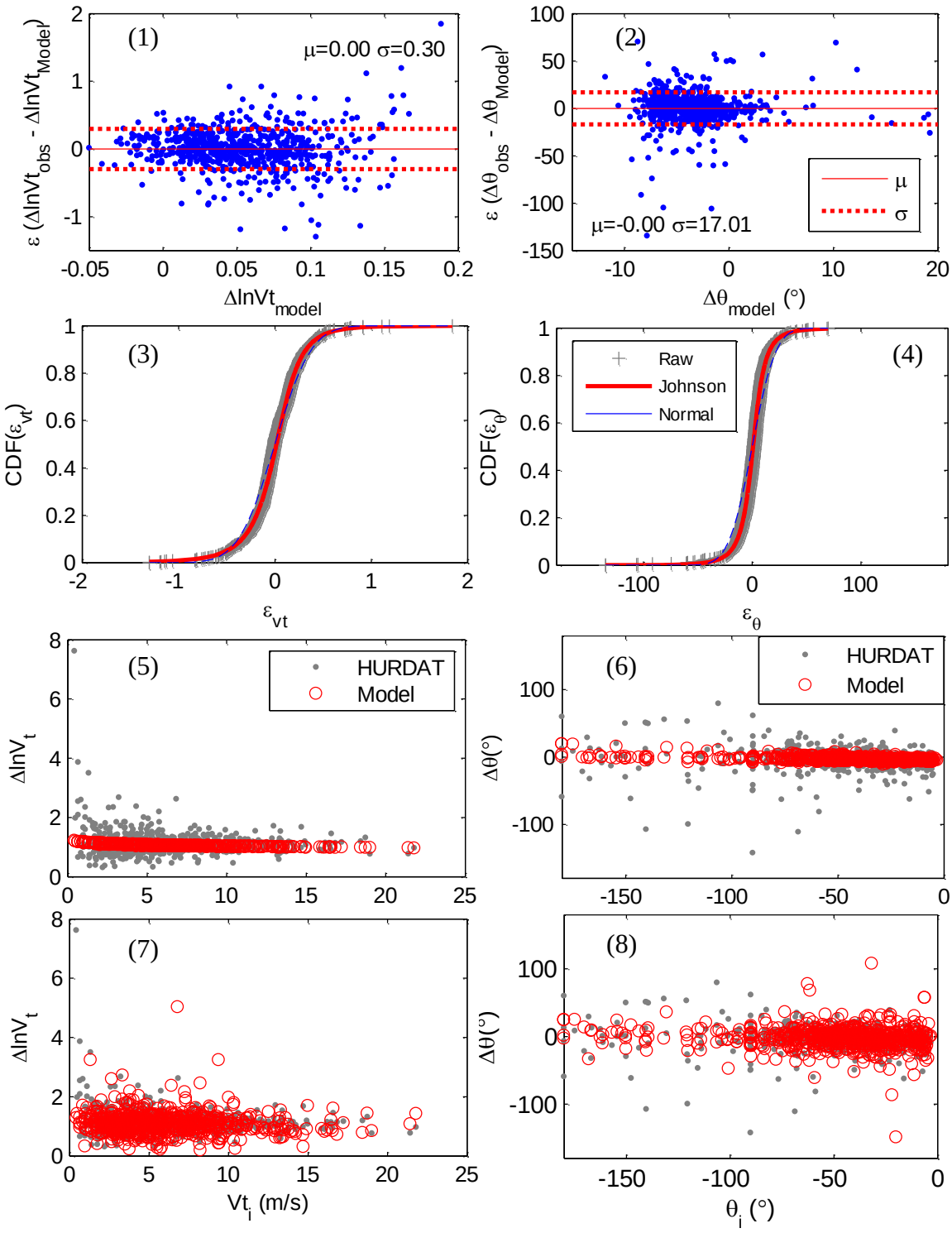


Figure B. 5: Tracking model information of Cell 95.

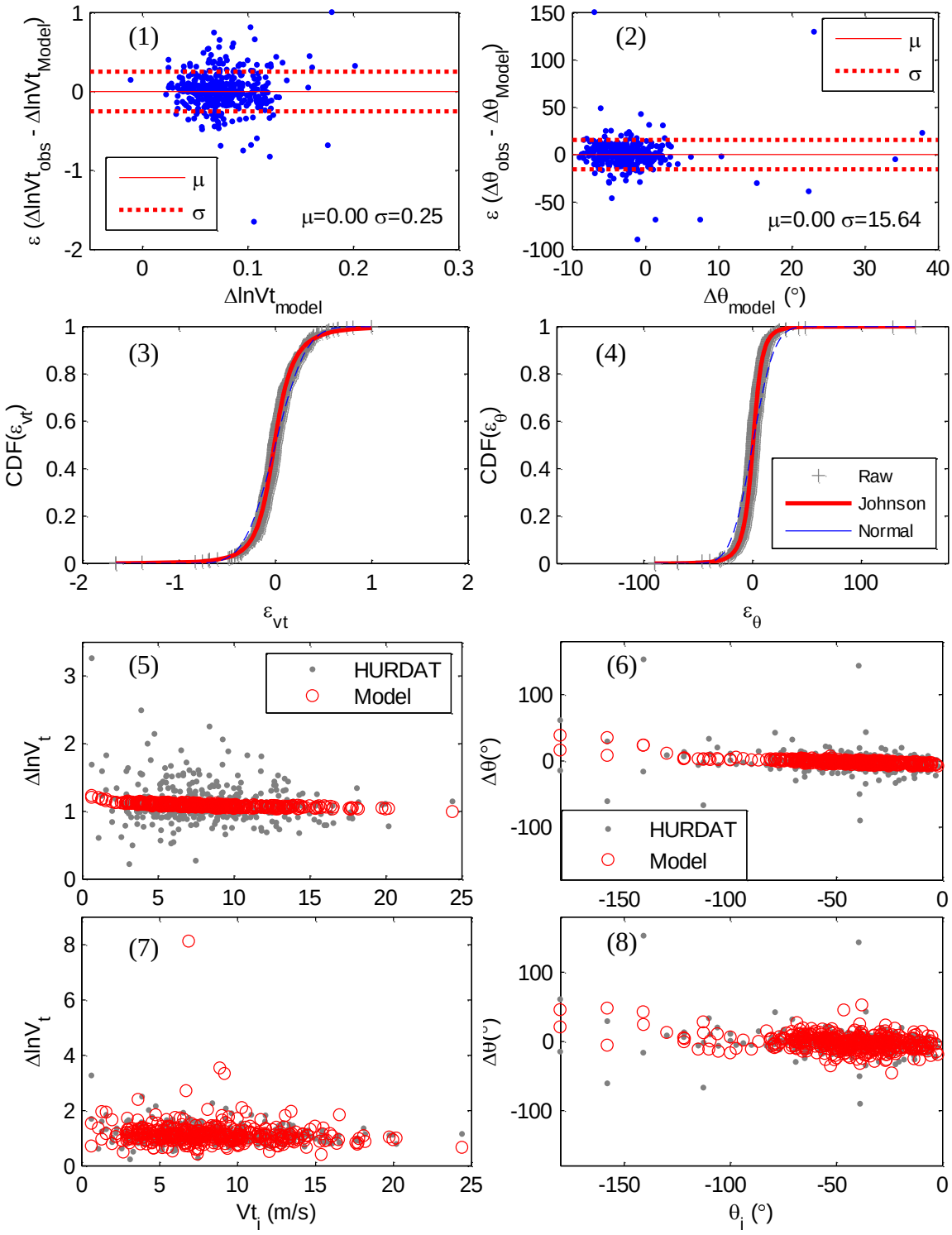


Figure B. 6: Tracking model information of Cell 118.

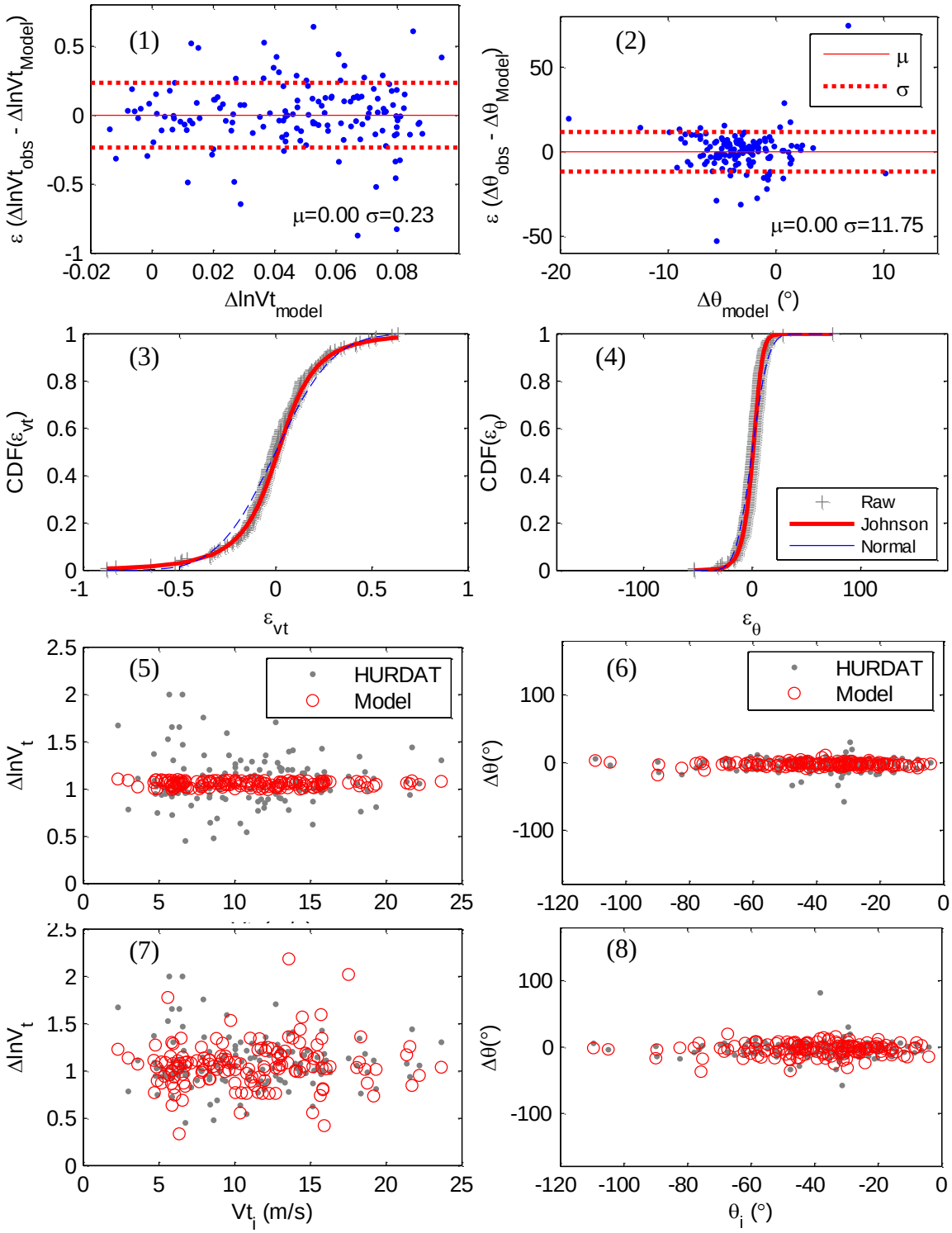


Figure B. 7: Tracking model information of Cell 140.

# APPENDIX C

## Assignment of Modeling Coefficients for Tracking and Relative Intensity Model on the Simulation Domain

The plots in this section show the assignments of modelling coefficients in tracking (Eqns. (5) and (6)) and relative intensity model (Eqn. (9)) over the simulation domain which is defined by latitudes from 10N˚ to 60N˚ and longitudes from 0˚ to 100W˚. The simulation domain is divided into 220 cells with dimension of 5˚ by 5˚. The numbers of the cells with more than six sets of raw data are shown in black font in the Figures. Those cells with insufficient records for coefficient fitting are shown in cyan color. To fill the entire simulation domain with coefficients, the numbers of cells from which the coefficients are copied are shown in blue color beneath the original number in the cells without sufficient data. The assignment for each cell might vary with the type of model (i.e. tracking or relative intensity) and heading direction of storm track (i.e. easterly or westerly).

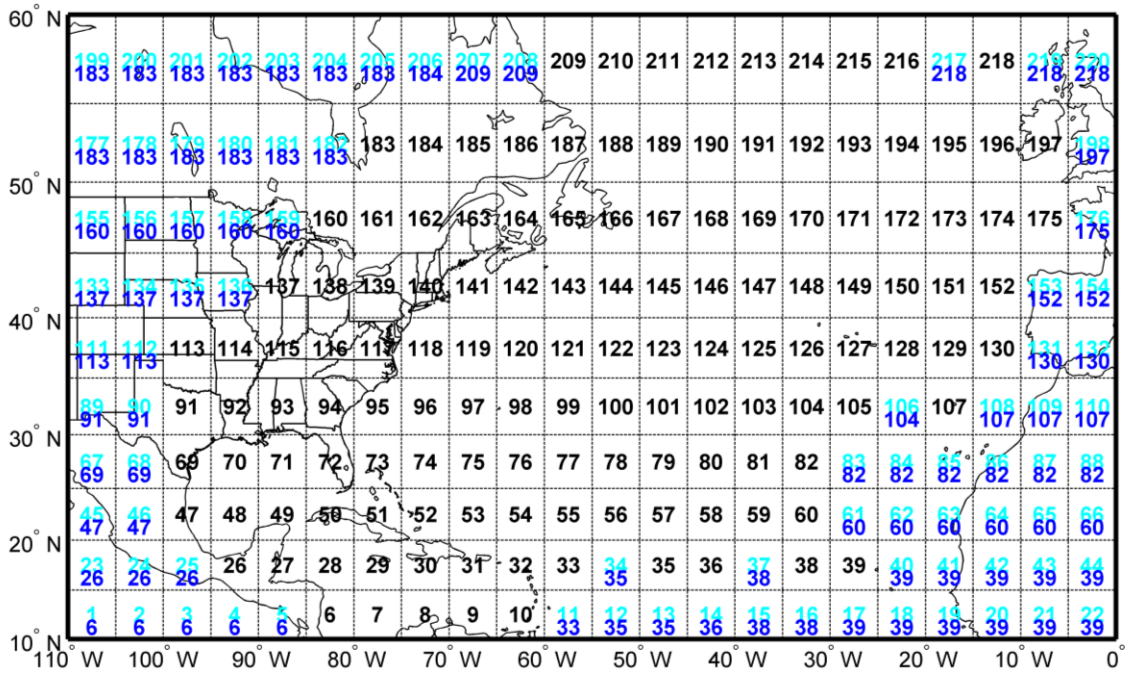


Figure C. 1: Coefficient assignments of tracking model for easterly travelling storms.

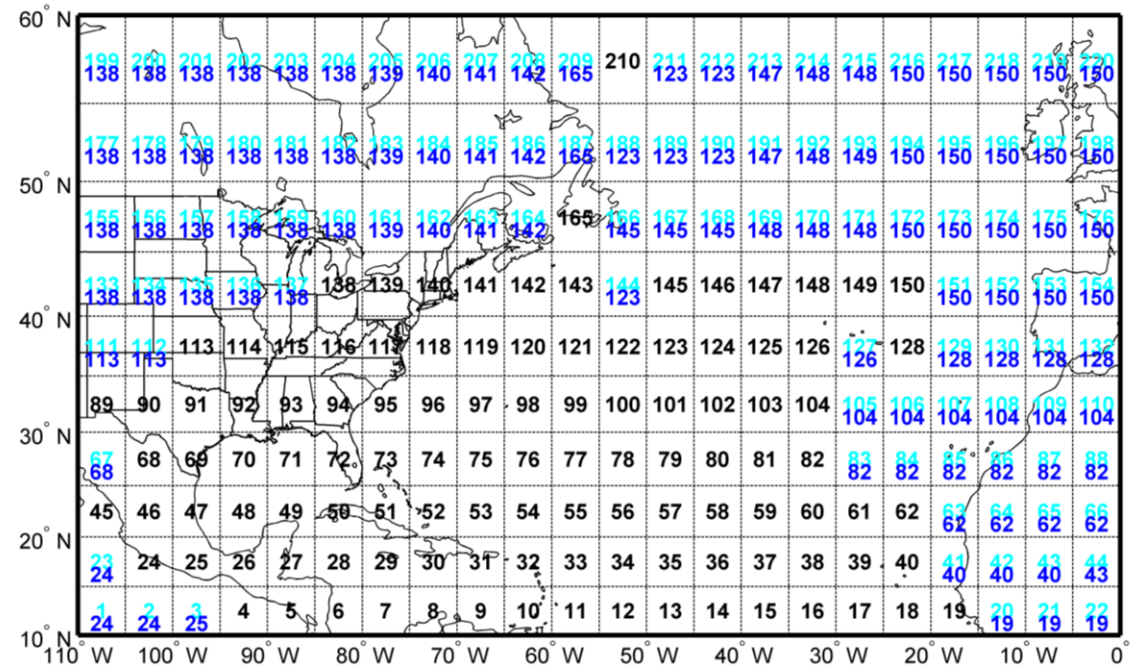


Figure C. 2: Coefficient assignments of tracking model for westerly travelling storms.

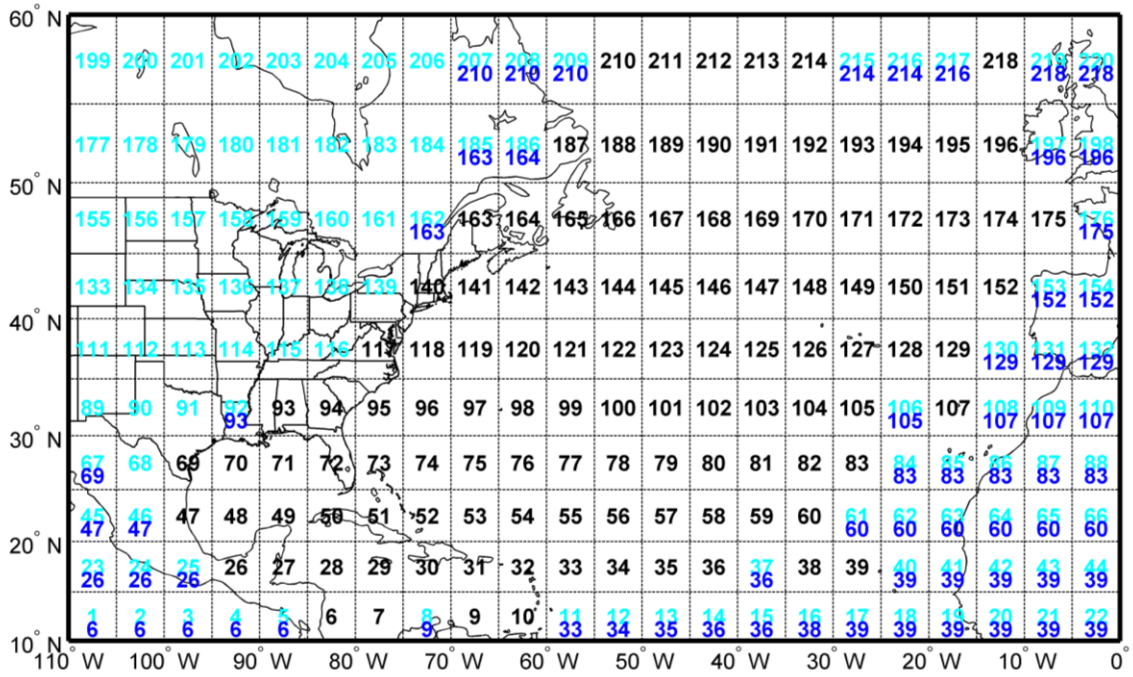


Figure C. 3: Coefficient assignments of relative intensity model for easterly travelling storms.

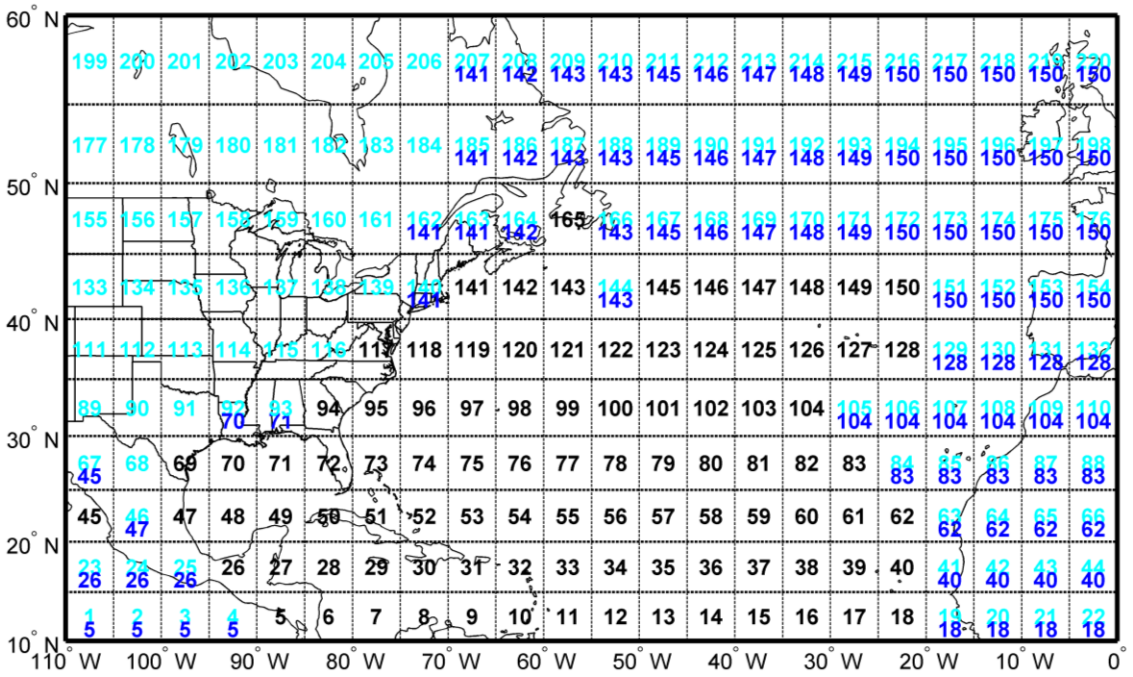


Figure C. 4: Coefficient assignments of relative intensity model for westerly travelling storms.

# APPENDIX D

## Relative Intensity Model Plots for Selected Cells

The Plots of relative intensity model for each cell include (1) scatter plot of logarithmic modeling errors; (2) CDF of modeling errors; (3) modeled central pressure without modeling error; (4) modeled central pressure with modeling error.

Cell 69, 70, 71, 72, 73, 95,118 and 141 are selected out of the total 220 cells in this session since they are the cells cover the coastline of the U.S. from the Gulf Coast to the New England Coast.

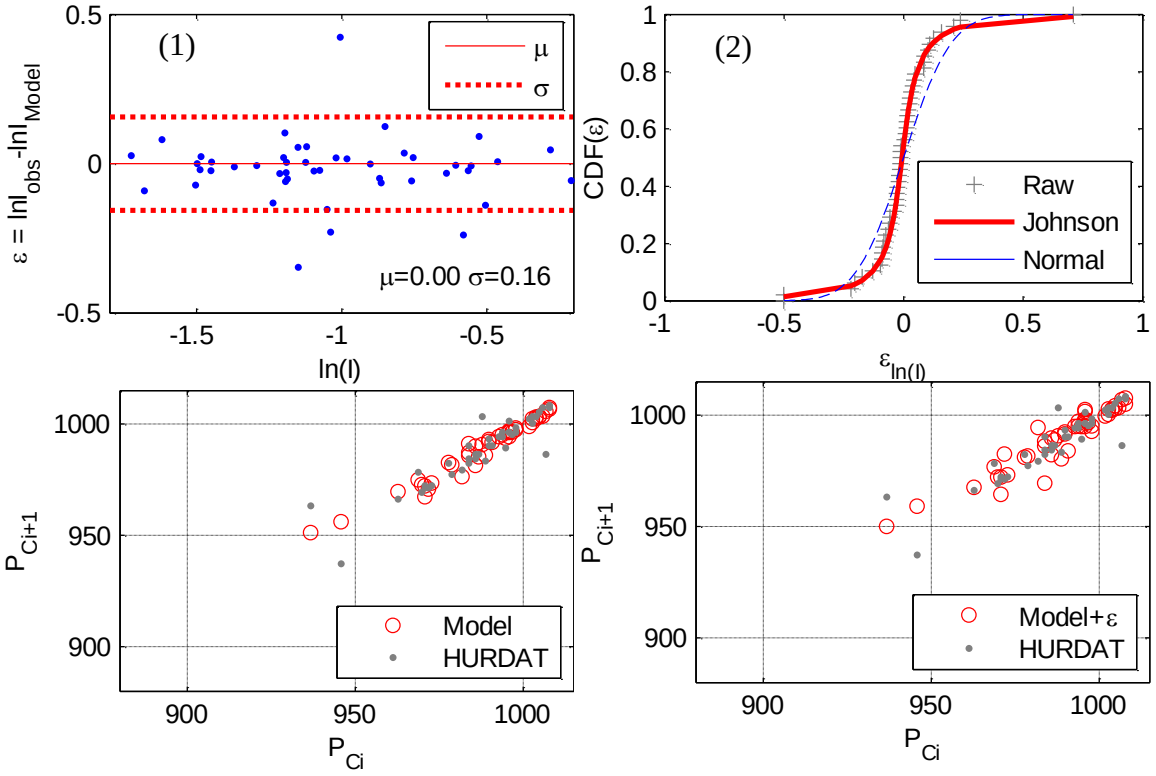


Figure D. 5: Central pressure model information of Cell 69.

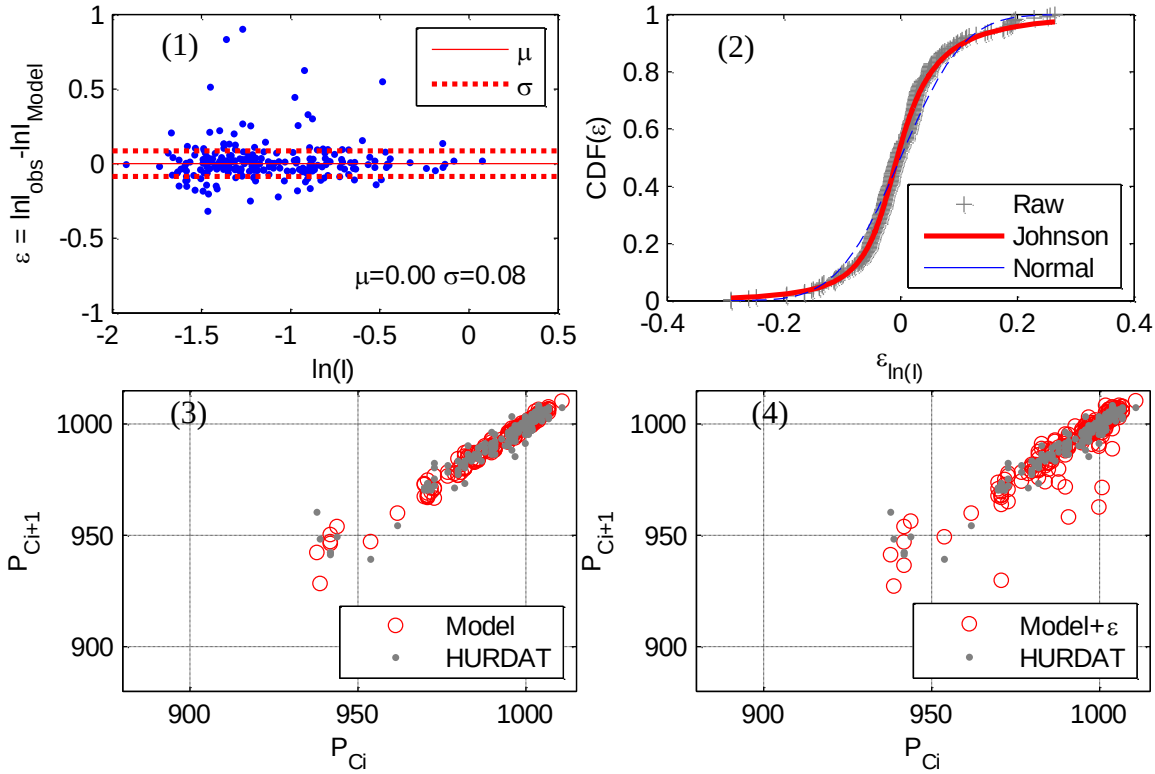


Figure D. 6: Central pressure model information of Cell 70.

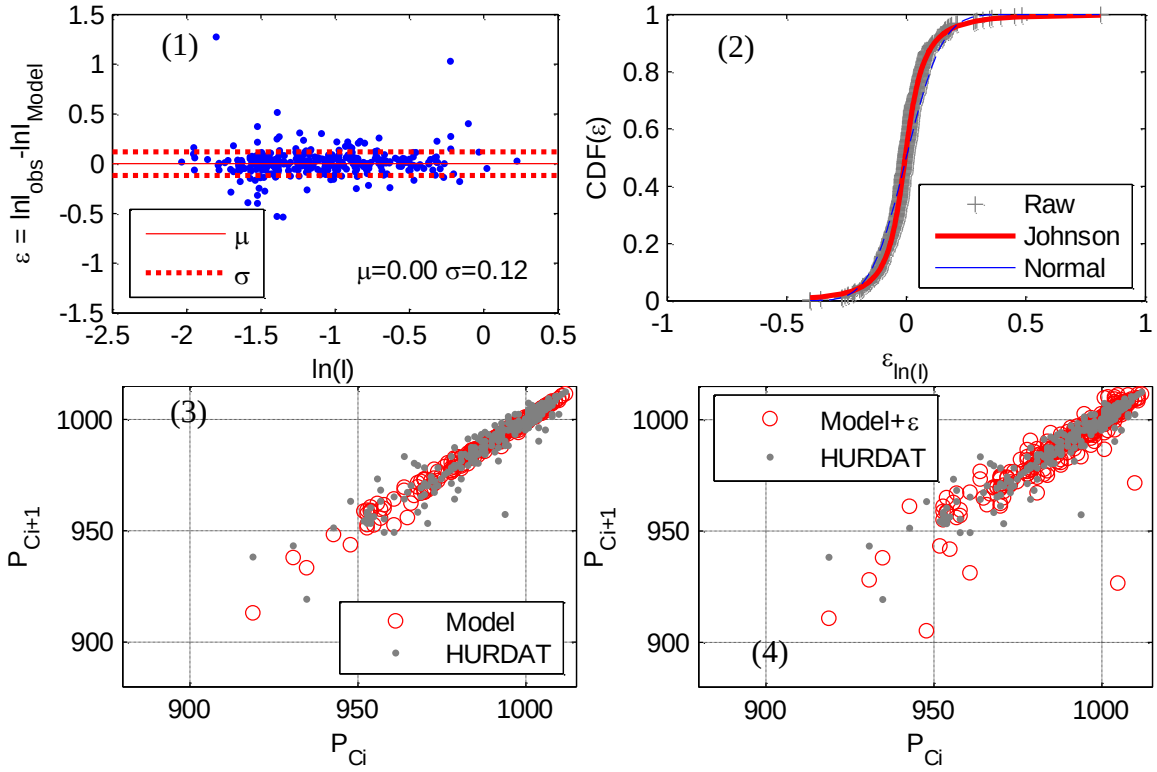


Figure D. 7: Central pressure model information of Cell 71.

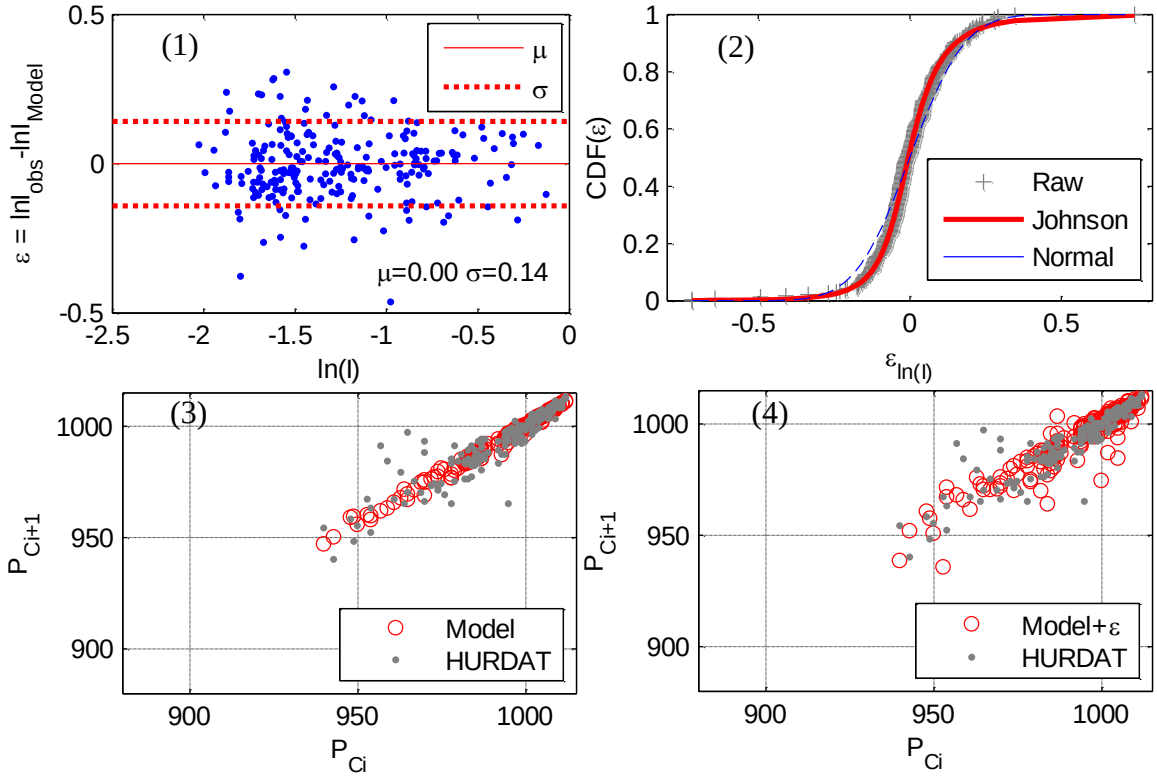


Figure D. 8: Central pressure model information of Cell 72.

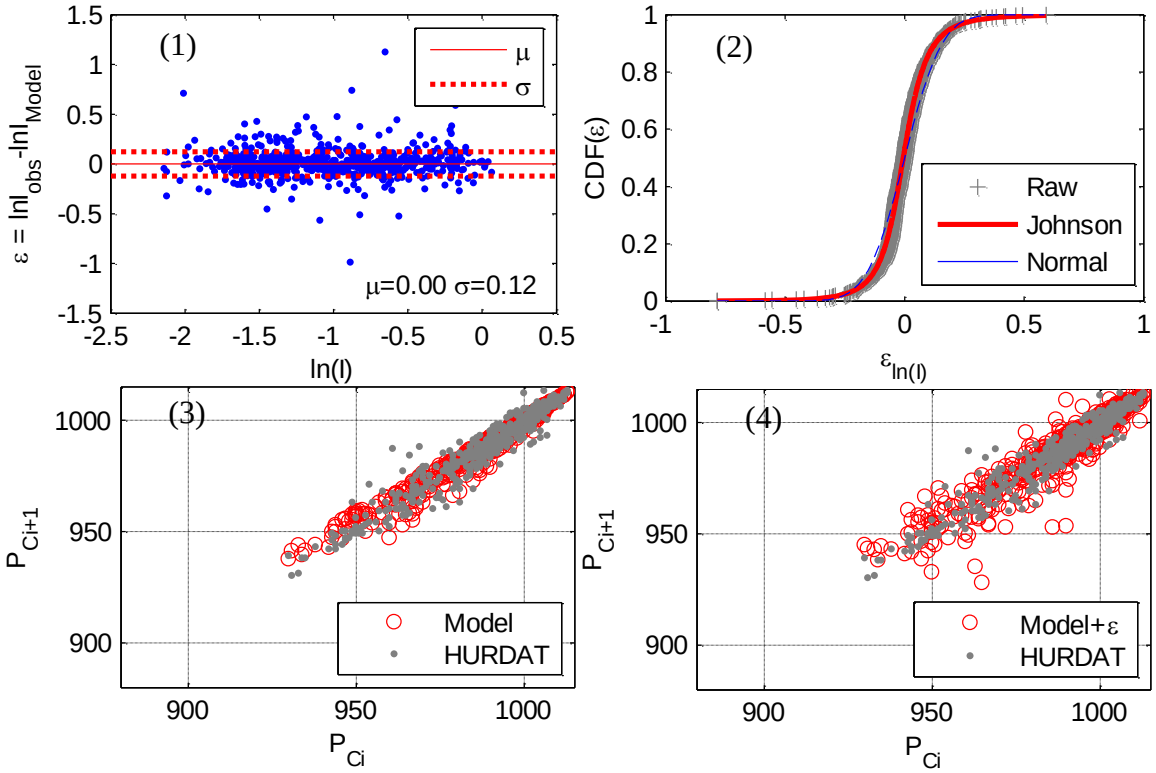


Figure D. 9: Central pressure model information of Cell 73.

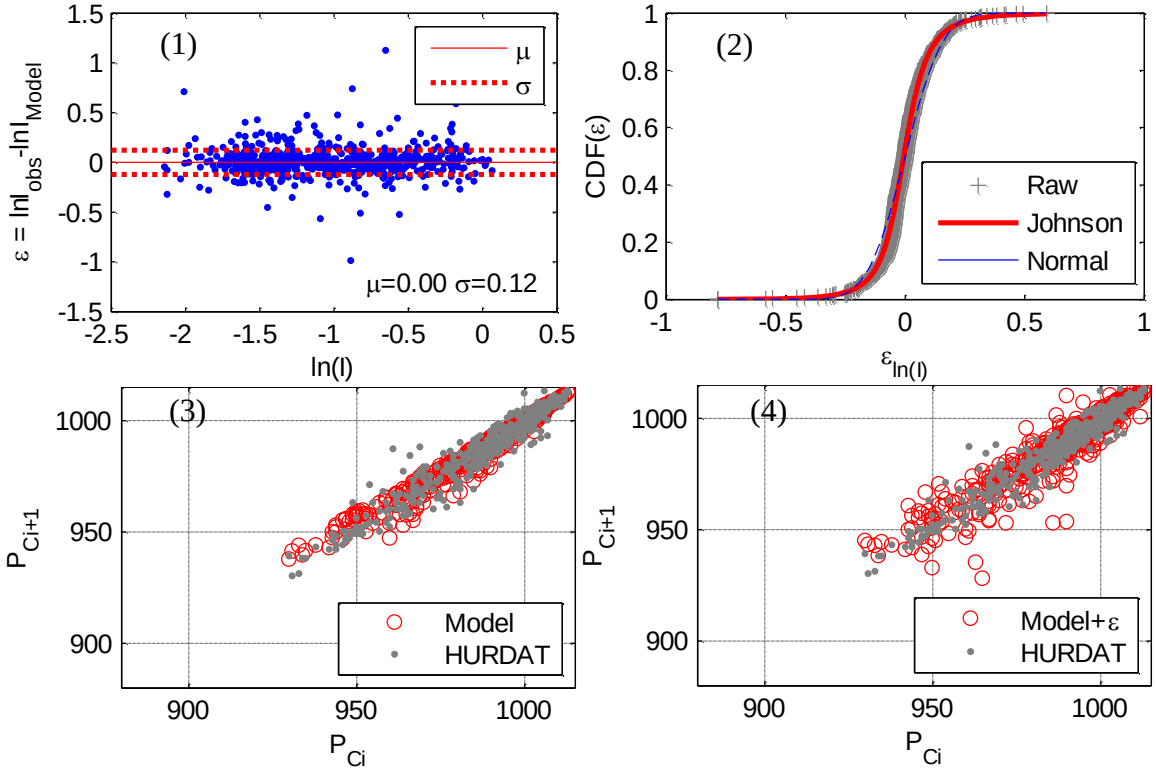


Figure D. 10: Central pressure model information of Cell 95.

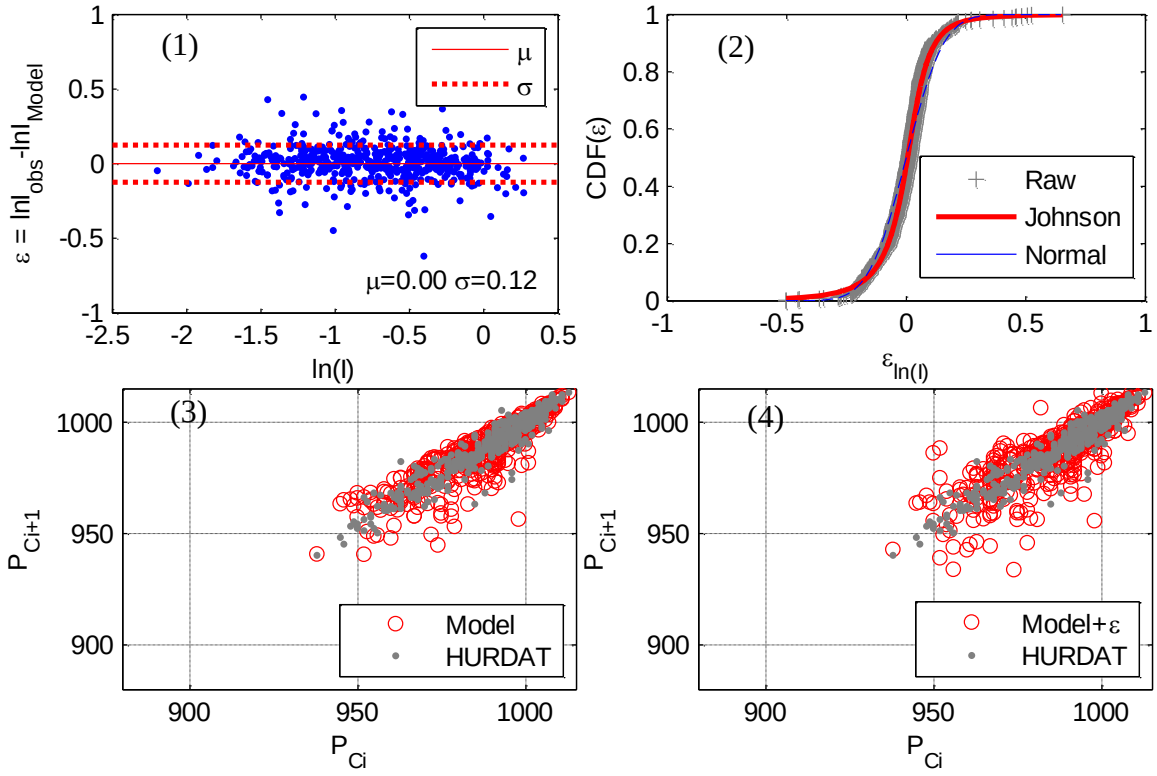


Figure D. 11: Central pressure model information of Cell 118.

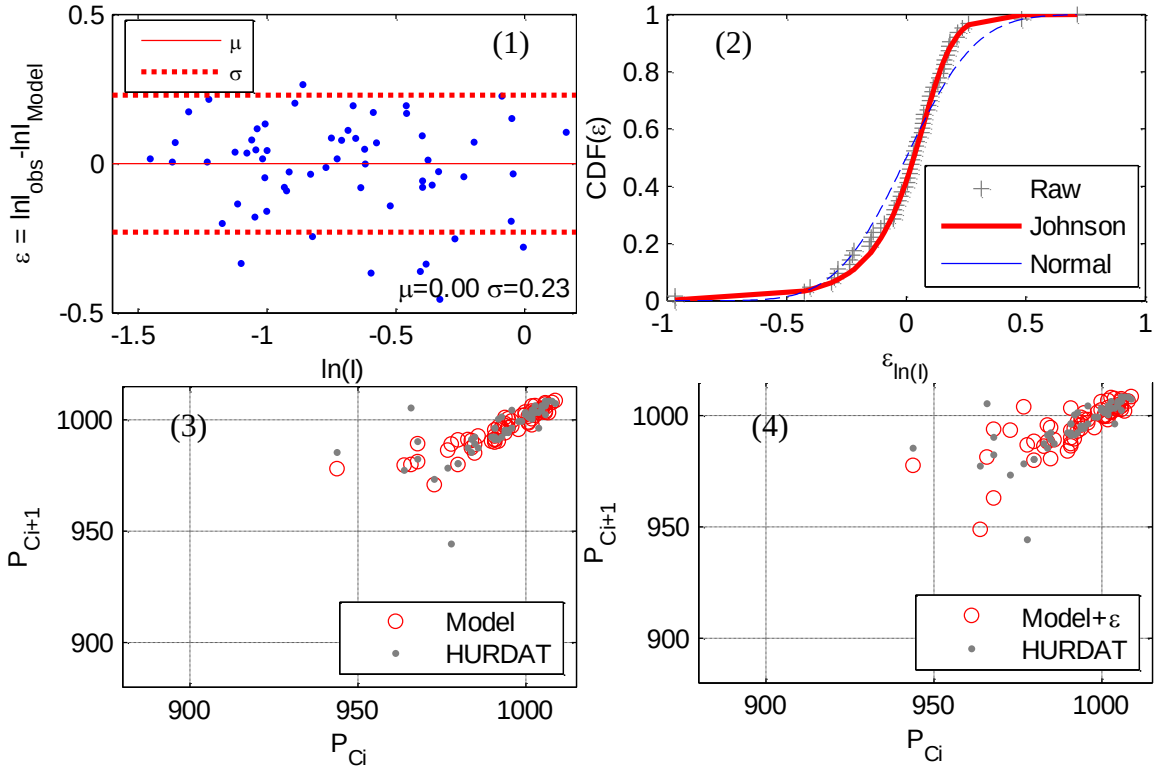


Figure D. 12: Central pressure model information of Cell 140.

# APPENDIX E

## Statistics of Characteristic Parameters from Baseline Simulations in Selected Cells

Figure (1) (3) and (5) show the distributions of heading angle, translational wind speed and central pressure in percentages fallen into four bins in the specified cell; Figure (2), (4) and (6) show the simulations of heading angle, translational wind speed and central pressure made at step *i* versus the values from its previous steps (step *i-1*) which served as the input in the models.

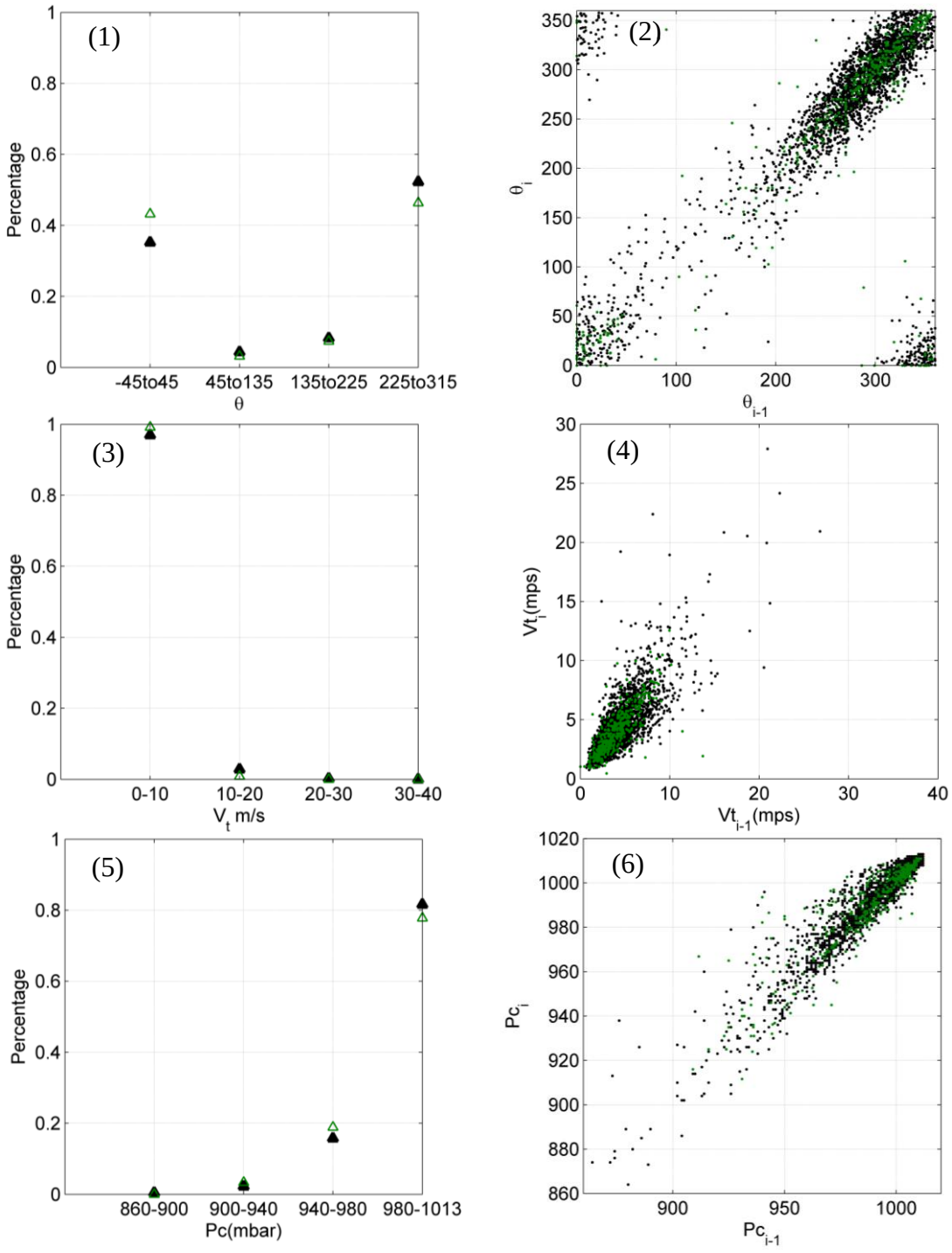


Figure E. 1: Statistics of hurricane parameters in Cell 69 (Black dots represent simulated results; green ones represent observations).

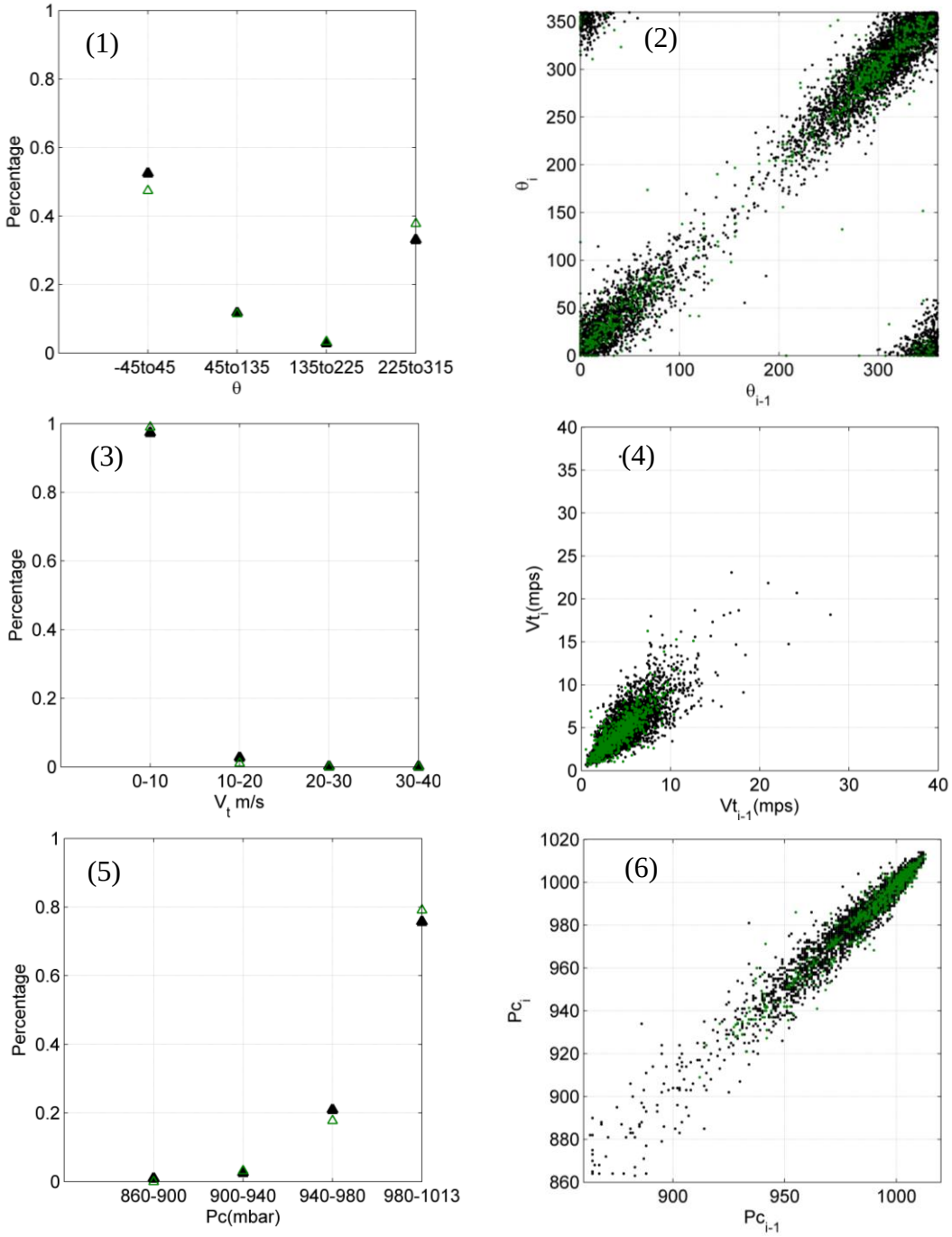


Figure E. 2: Statistics of hurricane parameters in Cell 70 (Black dots represent simulated results; green ones represent observations).

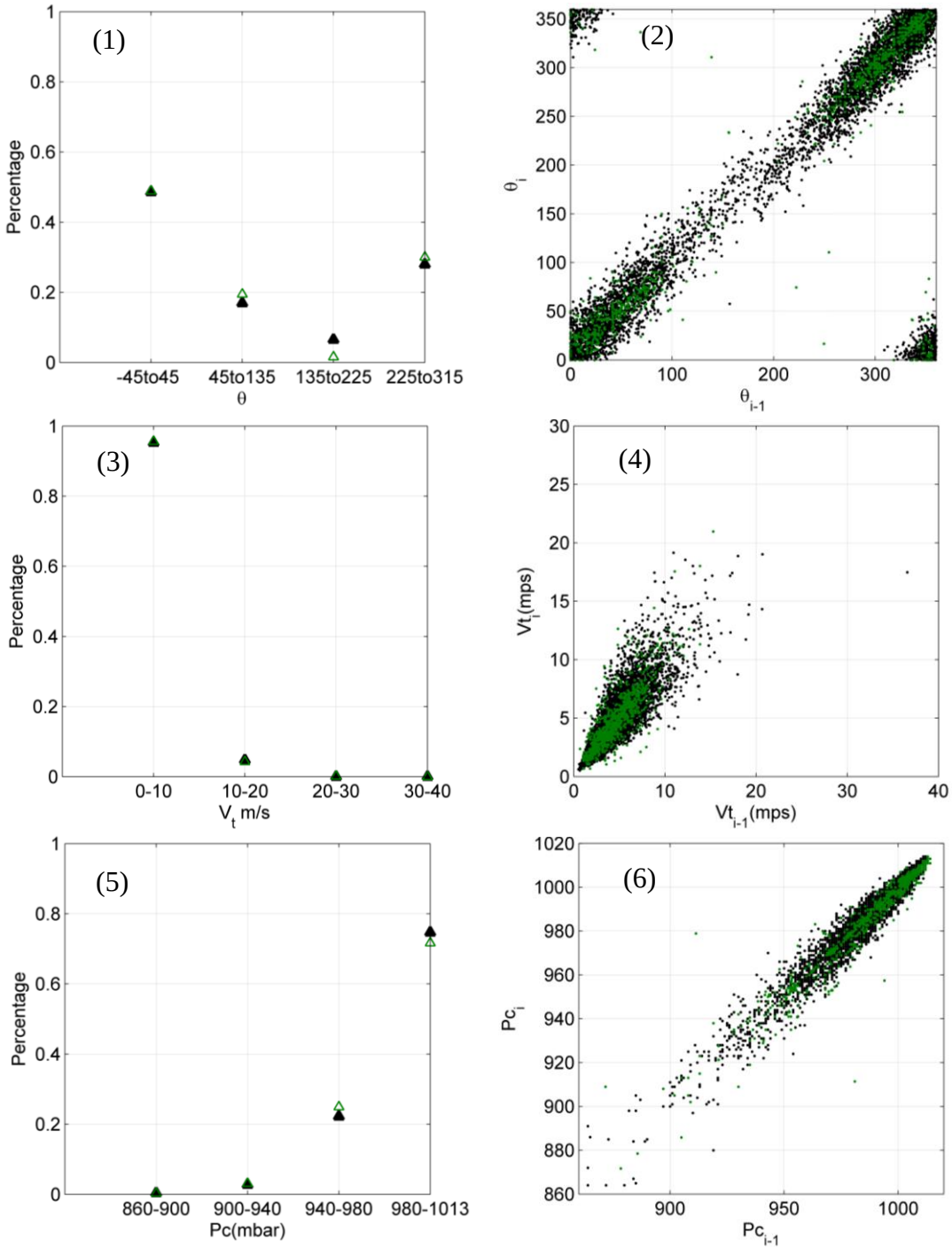


Figure E. 3: Statistics of hurricane parameters in Cell 71 (Black dots represent simulated results; green ones represent observations).

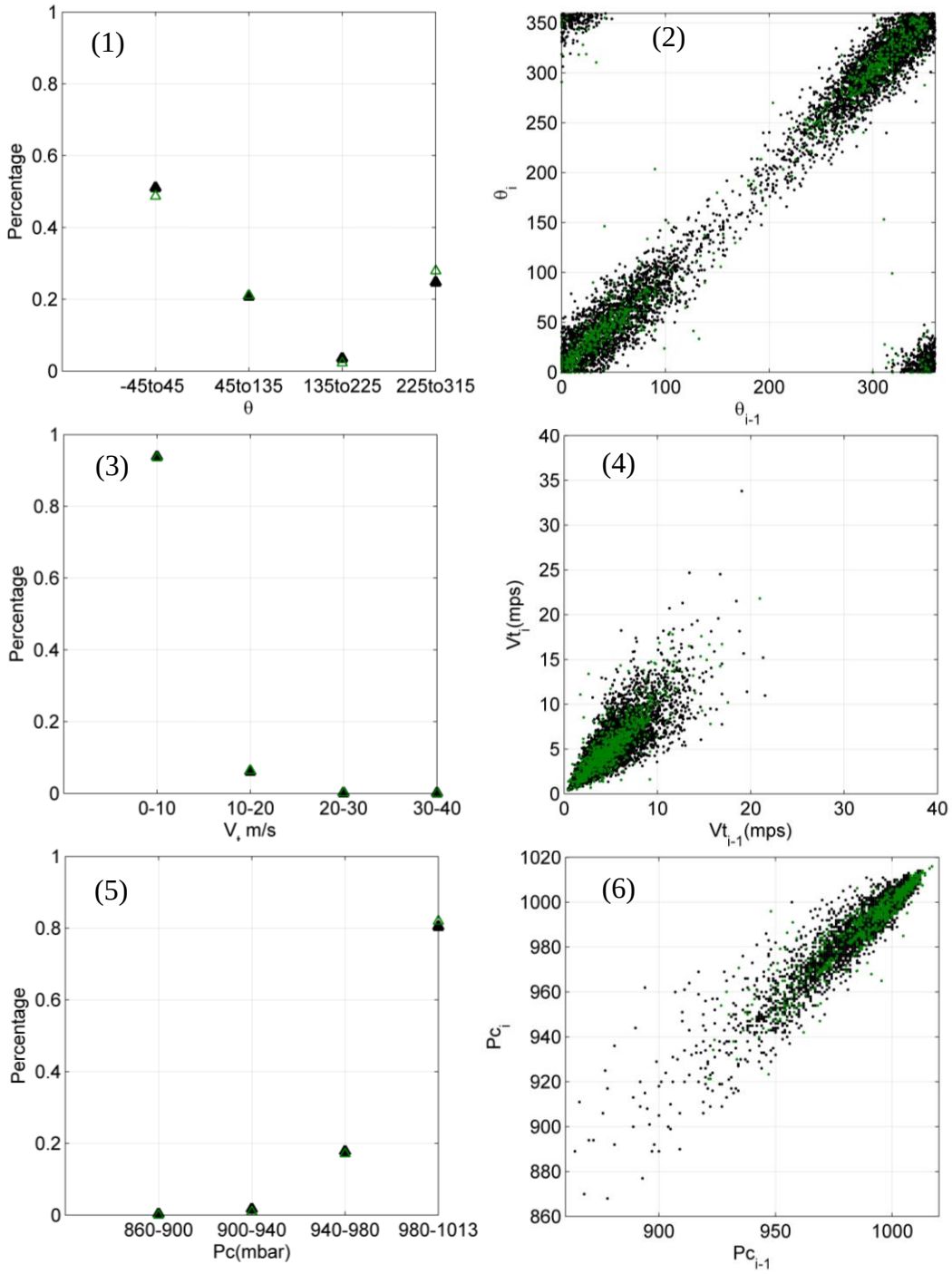


Figure E. 4: Statistics of hurricane parameters in Cell 72 (Black dots represent simulated results; green ones represent observations).

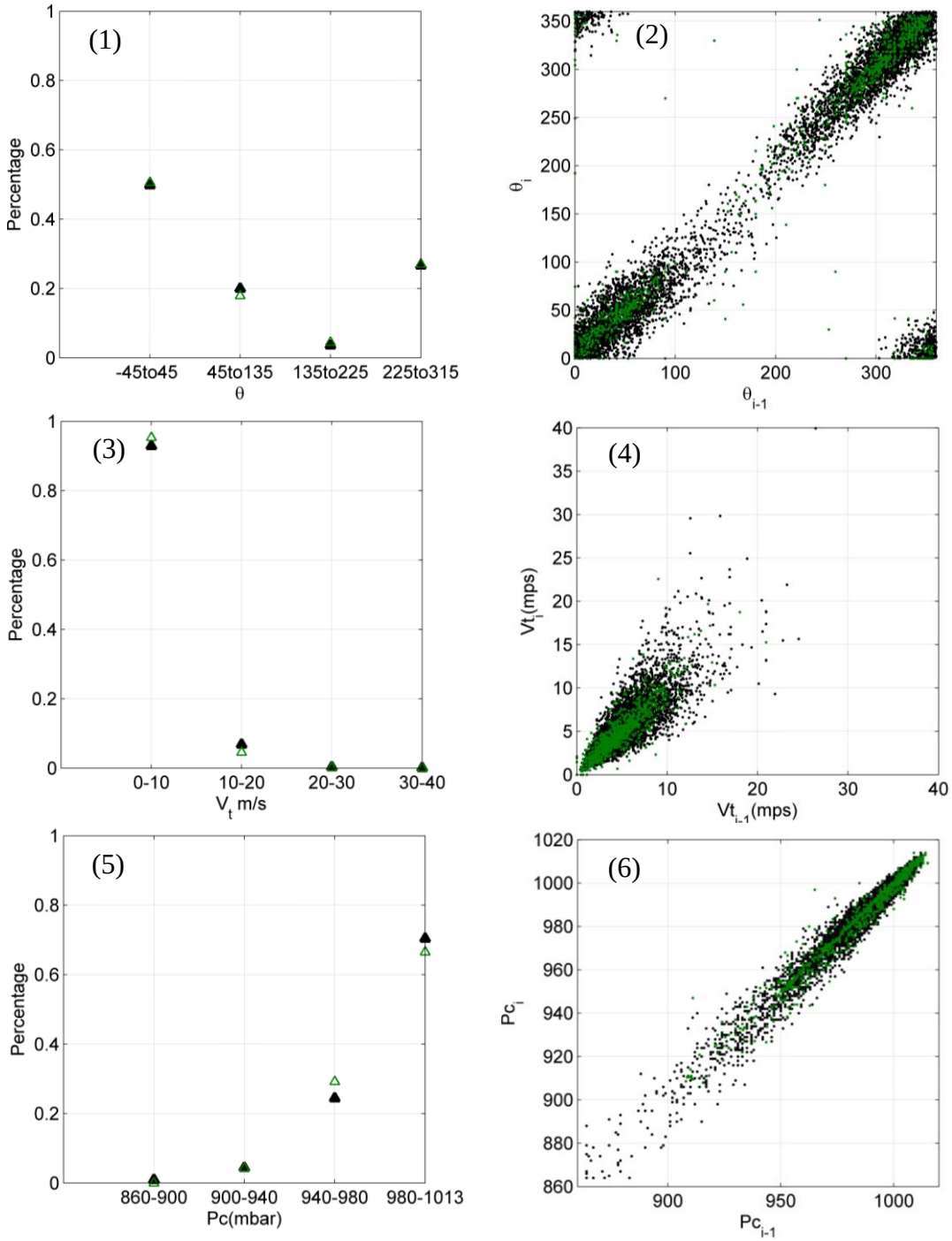


Figure E. 5: Statistics of hurricane parameters in Cell 73 (Black dots represent simulated results; green ones represent observations).

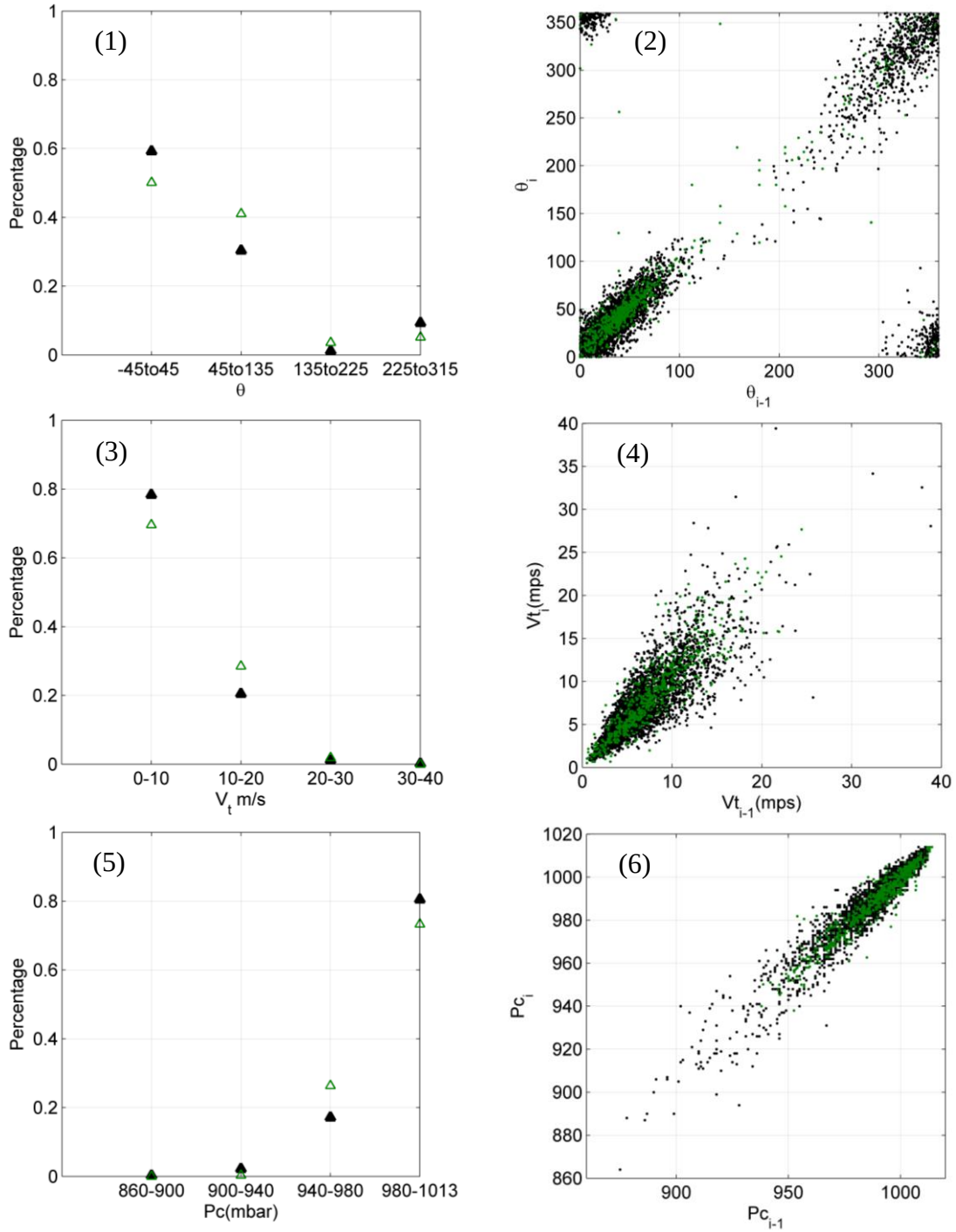


Figure E. 6: Statistics of hurricane parameters in Cell 118 (Black dots represent simulated results; green ones represent observations).

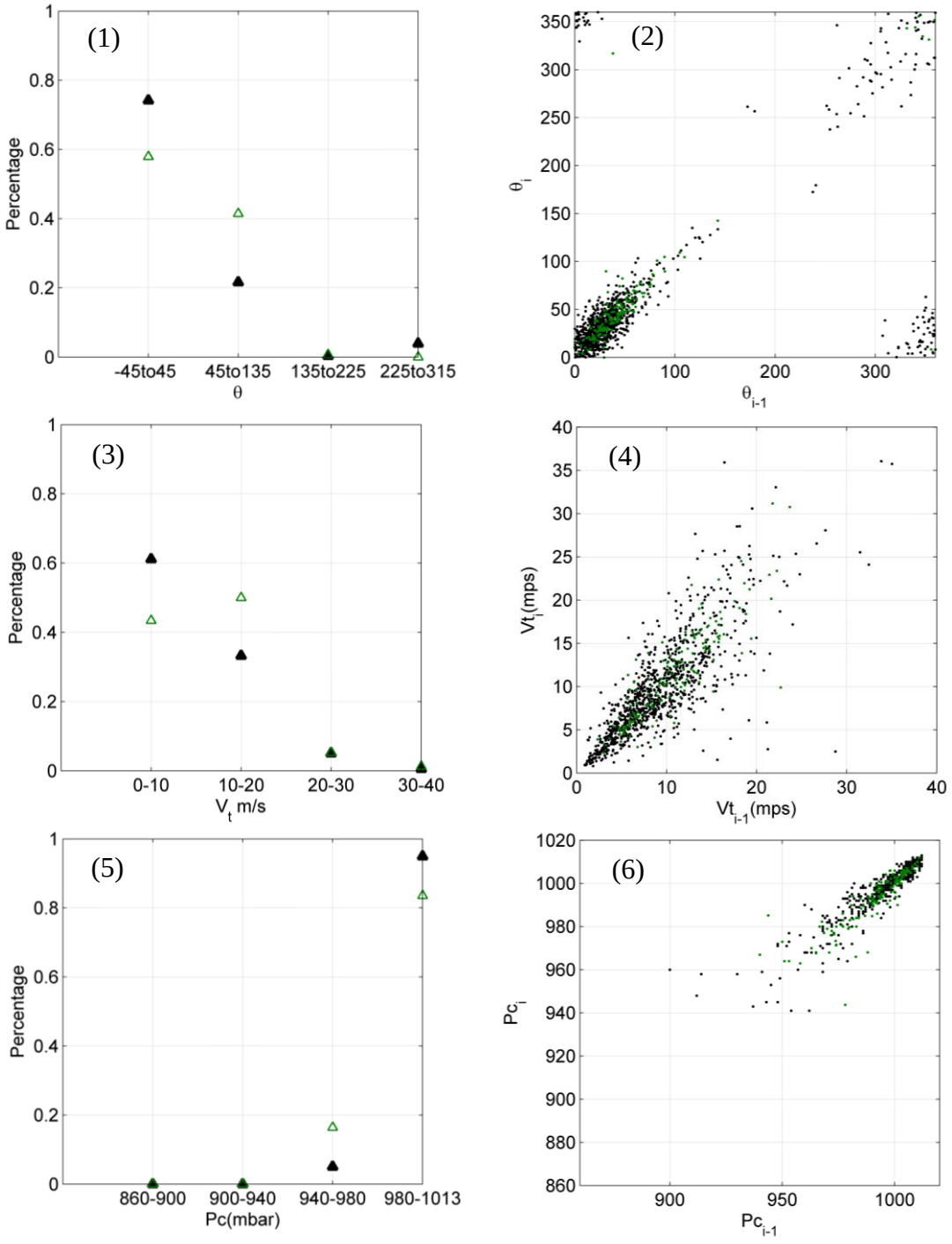


Figure E. 7: Statistics of hurricane parameters in Cell 140 (Black dots represent simulated results; green ones represent observations).

# APPENDIX F

## Statistics of Translational Wind Speed and Heading Angle at Mileposts from the Simulations in Sensitivity Study

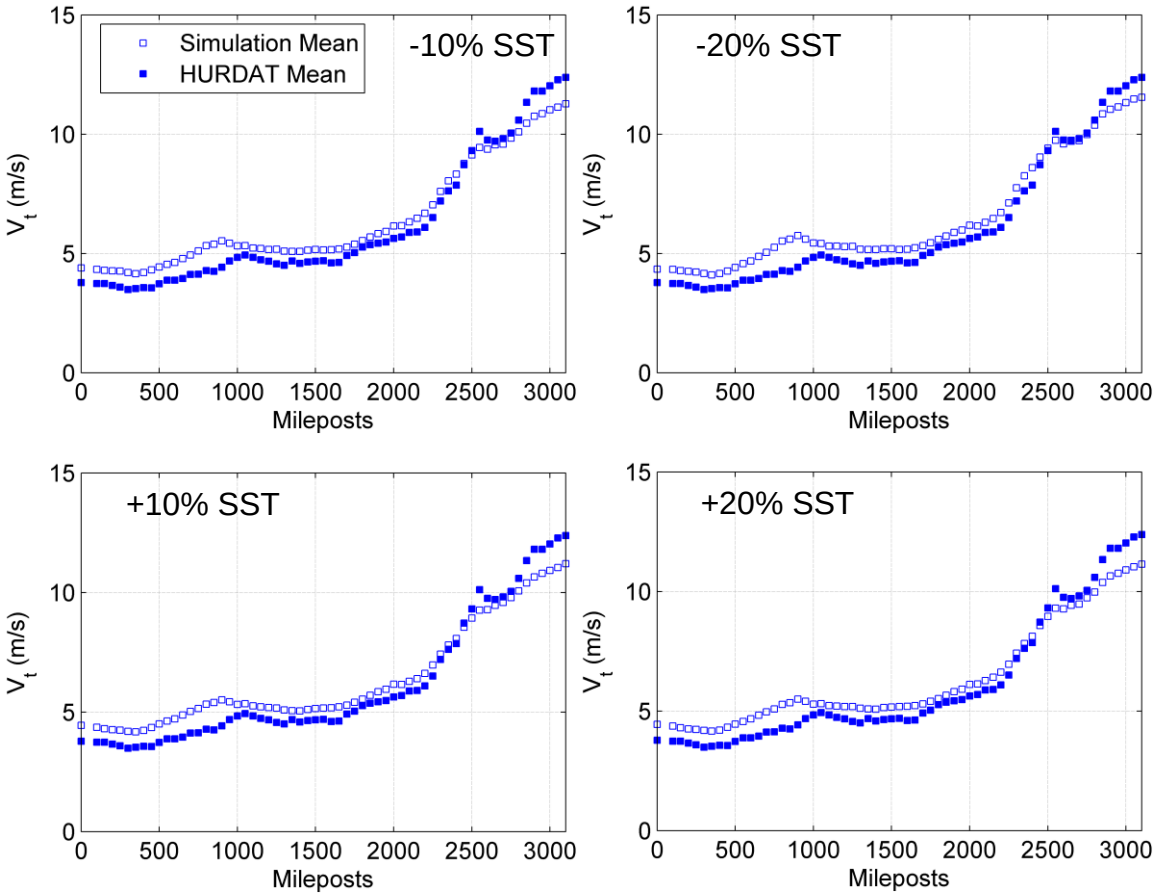


Figure F. 1: Statistics of translational wind speed at mileposts along the coastline in the sensitivity studies on SST.

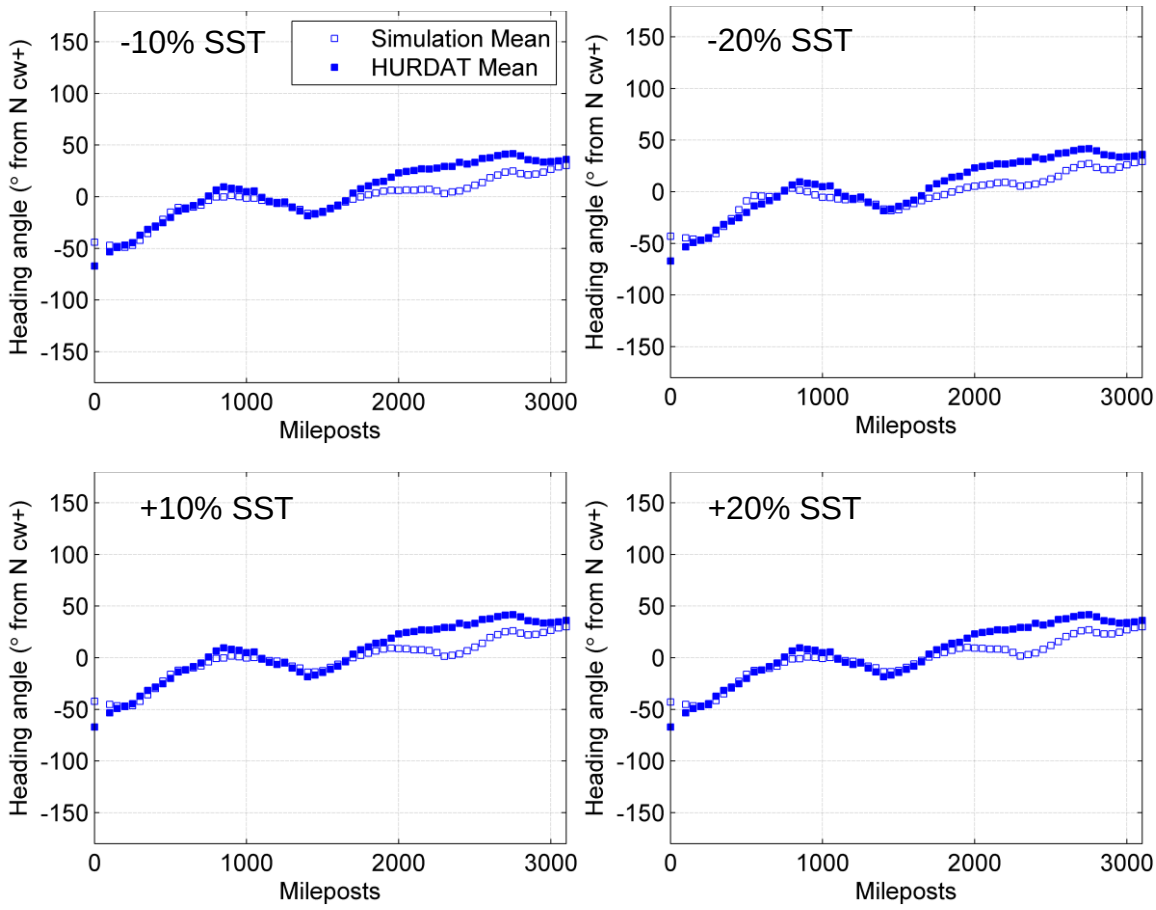


Figure F. 2: Statistics of heading angle at mileposts along the coastline in the sensitivity studies on SST.

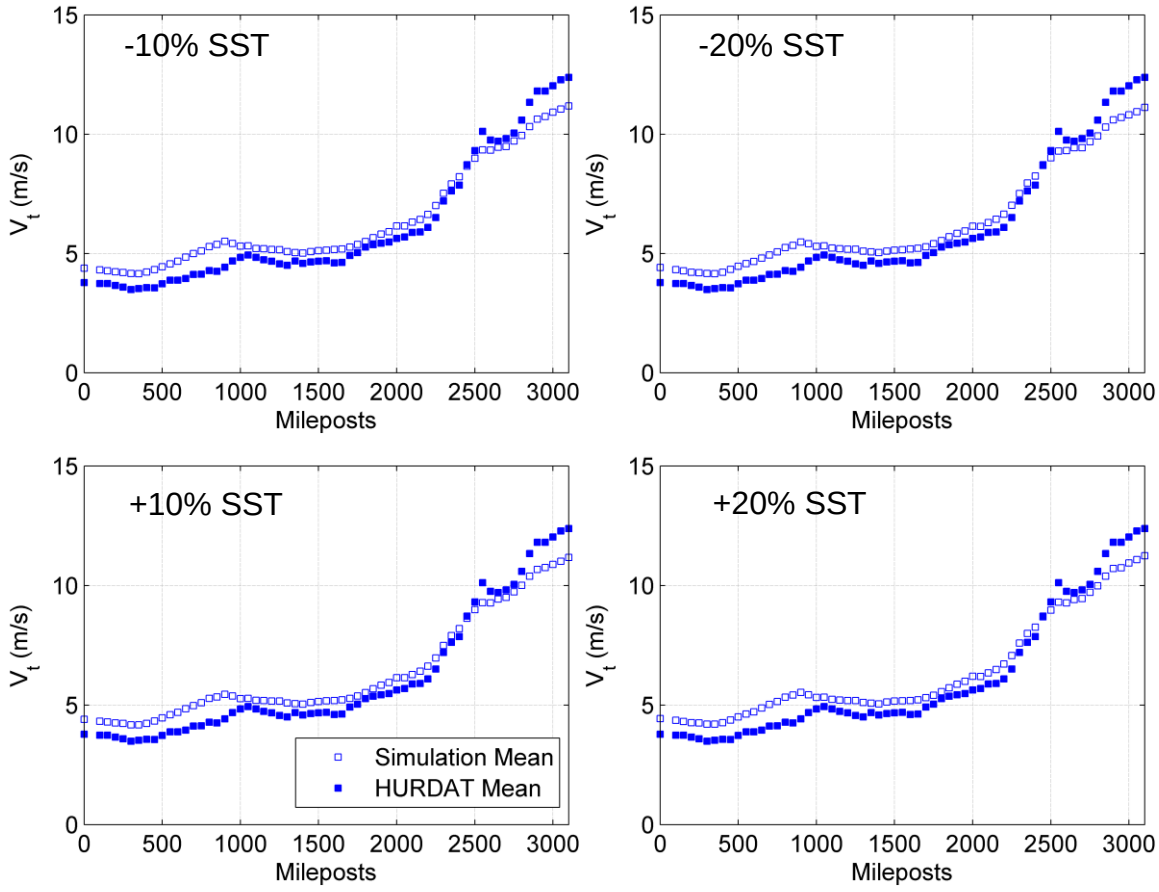


Figure F. 3: Statistics of translational wind speed at mileposts along the coastline in the sensitivity studies on annual formation rate.

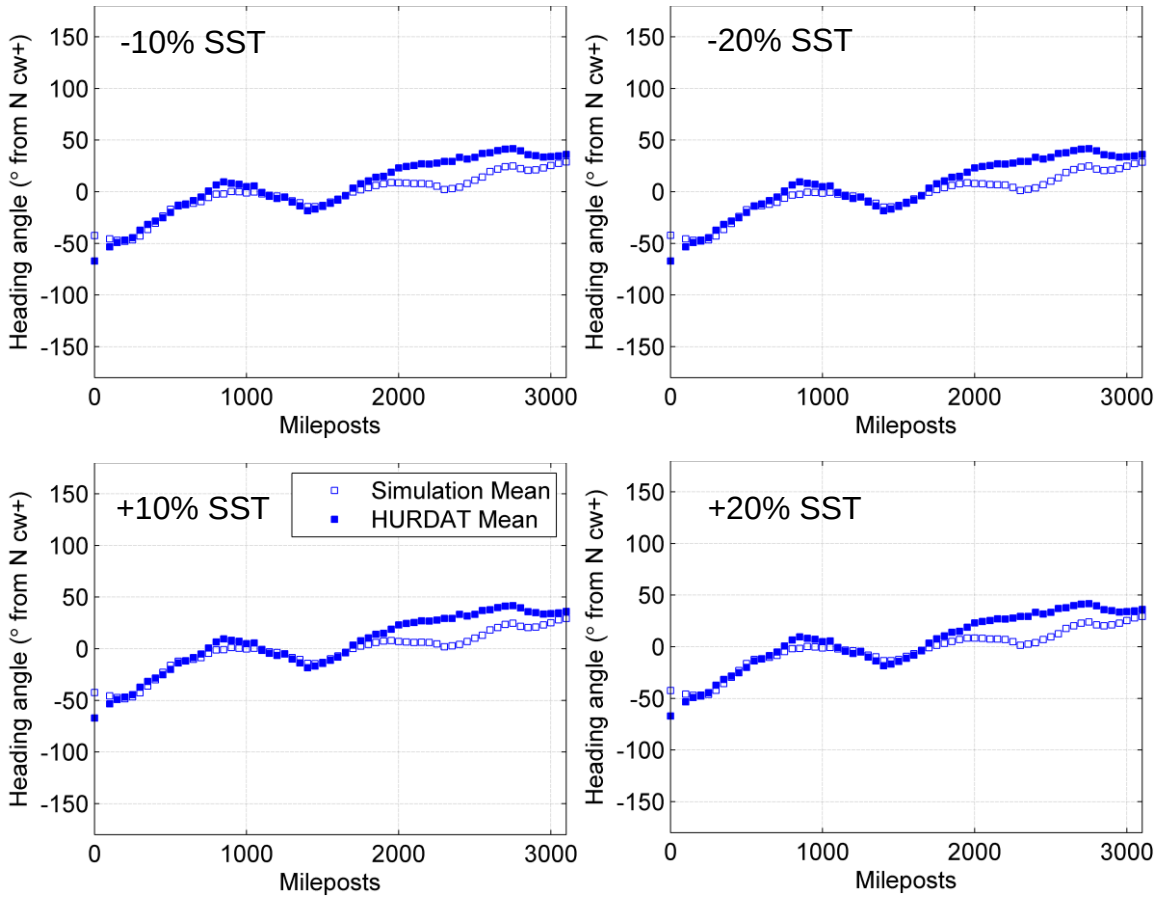


Figure F. 4: Statistics of heading angle at mileposts along the coastline in the sensitivity studies on annual formation rate.

# APPENDIX G

## Sea Surface Temperature with Adjustment of of ±10% and ±20% based on Historical Mean Record

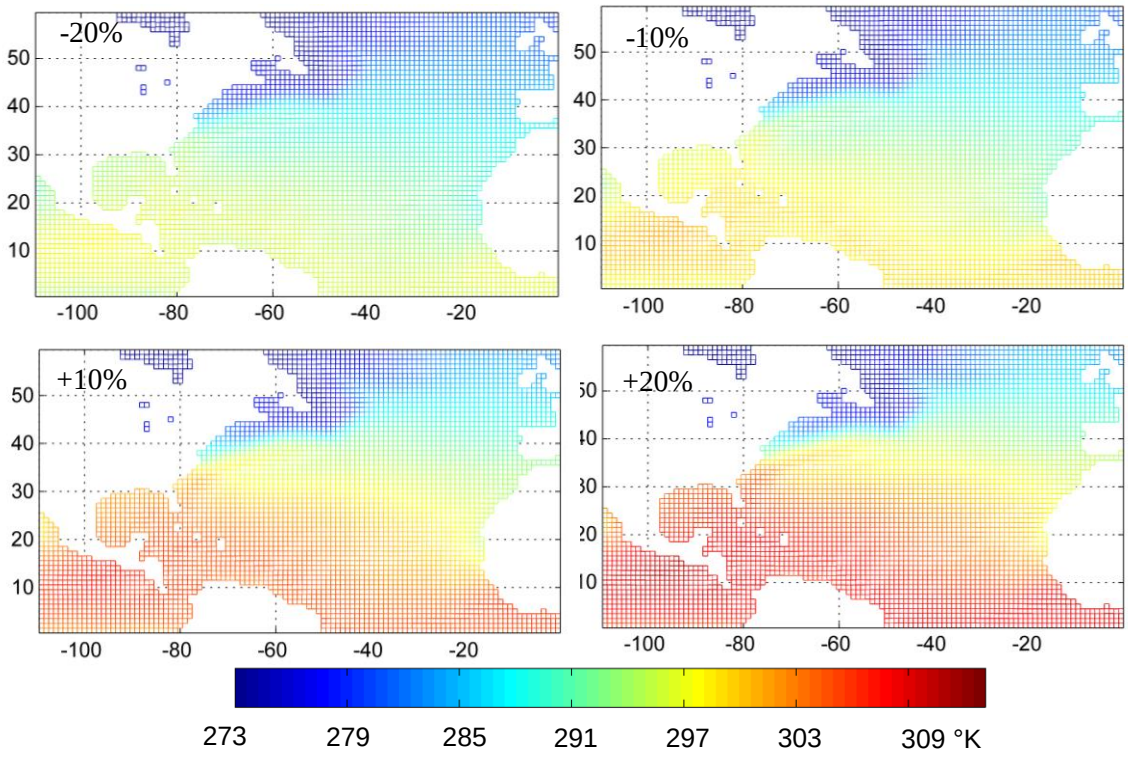


Figure G. 1: Grid maps of SST in May with adjustment of -20%, -10%, +10% and +20% based on the historical mean record.

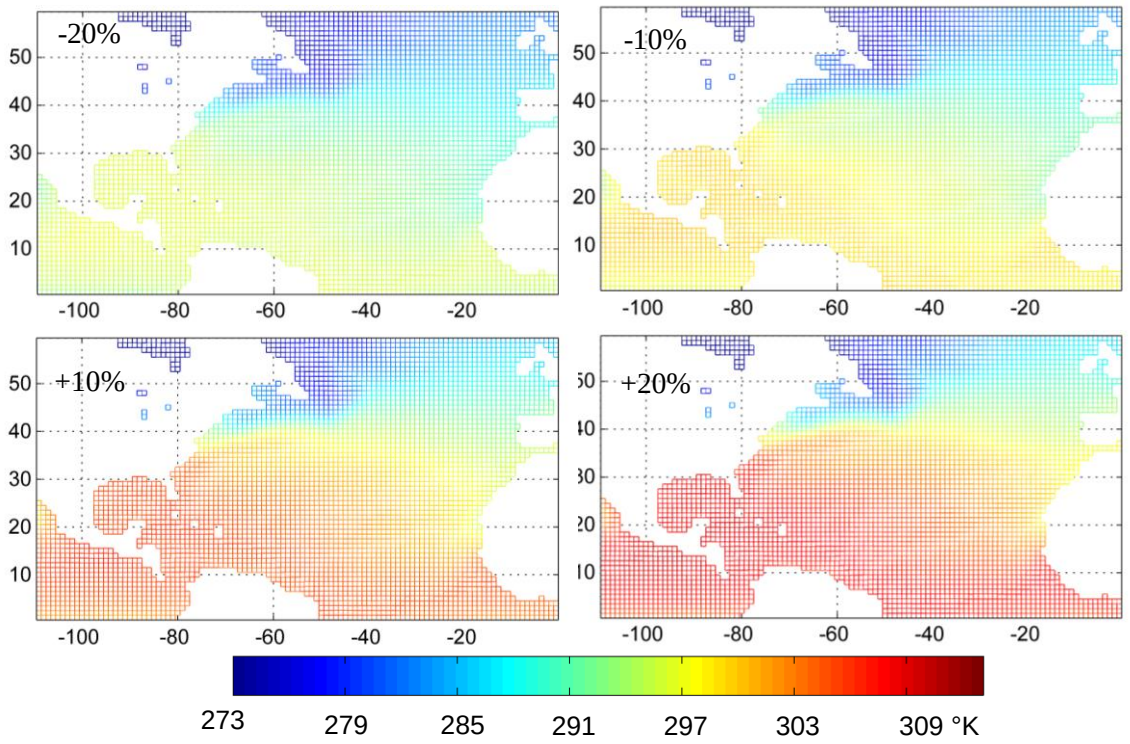


Figure G. 2: Grid maps of SST in June with adjustment of -20%, -10%, +10% and +20% based on the historical mean record.

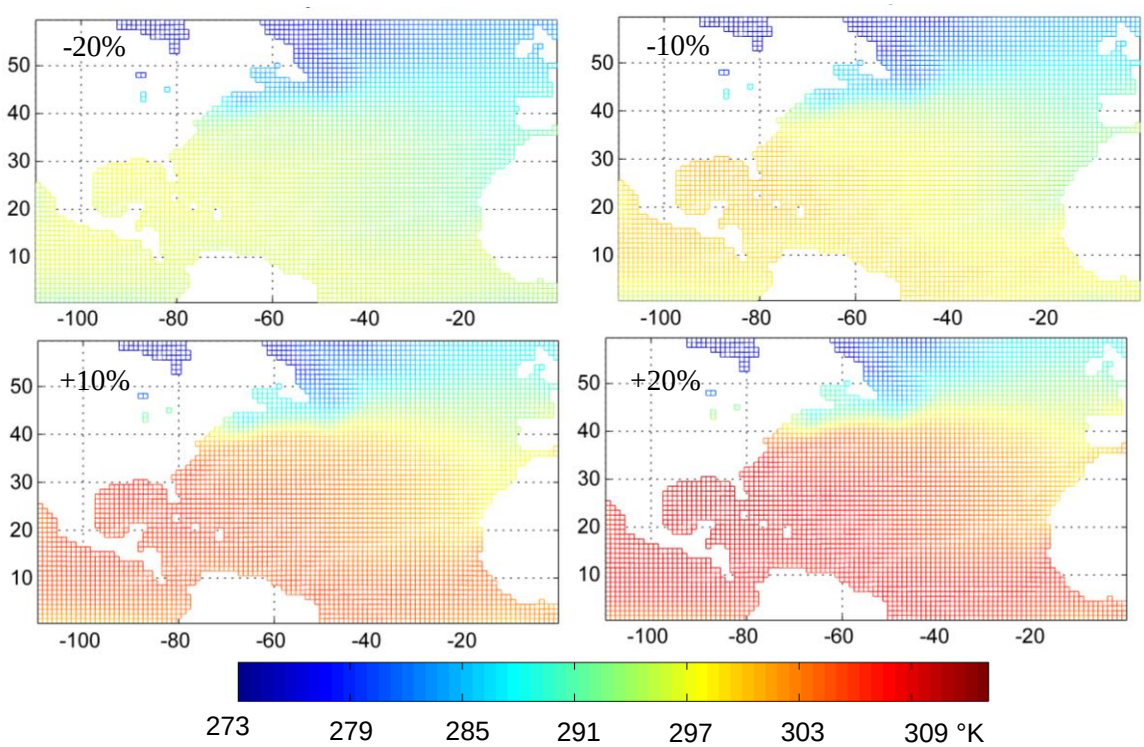


Figure G. 3: Grid maps of SST in July with adjustment of -20%, -10%, +10% and +20% based on the historical mean record.

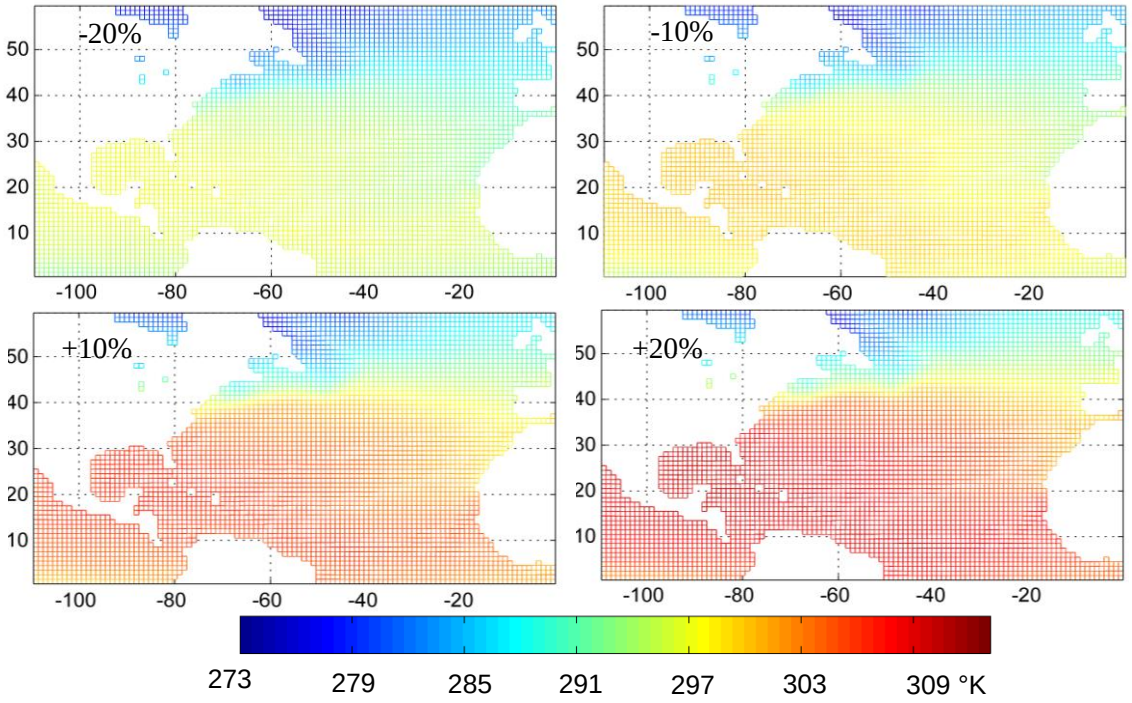


Figure G. 4: Grid maps of SST in September with adjustment of -20%, -10%, +10% and +20% based on the historical mean record.

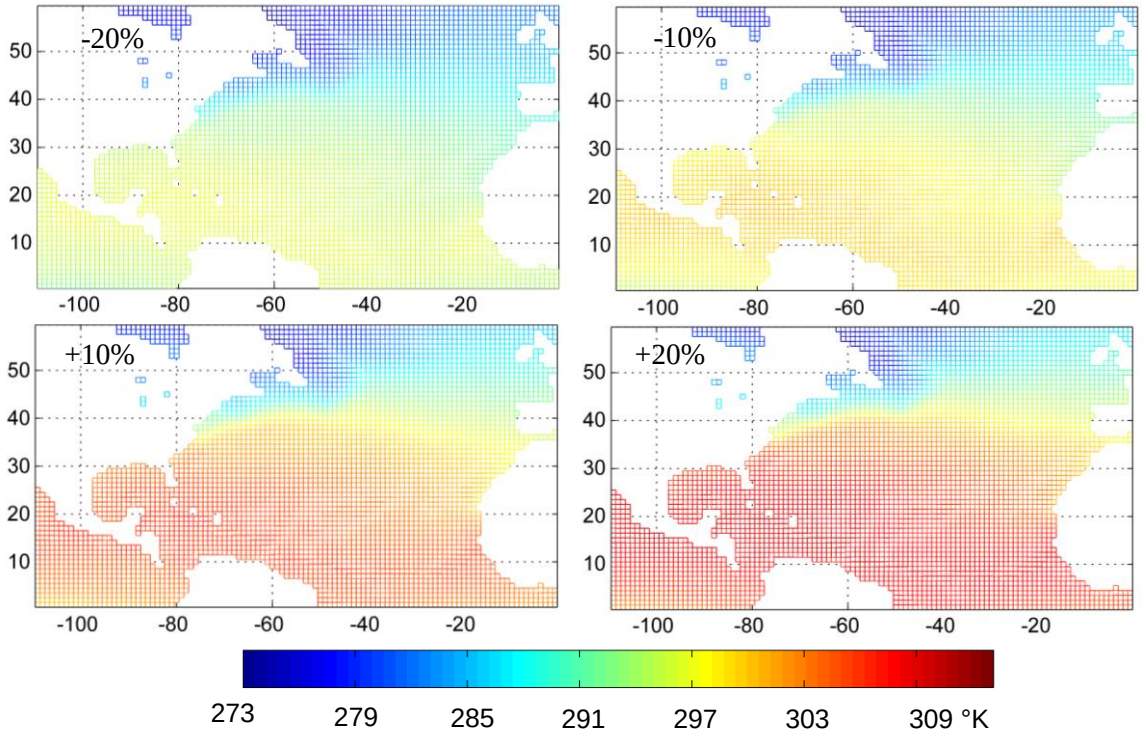


Figure G. 5: Grid maps of SST in October with adjustment of -20%, -10%, +10% and +20% based on the historical mean record.

# APPENDIX H

## Assessment of Tracking Model

The assessments of storm tracks using tracking model and initial tracking information of historical storms were performed in this session. To better demonstrate the simulation pattern and the geographic extent, 500 simulated paths were shown on each plot. The legends of all figures in this session are shown below.

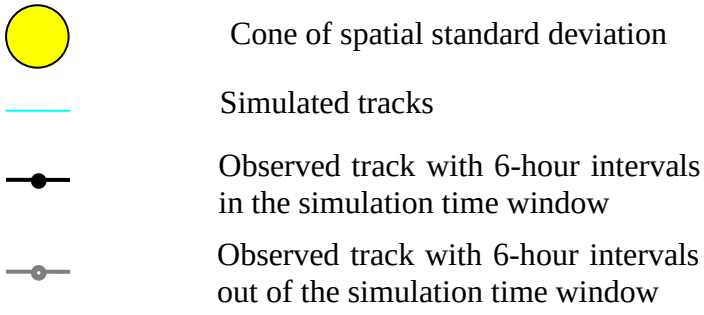


Figure H. 1: Hurricane Charley
2 days simulation from 2004-08-13 12:00 UTC

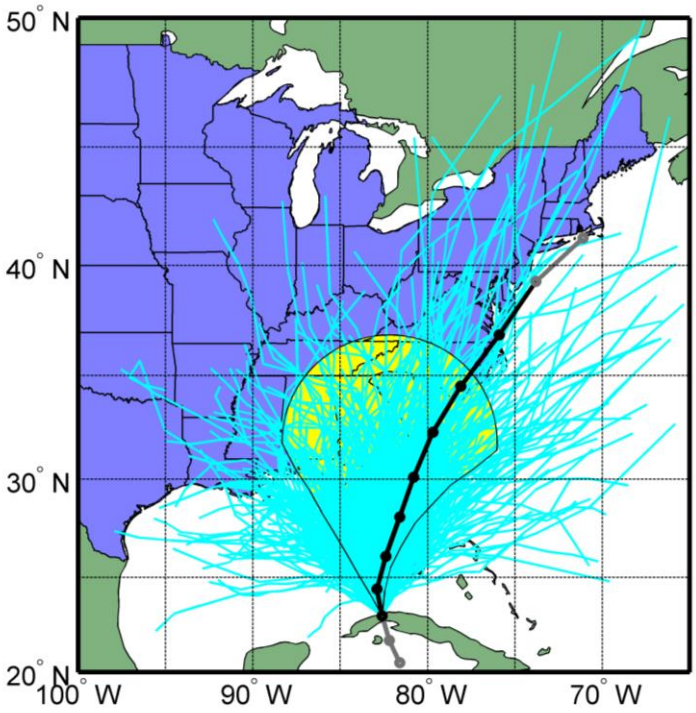

Figure H. 2: Hurricane Jeanne

3 days simulation
from 2004-09-23 18:00 UTC

3 days simulation
from 2004-09-26 00:00 UTC

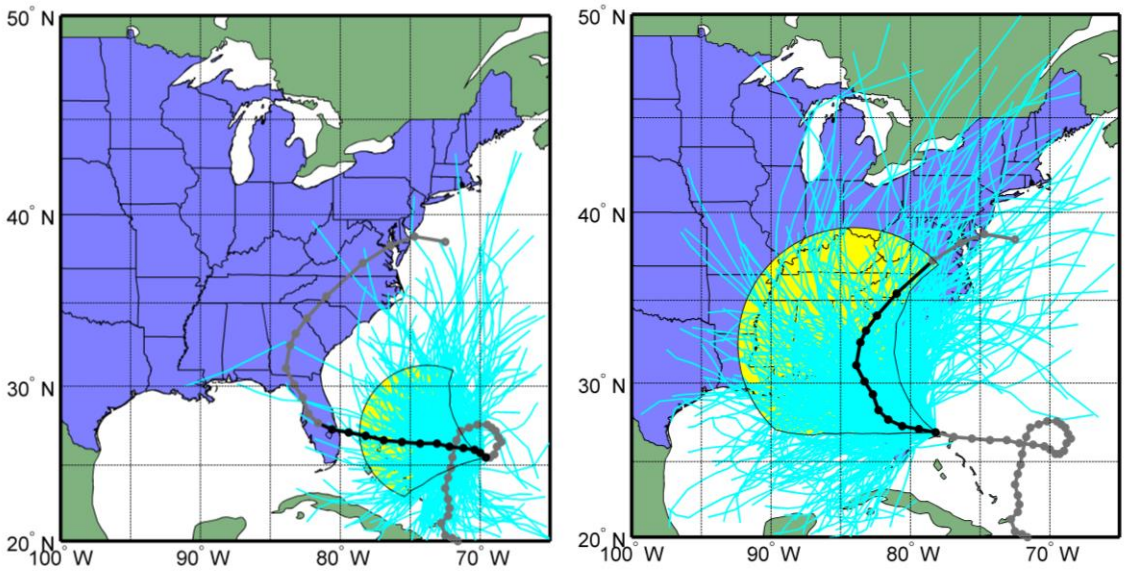


Figure H. 3: Hurricane Frances
3 days simulation from 2004-09-04 00:00 UTC

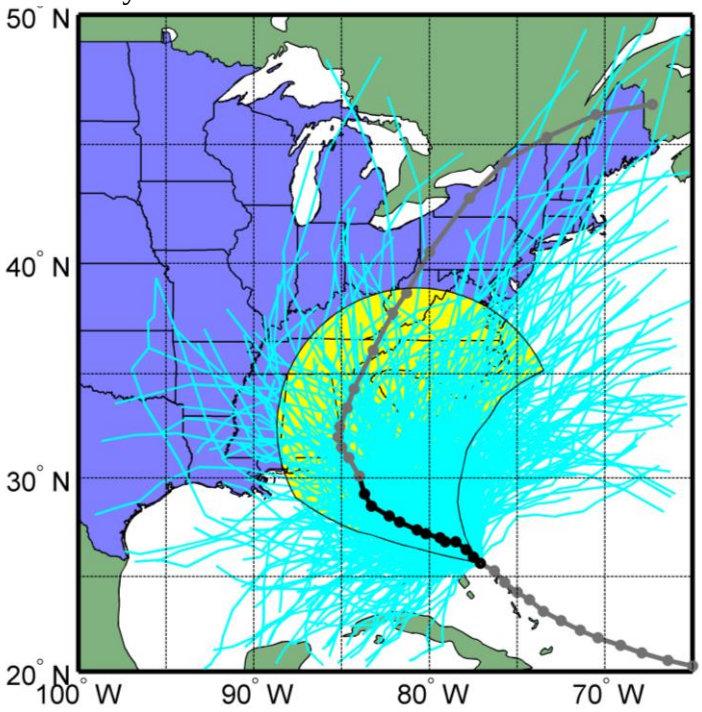

Figure H. 4: Tropical Storm Arlene
3 days simulation from 2005-06-11 06:00 UTC

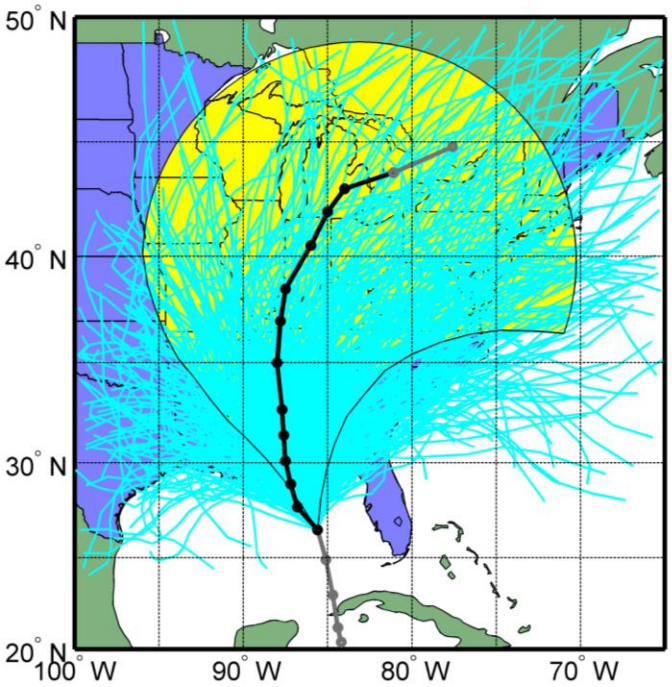


Figure H. 5: Tropical Storm Matthew
54 hours simulation from 2005-10-09 06:00 UTC

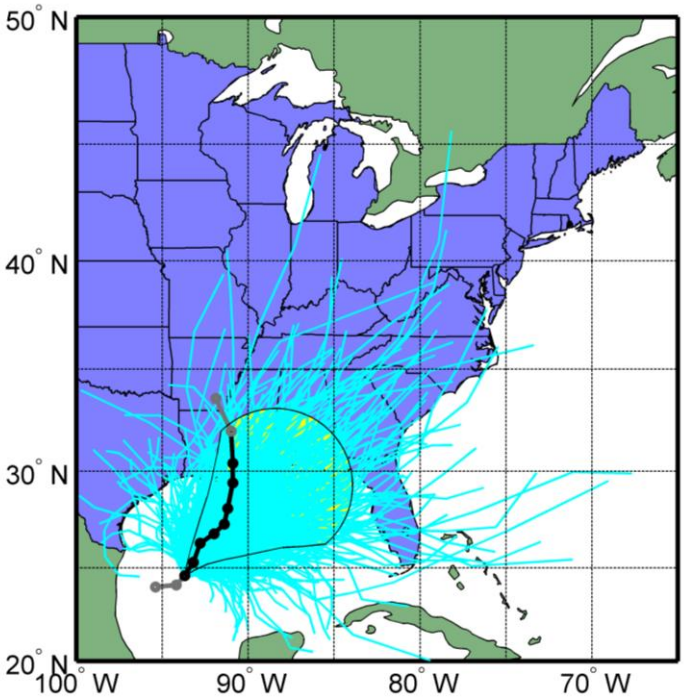

Figure H. 6: Hurricane Cindy
3 days simulation from 2005-07-05 18:00 UTC

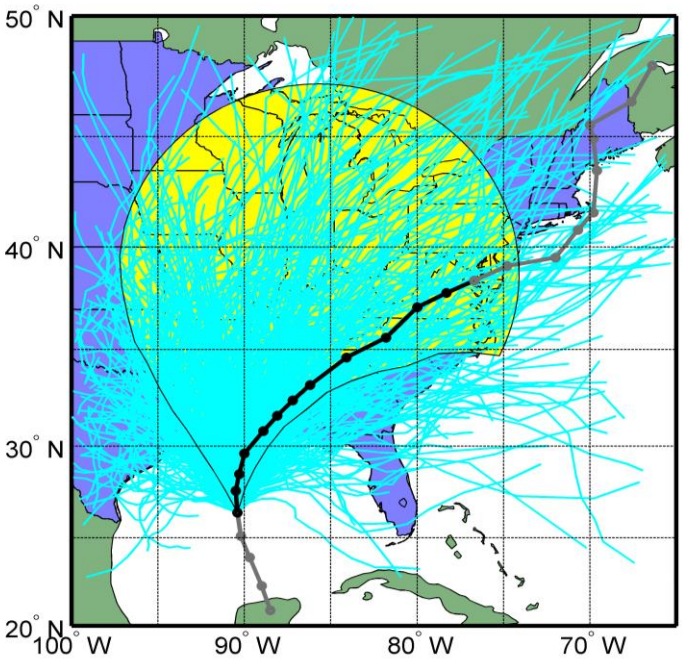


Figure H. 7: Hurricane Dennis
3 days simulation from 2005-07-10 18:00 UTC

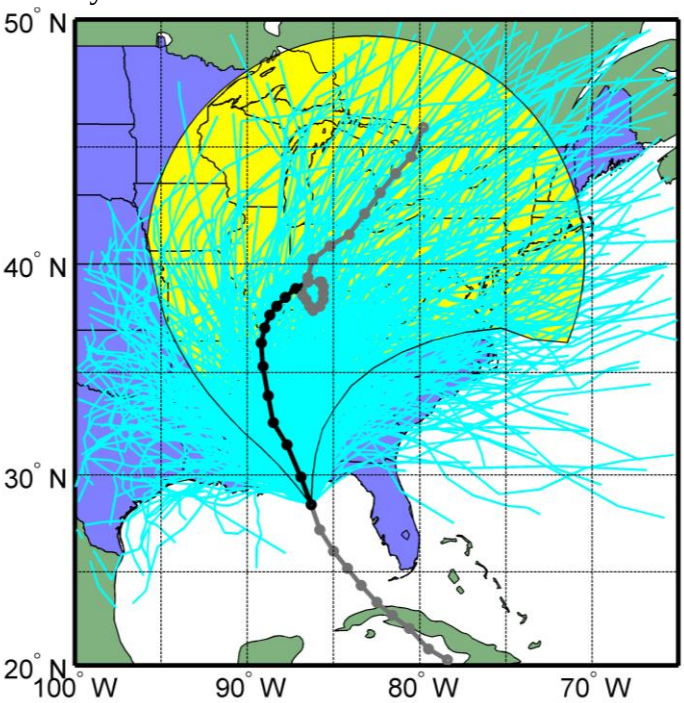

Figure H. 8: Hurricane Emily
3 days simulation from 2005-07-19 00:00 UTC

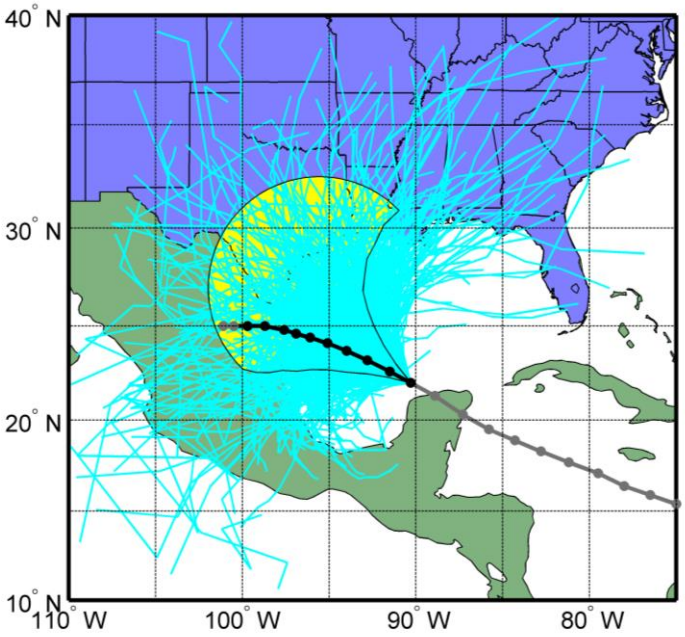


Figure H. 9: Hurricane Katrina
3 days simulation from 2005-08-28 18:00 UTC

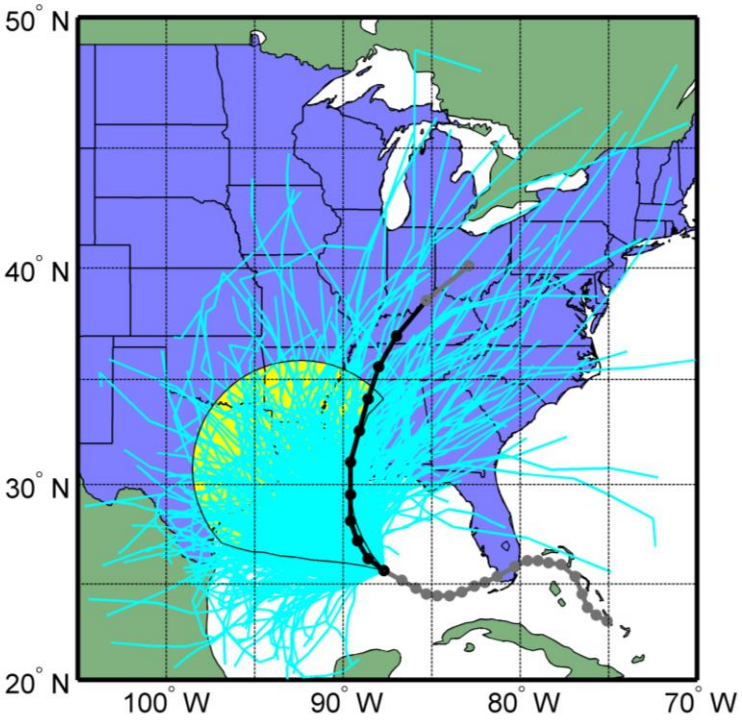

Figure H. 10: Hurricane Ophelia
3 days simulation from 2005-09-10 00:00 UTC

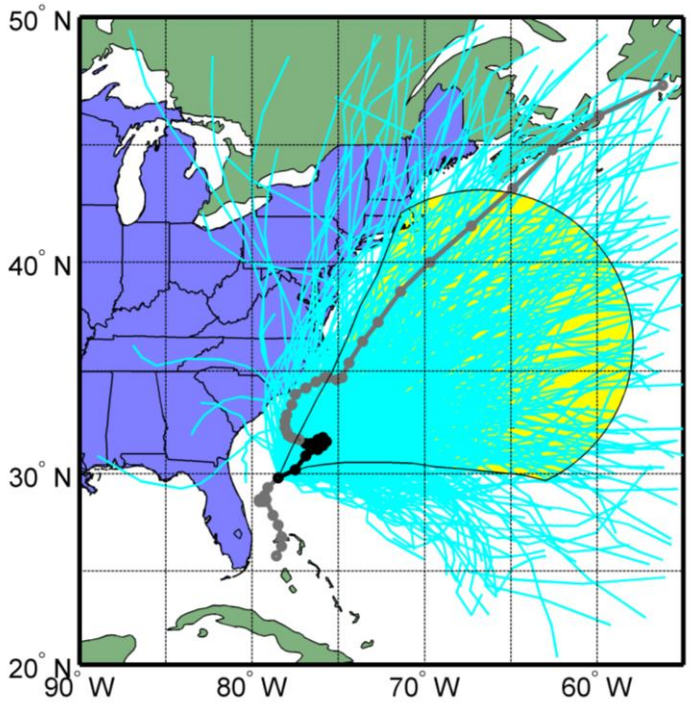


Figure H. 11: Hurricane Rita
3 days simulation from 2005-09-23 12:00 UTC

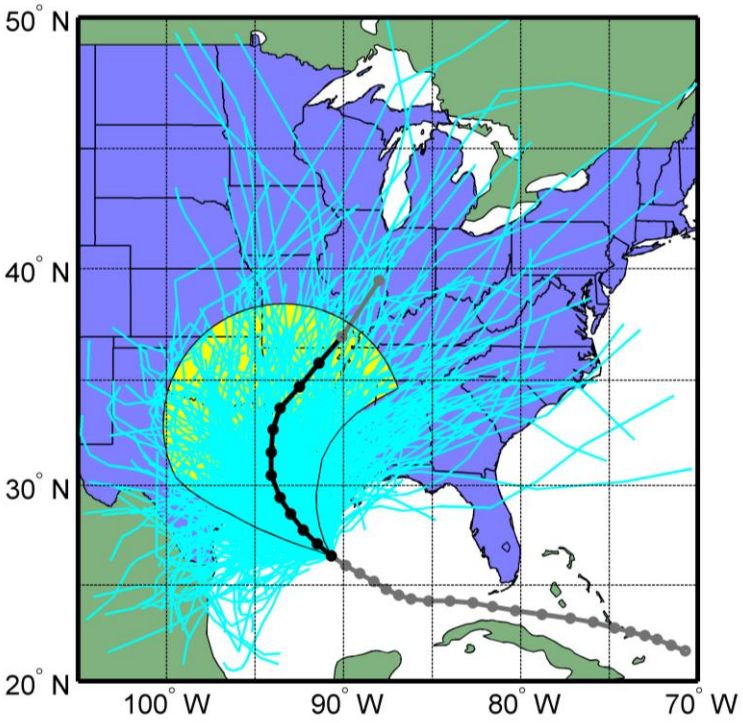

Figure H. 12: Tropical Storm Tammy
30 hours simulation from 2005-10-05 18:00 UTC

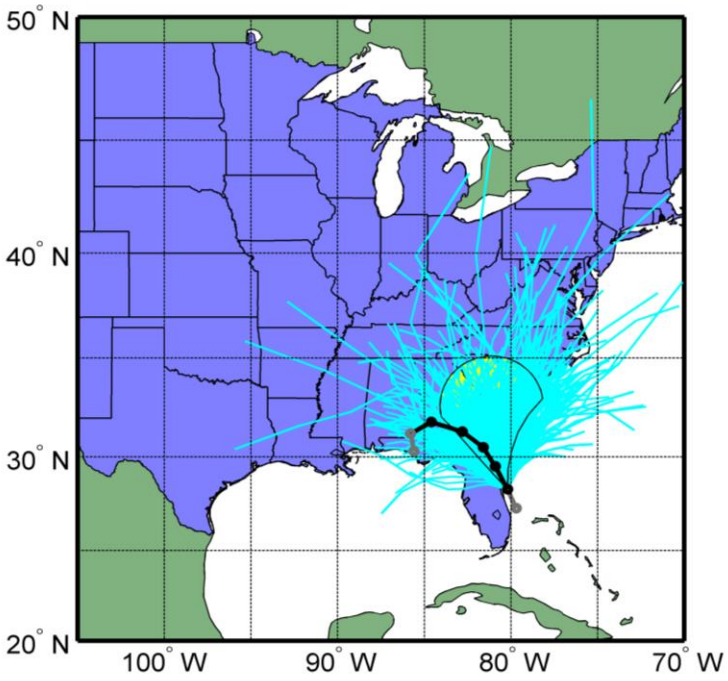


Figure H. 13: Hurricane Wilma
3 days simulation from 2005-10-23 18:00 UTC

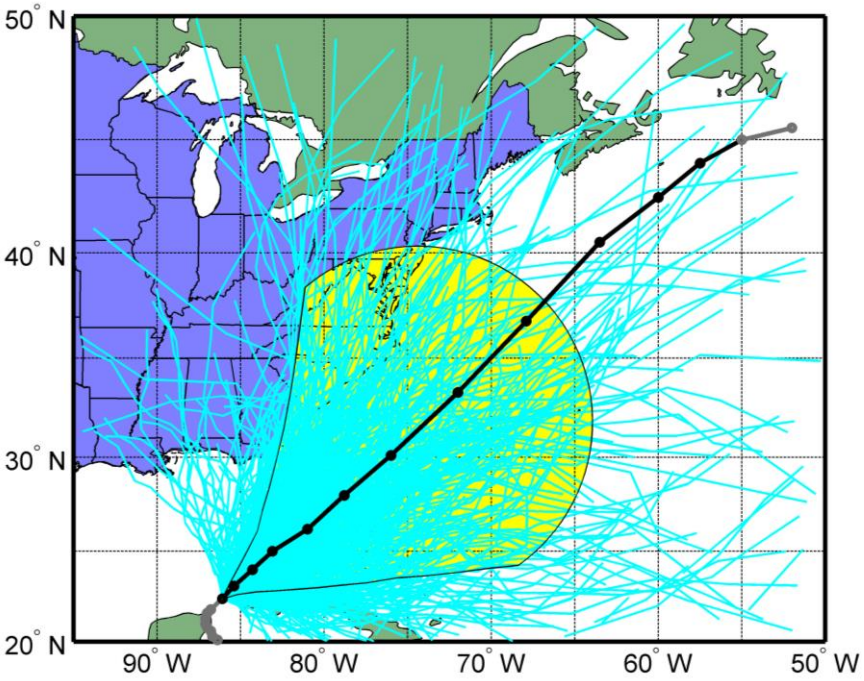

# APPENDIX I

## Assessment of Central Pressure Model

The assessments of storm central pressure using relative intensity model, central pressure decay model and initial information of historical storms were performed in this session. One thousand realizations were shown on each plot. The legends of all figures in this session are shown below.

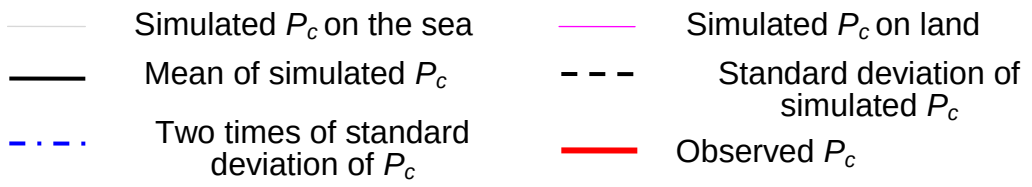


Figure I. 1: Hurricane Charley (2004)

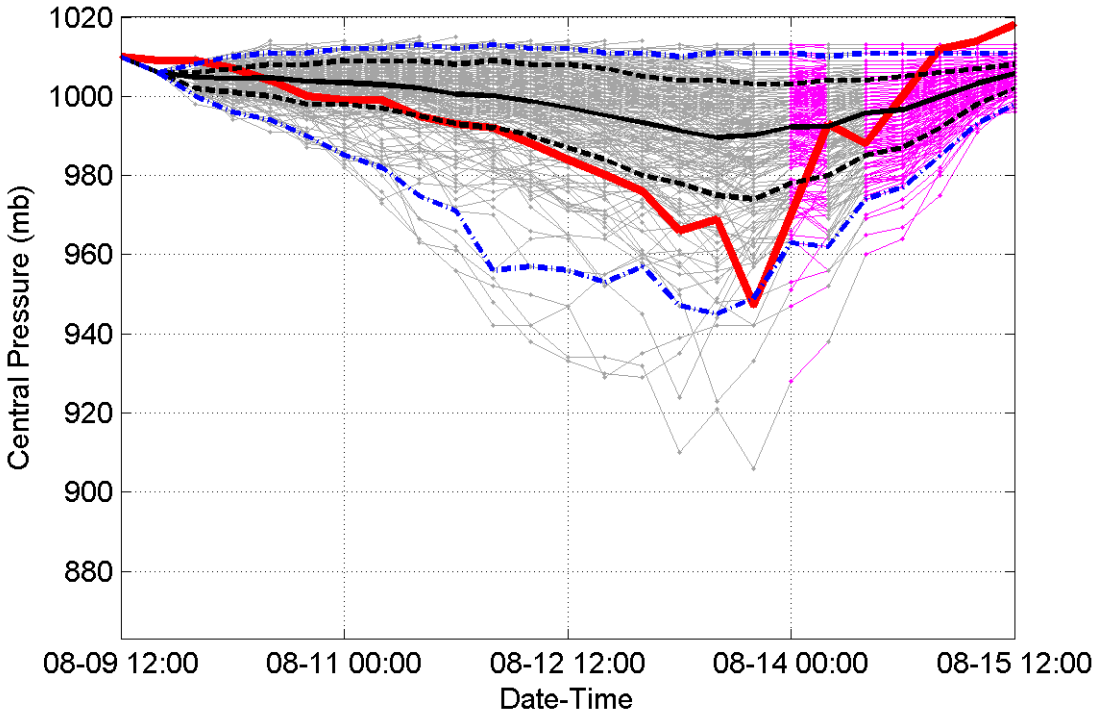

Figure I. 3: Hurricane Frances (2004)

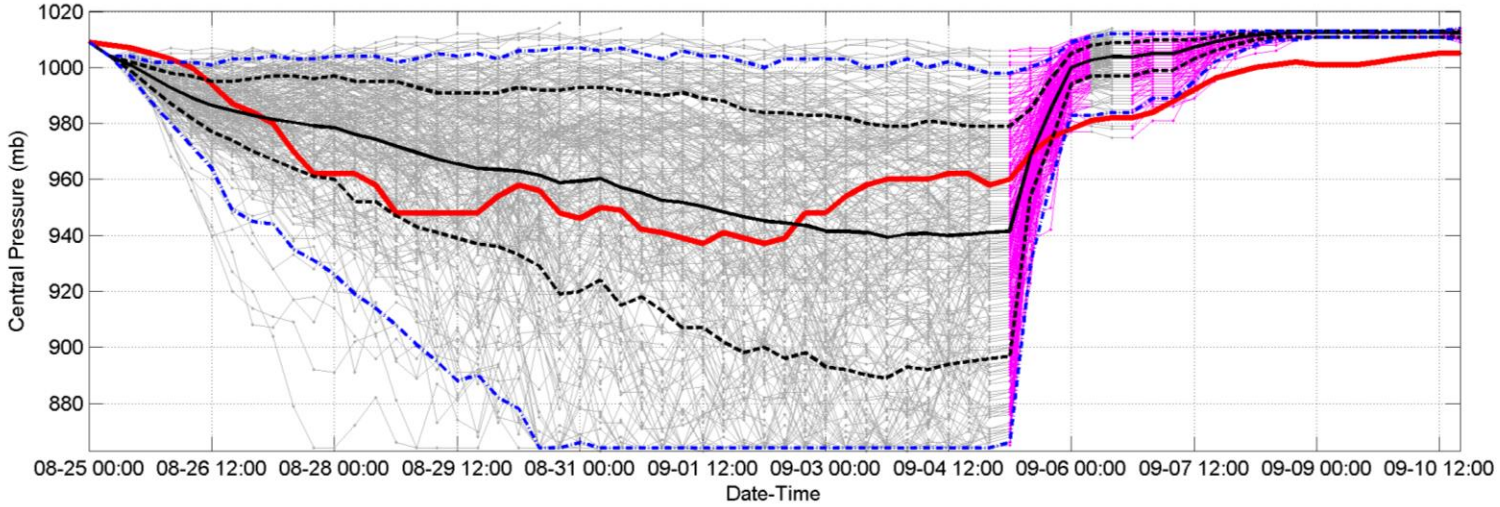


Figure I. 2: Hurricane Jeanne (2004)

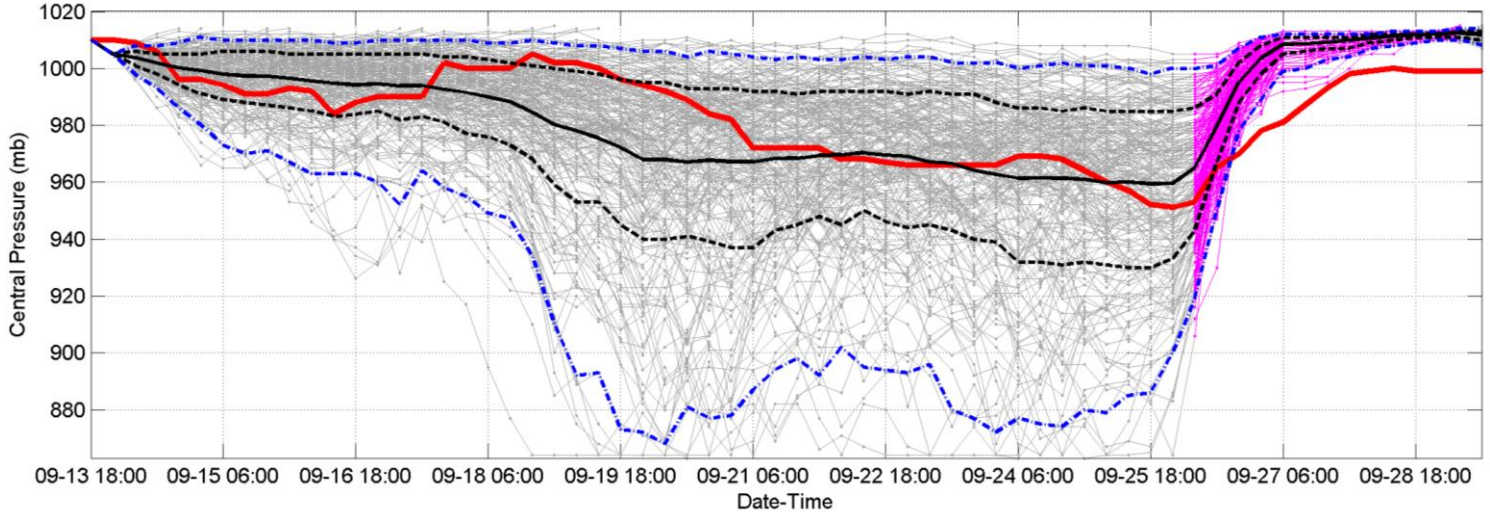

Figure I. 5: Tropical Storm Matthew (2004)

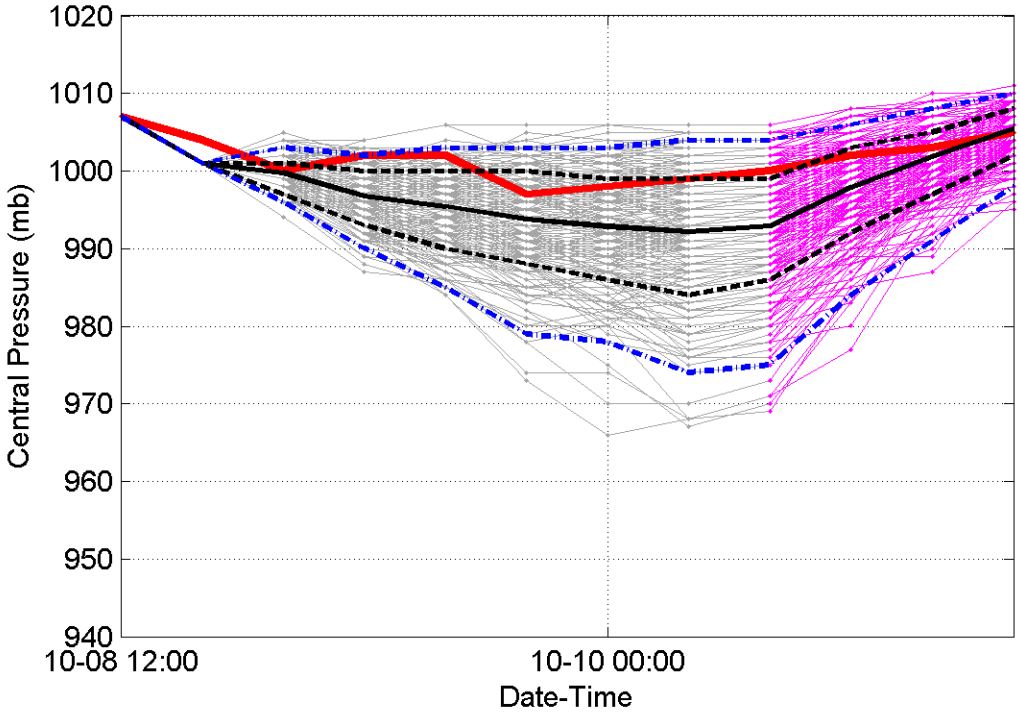


Figure I. 4: Hurricane Cindy (2005)

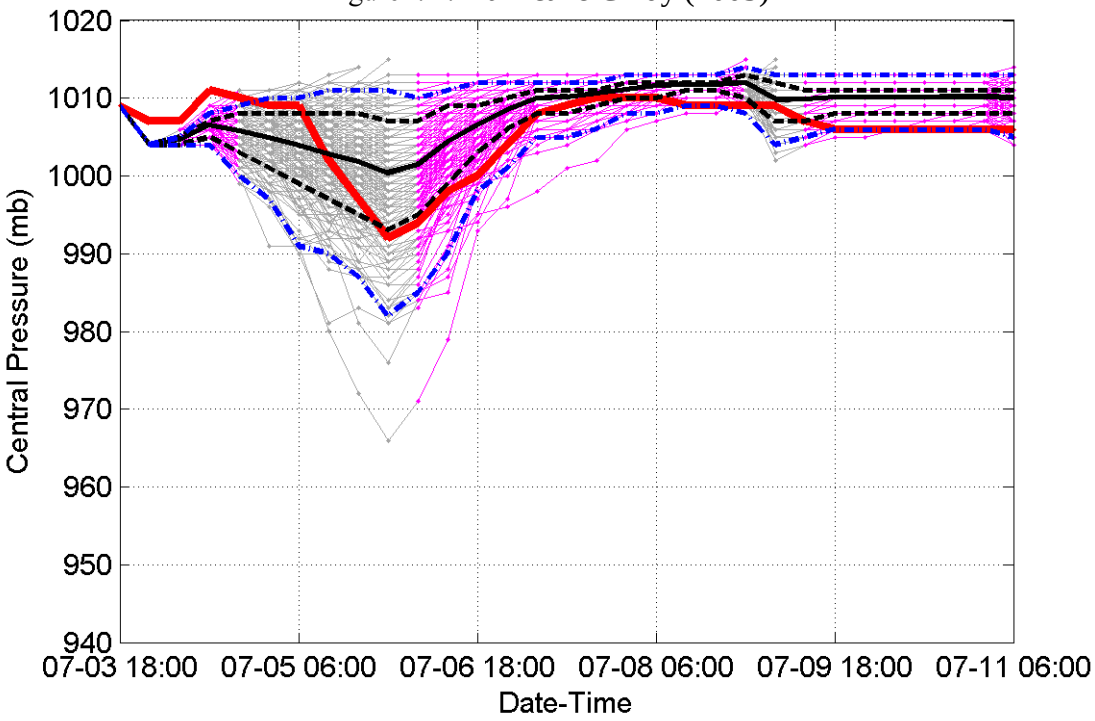

Figure I. 6: Hurricane Dennis (2005)

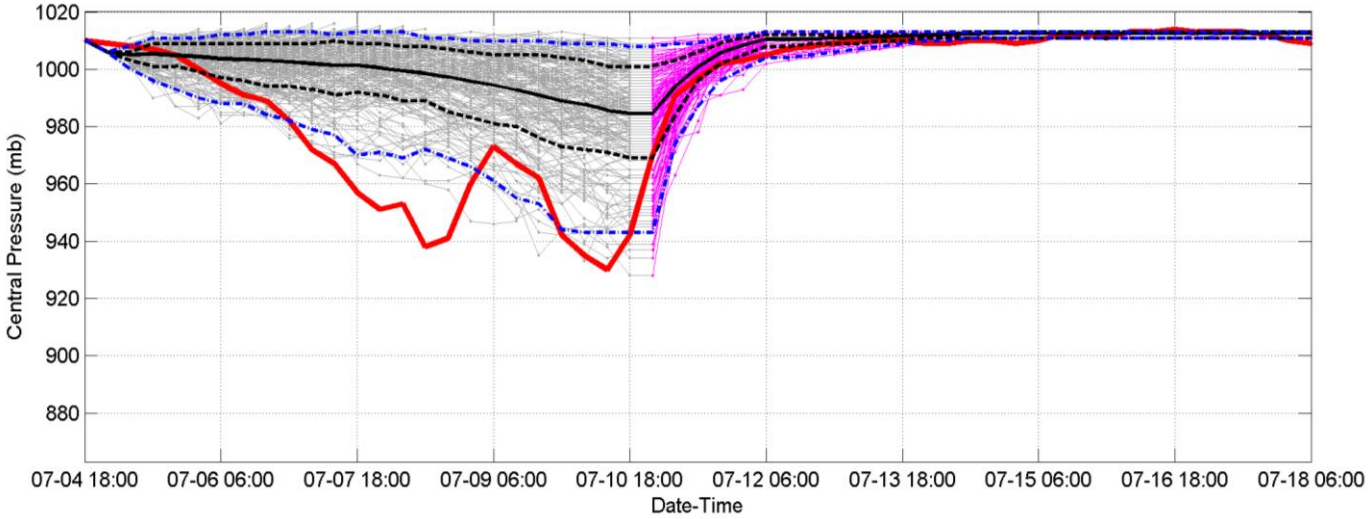


Figure I. 7: Hurricane Emily (2005)

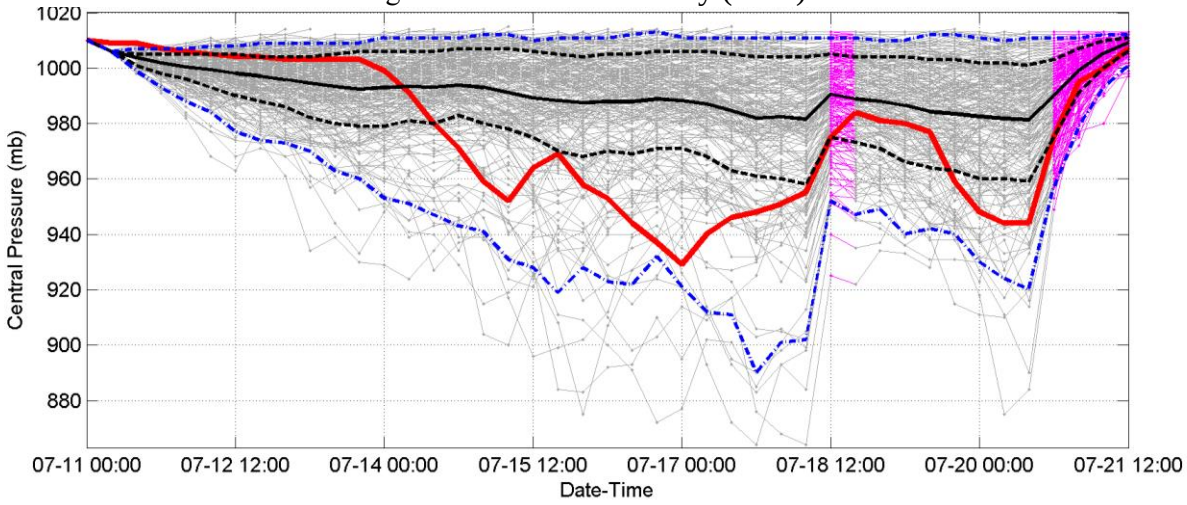

Figure I. 9: Hurricane Rita (2005)

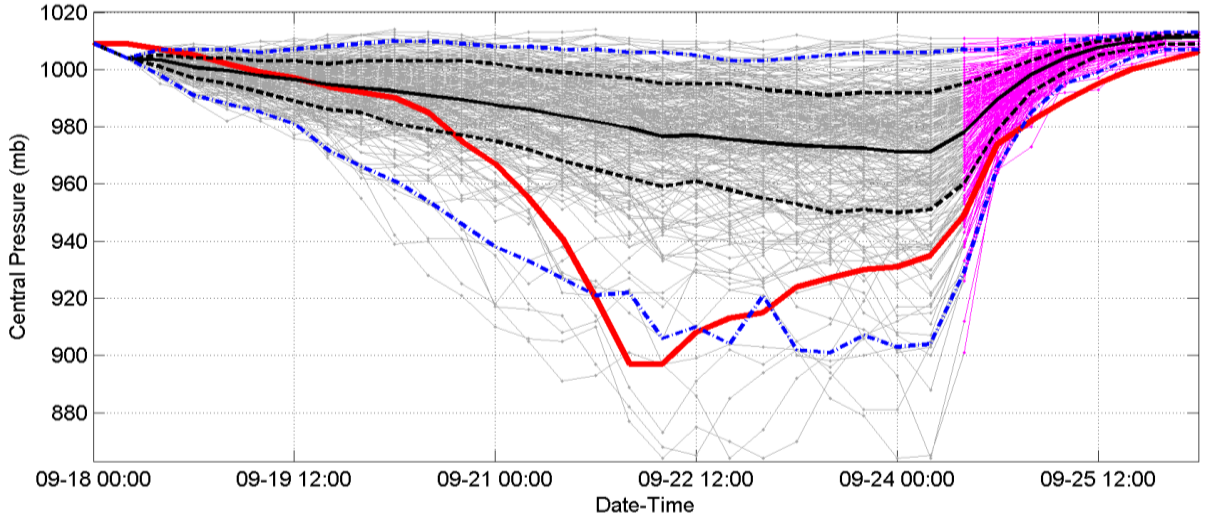


Figure I. 8: Hurricane Wilma (2005)

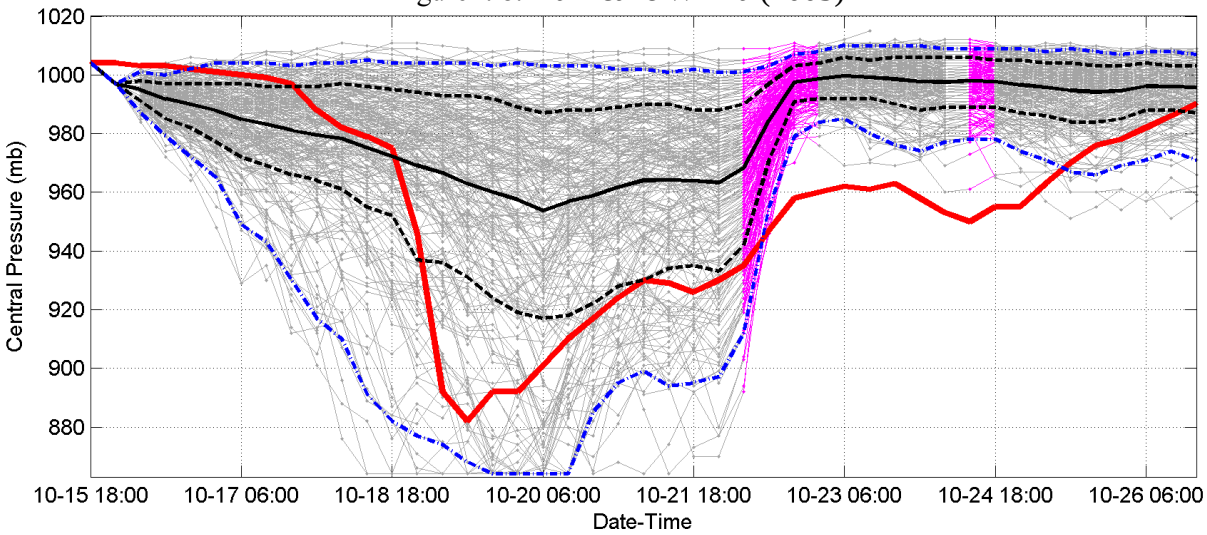

Figure I. 10: Tropical Storm Tammy (2005)

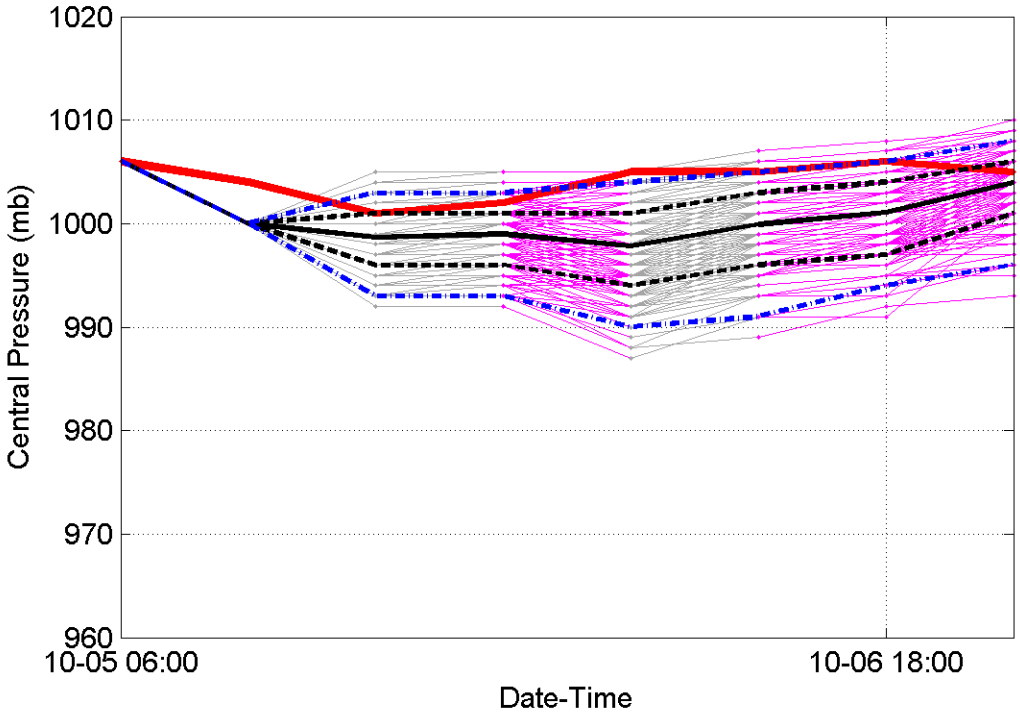

APPENDIX J

Configurations of Building Components in HAZUS

In this section, the detailed configurations of building conponents are extracted from HAZUS program. The path to extract the information in HAZUS is: Inventory-General Building Stock-Wind Building Characteristics Distribution-Scheme.

Table J.8.1: Building configurations of wood one story single-family house (WSF1)

| Categories | Building Characteristic | % (no-retrofit) | % (retrofitted) |
|---|---|---|---|
| Roof Shape | Hip | 19 | 19 |
| | Gable | 81 | 81 |
| | Total | 100 | 100 |
| Secondary Water Resistance | Yes | 0 | 100 |
| | No | 100 | 0 |
| | Total | 100 | 100 |
| Roof Deck Attachment | 6d @ 6"/12" | 37 | 0 |
| | 8d @ 6"/12" | 33 | 0 |
| | 6d/8d Mix @ 6"/6" | 0 | 0 |
| | 8D @ 6"/6" | 30 | 100 |
| | Total | 100 | 100 |
| Roof-Wall Connection | Toe-nail | 23 | 0 |
| | Strap | 77 | 100 |
| | Total | 100 | 100 |
| Garage, Houses w/o Shutters | None | 48 | 48 |
| | Weak | 26 | 26 |
| | Standard | 26 | 26 |
| | Total | 100 | 100 |
| Garage, Houses with Shutters | None | 48 | 48 |
| | SFBC 1994 | 52 | 52 |
| | Total | 100 | 100 |
| Shutters | Yes | 5 | 100 |
| | No | 95 | 0 |
| | Total | 100 | 100 |

Table J.8.2: Building configurations of wood two or more stories single-family house (WSF2)

| Categories | Building Characteristic | % (no-retrofit) | % (retrofitted) |
|---|---|---|---|
| Roof Shape | Hip | 18 | 18 |
| | Gable | 82 | 82 |
| | Total | 100 | 100 |
| Secondary Water Resistance | Yes | 0 | 100 |
| | No | 100 | 0 |
| | Total | 100 | 100 |
| Roof Deck Attachment | 6d @ 6"/12" | 37 | 0 |
| | 8d @ 6"/12" | 33 | 0 |
| | 6d/8d Mix @ 6"/6" | 0 | 0 |
| | 8D @ 6"/6" | 30 | 100 |
| | Total | 100 | 100 |
| Roof-Wall Connection | Toe-nail | 23 | 0 |
| | Strap | 77 | 100 |
| | Total | 100 | 100 |
| Garage, Houses w/o Shutters | None | 48 | 48 |
| | Weak | 26 | 26 |
| | Standard | 26 | 26 |
| | Total | 100 | 100 |
| Garage, Houses with Shutters | None | 48 | 48 |
| | SFBC 1994 | 52 | 52 |
| | Total | 100 | 100 |
| Shutters | Yes | 5 | 100 |
| | No | 95 | 0 |
| | Total | 100 | 100 |

Table J.8.3: Building configurations of wood multi-unit two stories house (WMUH2)

| Categories | Building Characteristic | % (no-retrofit) | % (retrofitted) |
|---|---|---|---|
| Roof Shape | Hip | 10 | 10 |
| | Gable | 81 | 81 |
| | Flat | 9 | 9 |
| | Total | 100 | 100 |
| Roof Cover Type | BUR | 85 | 85 |
| | SPM | 15 | 15 |
| | Total | 100 | 100 |
| Roof Cover Quality | Good | 50 | 50 |
| | Poor | 50 | 50 |
| | Total | 100 | 100 |
| Secondary Water Resistance | Yes | 0 | 100 |
| | No | 100 | 0 |
| | Total | 100 | 100 |
| Roof Deck Attachment | 6d @ 6"/12" | 37 | 0 |
| | 8d @ 6"/12" | 63 | 0 |
| | 6d/8d Mix @ 6"/6" | 0 | 0 |
| | 8D @ 6"/6" | 0 | 100 |
| | Total | 100 | 100 |
| Roof-Wall Connection | Toe-nail | 23 | 0 |
| | Strap | 77 | 100 |
| | Total | 100 | 100 |
| Shutters | Yes | 0 | 100 |
| | No | 100 | 0 |
| | Total | 100 | 100 |

Table J.8.4: Building configurations of masonry one-story single-family house (MSF1)

| Categories | Building Characteristic | % (no-retrofit) | % (retrofitted) |
|---|---|---|---|
| Roof Shape | Hip | 38 | 38 |
| | Gable | 62 | 62 |
| | Total | 100 | 100 |
| Secondary Water Resistance | Yes | 0 | 100 |
| | No | 100 | 0 |
| | Total | 100 | 100 |
| Roof Deck Attachment | 6d @ 6"/12" | 25 | 0 |
| | 8d @ 6"/12" | 32 | 0 |
| | 6d/8d Mix @ 6"/6" | 0 | 0 |
| | 8D @ 6"/6" | 43 | 100 |
| | Total | 100 | 100 |
| Roof-Wall Connection | Toe-nail | 10 | 0 |
| | Strap | 90 | 100 |
| | Total | 100 | 100 |
| Garage, Houses w/o Shutters | None | 48 | 48 |
| | Weak | 26 | 26 |
| | Standard | 26 | 26 |
| | Total | 100 | 100 |
| Garage, Houses with Shutters | None | 48 | 48 |
| | SFBC 1994 | 52 | 52 |
| | Total | 100 | 100 |
| Shutters | Yes | 30 | 100 |
| | No | 70 | 0 |
| | Total | 100 | 100 |
| Masonry Reinforcing | Yes | 68 | 68 |
| | No | 32 | 32 |
| | Total | 100 | 100 |

Table J.8.5: Building configurations of masonry two or more stories single-family house (MSF2)

| Categories | Building Characteristic | % (no-retrofit) | % (retrofitted) |
|---|---|---|---|
| Roof Shape | Hip | 38 | 38 |
| | Gable | 62 | 62 |
| | Total | 100 | 100 |
| Secondary Water Resistance | Yes | 0 | 100 |
| | No | 100 | 0 |
| | Total | 100 | 100 |
| Roof Deck Attachment | 6d @ 6"/12" | 25 | 0 |
| | 8d @ 6"/12" | 32 | 0 |
| | 6d/8d Mix @ 6"/6" | 0 | 0 |
| | 8D @ 6"/6" | 43 | 100 |
| | Total | 100 | 100 |
| Roof-Wall Connection | Toe-nail | 15 | 0 |
| | Strap | 85 | 100 |
| | Total | 100 | 100 |
| Garage, Houses w/o Shutters | None | 48 | 48 |
| | Weak | 26 | 26 |
| | Standard | 26 | 26 |
| | Total | 100 | 100 |
| Garage, Houses with Shutters | None | 48 | 48 |
| | SFBC 1994 | 52 | 52 |
| | Total | 100 | 100 |
| Shutters | Yes | 30 | 100 |
| | No | 70 | 0 |
| | Total | 100 | 100 |

Table J.8.6: Building configurations of steel engineered commercial building low-rise (SECBL)

| Categories | Building Characteristic | % (no-retrofit) | % (retrofitted) |
|---|---|---|---|
| Roof Cover Type | BUR | 85 | 85 |
| | SPM | 15 | 15 |
| | Total | 100 | 100 |
| Window Area | Low | 77 | 77 |
| | Medium | 11 | 11 |
| | High | 12 | 12 |
| | Total | 100 | 100 |
| Shutters | Yes | 0 | 100 |
| | No | 100 | 0 |
| | Total | 100 | 100 |
| Wind Debris | Res./Comm. | 12 | 12 |
| | Varies by direction | 42 | 42 |
| | Residential | 30 | 30 |
| | None | 16 | 16 |
| | Total | 100 | 100 |
| Metal Roof Deck Attachment | Standard | 100 | 0 |
| | Superior | 0 | 100 |
| | Total | 100 | 100 |

Table J.8.7: Building configurations of Manufactured home (MH76HUD)

| Categories | Building Characteristic | % (no-retrofit) | % (retrofitted) |
|---|---|---|---|
| Shutters | Yes | 0 | 100 |
| | No | 100 | 0 |
| | Total | 100 | 100 |
| Tie Downs | Yes | 75 | 100 |
| | No | 25 | 0 |
| | Total | 100 | 100 |

Table J.8.8: Building configurations of wood multi-unit three or more stories house (WMUH3)

| Categories | Building Characteristic | % (no-retrofit) | % (retrofitted) |
|---|---|---|---|
| Roof Shape | Hip | 5 | 5 |
| | Gable | 52 | 52 |
| | Flat | 43 | 43 |
| | Total | 100 | 100 |
| Roof Cover Type | BUR | 85 | 85 |
| | SPM | 15 | 15 |
| | Total | 100 | 100 |
| Roof Cover Quality | Good | 50 | 50 |
| | Poor | 50 | 50 |
| | Total | 100 | 100 |
| Secondary Water Resistance | Yes | 0 | 100 |
| | No | 100 | 0 |
| | Total | 100 | 100 |
| Roof Deck Attachment | 6d @ 6"/12" | 27 | 0 |
| | 8d @ 6"/12" | 73 | 0 |
| | 6d/8d Mix @ 6"/6" | 0 | 0 |
| | 8D @ 6"/6" | 0 | 100 |
| | Total | 100 | 100 |
| Roof-Wall Connection | Toe-nail | 40 | 0 |
| | Strap | 60 | 100 |
| | Total | 100 | 100 |
| Shutters | Yes | 0 | 100 |
| | No | 100 | 0 |
| | Total | 100 | 100 |

Table J.8.9: Building configurations of masonry multi-unit two stories house (MMUH2)

| Categories | Building Characteristic | % (no-retrofit) | % (retrofitted) |
|---|---|---|---|
| Roof Shape | Hip | 12 | 12 |
| | Gable | 28 | 28 |
| | Flat | 60 | 60 |
| | Total | 100 | 100 |
| Roof Cover Type | BUR | 85 | 85 |
| | SPM | 15 | 15 |
| | Total | 100 | 100 |
| Roof Cover Quality | Good | 50 | 50 |
| | Poor | 50 | 50 |
| | Total | 100 | 100 |
| Secondary Water Resistance | Yes | 0 | 100 |
| | No | 100 | 0 |
| | Total | 100 | 100 |
| Roof Deck Attachment | 6d @ 6"/12" | 27 | 0 |
| | 8d @ 6"/12" | 73 | 0 |
| | 6d/8d Mix @ 6"/6" | 0 | 0 |
| | 8D @ 6"/6" | 0 | 100 |
| | Total | 100 | 100 |
| Roof-Wall Connection | Toe-nail | 39 | 0 |
| | Strap | 61 | 100 |
| | Total | 100 | 100 |
| Shutters | Yes | 0 | 100 |
| | No | 100 | 0 |
| | Total | 100 | 100 |
| Masonry Reinforcing | Yes | 40 | 40 |
| | No | 60 | 60 |
| | Total | 100 | 100 |